Instabilités tournantes dans un diffuseur lisse de machine centrifuge

Meng Fan

HESAM UNIVERSITÉ

Arts et Métiers Sciences et Technologies

ÉCOLE DOCTORALE SCIENCES ET MÉTIERS DE L'INGÉNIEUR
[Laboratoire de Mécanique des Fluides de Lille - Campus de Lille]

THÈSE

présentée par : **Meng FAN**
soutenue le : **6 décembre 2023**

pour obtenir le grade de : **Docteur d'HESAM Université**

préparée à : **École Nationale Supérieure d'Arts et Métiers**
Spécialité : **Mécanique des fluides**

Instabilités tournantes dans un diffuseur lisse de machine centrifuge

THÈSE dirigée par : Antoine DAZIN

et co-encadrée par : Francesco ROMANO

Jury

M. Jean-Chirstophe ROBINET	Professeur, École nationale supérieure d'Arts et Métiers, Campus de Paris - Dynfluid	Président
M. Marcello MANNA	Professeur, Université de Naples Federico II	Rapporteur
M. Stephane AUBERT	Professeur, Ecole Centrale de Lyon – LMFA	Rapporteur
Mme. Silvia HIRATA	Maîtresse de conférences-HDR, Université de Lille – UML	Examinatrice
M. Antoine DAZIN	Professeur, École nationale supérieure d'Arts et Métiers, Campus de Lille - LMFL	Examinateur
M. Francesco ROMANO	Professeur, École nationale supérieure d'Arts et Métiers, Campus de Lille - LMFL	Examinateur

THÈSE

Acknowledgments

This research project would not have been possible without the support of many people. I wish to express my gratitude to my supervisors Antoine DAZIN, Francesco ROMANO, and Gerard BOIS for their supervision, advice, and guidance from the very early stage of this research as well as for giving me extraordinary experiences throughout the work.

I was lucky to meet Prof. Gerard BOIS seven years ago. He is a very accommodating and knowledgeable professor, thanks for his recommendation, I had the opportunity to join Prof. Antoine DAZIN's research team. Prof. DAZIN gave me a lot of help in my work and life. I would not have been able to complete my experimental research without his support. Moreover, he gave me opportunities to participate in academic conferences and provided with a good lab environment to communicate with peers and professors.

Furthermore, I would like to show my deepest gratitude to my secondary supervisor Prof. Francesco ROMANO who is conscientious, intelligent, and patient. We joined the research group four years ago simultaneously. I am truly grateful to have a relationship with him who is both mentor and friend. Without his persistence, professionalism, and ongoing support, I would not have such a wealth of academic achievements in this period.

I gratefully thank the jury members: Professor Marcello MANNA , Professor Stephane AUBERT, Professor Jean-Chirstophe ROBINET, and Doctor Silvia HIRATA, for their constructive comments on this thesis, and their precious advice.

Thanks to the China Scholarship Council for providing me with expenses for four years during my Ph.D program. I would also like to thank LMFL for providing me with numerical resources. Many thanks go in particular to my Chinese professors Jianping YUAN, Yanxia FU, and Qiaorui SI. Their support and recognition gave me the opportunity to come to France to study.

ACKNOWLEDGMENTS

Finally, I want to convey my deep affection and appreciation to my cherished family for their unwavering support and affection during my life. Special thanks to my girlfriend Xiao JIANG and my cat Toufu FAN, their company makes my life in France much warmer.

Résumé

Les instabilités se développant dans un diffuseur lisse d'une pompe centrifuge à écoulement radial sont étudiées théoriquement, numériquement et expérimentalement. Dans l'hypothèse d'un mécanisme d'écoulement 2D, une analyse de stabilité linéaire en utilisant un modèle analytique existant a été effectué. La stabilité de chaque mode a été étudiée par une analyse linéaire en 2D, et les composantes du bilan énergétique conduisant à un transfert d'énergie de l'état de base bidimensionnel vers les perturbations infinitésimales bidimensionnelles les plus dangereuses ont été caractérisées. Les capacités et les limites d'une telle approche pour prédire le développement du décrochage tournant ont été évaluées.

L'approche linéaire 2D repose exclusivement sur l'axisymétrie de l'écoulement en entrée du diffuseur et n'implique aucun forçage inhomogène en θ. De plus, l'effet des interactions non linéaires entre les modes de décrochage y est négligé. Nous avons donc effectué une simulation numérique 2D avec un mode de Fourier imposé à l'écoulement entrant pour imiter les sillages. Les instabilités rotatives en termes de nombre de cellules de décrochage et de vitesse de propagation ont été étudiées par transformée de Fourier rapide et analyse par ondelettes, et comparées aux prévisions théoriques.

Pour étudier plus en détail l'effet de la couche limite sur les instabilités, une simulation 3D d'ordre réduit est également réalisée pour le diffuseur isolé en excluant le reste de la machine centrifuge du domaine simulé. Pour obtenir les conditions limites réalistes de l'entrée du diffuseur. La vitesse en entrée du diffuseur est issue d'un modèle basé sur des simulations RANS de l'ensemble de la pompe. Les simulations ont permis d'identifier deux mécanismes d'instabilité différents : l'une apparait à débit partiel uniquement et l'autre est une instabilité du sillage de jet qui se produit à des débits plus importants.

Enfin, nous avons effectué des simulations URANS et des études expérimentales sur l'ensemble de

la pompe. Les comparaisons entre les résultats expérimentaux et numériques sur les performances globales de la pompe et du diffuseur sont présentées et discutées. Il a été constaté que les instabilités associées aux deux mécanismes différents que nous avons identifiés par l'approche d'ordre réduit existent dans une pompe réelle. L'influence des fuites en entrée du diffuseur d'entrée sur le développement des instabilités d'écoulement est spécifiquement abordée. L'effet du rapport d'aspect radial Γ sur les caractéristiques d'instabilité de l'écoulement est également discuté.

Mots-clés: Décrochage tournant, Instabilités, Diffuseur lisse, Machine centrifuge, Simulation numérique.

Abstract

The flow instabilities in a vaneless diffuser of a radial flow pump model are theoretically, numerically, and experimentally investigated. Under the hypothesis of a 2D core flow mechanism, we performed a linear analysis using the analytical model of Tsujimoto et al.. The stability of each stall mode was studied by the 2D linear analysis, and the components of the energy budget leading to a transfer of energy from the two-dimensional basic state to the two-dimensional most-dangerous infinitesimal perturbation are characterized. The capabilities and limits of such an approach to predict the development of the stall have been evaluated.

The 2D linear mean core-flow approach of Tsujimoto et al. relies exclusively on the skewness of the diffuser inflow and does not involve any inhomogeneous inflow in θ (no impeller wake model). Moreover, the effect of the non-linear interactions between stall modes is neglected. Hence, we carried out numerical simulation for the reduced-order 2D model with a Fourier mode imposed on the inflow to mimic the jet wakes. The rotating instabilities in terms of stall cell number and propagation velocity are investigated by fast Fourier transform and wavelet analysis, and compared to theoretical prediction.

To further study the boundary layer effect on the instabilities, a reduced-order 3D model is also simulated for the sole diffuser, excluding the rest of the centrifugal machine from the flow domain to simulate. To obtain the realistic diffuser inlet boundary conditions, a multi-stage scale-matching fitting approach is developed by fitting the diffuser inflow velocity derived from RANS simulations of the entire pump. Two different instability mechanisms are identified from this 3D model of the diffuser flow, one is the low flow rate mean flow instability and another one is the jet-wake instability that occurs at larger flow rates.

Finally, we conducted URANS simulations and experimental studies on the entire pump. Com-

parisons between experimental and numerical results on the overall pump and diffuser performances are presented and discussed. Moreover, we found that the instabilities associated with two different mechanisms we identified by the reduced-order approach exist in a real pump. The influence of inlet diffuser leakages on the development of flow instabilities is specifically addressed, owing to the remarkable impact that a small impeller-to-diffuser radial gap can have on the diffuser flow. The effect of the radial aspect ratios Γ on the instability characteristics of the flow is also discussed.

Keywords: Rotating stall, Instabilities, Vaneless diffuser, Centrifugal machine, Numerical simulation.

List of appended papers

Paper A

M. Fan, A. Dazin, F. Romanò, G. Bois, *Effect of leakage on the performance of the vaneless diffuser of a centrifugal pump model*, CMFF'22 (2022), 51–58.

Paper B

M. Fan, A. Dazin, G. Bois, F. Romanò, *Effect of inlet leakage flow on the instability in a radial vaneless diffuser*, Phys. Fluids, 35(1) (2023), 014105.

Paper C

M. Fan, A. Dazin, G. Bois, F. Romanò, *Instabilities identification based on a new centrifugal 3D impeller outflow model*, Aerosp. Sci. Technol (2023), 108466.

Paper D

M. Fan, A. Dazin, G. Bois, F. Romanò, *Instabilities in a turbulent swirling source flow between parallel rings*, Phys. Fluids, 35(10) (2023), 101701.

Paper E

M. Fan, A. Dazin, G. Bois, F. Romanò, *Effect of radius ratio on the instabilities in a vaneless diffuser*. Eur. J. Mech. B/Fluids, 104 (2024), 1–7.

Contents

List of Tables

List of Figures

Symbols

Symbol	Definition	Unit
Latin letters		
A_{inlet}	Amplitude of the inflow Fourier mode	$(-)$
A_{p}	Amplitude of the Fourier spectrum	$(-)$
b_2	Impeller outlet width	mm
b_3	Diffuser constant width	mm
c	Speed of sound	m/s
C	Courant number	$(-)$
C_p	Pressure coefficient	$(-)$
E^{kin}	Total kinetic energy	$(-)$
f	Frequency	Hz
f_{imp}	Impeller frequency	Hz
f_{blade}	Blade passing frequency	Hz
$f_{\text{stall},Q_{\text{d}}}$	Rotating stall frequency at Q_{d}	Hz
$f_{\text{stall},0.25Q_{\text{d}}}$	Rotating stall frequency at $0.25Q_{\text{d}}$	Hz
H_{b}	Outflow box height	mm
I	Turbulence intensity	$(-)$
$I_k^{'}$	Kinetic energy densities	$(-)$
k	Turbulent kinetic energy at the inlet	$(-)$
k_{in}	Turbulent kinetic energy along the walls	$(-)$
k^{out}	Transport of perturbation energy through the outlet	$(-)$
k_{wall}	Turbulent kinetic energy	$(-)$
K	Mean blade thickness	mm
L	Impeller-to-diffuser radial gap	mm
Ma	Mach number	$(-)$
m_{F}	Inflow Fourier mode number	$(-)$
n	Number of stall cells/number of modes	$(-)$
N	Rotational speed of impeller	RPM
P	Pressure	Pa
Q	Actual flow rates measured at the suction pipe	m^3/s
Q_{c}	Critical flow rate	m^3/s
Q_{d}	Design flow rate	m^3/s

Q_{I}	Effective impeller flow rate	m^3/s
Q_{D}	Effective diffuser flow rate	m^3/s
R_1	Impeller tip inlet radius	mm
R_2	Impeller outlet radius	mm
R_3	Diffuser inlet radius	mm
R_4	Diffuser outlet radius	mm
R_b	Outflow box outlet radius	mm
Re	Reynolds number	$(-)$
S	mean rate of strain tensor	$(-)$
S^{out}	Outlet surface of the 2D linear model	$(-)$
t	Time	s
T	Impeller period	s
U_{r}	Radial component of the absolute velocity	m/s
U_θ	Tangential component of the absolute velocity	m/s
U_{z}	Axial component of the absolute velocity	m/s
Z	Number of blades	$(-)$
Greek letters		
α	Flow angle	$\circ$
α_{c}	Critical flow angle	$\circ$
Γ	Diffuser radial aspect ratio	$(-)$
δ	relative error	$(-)$
Δ	Difference	$(-)$
θ	Circumferential direction	$(-)$
ν	kinematic viscosity	m^2/s
ρ	Density	kg/m^3
τ	Reynolds stress tensor	$(-)$
ω	Angular velocity	rad/s
ω_{imp}	Angular speed of impeller	rad/s
$\omega_{\mathrm{stall},Q_d}$	Rotating stall propogation velocity at Q_{d}	rad/s
$\omega_{\mathrm{stall},0.25Q_d}$	Rotating stall propogation velocity at $0.25Q_{\mathrm{d}}$	rad/s
ω_{in}	Turbulent specific dissipation rate at the inlet	$(-)$
ω_{wall}	Turbulent specific dissipation rate along the walls	$(-)$

Subscripts		
0	Basic state	$(-)$
1	Impeller inlet	$(-)$
2	Impeller outlet	$(-)$
3	Diffuser inlet	$(-)$
4	Diffuser outlet	$(-)$
inlet	2D linear model inlet	$(-)$
imp	Impeller rotation	$(-)$
blade	Impeller blade	$(-)$
I	Impeller component	$(-)$
c	Critical threshold	$(-)$
D	Diffuser component	$(-)$
in	Suction pipe inlet	$(-)$
wall	Wall boundaries	$(-)$
stall	Rotating stall	$(-)$
F	Inflow Fourier mode	$(-)$
r	Radial direction	$(-)$
θ	Tangential direction	$(-)$
z	Axial direction	$(-)$
$*$	$\{r, \theta, z\}$	$(-)$
$\parallel$	Tangential component	$(-)$
$\perp$	Normal component	$(-)$
Superscripts		
bulk	Bulk flow region	$(-)$
core-flow	Core-flow instability	$(-)$
jet-wake	Jet-wake instability	$(-)$
$\rightrightarrows$	Tensor	$(-)$
$\rightarrow$	Vector	$(-)$
$-$	Averaged	$(-)$
$\hat{}$	Nondimensionalized	$(-)$
$'$	Perturbation term	$(-)$
$\sim$	Radial functional distribution of the perturbation	$(-)$

Chapter 1

Introduction

Contents

Turbomachinery is widely used in various industries such as water supply [3], aviation [4], shipping [5], and air conditioning [6]. However, the operating capability of turbomachinery is limited by unstable internal flows. A prominent example of these instabilities is the rotating stall of a compressor or a pump. Rotating stall has undesirable consequences such as noise [7], vibration [8], mechanical damage [9], and reduced performance [10], and must be prevented. To expand the range of applications, understanding the flow dynamics behind the rotating stall mechanism must be enhanced as a preliminary step for controlling.

1.1 Rotating stall in centrifugal machines

Centrifugal machines, typically known as centrifugal pumps or centrifugal compressors, are mechanical devices that utilize centrifugal force to transfer or compress liquids or gases. They have various applications across various industries from the aviation field [4] (high-pressure ratio, up to 8:1) to the process industry [11]. As an example, Fig. 1.1 depicts a schematic of a single-stage centrifugal compressor, the operating device is characterized by an outer volute casing containing an impeller firmly connected to the shaft. The impeller is driven in rotation by either a gas turbine, a steam turbine, or an electric motor, imparting kinetic energy to the gas. After leaving the impeller, the high-velocity flow enters the diffuser (a stationary passage of gradually increasing cross-sectional area). The diffuser slows down the velocity and converts the kinetic energy into pressure energy. Finally, the high-pressure fluid is discharged through the outlet of the compressor.

In the last few years, centrifugal machines have reached high levels of performance, mainly due to their compact construction, the low number of components, and the use of new materials [11]. The efficiency of centrifugal machines is now possible to go beyond 80% [12]. The flow field is rather complicated within centrifugal machines. This is attributed to a wide range of temporal and spatial scales, as well as the occurrence of flow instabilities [13]. During normal operating conditions, the airflow through the compressor is essentially stable and periodic in the rotating coordinate system. However, the operating range of centrifugal compressors is significantly bounded by the onset of two instabilities at low mass-flow rates, e.g. rotating stall and surge [14]. Centrifugal compressor surge occurs due to a stage stall, which can be described as either a collective stall of multiple compressor elements or an intense stall of a single component. Such instabilities typically lead to large vibrations and significant noise levels. Prolonged operation under such adverse conditions may lead to mechanical

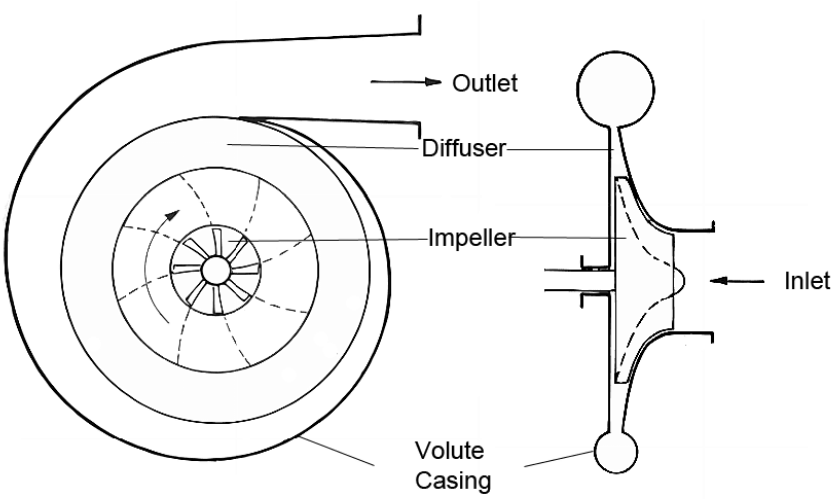

Figure 1.1: Schematic of a single-stage centrifugal compressor.

failure. The compressor performance characteristics at different operating conditions are generally represented by compressor maps (see Fig. 1.2). In turbomachinery applications, the safe and efficient operation of the compression system is imperative. To run the compressor efficiently without damage, the compressor must be controlled to prevent the operating point of the compression system from entering the unstable regime to the left of the stall and surge lines which are the stability boundaries [14, 15].

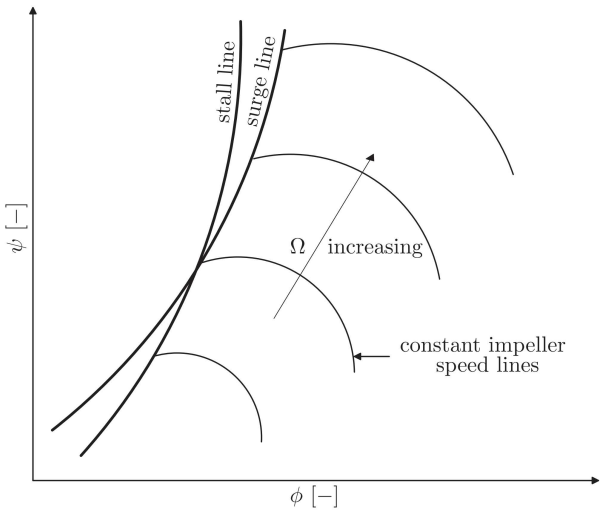

Figure 1.2: Schemetic of a compressor map.

Although instability in turbomachinery has been extensively studied in the literature, minor effort

has been paid to the rotating stall in centrifugal compressors compared to stall in axial compressors. Moreover, the inducement of the rotating stall in the centrifugal compressors is normally more intricate because of the different types of the rotating stall. Based on the location where the stall occurs, rotating stall in centrifugal compressors can roughly classify as impeller and diffuser rotating stall, which can be further subdivided into vaned diffuser and vaneless diffuser rotating stall. The occurrence of rotating stall in impellers and vaneless diffusers has similarities to the rotating stall in axial compressors, as it is caused by an excessive positive angle of attack. However, in the case of vaneless diffusers, where vanes are absent, the mechanism behind the rotating stall cannot be explained solely by the concept of the angle of attack. Understanding the flow dynamics and mechanisms underlying rotating stalls is crucial for the design and operation of efficient and reliable centrifugal machines.

1.2 Vaneless diffuser rotating stall

Diffusers in centrifugal machines are specifically designed to convert the high-velocity kinetic energy of the fluid leaving the impeller into a static pressure rise, by gradually expanding the flow area and slowing down the fluid velocity.

Vaneless diffusers are widely used in process compressors, refrigeration compressors, and automotive turbochargers due to their wide operating range and low costs. Generally, the vaneless diffuser needs a large radial aspect ratio due to its low diffusion ratio [16]. The vaneless diffuser demonstrates lower pressure recovery by as much as 20% and lower stage efficiency by 10% compared to a conventional vaned diffuser [17]. However, the absence of vanes in a vaneless diffuser reduces potential flow disturbances caused by the interaction between the fluid flow and the fixed vanes and provides shock-free deceleration with a simple design that is more resistant to corrosion and fouling than a vaned diffuser. For these reasons, they are often preferred to those vaned which allow a high-pressure recovery but a limited range of operation.

At the same time, the absence of guide vanes reduces the ability of vaneless diffusers to control the flow angle α (defined as the angle between the flow path and the tangential direction) and promotes uniform flow distribution. Hence, vaneless diffusers are more susceptible to flow instabilities and rotating stall compared to vaned diffusers. The diffuser rotating stall is the most common rotating stall type in centrifugal compressors [18]. Although the rotating stall was studied in many aspects, some

of the mechanisms of the instability and their effects on the diffuser behavior are still unknown. There is no uniform agreement on the mechanisms leading to the rotating stall, especially in the vaneless diffuser with a simple structure. For the above reasons, this study only focuses on the vaneless diffuser rotating stall, in an attempt to shed light on the underlying physics of the instability.

1.2.1 Theoretical study

Several researchers summarized that the occurrence of rotating stall instability in vaneless diffusers can be linked to the involvement of two or more distinct flow mechanisms that lead to the formation and propagation of stall cells within the diffuser. The interaction between these mechanisms depends on the specific compressor operating conditions as well as on its design. In earlier literature, numerous researchers have demonstrated that the occurrence of the vaneless diffuser rotating stall can be traced back to a three-dimensional wall boundary layer instability. Jansen [19], Senoo and Kinoshita [20], Senoo et al. [21], Fringe et al. [22], and Dou and Mizuki [23] applied the wall-boundary-layer theory to investigate rotating stall in vaneless diffusers. In the following years, a number of studies state that the vaneless diffuser rotating stall originates from two-dimensional core flow instabilities. A two-dimensional method that does not consider the effect of the wall boundary layers was utilized by Jansen [19], Abdelhamid [24], Moore [25], Tsujimoto et al. [1], Heng et al. [18] to study the vaneless diffuser rotating stall.

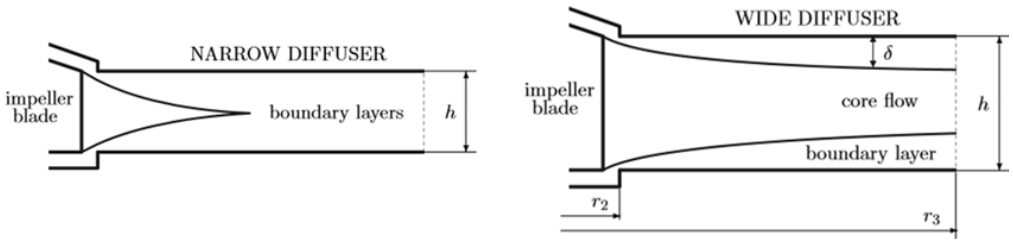

Figure 1.3: Schematic of the flow in narrow and wide diffusers (Lejvar, 2007).

According to previous research, Lejvar [26] proposed different stall mechanisms in two types of diffusers (see Fig. 1.3) depending on the ratio of diffuser width to impeller outlet radius b_3/R_2:

- in narrow diffusers ($b_3/R_2 < 0.1$), the mechanism is associated with the three-dimensional wall boundary layer instability occurring in diffusers;
- in wide diffusers ($b_3/R_2 > 0.1$), the mechanism is associated with the two-dimensional core-flow

instability occurring in vaneless diffusers when inlet flow angle α reached the critical value α_c.

Besides, Heng et al. [18] pointed out that the diffuser radius ratio is also important to define the type of diffuser. According to the previous diffuser definition, it is obvious that the boundary layers interaction at the core of the corresponding instability in a "wide vaneless diffuser" can occur in narrow vaneless diffusers if the diffuser radius ratio is large enough. In addition, the decrease of the mass flow rate results in a smaller inlet flow angle of the diffuser and an increase in the streamline length. Therefore, the thickness of the boundary layer will increase and the flow topology in a wide vaneless diffuser will be similar to the flow topology in a narrow vaneless diffuser. Therefore, there is no clear single-parameter geometry ratio for advocating that a wide vaneless diffuser and a narrow vaneless diffuser must lead to different instability mechanisms.

1.2.1.1 Three-dimentional rotating stall induced by boundary layer separation

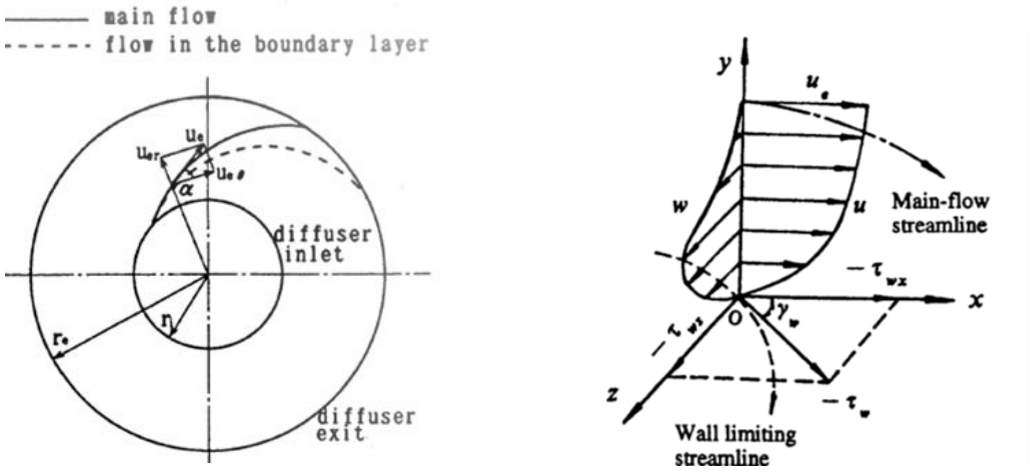

(a) (b)

Figure 1.4: (a) Flow in a vaneless diffuser and (b) velocity component profiles in the three-dimensional boundary layer (Dou, 1998).

The three-dimensional vaneless diffuser rotating stall was investigated utilizing the boundary layer theory. Jansen [19] first pointed out the connection between the onset of the rotating stall and the flow separation, and indicated that the inward flow takes place when a three-dimensional boundary layer separation occurs. Since it is difficult to determine the flow condition at the impeller exit (diffuser inlet), some assumptions for the inlet condition have been generally made in the analyses:

- the flow is steady, incompressible, and axisymmetric,
- the velocity vector distribution at the diffuser inlet is uniform,
- The boundary layer on diffuser walls is fully turbulent.

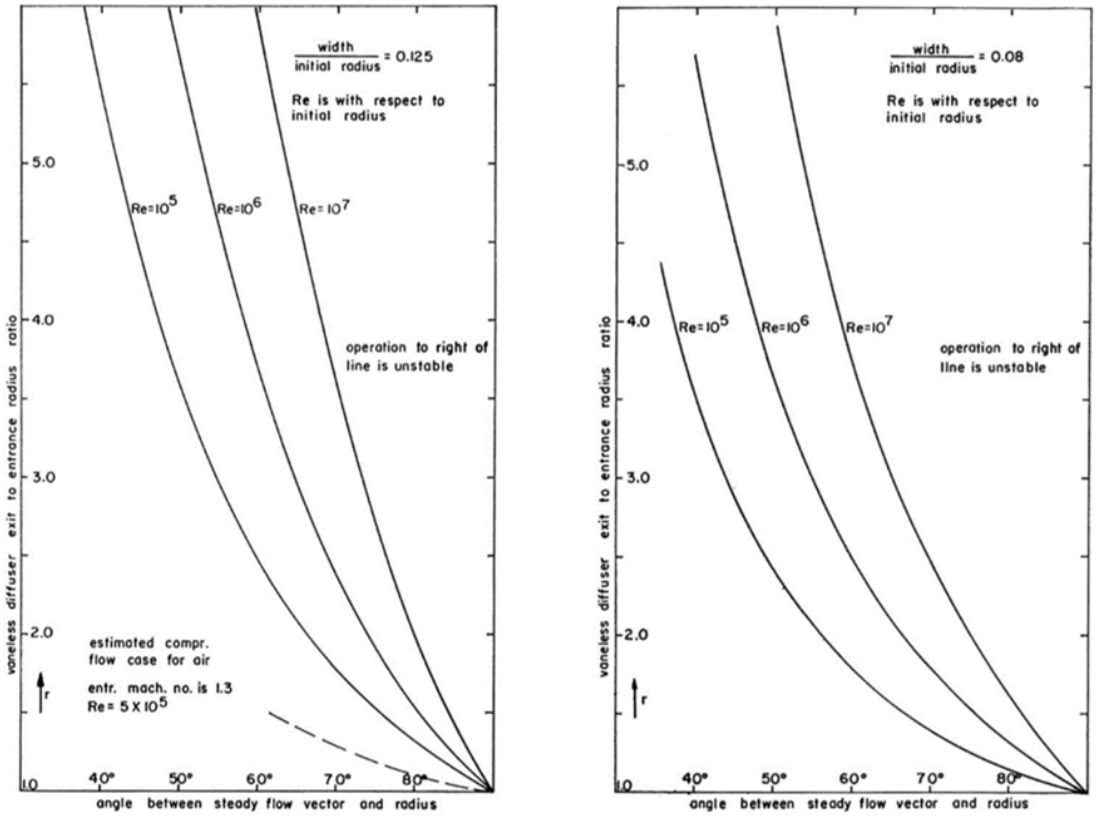

Figure 1.5: Stable operating range of vaneless diffusers (Jansen, 1964).

The inviscid core flow in vaneless diffusers is assumed to trace an ideal logarithmic spiral curve (see Fig. 1.4(a)), while the boundary layer near the walls is skewed owing to the pressure gradient and the streamline curvature. The velocity vector in the boundary layer gradually deviates from the main flow direction from the outer edge of the layer to the wall surface [23]. The direction of the wall limiting streamline deviates from the primary streamline by an angle γ_w (see Fig. 1.4(b)) which increases along the radius downstream. When the direction of the wall-limiting streamline coincides with the tangential direction, a three-dimensional separation occurs [27]. The separation of the boundary layer results in the formation of a reverse flow zone and, hence, may further induce the rotating stall. The criterion to predict the boundary layer separation is given in Fig. 1.5. The flow separation leading to

the rotating stall will be present when the machine is operated in the region on the right of the curves (see Fig. 1.5).

1.2.1.2 Two-dimentional rotating stall induced in the inviscid core flow

Another mechanism for the rotating stall in the vaneless diffuser is associated with a two-dimensional core flow instability, while the effect of the boundary layer is weak and negligible. Tsujimoto et al. [1] proposed a 2D linear model to study the characteristics of the rotating stall considered vaneless diffuser ($r_3 \leq r \leq r_4$) downstream of an centrifugal impeller with vane angle β and with infinite number of vanes. Several assumptions were made for this model:

- a two-dimensional incompressible and inviscid flow is considered,
- the flow field is described as a superposition of a steady basic state and an infinitesimal rotating perturbation determined by linear stability analysis,
- The basic state is assumed to be:

$$U_{0,r} = \frac{Q}{2\pi r}, \qquad U_{0,\theta} = \frac{\gamma_{\mathrm{i}}}{2\pi r}. \tag{1.1}$$

For a given diffuser radius ratio and the number of stall cells, the corresponding flow angles and propagation velocities for the neutral steady mode can be solved by this linear model as depicted in Fig. 1.6. Such a 2D linear model has also been employed in our study, and more details will be introduced in Sec. 3.1.1.

1.2.2 Experimental and numerical study

In addition to the theoretical analysis, extensive experiments and numerical simulations have been performed to investigate the vaneless diffuser rotating stall.

1.2.2.1 Effect of flow conditions and geometries

Experimental and numerical work shows a significant influence of the geometrical parameters on the vaneless diffuser performance and stability and on the rotating stall characteristics. The main studies that have been conducted on these subjects are summarized as follows.

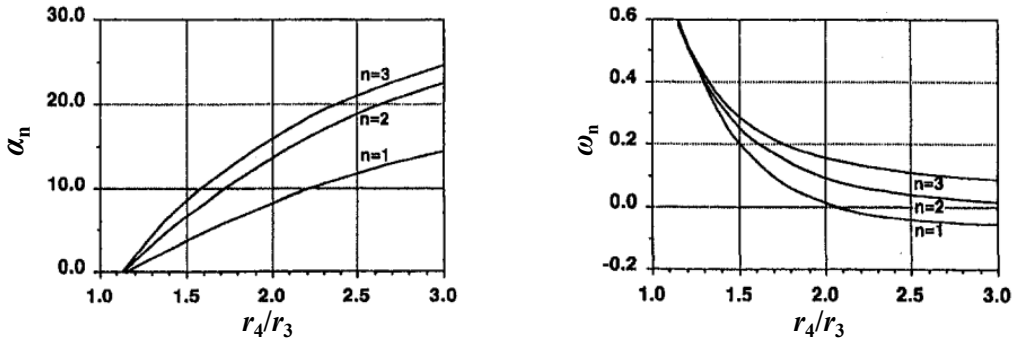

(a) (b)

Figure 1.6: The predicted (a) flow angle and (b) propagation velocity for the neutral steady modes (Tsujimoto et al., 1996).

The effect of radius aspect ratio on the internal flow characteristics of vaneless diffusers is undoubtedly one of the most studied in the past few decades. Senoo and Kinoshita [21] pointed out that the decrease in radius ratio helps to suppress the reverse flow which is expected at the rear part of a wide vaneless diffuser, and leads to a decrease of the critical inlet flow angle. Abdelhamid [28] subsequently pointed out that the rotational speed of stall cells varied inversely with the diffuser radius ratio, and the critical flow angle of stall inception increased with the diffuser radius ratio. Tsurusaki et al. [29] and Tsujimoto et al. [1] also came to similar conclusions that the critical flow angle of the rotating stall decreases with the decrease of the diffuser radius ratio. Ferrara et al. [30] indicated that in a shorter vaneless diffuser, a smaller stall inception flow angle is expected but the stall pattern becomes more complex. By carrying out the reduced-order 2D numerical study, Lejvar [26] find that the critical angle of the rotating stall decreases with decreasing diffuser radius ratio, and the number of stall cells and their propagation velocity decreases with the increase of the diffuser radius ratio.

The cross-sectional aspect ratio is also a research parameter of great interest. Jansen [19] pointed out that a decrease in the diffuser width ratio will increase the flow angle at the diffuser inlet, and thus keep the flow angle away from the critical stall condition. Tsurusaki et al. [29] and Ötügen et al. [31] reached conclusions consistent with Jansen, i.e. the critical flow angle of the rotating stall decreases with the decreased diffuser width ratio resulting in the onset of the rotating stall delayed. Moore [25] indicated that the boundary layer displacement makes the flow in narrow diffusers more convergent than in wide ones. Ferrara et al. [30] pointed out that the diffuser width strongly influences the critical

flow rate of stall inception but seems to not influence very much the stall evolution. Studies of Ishida et al. [32] show that the operation range of narrow diffusers is larger than wide ones.

Several researchers investigated the effect of diffuser structures on the flow within the vaneless diffuser. One of the representative studies is conducted by Zhu and Sjolander [33]. They studied the diffusers with divergent or convergent structures, the results showed that the convergent diffuser can help to stabilize the inner flow because it helps to reduce or eliminate the reverse flow which is the main cause of rotating stall in a wide vaneless diffuser. However, the penalty of the convergence diffuser is the performance reduction.

Several studies showed that impeller-to-diffuser leakage has a significant effect on diffuser behavior. The study of Yoshida et al. [34] showed that the clearance between the impeller and diffuser has a great effect on rotating stall characteristics. With the decrease of the clearance, the rotating stall became weakened and exists in a narrower flow range. Sano et al. [35] indicated that with the increase of the clearance between the impeller and the diffuser in the present calculation model, the diffuser rotating stall occurs more easily caused by the decoupling of impeller/diffuser flow. A small clearance leads to an increase in the safe margin.

Numerous researchers also investigated how the vaneless diffuser behavior is influenced by the Mach number. Senoo and Kinoshita [20] found that the critical flow angle increases with the increase of Mach number because a larger Mach number results in a greater density and consequently a decrease of the flow angle. The influence is strong for large-width ratio diffusers because the reverse flow occurs at a larger radius and the effect of Mach number is magnified. Ferrara et al. [30] indicated that the Mach number variation usually only scales the stall frequencies leaving approximately unchanged the main structure of stall evolution and the ratio between stall and rotating frequency. Only for short diffusers was some influence on stall pattern observed.

1.2.2.2 Characteristics of rotating stall itself

Some authors of literature focused on the detection and characteristics of the rotating stall itself, such as the critical flow angle, stall cell size, propagation velocity, frequency, and number of stall cells. These types of research were performed by Suzuki et al. [36], Abdelhamid [24], Caignaert and Desmet [37], Cellai et al. [38], Dazin et al. [39, 10], Pavesi et al. [40], Heng et al. [41, 18]. The PIV results presented by Dazin et al. [10] have clearly shown the topology of the rotating stall in a

wide vaneless diffuser. Three stall cells can be identified, which are located near the outlet and are characterized by inward and outward radial velocities. Their propagation velocity is proved to be a fraction of the impeller speed (Dazin et al. [39]). The stalled regions are characterized by relative negative tangential velocity. In the axial direction, it has been found that the stall cells are developing in the hub-to-shroud direction.

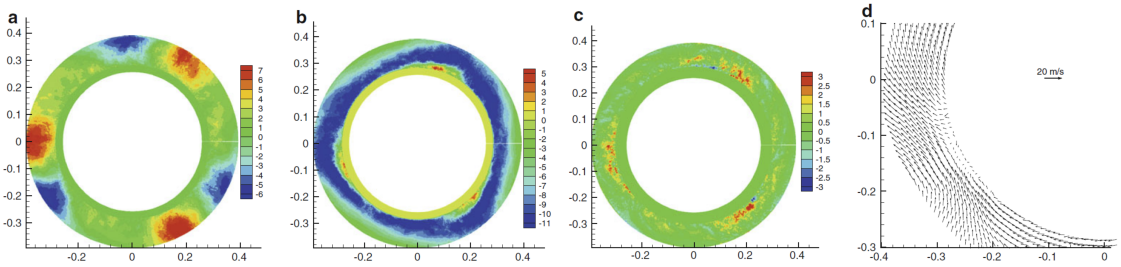

Figure 1.7: Rotating stall in a vaneless diffuser: (a) radial, (b) tangential, (c) axial velocity distributions, and (d) velocity vectors (Dazin et al, 2011).

1.2.3 Control method

One of the critical challenges in turbomachinery is the suppression of unstable flow phenomena, such as rotating stall and surge. As mentioned above, one of the rotating stall mechanisms in the vaneless diffuser is associated with the three-dimensional boundary layer separation. Therefore, controlling this instability may be an effective way to suppress the rotating stall. Sakaguchi et al. [42] proposed a new technique that effectively suppressed the rotating stall in vaneless diffusers through wall roughness control. By increasing the roughness of the hub wall, the stall limit was significantly improved by 42%, with less than a 1% drop in performance. The effectiveness of this technique was subsequently confirmed by Ishida et al. [32]. From a theoretical standpoint, the increment of wall roughness significantly decreased the skewness of the three-dimensional boundary layer. Meanwhile, the rough wall also leads to an increase in the turbulence intensity in the boundary layer. The above two factors might result in the suppression of the three-dimensional separation. Ahmed et al. [43] also experimentally examined the feasibility of controlling the stall in the radial diffuser using rough surfaces. The results showed that the occurrence of the rotating stall within the diffuser was postponed to around 70% of the flow coefficient observed with a smooth surface.

On the other hand, control techniques based on the two-dimensional core flow instability mechanism

associated with the core flow angle are proposed to delay the occurrence of the rotating stall by several researchers. Kurokawa et al. [44] proposed a passive method of utilizing radial shallow grooves to control the rotating stall in a parallel-wall vaneless diffuser. The effect of groove length, width, and depth are theoretically and experimentally studied. The results show that all different radial grooves contribute to the limit of the rotating stall in a vaneless diffuser. Theoretical consideration is that the mixing between the main flow and the groove flow results in a significant decrease in tangential velocity at the diffuser inlet, while the groove reverse flow leads to a remarkable increase in radial velocity. Both effects equally contribute to the augmentation of the flow angle. Gao et al. [45] numerically verified that the radial grooves in vaneless diffuser walls are simple and powerful devices for suppressing the rotating stall. The CFD analysis indicated that the effectiveness of the grooves increases the flow angle thus delaying the diffuser wall flow reversals. Besides, the grooves are recommended to place within the region characterized by reverse flow. By employing such locally fixed grooves, the rotating stall can be effectively delayed without incurring excessive pressure loss. Tsurusaki and Kinoshita [46] carried out experimental studies to examine the effects of the jets installed at the mid-height of the diffuser on the occurrence of the rotating stall. The results indicated that the implementation of a jet directed opposite to the vector of the impeller's peripheral velocity effectively suppressed the occurrence of the rotating stall. This is because the mass flow rate is kept constant, i.e. the radial velocity remained constant, while the jet flow in the opposite direction to the impeller peripheral velocity vector reduced the tangential velocity, so the flow angle increased.

1.3 Research objectives and approach

The present work focuses on the instability in a vaneless diffuser of a centrifugal machine. Although the vaneless diffuser rotating stall has been widely studied in many aspects as listed above (mechanisms, characteristics, influences, controlling, etc), the standard for distinguishing between a wide vaneless diffuser and a narrow vaneless diffuser leading to different instability mechanisms is still not clear. Besides, many studies have shown that several unstable modes can coexist in a vaneless diffuser at a given operating range. Previous two-dimensional linear stability analyses are not able to consider the interactions between these modes and are limited to critical conditions. Moreover, the effect of the asymmetric inflow and the jet wake characteristics on the instability are not fully studied. Based on the above reasons, the objectives and approaches of this work are listed as follows:

(1) Conduct new experiments to test the performance of the entire machine and the sole vaneless diffuser, as the basis for verifying the subsequent numerical simulation work.

(2) Conduct numerical simulations for the entire centrifugal machine in OpenFOAM to study the effect of leakage flow and diffuser radius ratios on the machine performance and instability characteristics in the vaneless diffuser.

(3) Develop a three-dimensional reduced-order model based on a scale-matching fitting approach that considers the boundary layer effect for an affordable parametric study to test the effects of asymmetric inflows, inflow wavenumbers, and inflow amplitudes on the instability in the vaneless diffuser.

(4) Compare the two-dimensional linear stability analysis results with nonlinear solutions of two-dimensional numerical simulation for the core flow and three-dimensional simulations for our reduced order model to analyze the unstable modes associated with different instability mechanisms that coexist in a vaneless diffuser.

1.4 Structure of the thesis

The experimental and numerical studies of the entire machine are first carried out to characterize different kinds of instabilities in the vaneless diffuser, and to study the instability characteristics and the effect of geometric parameters (effect of impeller-to-diffuser leakage effect and diffuser radius ratio).

Then we conducted theoretical and numerical studies of reduced-order models to evidence the different instabilities identified in the entire machine study and trace the instabilities to different physical mechanisms. Different levels of complexity are taken care of by three different reduced-order models. First, we carried out a 2D linear stability analysis of 1D homogeneous inviscid flow to determine the infinitesimal perturbation and to analyze the kinetic energy transferred between the basic state and the critical instability modes. Second, we carried out a 2D URANS simulation considering the viscosity, nonlinear interaction, and effect of jet-wake inflow. Last, we carried out a 3D reduced-order URANS simulation to study the boundary layer and asymmetric inflow effect.

Chapter 2

Methodology

Contents

A. This part has already been published in the appended paper A: M. Fan, A. Dazin, G. Bois, F. Romanò, *Effect of leakage on the performance of the vaneless diffuser of a centrifugal pump model*, CMFF'22 (2022), 51–58.

B. This part has already been published in the appended paper B: M. Fan, A. Dazin, G. Bois, F. Romanò, *Effect of inlet leakage flow on the instability in a radial vaneless diffuser*, Phys. Fluids, 35(1) (2023), 014105.

C. This part has already been published in the appended paper C: M. Fan, A. Dazin, G. Bois, F. Romanò, *Instabilities identification based on a new centrifugal 3D impeller outflow model*, Aerosp. Sci. Technol (2023), 108466.

2.1 Experimental apparatus[A]

The experimental setup consisting of a radial impeller together with a vaneless diffuser is depicted in Fig. 2.1(a). Such an experimental test case which includes an impeller (flange-mounted) and a diffuser but no volute has been specifically designed to provide experimental optical access for unsteady flow analysis and has a well-defined constant outlet pressure boundary condition, as previously described by Fan et al. [47], Wuibaut et al. [48] and Dazin et al.[10]. An inflow tank equipped with replaceable diaphragms (with different inlet diameters) is placed at the top of the suction pipe to control the flow rate Q. Meanwhile, a honeycomb flow straightener is installed at the bottom of the tank to stabilize the airflow before it enters the suction pipe.

Compared to conventional radial flow machine designs, this arrangement differs in that it lacks a carter connecting the diffuser inlet and the inlet-pipe outlet, i.e. leaving the impeller without a casing. With the outlet static pressure kept at atmospheric conditions, the radial gap between the fixed diffuser inlet and the rotating impeller outlet of this test rig allows for a positive leakage inflow which commonly exists in radial ventilation and extraction equipment. Consequently, all the local static pressures within the pump remain below atmospheric pressure.

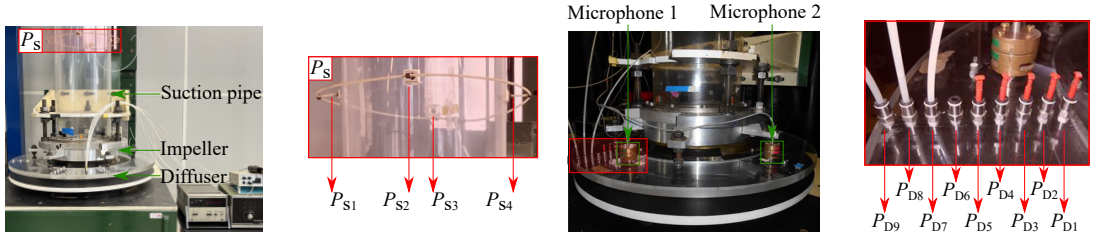

(a) (b)

Figure 2.1: Experimental set-ups of the radial flow machine with (a) a zoom-in view of the four static pressure probes equipped on the suction pipe (red rectangle) and (b) two microphones and a zoom-in view of nine static pressure taps installed on the vaneless diffuser (red rectangle).

To assess the impact of the rotating stall, the performance of the entire machine and the sole diffuser are measured. The static pressure in the suction pipe is calculated by averaging the data obtained by four pressure probes uniformly equipped on a circumference ($P_{s1} - P_{s4}$), as illustrated in Fig. 2.1(a). Therefore, the performance of the entire machine is characterized by the static pressure variation between the suction pipe (P_s) and diffuser outlet. Furthermore, nine steady pressure taps

are flush-equipped along a radial line (spaced evenly from $r = 264\,\text{mm}$ to $r = 384\,\text{mm}$) on the diffuser shroud wall. Hence, the diffuser performance is characterized by the pressure recovery from the diffuser inlet to the outlet. The uncertainty of the above static pressure measurements is estimated to be $\pm 2\,\text{Pa}$.

The transient pressure fluctuation is measured by two condenser micro-phones (Brüel & Kjaer, Type 4135)) flush-mounted at the same radial position ($r = 320\,\text{mm}$) with an angular shift of $\Delta\theta = 60\,^\circ$ on the diffuser shroud wall. The LMS Test Xpress (SIEMENS, Munich, Germany) is used to acquire data over a total duration of 600 s, with a sampling frequency of 4096 Hz. The uncertainty of the above measurement is estimated at less than 1%. Further details of the experimental apparatus can be found in previous studies [39, 10] which operated the same apparatus. The unsteady pressure measurements will be employed to conduct the FFT and wavelet analysis.

The experiments were performed in the air with constant rotating speed $N = 1200\,\text{rpm}$ (i.e. $\omega_{\text{imp}} = 125\,\text{rad/s}$). The flow rate is reduced from stable condition to unstable condition $Q/Q_{\text{d}} \in [0.26,\ 1.53]$, where Q denotes the actual flow rates measured at the suction pipe and Q_{d} denotes the design flow rate.

2.2 Problem formulation[A,B,C]

2.2.1 Geometry

2.2.1.1 3D full machine model

In order to study the flow in a vaneless diffuser, a three-dimensional centrifugal pump is considered. The geometry of the numerical model matches the experimental setup (see details in Sec. 2.1), which corresponds to an enlarged air model called Société Hydrotechnique de France (SHF) pump. Figure. 2.2 depicts the three-dimensional configuration consisting of a suction pipe (yellow), a centrifugal impeller (gray), a radial vaneless diffuser (dark green), and an outflow box (light green) attached to the diffuser domain to prevent the outflow boundary conditions from being set too close to the machine.

The key parameters of our centrifugal pump are listed in Tab. 2.1. The inlet velocity boundary conditions are given at the top of the circular suction pipe with a length of $H_c = 10R_1$, where R_1 denotes the impeller tip inlet radius R_1. The static pressure outlet boundary conditions are set at boundaries of the outflow box with a height of $H_b = 15b_3$ and a radius of $R_b = 3R_4$. To inspect

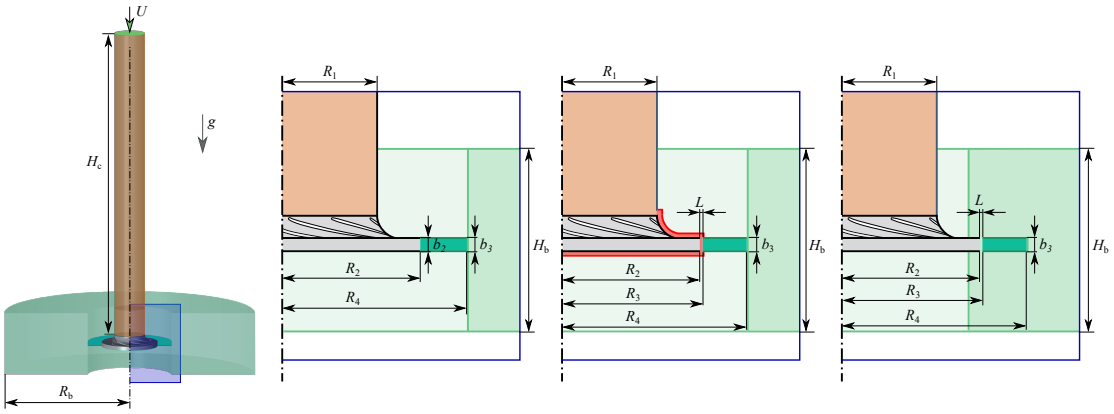

Figure 2.2: Schematic of (a) the three-dimensional radial flow machine and the zoom-in view of the three conceptually different leakage configurations: (b) zero-, (c) negative-, and (d) positive-leakage case.

Table 2.1: Main geometrical characteristics of the impeller and diffuser.

SHF impeller characteristics		
R_1	Impeller tip inlet radius	141.1 (mm)
R_2	Impeller outlet radius	257.5 (mm)
b_2	Impeller outlet width	38.5 (mm)
Z	Number of blades	7
β_{2c}	Outlet blade angle	22.5 (°)
K	Mean blade thickness	9mm
Q_d	Design flowrate(1200rpm)	0.236 (m^3/s)
Vaneless diffuser characteristics		
R_3	Inlet radius without leakage	257.5 (mm)
	Inlet radius with leakage	260.075 (mm)
R_4	Diffuser outlet radius	385.5 (mm)
b_3	Diffuser constant width	38.5 (mm)
$Re = \rho V_3 b_3/\mu$	Reynolds number ($Q/Q_d = 1.0$, $N = 1200$ RPM)	9.08×10^4

the leakage effect on the flow field of the radial vaneless diffuser, three conceptually different leakage configurations are studied. Based on the direction of the leakage flow entering the machine, these are referred to as zero, negative and positive leakage cases.

Zero-leakage: corresponds to a ideal scenario where there is no gap between the impeller and the vaneless diffuser (see Fig. 2.2(b)), i.e. the radial gap between them being set to zero.

Plus, we consider no axial gap between the suction pipe outlet and impeller inlet;

Negative-leakage: corresponds to a typical centrifugal machine setup as shown in Fig. 2.2(c). An impeller-to-diffuser radial gap $L = R_3 - R_2$ is introduced with a casing surrounding the impeller that permits leakage flow from the impeller outlet to the impeller inlet section. The distance between the impeller and the casing wall is constantly equal to the gap width L;

Positive-leakage: corresponds to a scenario that replicates the experimental setup available at ENSAM (shown in Fig. 2.2(d)). Note that the experimental impeller-to-diffuser radial gap width is $L = 1mm$, while the numerical radial gap is intentionally increased to $L = 3mm$ ($L/R_2 = 1\%$) to demonstrate the impact of positive-leakage flow clearly. The axial gap between the outlet of the suction pipe and the inlet of the impeller is not taken into account. This case is selected as a reference one, the machine performance comparison between the experiment and numerical simulation are all made using this case, which is utilized for validating and discussing the results of the numerical simulations.

2.2.1.2 3D reduced-order model

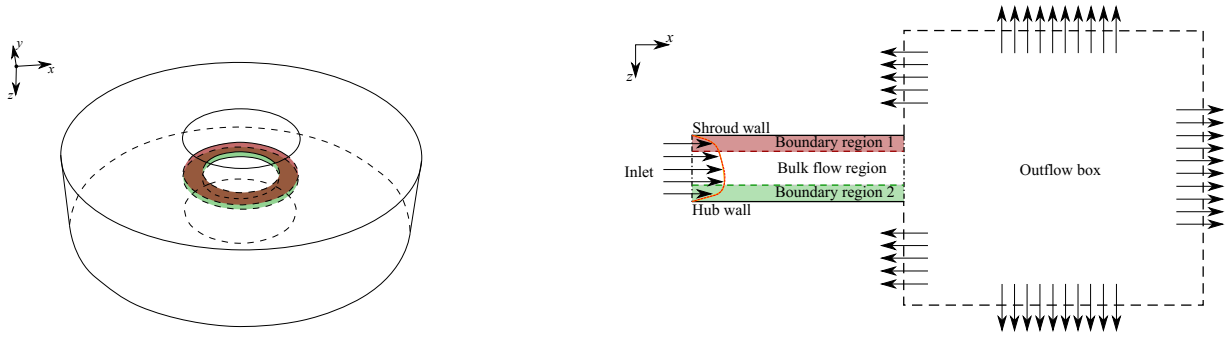

(a) (b)

Figure 2.3: Schematic of (a) the three-dimensional reduced-order model (red and green markings indicate the diffuser shroud and hub walls respectively) and (b) the meridian section of the reduced-order model, where the outflow box is not drawn to scale.

To conduct a parametric analysis of the flow within the vaneless diffuser at an affordable computa-

tional cost, a reduced-order simulation approach will be proposed in the following chapters. Differing from the computational domain of the entire machine, this model omits the suction pipe and the centrifugal impeller, i.e. only the vaneless diffuser and the outflow box domains are simulated (see Fig. 2.3). The inflow boundary condition will be given by fitting the azimuthally averaged diffuser inlet velocity profile obtained from the full machine simulation and superposing a Fourier mode (see details in Sec. 2.3.3).

2.2.1.3 2D reduced-order model

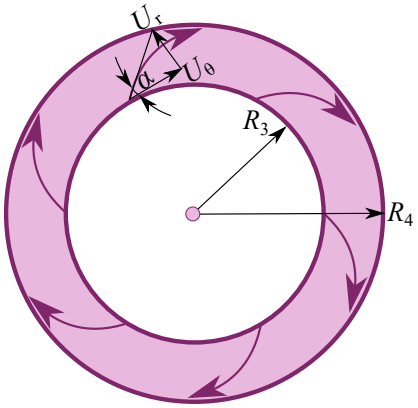

Figure 2.4: Schematic of the two-dimensional core flow at the mid-height of the diffuser, where the flow angle α is defined as the angle between the flow path and the tangential direction, i.e. $\alpha = \arctan(U_\mathrm{r}/U_\theta)$.

To study the core flow instability in the radial vaneless diffuser, the two-dimensional flow at the mid-height of the diffuser with finite radial aspect ratio $\Gamma = R_4/R_3$ (as depicted in Fig. 2.4) is modeled. Based on the assumption that the core flow of the vaneless diffuser is two-dimensional, the diffuser width is not considered here, i.e. the effect of wall boundary layers is neglected. Linear stability analysis and URANS simulations are performed on this model with homogeneous inflow in θ and mimicked jet-wake inflow respectively (see details in Sec. 2.3.3).

2.2.2 Governing equation

This study considers the flow in the radial flow machine as an incompressible viscous fluid flow according to the flow Mach number of $Ma = R_2\omega_\mathrm{imp}/c = 0.095 \ll 0.3$, where ω_imp is the impeller rotation rate and $c = 340\dot{\mathrm{m}}/\mathrm{s}$ is the speed of sound. The flow is investigated by using the unsteady

Reynolds-Averaged Navier-Stokes (URANS) equations, which can be written as:

$$\frac{\partial \overrightarrow{U}}{\partial t} + (\overrightarrow{U} \cdot \nabla)\overrightarrow{U} + \nabla P = \nabla \cdot (2\nu \overrightarrow{\overrightarrow{S}} - \overrightarrow{\overrightarrow{\tau}}), \quad \nabla \cdot \overrightarrow{U} = 0, \tag{2.1}$$

where $\overrightarrow{U} = \overrightarrow{U}(\overrightarrow{x};\, t) = (U_1, U_2, U_3)$ denotes the mean part of the velocity vector, $(\overrightarrow{x};\, t) = (x_1, x_2, x_3;\, t)$ are the spatial and temporal coordinates, $P = P(\overrightarrow{x}, t)$ is the mean pressure field, ν is the kinematic viscosity, $\overrightarrow{\overrightarrow{S}} = \frac{1}{2}(\nabla \overrightarrow{U} + \nabla^T \overrightarrow{U})$ is the mean rate of strain tensor, $\overrightarrow{\overrightarrow{\tau}}$ is the Reynolds stress tensor.

2.2.3 Turbulence modelling

As demonstrated in Appendix A, $k-\omega$ SST model is the most suitable approach for simulating the flow in the vaneless diffuser. Moreover, the effectiveness, robustness, and efficiency of the $k-\omega$ SST model have been showcased in several centrifugal machine simulations in literature, as demonstrated through numerous examples [49, 50, 51, 52, 53]. The $k-\omega$ SST model is a two-equation model that relies on the Boussinesq hypothesis. To determine the eddy viscosity ν_T, two additional transport equations need to be solved: the turbulent kinetic energy and a value defining its dissipation. The turbulent kinetic energy k is governed by:

$$\frac{\partial k}{\partial t} + (\overrightarrow{u} \cdot \nabla)k = P_k - \beta^* \omega k + \nabla \cdot [(\nu + \sigma_k \nu_T)\nabla k], \tag{2.2}$$

while the specific dissipation rate ω:

$$\begin{aligned} \frac{\partial \omega}{\partial t} + (\overrightarrow{u} \cdot \nabla)\omega =& \alpha S^2 - \beta \omega^2 + \nabla \cdot [(\nu + \sigma_\omega \nu_T)\nabla \omega] \\ &+ 2(1 - F_1)\frac{\sigma_{\omega 2}}{\omega} \nabla k \cdot \nabla \omega, \end{aligned} \tag{2.3}$$

where the production term P_k is expressed as:

$$P_k = \nu_T \overrightarrow{\overrightarrow{S}}(u) : \overrightarrow{\overrightarrow{S}}(u), \tag{2.4}$$

and the blending function F_1 is defined as:

$$F_1 = \tanh\left\{\left\{\min\left[\max\left(\frac{2\sqrt{k}}{\beta^* \omega y}, \frac{500\nu}{y^2 \omega}\right), \frac{4\rho\sigma_{\omega 2} k}{CD_{k\omega} y^2}\right]\right\}^4\right\}, \tag{2.5}$$

with $CD_{k\omega} = \max\left(2\rho\sigma_{\omega 2}\frac{1}{\omega}\nabla k \cdot \nabla \omega, 10^{-10}\right)$, y being the normal distance to the nearest wall. Finally, the turbulence kinematic viscosity is defined as:

$$\nu_T = \frac{\alpha_1 k}{max(\alpha_1 \omega, SF_2)}, \tag{2.6}$$

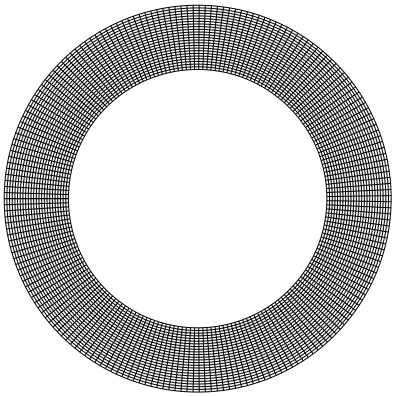

Figure 2.5: Two-dimensional mesh.

where F_2 is a second blending function defined as:

$$F_2 = \tan\left[\left[\max\left(\frac{2\sqrt{k}}{\beta^*\omega y}, \frac{500\nu}{y^2\omega}\right)\right]^2\right]. \tag{2.7}$$

For more information about the modeling techniques and constants ($\beta, \beta^*, \sigma_k, \sigma_{\omega 2}, \alpha_\omega$) used in this model, refer to Menter [54].

2.3 Numerical method[B]

2.3.1 Mesh generation

Hexahedral meshes are chosen in this study due to the high accuracy, efficiency, stability, and ease of post-processing. For two-dimensional simulations, the functionality `blockmesh` in OpenFOAM is employed for meshing. The mesh is constructed through a set of hexahedral blocks in `blockmesh` by placing vertices, creating blocks, and defining the faces with the correct orientation [55]. For each block in each direction, the number of cells and the expansion ratio (the ratio of the lengths of the first and last cells) can be customized. The two-dimensional mesh in `blockmesh` can be done by specifying one cell in the axial direction (see Fig. 2.5).

For the entire machine simulation, the mesh generation becomes a more complex task due to the intricate geometry of the blade surfaces and the flow passages of the centrifugal impeller. The commercial software ICEM CFD is employed for generating such a complex mesh. The mesh generated by ICEM CFD is outputted to `msh` format and then converted into OpenFOAM by the functionality

`fluent3DmeshToFoam`. As mentioned before, a long part of the suction pipe and an outflow box are just included to prevent the inflow/outflow boundary conditions from being set too close to the machine, hence the grid in these two regions is coarser. On the other hand, the grid in the short part of the suction pipe, centrifugal impeller, and vaneless diffuser regions is finer as illustrated in Fig. 2.6. Note the impeller is flange-mounted, and the example of the mesh depicted in Fig. 2.6 corresponds to the ideal case (no leakage between the impeller and the vaneless diffuser). To ensure that the mesh captures the flow physics accurately, the mesh is refined using an expansion ratio of 1.5 in the direction normal to the walls to keep the y^+ values close to 1 near the walls of the short suction pipe, centrifugal impeller, and vaneless diffuser. We further stress that the maximum value of y^+ is less than 1 in the areas of interest (all over the diffuser walls and most of the impeller blades).

For the reduced-order three-dimensional simulations, the mesh is also generated using the functionality `blockmesh`, since the complex impeller region is excluded. The parameters (number of cells and the expansion ratio) refer to the same setting in ICEM CFD.

(a) (b)

Figure 2.6: Top view (a) and side view (b) of a typical mesh of the zero-leakage case used to perform the three-dimensional numerical simulations.

In order to determine if the solution is dependent on the grid, test calculations are conducted for the entire machine with four different grid resolutions. Tab. 2.2 presents a comparison of the predicted mass-weighted average static pressure difference (PSI) between the suction pipe inlet and the diffuser outlet of the centrifugal machine at the design flow rate Q_{d}, using different grid resolutions. As the grid size increased from 618k cells (Grid 1) to ≈1.1M cells (Grid 2), the relative error in the predicted pump performance increased but then decreased to 0.93% for 2.3M cells (Grid 3). Consequently, a mesh size of 2.3M finite volumes was chosen for numerical simulations of the entire machine in our study. For the two-dimensional and the reduced-order three-dimensional simulations, the mesh size is

Table 2.2: Grid independence verification. The relative error δ is calculated with respect to the finest grid (denoted by Case 4), and is given by the equation: $\delta = |\text{PSICase 4} - \text{PSICase *}|/|\text{PSI}_{\text{Case 4}}|$. Here, PSI represents the mass-weighted average static pressure difference between the inlet of the pipe and the outlet of the diffuser, and the hashtag denotes either Grid 1, Grid 2, or Grid 3.

Grid #	Cells number					PSI	δ
	inlet pipe	impeller	diffuser	outflow box	total		
1	113155	267008	145728	91800	617691	0.3843	1.75%
2	238853	493920	210600	175446	1118819	0.3864	2.30%
3	406462	1051176	590976	267786	2316400	0.3742	0.93%
4	1218825	2456160	1379448	352350	5406783	0.3777	–

matched to the entire machine setup.

2.3.2 Numerics in OpenFOAM

OpenFOAM, an open-source software written in C++, was used in this study. The numerical simulations in OpenFOAM use finite-volume discretization schemes to solve the incompressible Navier-Stokes equations on a computational mesh. The `simpleFoam` and `pimpleFoam` solver from OpenFoam v19212 have been used for the RANS and URANS simulations, respectively. OpenFOAM uses linear solvers for a system of equations and these are of 4 types; Preconditioned (bi-)conjugate gradient (PCG/PBiCG), smooth solver, Generalised geometric-algebraic multi-grid (GAMG), and Diagonal solver for explicit systems (diagonal) [56]. The pressure correction equation is solved using the GAMG algorithm. The velocity and turbulence equations are solved using smoothSolver. The Gauss-seidel smoother is used for multi-grid smoothing. The Under-relaxation factors are used in order to improve the stability of the computation and the residual levels are controlled by setting the solution tolerances. To couple pressure and velocity the SIMPLE (Semi-Implicit Method for Pressure-Linked Equations) algorithm is applied for steady-state calculations, whereas the PIMPLE (PISO/SIMPLE) algorithm is applied for the transient calculations. The latter one is a hybrid algorithm that combines features of the SIMPLE and PISO (Pressure-Implicit with Splitting of Operators) algorithms which alternates between a segregated approach (similar to SIMPLE) and a coupled approach (similar to PISO) to improve convergence and stability.

The time discretization terms are discretized using a second–order `backward` differentiation scheme in OpenFOAM for URANS simulations. The gradient terms are discretized using the first-order

Table 2.3: Numerical methods and schemes employed in OpenFOAM v1906.

Types	RANS	URANS
Numerical method		
Solver	simpleFoam	pimpleFoam
Pressure-velocity coupling	SIMPLE	PIMPLE
Matrices-solver	p: `GAME`; U, k, ω: `smoothSolver`	p: `GAME`; U, k, ω: `smoothSolver`
Relaxation factor	$p : 0.5;\ U : 0.8;\ k, \omega : 0.7$	$U, k, \omega : 0.7$
Discretization scheme		
Time	`steadyState`	`backward`
Gradient	`Gauss linear`	`Gauss linear`
Divergence	`Gauss linearUpwind`	`Gauss linearUpwind`
Laplacian	`Gauss linear corrected`	`Gauss linear corrected`
Interpolation	`linear`	`linear`

scheme `Gauss linear`. The convection terms of the momentum equations are discretized using the second-order accurate scheme `Gauss linear upwind`. The laplacian terms are discretized using the second-order conservative `Guass linear corrected` scheme and the interpolation terms, and `linear` interpolation schemes are employed used to compute values at the faces or cell interfaces within a computational grid.

2.3.3 Boundary conditions

For the two-dimensional simulation, a boundary condition used to specify a fixed value at a boundary of a computational domain termed `codedFixedValue` in OpenFOAM is adopted for the inlet. This boundary condition is implemented using user-defined code, which allows for more flexibility and customization compared to other built-in boundary conditions. The mean tangential velocity is specified as $\overline{U}_\theta = \omega_{\text{imp}} R_2$, and the radial velocity is specified as $\overline{U}_r = Q/2\pi R_2 b_2$ corresponding to a pre-set value of the inlet flow rate Q. Besides, a jet wake structure perturbation is approximately mimicked by superposing a m_{F}-periodic Fourier mode in the circumferential direction which is not included in linear stability analysis (see Fig. 2.7 for example):

$$U_r(\theta) = \overline{U}_r \cdot \{1 + A_{\text{inlet}} \cos[m_{\text{F}}(\theta - \omega_{\text{imp}} t)]\}, \tag{2.8a}$$

$$U_\theta(\theta) = \overline{U}_\theta \cdot \{1 + A_{\text{inlet}} \sin[m_{\text{F}}(\theta - \omega_{\text{imp}} t)]\}, \tag{2.8b}$$

where A denotes the amplitude of the Fourier mode and m is its wave number. For the outlet, a boundary condition used to specify a constant value of a computational domain termed `fixedValue` in OpenFOAM is used with the static pressure $p = 0\,\text{Pa}$.

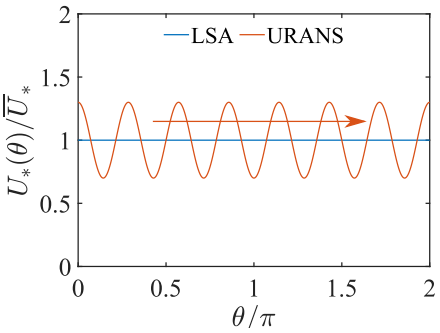

Figure 2.7: The homogeneous inlet velocity boundary condition for 2D linear stability analysis and an example of the mimicked jet wake boundary condition ($A_{\text{inlet}} = 0.03$, $m_{\text{F}} = 7$) for 2D URANS simulation. Note that $*$ denotes the r and θ direction.

For the three-dimensional entire machine simulation, a boundary condition that can be used to impose a fixed volumetric flow rate at an inlet boundary of a computational domain termed `flowRateInletVelocity` in OpenFOAM is adopted for the inlet. For the outlet, a boundary condition allowing for two-way flow through the boundary (a combination of the inlet and outlet boundary conditions) termed `inletOutlet` is employed with the static pressure set to 0 Pa at the outflow box. This boundary condition is commonly used when the flow through the boundary is not fully developed and the flow direction may change. The `noSplip` routine in OpenFOAM is employed for fixed walls, while the `rotatingWallVelocity` routine is employed for the rotating walls to specify the constant rotation velocity of the impeller. The interfaces between separate regions of the computational domain are coupled by the `cyclicAMI` routine. By enforcing mass and momentum conservation, the `cyclicAMI` routine ensures that the fluid flows smoothly between two regions connected by a rotating or oscillating interface. The OpenFOAM routines used for all boundary conditions in the three-dimensional entire machine simulation are listed in detail in Tab. 2.4.

The turbulent kinetic energy k and the turbulent specific dissipation rate ω at the inlet are calculated by:

$$k_{\text{in}} = \frac{3}{2}(I|u_{\text{ref}}|)^2, \tag{2.9}$$

$$\omega_{\text{in}} = \frac{k_{\text{in}}^{0.5}}{C_{\mu}^{0.25} l}, \tag{2.10}$$

where u_{ref} denotes the reference velocity determined using the radial velocity at the inlet of the suction

Table 2.4: Boundary condition types used in OpenFOAM v1906.

Boundary surface	p	U	k	ω
Inlet	`zeroGradient`	`flowRateInletVelocity`	`fixedValue`	`fixedValue`
Outlet	`fixedValue`	`inletOutlet`	`inletOutlet`	`inletOutlet`
Interfaces	`cyclicAMI`	`cyclicAMI`	`cyclicAMI`	`cyclicAMI`
Fixed walls	`zeroGradient`	`noSlip`	`fixedValue`	`omegaWallFunction`
Rotating walls	`zeroGradient`	`rotatingWallVelocity`	`fixedValue`	`omegaWallFunction`

pipe, I denotes the turbulence intensity defined as:

$$I = 0.16(Re)^{-\frac{1}{8}}, \tag{2.11}$$

C_μ is an empirical constant specified in the turbulent model equal to 0.09, and l is the turbulence length determined using the suction pipe diameter in our simulations. For the boundary condition of the turbulence model along the walls, we set

$$k_{\text{wall}} = 0, \tag{2.12}$$

$$\omega_{\text{wall}} = \frac{60\nu}{0.075} y_1^2, \tag{2.13}$$

where y_1 denotes the distance from the first cell center to the nearest wall [55]. We stress that the characteristic turbulence properties are not measured in the experiments, hence they cannot be exactly reproduced in the simulations. However, the robustness of our numerical solution is validated by comparison with the experimental measurements (see the following sections for a detailed discussion). This lets us conclude that the flow is not too sensitive to the inlet turbulence characteristics as a good agreement between numerics and experiments is achieved even if the turbulent inflows are not perfectly matched at the inlet pipe.

For the reduced-order three-dimensional simulation, only the vaneless diffuser and the outflow box are simulated, as described previously. The boundary conditions of the outlet and the diffuser walls keep consistent with the entire machine simulation settings. For the inflow boundary condition, the azimuthally-averaged velocity profiles of the three velocity components ($\overline{U}_r(z)$, $\overline{U}_\theta(z)$, and $\overline{U}_z(z)$) at the impeller outlet derived from numerical simulations are fitted with explicit analytical functions, and then inserted with an m-periodic Fourier mode into OpenFOAM by the `codedFixedValue` routine:

$$U_r(\theta, z) = \overline{U}_r(z) \cdot \{1 + A_{\text{inlet}} \cos[m_{\text{F}}(\theta - \omega_{\text{imp}} t)]\}, \tag{2.14a}$$

$$U_\theta(\theta, z) = \overline{U}_\theta(z) \cdot \{1 + A_{\text{inlet}} \sin[m_{\text{F}}(\theta - \omega_{\text{imp}} t)]\}, \tag{2.14b}$$

$$U_z(\theta, z) = \overline{U}_z(z) \cdot \{1 + A_{\text{inlet}} \cos[m_{\text{F}}(\theta - \omega_{\text{imp}} t)]\}, \tag{2.14c}$$

the phase shift between radial and axial velocities ($\sim \cos(m_{\text{F}}\theta)$) compared to the tangential velocity ($\sim \sin(m_{\text{F}}\theta)$) is motivated by the single-Fourier mode continuity equation in cylindrical coordinates.

To balance the numerical precision and overall computational expense, a time step $\Delta t = \Delta\theta/(2\pi\omega_{\text{imp}})\times 2\pi/180°$ corresponding to $\Delta\theta = 0.5°$ of the runner revolution, was chosen. The time step Δt leads to an angular displacement of the mesh to be less than half of one grid cell at the rotor-stator interface and results in an averaged Courant number for the whole domain of $\overline{C} = 0.0075$ all our simulations at the nominal flow rate. Several literature studies [57] support using $\Delta\theta \leq 1°$, which is consistent with our choice.

With a special focus on the fully-developed instabilities in the diffuser, the startup phase of the machine is excluded by initializing the URANS simulations with corresponding RANS simulation results (simulated for 10000-time steps). In order to ensure that all results presented are under fully-developed conditions, a long physical simulation time $t_{\text{fin}} = 70T$ (where T denotes one impeller revolution period) is set for all URANS simulations to resolve the low-frequency range, as the impeller rotational velocity is higher than the propagation velocity of the instabilities of interest in this study.

2.4 Fitting method^{C}

A simplified simulation approach is proposed to allow for a parametric investigation of the flow in the vaneless diffuser at an affordable computational cost. In order to model the diffuser inflow, a parametric fitting protocol will be employed, based on three underlying assumptions:

- The fitting protocol assumes that the inlet flow conditions of the vaneless diffuser can be extracted from solely tangentially averaged RANS simulation results for several flow rates.
- It is implicitly assumed that no mutual interactions are present between an impeller and the vaneless diffuser as far as rotating instabilities are concerned. This is further motivated by the

study of flow instabilities [2], whose mechanism is related to the flow behavior solely inside the diffuser itself.

- The three velocity components at the impeller outlet will be fitted with explicit analytical functions.

To reproduce the inlet boundary conditions, the diffuser inlet velocity profile is fitted as a function of the flow rate $\hat{Q} = Q/Q_d$, using the RANS simulation results as a fitting database. We start by fitting the flow profiles azimuthally averaged at the diffuser inlet. To fit the z-dependent inlet velocity profile $\vec{U}(z)$, the full range $z \in [-b_3/2, b_3/2]$ is subdivided into two boundary layer regions and a bulk flow region (see Fig.2.3(b)). The fitting was constructed by scale-matching logic starting from the leading order effects with the highest gradients (boundary layers have the highest sensitivity) to the leading order effects with lower gradients (bulk region) to higher order effects (oscillations). In other words, we match one scale per fitting step and then match all scales in the last step. We stress that our approach allows us to include the boundary scale, which is the key to preserving the model's physics. The two boundary regions are fitted with a power-law function, and their thickness δ_i is numerically determined by finding the length that allows fitting the boundary layer at best. The velocity component $U_*(z)$, where $*$ denotes the r, θ, and z direction, is approximated by dedicated functional dependencies within each region according to

$$\text{Boundary region 1,} \qquad z \in [z_{\min}, z_{\min} + \delta_1]: \quad U_* \approx a_{*0} \left(\frac{b_3}{2} + z \right)^{a_{*1}}, \tag{2.15a}$$

$$\text{Boundary region 2,} \qquad z \in [z_{\max} - \delta_2, z_{\max}]: \quad U_* \approx b_{*0} \left(\frac{b_3}{2} - z \right)^{b_{*1}}, \tag{2.15b}$$

$$\text{Bulk flow region,} \qquad z \in [z_{\min} + \delta_1, z_{\max} - \delta_2]: \quad U_* \approx U_*^{\text{bulk}}(z), \tag{2.15c}$$

where the thickness of the boundary layer regions δ_i is specified for different cases, h denotes the width of the diffuser, a_{*0} and b_{*0} are fitting coefficients, $U_*^{\text{bulk}}(z) = \sum_{i=1}^{n} U_*^{\text{bulk,i}}(z)$ consists of the sum of a linear, a quadratic, a fourth power, and/or a trigonometric function as detailed below. For more details, we refer to our previous publication [58].

Building on the fitting developed in this study, we will be capable of further controlling the diffuser inflow and perturbing it ad hoc to study the effect of first harmonic modulations on the mean inflow obtained via the fit.

2.5 Validation[C]

2.5.1 Validation for the simulation

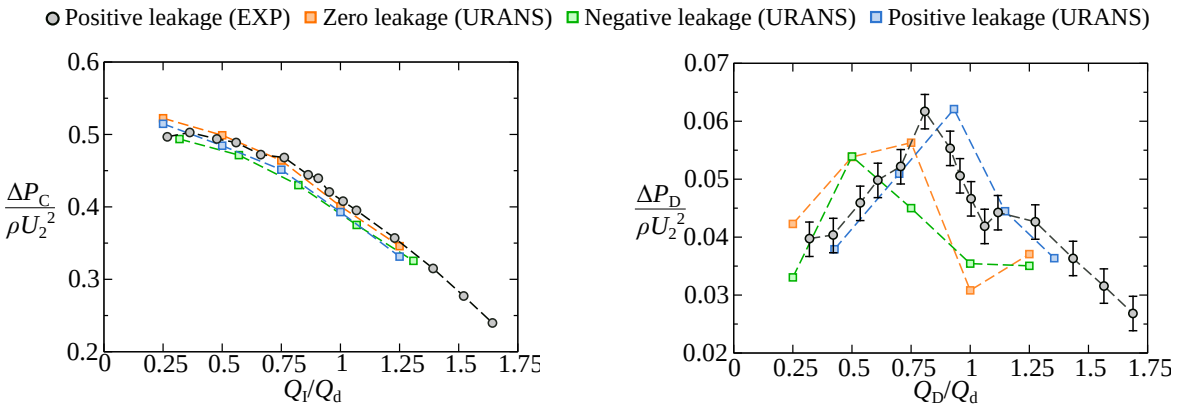

(a) (b)

Figure 2.8: Corrected performance curves of (a) pump and (b) diffuser for three different geometries obtained from experimental and URANS numerical simulation results.

To validate our numerical simulations, the performance of the entire machine, encompassing the impeller and the diffuser, as well as the sole diffuser performance evaluated in terms of static pressure rise obtained from the URANS simulations are compared with the experimental results as depicted in Figs. 2.8(a,b). Concerning the performance of the entire machine (see Fig. 2.8(a)), most of the experimental results are located between the numerical results of the zero- and positive-leakage cases. This is expected since we considered a larger leakage gap in the numerical simulations than in the experiments. Therefore, the effective leakage flow of the experiments is within the positive- and zero-leakage cases simulated by URANS. For the negative-leakage case, the deviation is larger, but the maximum deviation still does not exceed 5%. It has to be mentioned that the volume flow Q is measured far upstream of the pump inlet, i.e. in the upstream part of the inlet pipe, while the Q_{I} here denotes the flow rate inside the impeller, already taking into account the leakage flow rate. The evaluation of the leakage flow at the impeller inlet and outlet is essential, the corrections for the flow rates we refer to our published papers[2].

Taking into account the previously mentioned leakage effect, the diffuser performance versus the diffuser flow rate Q_{D} is illustrated in Fig. 2.8(b). The results show that the diffuser performance curve of the positive-leakage case demonstrates a closer agreement with the experimental data. For the other

two numerical configurations, the deviation at the small flow rates and the design flow rate is big. This is attributed to the occurrence of rotating instability which will be discussed in the following section.

2.5.2 Validation for the fitting method

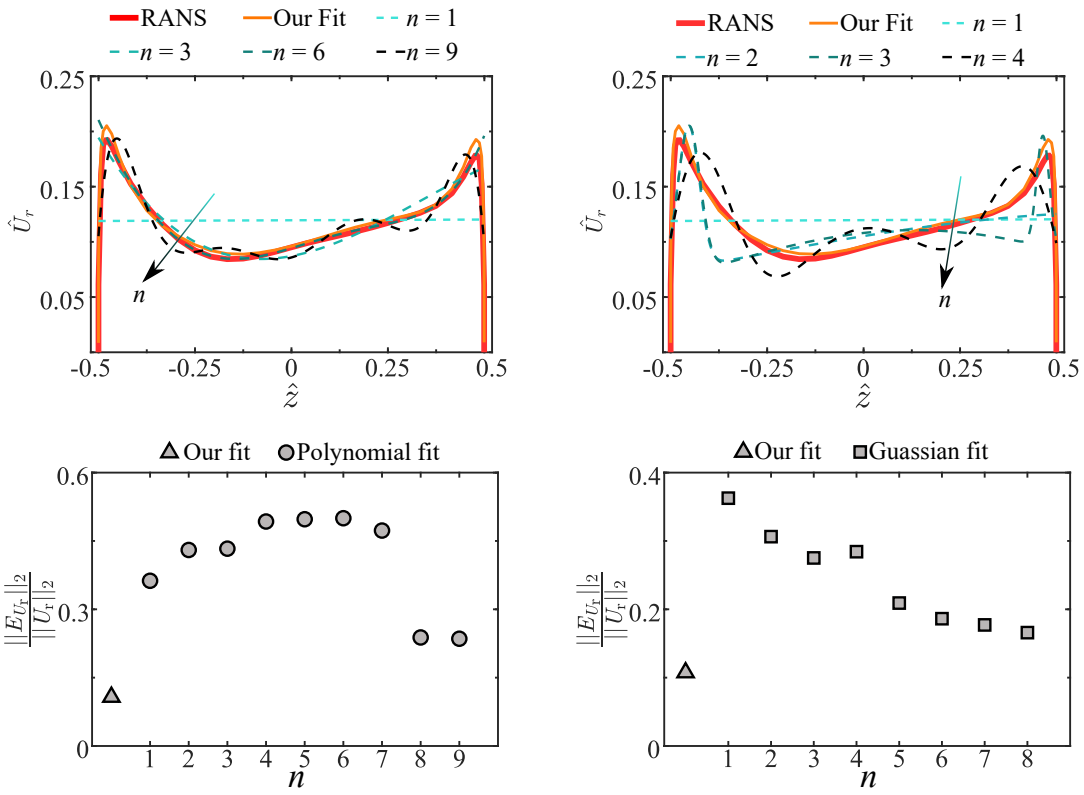

(a) (b)

Figure 2.9: Comparison between the radial velocity profiles U_{r} of the zero-leakage case at the design flow rate Q_d fitted by our multi-stage fitting method and (a) algebraic polynomials and (b) Gaussian functions.

In order to verify the superiority of our proposed scale-matching-like fitting method, the diffuser inflow velocity profiles approximate by conventional one-stage fitting methods utilize algebraic polynomials

$$\hat{U}_*(z) \approx \sum_{i=0}^{n} a_{*i}^{P} z^i, \tag{2.16}$$

or Gaussian functions

$$\hat{U}_*(z) \approx \sum_{i=1}^{n} a_{*i}^{G} \exp\left[-\left(\frac{z - b_{*i}^{G}}{c_{*i}^{G}}\right)^2\right], \tag{2.17}$$

are contrasted with our multi-stage fitting results, where $*$ denotes r, θ or z component of the velocity, n represents either the degree of the polynomial functions or the count of Gaussian bells, and a_i,

b_i, and c_i are the fitting coefficients, P and G represent polynomial or Gaussian fits, respectively. As an example, the fitting results of the radial velocity profile of the zero-leakage case at the design flow rate are presented in Fig. 2.9. Concerning the algebraic polynomial fitting (see top panel of Fig. 2.9(a)), lower-order fits fail to capture the boundary layer, while higher-order fits introduce artificial oscillations. Moreover, the L2 norm of the error for our scale-matching fit is significantly lower compared to the polynomial fits (see bottom panel of Fig. 2.9(a)). On the other hand, the Gaussian fit also introduces fictitious velocity profile oscillations (see top panel of Fig. 2.9(b)). The L2 norm of the error (see the bottom panel of Fig. 2.9(b)) demonstrates the superior accuracy of our scale-matching-like fit. Although the implementation of traditional single-stage fitting functions is considerably easier and faster compared to our method, this cost-saving advantage comes at the expense of a substantial reduction in accuracy and the presence of several numerical artifacts including a boundary condition discontinuity and a wavy profile. As demonstrated in previous research [59], it is difficult that traditional single-stage fitting algorithms could be effectively employed to accurately study the stability of flow in the presence of shear flow oscillations. On the contrary, Our scale-matching-like approach prevents the introduction of artificial waviness in the fitted profile, thereby enhancing the reliability of our method compared to conventional fitting approaches.

To examine the performance of the fitted profiles in reproducing the flow field, new simulations are carried out using some of the inflow profiles derived from existing fitting methods. For algebraic polynomials functions, degrees lower than 4 are not considered since they do not conform to the no-slip boundary conditions at the diffuser wall. To maximize the reliability of the fit among various values of n, 8th-degree polynomials are selected based on the minimum root-mean-square distance from the reference profile (this observation is evident in the L2-norm depicted in Fig. 2.9(a)). For Gaussian fits, the boundary layer features of the inlet profile can be qualitatively reproduced with $n \geq 4$. Therefore, Gaussian fit with 4 and 8 Gaussian bells is selected for comparison.

A comparison of the azimuthally averaged flow fields in the meridional section for the full machine simulation, the reduced-order simulation using a scale-matched fit, the reduced-order simulation using an 8th polynomial fit, and the reduced-order simulation using Gaussian fit with 4 and 8 Gaussian bells is depicted in the Fig. 2.10. When traditional methods are employed, notable mean flow separation occurs on the hub wall (see the blue region in $\hat{U}_r$, $\hat{U}_\theta$, and $\hat{U}_z$) and the velocity at the shroud wall is consistently overestimated (see the yellow region in $\hat{U}_r$ and $\hat{U}_\theta$). Furthermore, at the diffuser inlet, the

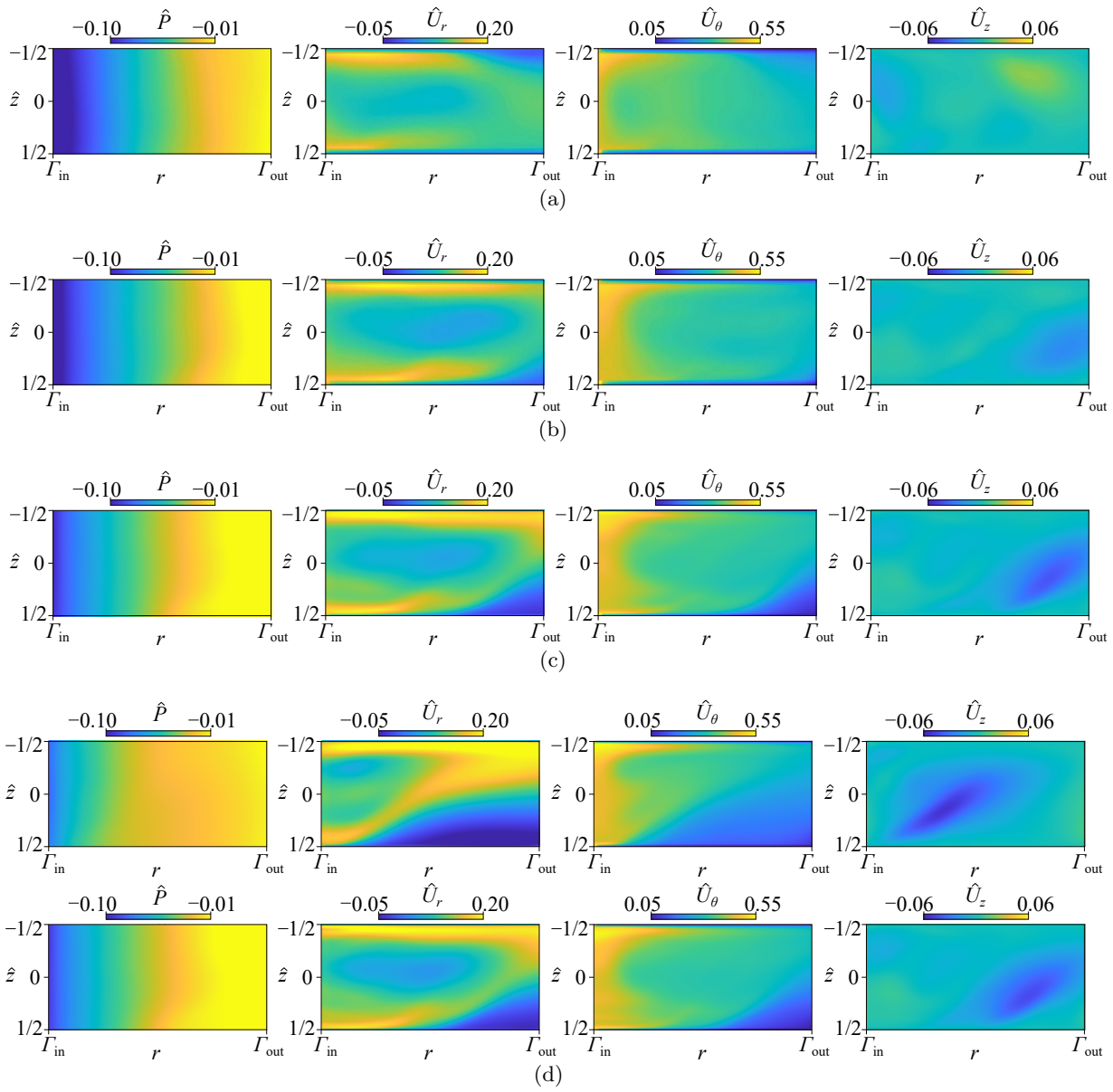

Figure 2.10: Comparison of the azimuthally-averaged color maps of the static pressure, radial, tangential, and axial velocity (from left to right) of RANS simulation for the design flow rate Q_d of (a) the entire machine and of the diffuser only using inlet mean velocity profiles fitted with different approaches: (b) our scale-like matching fit, (c) $n = 8$ polynomial fit, and (d) $n = 4$ (top) and $n = 8$ (bottom) Gaussian fits.

presence of waviness in the polynomial and Gaussian fits for the inlet profile results in the entrainment of an azimuthal velocity finger within the bulk flow (see the wavy yellow region in Figs. 2.10(c,d)). The presence of this unphysical artifact is significantly reduced when our scale-matching approach is

utilized, as depicted in Fig. 2.10(b), aligns with the corresponding full-pump simulations shown in Fig. 2.10(a). Moreover, our scale-matching method proposed correctly reproduces the pressure gradient, which is underestimated by traditional polynomial and Gaussian fits. Based on the aforementioned findings, it can be concluded that our scale-like matching fitting method outperforms the classic fitting techniques we examined to a significant degree.

Chapter 3

Results

Contents

B. This part has already been published in the appended paper B: M. Fan, A. Dazin, G. Bois, F. Romanò, *Effect of inlet leakage flow on the instability in a radial vaneless diffuser*, Phys. Fluids, 35(1) (2023), 014105.

D. This part has already been published in the appended paper D: M. Fan, A. Dazin, G. Bois, F. Romanò, *Instabilities in a turbulent swirling source flow between parallel rings*, Phys. Fluids, 35(10) (2023), 101701.

E. This part has already been published in the appended paper E: M. Fan, A. Dazin, G. Bois, F. Romanò, *Effect of radius ratio on the instabilities in a vaneless diffuser*, Eur. J. Mech. B/Fluids, 104 (2024), 1–7.

3.1 Results of reduced-order models

3.1.1 2D linear stability analysis[B]

Under the hypothesis of a two-dimensional core flow mechanism, a two-dimensional linear stability analysis was first performed using the analytical model of Tsujimoto et al .[1]. Note the linear stability analysis model considers the core flow at the mid-height of the diffuser (perpendicular to the z axis), rather than at the meridional section. This model has successfully predicted the mode-3 instability observed in Heng et al.[41, 18] and it will further help to clarify the origin of the rotating stall at low flow rates. We recall that several assumptions are made in the model of [1] as follows:

- a two-dimensional incompressible and inviscid flow is considered,
- the boundary conditions are axisymmetric, i.e. uniform static pressure at diffuser outlet and imposed velocity magnitude and flow angle at inlet,
- the flow field is described as a superposition of a steady basic state and an infinitesimal rotating perturbation determined by linear stability analysis.

Under these assumptions, the basic state streamlines in the vaneless diffuser take the form of logarithmic spirals extending from the diffuser inlet to the outlet. By utilizing scaling factors for length, time, velocity, and pressure, denoted as R_3, $(2\pi R_3^2)/Q$, $Q/2\pi R_3$, and $\rho Q^2/(2\pi R_3)^2$, respectively, the velocity $\vec{U}_0 = (U_{0,r}, U_{0,\theta})$ and pressure of the basic state are non-dimensioned as:

$$\begin{aligned} U_{0,r} &= \frac{1}{r}, \\ U_{0,\theta} &= \frac{\mu}{r}, \\ P_0 &= -\frac{1}{2}\left(1+\mu^2\right)\left(\frac{1}{r^2}+\frac{1}{R^2}\right), \end{aligned} \tag{3.1}$$

where $\mu = U_{0,\theta}/U_{0,r}|_{r=1}$ and $1 < r < R = R_4/R_3$. We further remark that such a basic state is irrotational, i.e. $\nabla \times \vec{U}_0 = 0$. Carrying out a linear stability analysis, the total flow in the vaneless diffuser results from the sum of the basic state and the infinitesimal perturbation (prime sign):

$$\begin{aligned} U_r &= U_{0,r}(r) + u'_r(r,\theta,t), \\ U_\theta &= U_{0,\theta}(r) + u'_\theta(r,\theta,t), \\ P &= P_0(r) + p'(r,\theta,t), \end{aligned} \tag{3.2}$$

where $\vec{u}' \ll \vec{U}_0$ and $p' \ll P_0$. As the basic state is steady and homogeneous in θ, the ansatz for the infinitesimal perturbation is:

$$\{u'_r, u'_\theta, p'\}(r,\theta,t) = \{\tilde{u}_r, \tilde{u}_\theta, \tilde{p}\}(r) e^{i\xi t - im\theta}, \tag{3.3}$$

where m is the wavenumber, i.e. the number of rotating stall cells. The complex frequency ξ could be divided in a real χ and complex σ part, i.e. $\xi = \chi - i\sigma$. The real part χ is the angular frequency, while σ is the growth rate of the instability. The flow is unstable (stable) when $\sigma > 0$ ($\sigma < 0$) and the mathematical problem is closed by enforcing the boundary conditions proposed by Tsujimoto et al. [1]:

$$r = 1 : \tilde{u}_r = \tilde{u}_\theta = 0; \qquad r = R : \tilde{p} = 0. \tag{3.4}$$

The neutral stability modes are then obtained by setting $\sigma = 0$, fixing m, and following the algorithm proposed by Heng et al. [41], which makes use of a shooting method for approaching the analytical solution by successive iterations.

We carried out the linear stability analysis for three different diffuser radius ratios, i.e. $\Gamma \in \{1.25, 1.50, 2.00\}$. The flow angle α (defined as the angle between the flow path and the tangential direction, i.e. $\alpha = \arctan(U_r/U_\theta)$) and corresponding propagation velocity ω_{stall} predicted for different neutral stability modes are depicted in Fig. 3.1. The results show that the critical flow angle α_c (defined as the critical threshold of the flow angle α that leads to the onset of the rotating stall) of the rotating stall is approximately 6°, 10°, and 16° for $\Gamma = 1.25$, 1.50, and 2.00 respectively. The most unstable modes for different Γ are also shed by this plot.

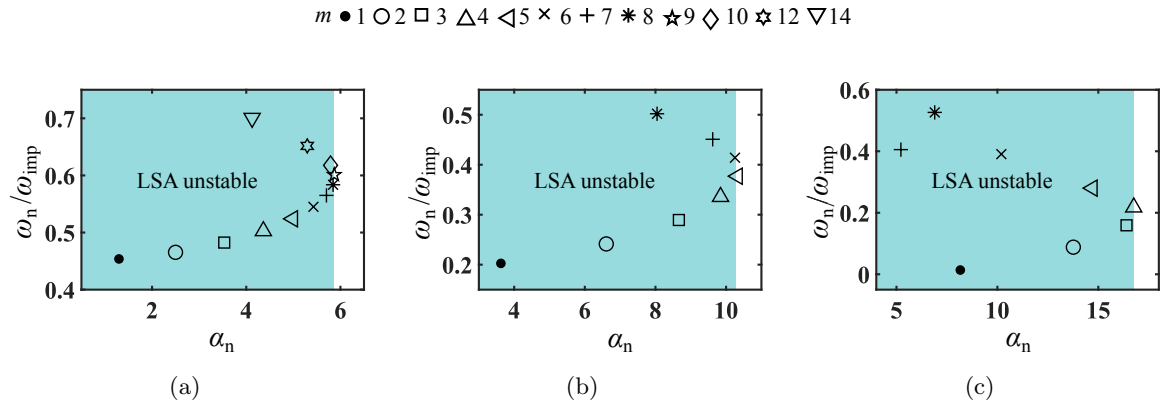

Figure 3.1: Critical flow angle and propagation velocity for different neutral modes with three different radius ratios: (a) $\Gamma = 1.25$,(b) $\Gamma = 1.50$, (c) $\Gamma = 2.00$.

Table 3.1: Critical flow angle, critical propagation velocity, and normalized energy production rates for different modes with radius ratio $\Gamma = 1.25$.

$\Gamma = 1.25$	m = 1	m = 2	m = 3	m = 4	m = 5	m = 6	m = 7	m = 8
α_{n}	1.2969	2.4981	3.5320	4.3632	4.9888	5.4266	5.7029	5.8436
$\omega_{\mathrm{n}}/\omega_{\mathrm{imp}}$	0.4538	0.4653	0.4824	0.5027	0.5240	0.5451	0.5650	0.5837
$\int_{\mathrm{V}} I_1^{'}$	-0.0009	-0.0034	-0.0078	-0.0141	-0.0222	-0.0320	-0.0433	-0.0553
$\int_{\mathrm{V}} I_2^{'}$	0.1894	0.2039	0.2275	0.2593	0.2978	0.3405	0.3840	0.4238
$\int_{\mathrm{V}} I_3^{'}$	0.1894	0.2039	0.2275	0.2593	0.2978	0.3405	0.3840	0.4238
$\int_{\mathrm{V}} I_4^{'}$	0.1566	0.1575	0.1587	0.1596	0.1596	0.1579	0.1538	0.1468
K_{out}	-0.5345	-0.5618	-0.6059	-0.6642	-0.7329	-0.8067	-0.8786	-0.9391
$\frac{dE_{\mathrm{kin}}}{dt}$	0.00002	0.00002	0.00002	0.00002	0.00002	0.00002	0.00002	0.00002
$\Gamma = 1.25$	m = 9	m = 10	m = 11	m = 12	m = 13	m = 14	m = 15	m = 16
α_{n}	5.8688	5.7900	5.6061	5.2955	4.7986	4.1246	3.6220	3.3051
$\omega_{\mathrm{n}}/\omega_{\mathrm{imp}}$	0.6011	0.6177	0.6342	0.6517	0.6729	0.7005	0.7250	0.7433
$\int_{\mathrm{V}} I_1^{'}$	-0.0672	-0.0777	-0.0847	-0.0851	-0.0742	-0.0531	-0.0384	-0.0302
$\int_{\mathrm{V}} I_2^{'}$	0.4538	0.4662	0.4507	0.3943	0.2844	0.1540	0.0859	0.0547
$\int_{\mathrm{V}} I_3^{'}$	0.4538	0.4662	0.4507	0.3943	0.2844	0.1540	0.0859	0.0547
$\int_{\mathrm{V}} I_4^{'}$	0.1362	0.1213	0.1018	0.0776	0.0501	0.0279	0.0189	0.0154
K_{out}	-0.9765	-0.9759	-0.9184	-0.7811	-0.5448	-0.2828	-0.1522	-0.0945
$\frac{dE_{\mathrm{kin}}}{dt}$	0.00002	0.00001	0.00000	-0.00001	-0.00002	-0.00001	0.00002	0.00004

Table 3.2: Critical flow angle, critical propagation velocity, and normalized energy production rates for different modes with radius ratio $\Gamma = 1.50$.

$\Gamma = 1.50$	m = 1	m = 2	m = 3	m = 4	m = 5	m = 6	m = 7	m = 8
α_{n}	3.6239	6.6078	8.6631	9.8425	10.3252	10.2517	9.6208	8.0450
$\omega_{\mathrm{n}}/\omega_{\mathrm{imp}}$	0.2026	0.2415	0.2894	0.3358	0.3771	0.4140	0.4509	0.5020
$\int_{\mathrm{V}} I_1^{'}$	-0.0131	-0.0545	-0.1290	-0.2383	-0.3755	-0.5153	-0.5931	-0.4543
$\int_{\mathrm{V}} I_2^{'}$	0.3913	0.5416	0.7895	1.1133	1.4561	1.7017	1.6316	0.8951
$\int_{\mathrm{V}} I_3^{'}$	0.3913	0.5416	0.7895	1.1133	1.4561	1.7017	1.6316	0.8951
$\int_{\mathrm{V}} I_4^{'}$	0.9545	0.9916	1.0313	1.0475	1.0098	0.8847	0.6389	0.2807
K_{out}	-1.7239	-2.0202	-2.4812	-3.0358	-3.5464	-3.7727	-3.3090	-1.6167
$\frac{dE_{\mathrm{kin}}}{dt}$	0.00004	0.00004	0.00006	0.00006	0.00006	0.00003	-0.00003	-0.00005

Table 3.3: Critical flow angle, critical propagation velocity, and normalized energy production rates for different modes with radius ratio $\Gamma = 2.00$.

$\Gamma = 2.00$	m = 1	m = 2	m = 3	m = 4	m = 5	m = 6	m = 7	m = 8
α_{n}	8.1631	13.7638	16.3984	16.7557	14.7084	10.1955	5.2188	6.8950
$\omega_{\mathrm{n}}/\omega_{\mathrm{imp}}$	0.0138	0.0881	0.1593	0.2178	0.2801	0.3907	0.4054	0.5264
$\int_{\mathrm{V}} I_1^{'}$	-0.1466	-0.6609	-1.6722	-3.0964	-3.5827	-1.3013	-0.4639	-0.3130
$\int_{\mathrm{V}} I_2^{'}$	0.1417	1.2891	3.3704	5.7661	5.2232	0.8781	0.1776	0.0498
$\int_{\mathrm{V}} I_3^{'}$	0.1417	1.2891	3.3704	5.7661	5.2232	0.8781	0.1776	0.0498
$\int_{\mathrm{V}} I_4^{'}$	5.1147	5.8333	6.4290	5.9981	3.1013	0.7055	0.3294	0.2613
K_{out}	-5.2515	-7.7505	-11.4974	-14.4338	-9.9652	-1.1600	-0.2212	-0.0481
$\frac{dE_{\mathrm{kin}}}{dt}$	-0.00001	0.00006	0.00011	0.00005	-0.00019	0.00048	-0.00046	-0.00008

Besides, a posterior analysis of the kinetic energy transferred between the basic state and the critical mode is employed to identify the physical mechanisms leading to the flow instability and to validate the overall energy conservation of our neutral mode. To that end, we numerically evaluate all terms of the inviscid Reynolds-Orr-equation

$$\frac{dE^{kin}}{dt} = \sum_{k=1}^{4} \int_V I_k' dV + K^{out}, \tag{3.5}$$

where E_{kin} is the total kinetic energy, I_k' are the kinetic energy densities resulting from the non-linear term of the incompressible Euler equations, and

$$K^{\mathrm{out}} = -\frac{1}{2} \int_S U_{0,r} {u_r'}^2 S^{\mathrm{out}}, \tag{3.6}$$

is the transport of perturbation energy through the outlet surface S^{out}. Since $\tilde{u} = 0$ at the inlet, no perturbation energy is advected into the system from upstream. Moreover, the work done by pressure forces does not contribute to the energy budget as we assume that the pressure perturbations vanish at the outlet (i.e. $\tilde{p} = 0$ at $r = R$). To ease the interpretation of the energy budget, the local energy production rates are decomposed along the streamlined coordinates of the basic state, i.e.

$$\vec{u}' = \vec{u}_{\parallel}' + \vec{u}_{\perp}', \tag{3.7}$$

where $\vec{u}_{\parallel}'$ is the perturbation component projected along the basic state streamlines, while $\vec{u}_{\perp}' = \vec{u}' - \vec{u}_{\parallel}'$ is the normal component. The corresponding energy density terms I_k' read:

$$\begin{aligned} \sum_{k=1}^{4} I_k' = -[&\vec{u}_{\perp}' \cdot (\vec{u}_{\perp}' \cdot \nabla \vec{U}_0) + \vec{u}_{\parallel}' \cdot (\vec{u}_{\perp}' \cdot \nabla \vec{U}_0) \\ &+ \vec{u}_{\perp}' \cdot (\vec{u}_{\parallel}' \cdot \nabla \vec{U}_0) + \vec{u}_{\parallel}' \cdot (\vec{u}_{\parallel}' \cdot \nabla \vec{U}_0)], \end{aligned} \tag{3.8}$$

where k numbers all terms on the right-hand side consecutively. The sign of the integrands I'_k determines whether the local energy transfer acts as a destabilizing (positive) or a stabilizing (negative) contribution. If the rate of change of the kinetic energy $\frac{dE^{kin}}{dt}$ is positive, the basic flow is unstable, and vice versa. Hence the energy budget is also used to verify the linear stability results, because the rate of change of the kinetic energy must vanish for the neutral modes, i.e.

$$\frac{dE^{kin}}{dt}|_{\sigma=0} = 0. \tag{3.9}$$

In our computations, such a condition is verified at the 5th digit, hence we can consider our computation of the neutral mode validated.

To complement the qualitative interpretation done so far relying on the scalar fields of I'_k, the total energy budget is also reported in Tab. 3.1, Tab. 3.2, and Tab. 3.3 for $\Gamma = 1.25$, 1.50, and 2.00 respectively. Our results show that for the three different radius ratios Γ with different instability modes, the instability mechanism is similar, $\int_V I'_2 dV$, $\int_V I'_3 dV$, and $\int_V I'_4 dV$ are always contributing to the destabilization of the basic state. On the other hand, $\int_V I'_1 dV$ has a minor stabilizing effect, while most of the energy produced by $\int_V I'_2 dV$, $\int_V I'_3 dV$ and $\int_V I'_4 dV$ is transported outside of the diffuser leading to a high-magnitude, negative K^{out}. There are, therefore, two mechanisms contributing to the instability of the diffuser basic state:

1. The lift-up mechanism, that describes how the basic flow momentum is transported in the normal direction to the basic state streamlines by $\vec{u}'_\perp \cdot \nabla \vec{U}_0$ and feeds back on the parallel component of the critical perturbation $\vec{u}'_\parallel$. This is represented by the $I'_2 = -\vec{u}'_\parallel \cdot (\vec{u}'_\perp \cdot \nabla \vec{U}_0)$, which in our flow coincides with the I'_3, where I'_3 denotes the reverse lift up mechanism.

2. The strong streamwise deceleration due to the radial increase of the diffuser cross-section. This is always a destabilizing effect because I'_4 has a quadratic term in $\vec{u}_\parallel$, hence its sign is solely determined by the gradient of the basic flow momentum transported along the streamlines. A decrease of basic state momentum leads to a positive contribution of $I'_4 = -\vec{u}'_\parallel \cdot (\vec{u}'_\parallel \cdot \nabla \vec{U}_0)$, therefore to a transfer of energy from the basic state to the perturbation.

The lift-up effect is a typical destabilization mechanism proper of shear flows, and in our case, it plays a significant role because the basic state streamlines are logarithmic spirals, hence a fluid element would be subject to a shear if displaced in cross-stream direction. On the other hand, the streamwise deceleration is a destabilizing mechanism important in all the diffusers and jet flows.

For $\Gamma = 1.25$, $\int_V I_4' dV$ is always lower in magnitude compared to $\int_V I_2' dV$ and $\int_V I_3' dV$. This is expected because the diffuser is too short, and the streamwise deceleration effect is weaker. For $\Gamma = 1.50$, with the instability mode number $m \leq 3$, $\int_V I_4' dV$ being slightly dominant in magnitude, the streamwise deceleration effect becomes stronger. As m increases above 3, the lift-up mechanism plays a more important role in the destabilizing effect. For $\Gamma = 2.00$, the streamwise deceleration mechanism is the dominant mechanism except $m = 5$ and $m = 6$.

3.1.2 Reduced-order 2D simulations

The linear stability analysis neglected the effect of the non-linear interactions between perturbation modes. The present linear stability is proven to be capable of predicting the instability mode which is observed in the experiment of this diffuser. However, the linear approach is clearly limited to predicting the asymptotic stability of each standalone perturbation mode. Moreover, the linear approach based on the model of Tsujimoto et al. [1] relies exclusively on the skewness of the diffuser inflow and does not involve any inhomogeneous forcing in θ. Hence, we carried out the 2D numerical simulation which considers the nonlinear effect and the inflow modulation in θ direction. We further recall that the inflow jet wake structure perturbation is approximately mimicked by superposing a m_{F}-periodic Fourier mode with different amplitude A_{inlet} in the circumferential direction (see Eq. 2.8 in Sec. 2.3.3) as depicted in Fig. 3.2.

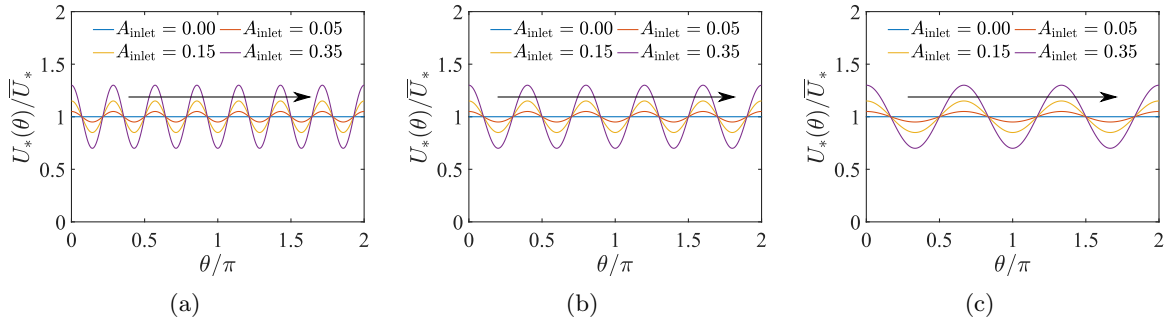

Figure 3.2: The mimicked jet wake boundary condition with different amplitudes A_{inlet} and different Fourier mode numbers for 2D URANS simulation: (a) $m_{\mathrm{F}} = 7$, (b) $m_{\mathrm{F}} = 5$, (c) $m_{\mathrm{F}} = 3$. Note that $*$ denotes the r and θ direction.

Two numerical probes are placed at the mid-radial distance of the diffuser with an angular phase shift of 60°. The rotating instability characteristics in terms of the number of instability patterns and propagation velocity can be detected by the analysis of the cross-power spectra of two probes

located at the same radius with an angular difference [36, 37]. Such instability characteristics are further confirmed by visualizing the flow fields. As an example, the flow field and the FFT result for the diffuser radius ratio $\Gamma = 1.25$ with homogeneous inflow ($A_{\text{inlet}} = 0$) with inflow angle $\alpha = 2.5$ (corresponds to the flow rate $Q/Q_{\text{d}} = 0.25$) is depicted in Fig. 3.3. For all other cases, the instability propagation velocity and mode diagram are summarized in Fig. 3.4, Fig. 3.5, and Fig. 3.6 for the radius ratios $\Gamma \in \{1.25, 1.50, 2.00\}$. More detailed information including the instability frequency f_{stall} and amplitude A_{p} is summarized in Appendix B.1.

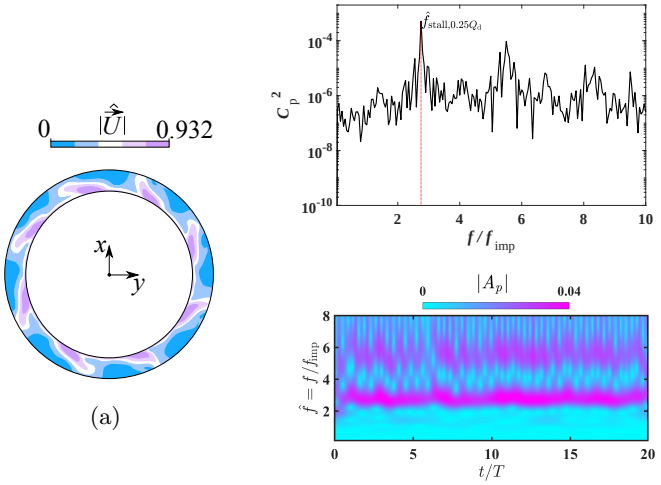

(a)

(b)

Figure 3.3: (a) Color maps of instantaneous velocity magnitude distribution and (b) Fourier and wavelet analysis results of the reduced-order 2D model for $\Gamma = 1.25$ at $Q/Q_{\text{d}} = 0.25$ with homogeneous inflow ($A_{\text{inlet}} = 0$).

Figure 3.4 depicts the comparison of propagation velocity ω_{stall} and mode diagram of the instability identified for the short diffuser ($\Gamma = 1.25$) with four different amplitude of the inflow Fourier mode $A_{\text{inlet}} \in \{0, 0.05, 0.15, 0.35\}$ with three different periodic $m_{\text{F}} \in \{7, 5, 3\}$ imposed to the inflow. Concerning the result with mean inflow ($A_{\text{inlet}} = 0$), the dominant instability mode number is m = 8 (see cyan shadow in the bottom of Fig. 3.4(a-c)). As 7-periodic Fourier mode with different amplitudes applied to the inflow, the mode-7 instability is triggered (see orange shadow in the bottom of Fig. 3.4(a)). Besides, for the highest amplitude $A_{\text{inlet}} = 0.35$, superharmonics lead to a mode-14 instability (see purple shadow in the bottom of Fig. 3.4(a)). The propagation velocity ω_{stall} of the mode-14 instability is slower than the other modes. With the increase of the flow angle α, propagation

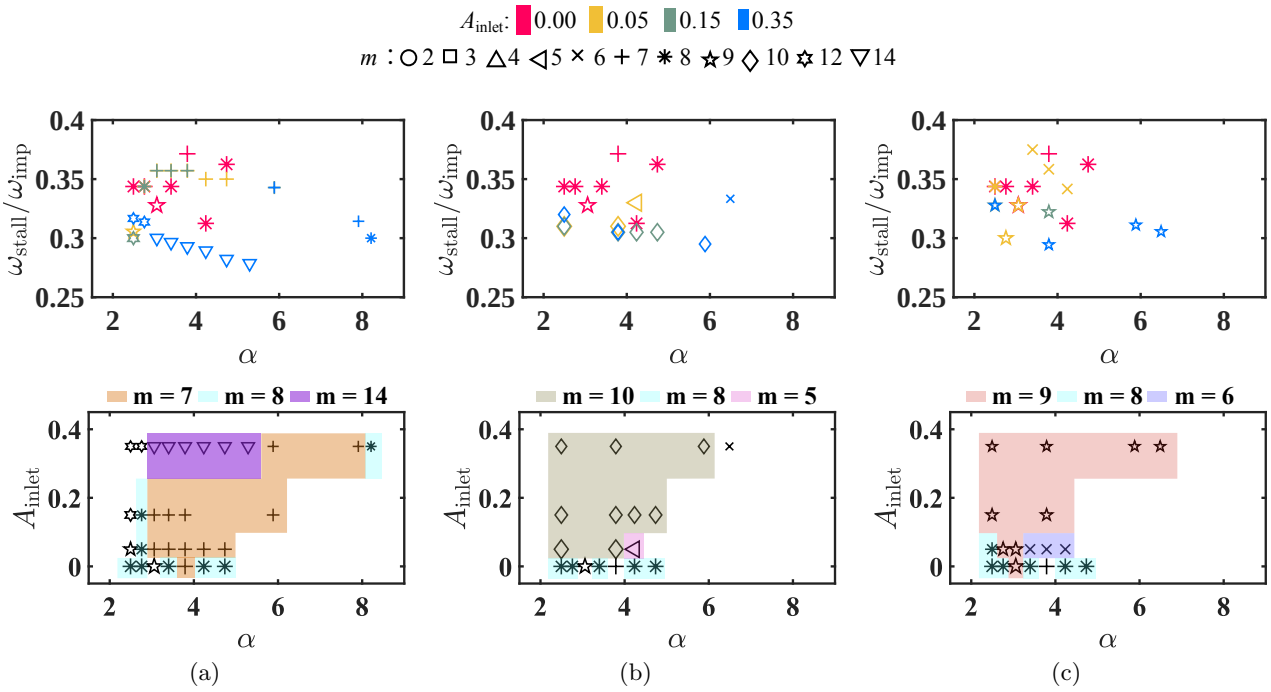

Figure 3.4: Instability characteristics of the flow in the diffuser of radius ratio $\Gamma = 1.25$ with 3 different periodic of inflow Fourier mode m_F: (a) $m_F = 7$, (b) $m_F = 5$, (c) $m_F = 3$.

velocity ω_{stall} of mode-14 shows a linear downward trend, as the one reported for a 3D stall in full pumps (see Fan et al. [2]). For the results with a 5-periodic inflow Fourier mode (see Fig. 3.4(b)), the superharmonic of the inflow Fourier mode results in a mode-10 instability for most flow conditions. The mode 5 instability is only triggered with the inflow Fourier amplitude $A_{inlet} = 0.05$ at the flow angle $\alpha = 4.2°$ (corresponds to the flow rate $Q/Q_d = 0.4$). We rationalize the 2D simulations based on the linear stability analysis. Higher harmonics are unstable because they are linearly unstable and triggered by forcing (7 blades -> mode 14, 5 blades -> mode 10), and they amplify the transfer of energy from the basic state to the instability by means of I'_2 and I'_3 terms (lift up and amplify up). On the contrary, too-high wave numbers are prevented by viscous diffusion that dissipates the stall perturbation energy. It is also expected that for larger inflow modes the instability switches from m=5 to m=10 because the strength of the modeled jet-wake penetrates deeper in the diffuser and allows for perturbation energy production well in-depth inside the diffuser making advantageous the transfer of energy to higher harmonics (m = 14 and 10 rather than m = 7 and 5, respectively, for A>0.05). Overall, the instability propagation velocity ω_{stall} decreases with the increase of the inflow angle α. Concerning the results with a 3-periodic inflow Fourier mode (see Fig. 3.4(c)), the super-

harmonics of the Fourier mode triggers mode-6 (see light purple shadow in the bottom of Fig. 3.5(c)) and mode-9 (see light red shadow in the bottom of Fig. 3.5(c)) instability. Similar to previous results, the instability propagation velocity ω_{stall} decreases with the increase of the inflow angle α.

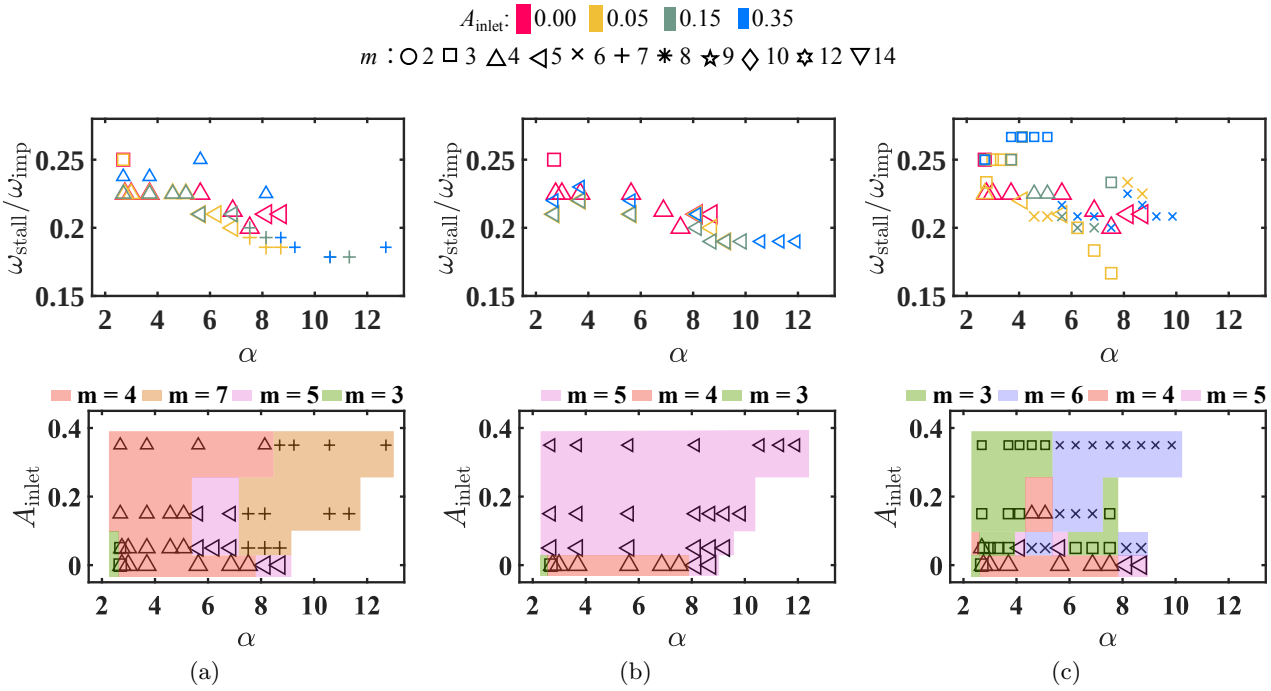

Figure 3.5: Instability characteristics of the flow in the diffuser of radius ratio $\Gamma = 1.50$ with 3 different periodic of inflow Fourier mode m_{F}: (a) $m_{\text{F}} = 7$, (b) $m_{\text{F}} = 5$, (c) $m_{\text{F}} = 3$.

Figure 3.5 depicts the comparison of propagation velocity ω_{stall} and mode diagram of the instability identified for the medium diffuser ($\Gamma = 1.50$) with four different amplitude of the inflow Fourier mode $A_{\text{inlet}} \in \{0, 0.05, 0.15, 0.35\}$ with three different periodic $m_{\text{F}} \in \{7, 5, 3\}$ imposed to the inflow. The dominant instability mode number with mean inflow ($A_{\text{inlet}} = 0$) is m = 3 with the inflow angle $\alpha = 2.7°$ (corresponds to the flow rate $Q/Q_{\text{d}} = 0.25$). As the flow angle α increased, the dominant instability mode number changed to m = 4 with the inflow angle $2.7° < \alpha < 8.1°$ (corresponds to the flow rate $0.25 < Q/Q_{\text{d}} < 0.625$). And the mode 5 instability is dominant (see light red shadow in the bottom of Fig. 3.5(a)) when the inflow angle $\alpha > 8.1°$ (corresponds to the flow rate $Q/Q_{\text{d}} > 0.625$). As 7-periodic Fourier mode with different amplitudes A_{inlet} applied to the inflow, the primary linearly unstable mode-4 and mode-5 instability is still dominant for lower flow angles. However, for larger flow angles, the mode-7 instability is dominant. We presume that the inflow Fourier mode m_{F} just selects the m= 7 mode already linearly unstable. Hence this case still relies on the linear instability of the

mean core flow and not on the jet-wake instability. Besides, we can find that the propagation velocity ω_{stall} of mode 7 instability is lower than the mode 4 instability. For the results with a 5-periodic inflow Fourier mode (see Fig. 3.5(b)), the mode-5 instability is triggered as a dominant mode for all different inflow angles. With the increment of the amplitude A_{inlet} of the inflow Fourier mode, such instability occurs for higher flow angle α. The propagation velocity ω_{stall} of the instabilities decreases with the increase of the flow angle α and then maintains the same level after the flow angle α reaches about 8.5°. Concerning the result with a 3-periodic inflow Fourier mode (see Fig. 3.5(c)), a mode-3 instability triggered for lower flow angles. Besides, a mode 6 instability occurred at higher flow angles due to the superharmonic of the inflow Fourier mode. Compared to the other instability modes, the mode-6 instability has a lower propagation velocity ω_{stall}. This reconfirms that the inflow Fourier mode m_{F} can have a significant role in determining which linearly unstable mode gets selected by the flow.

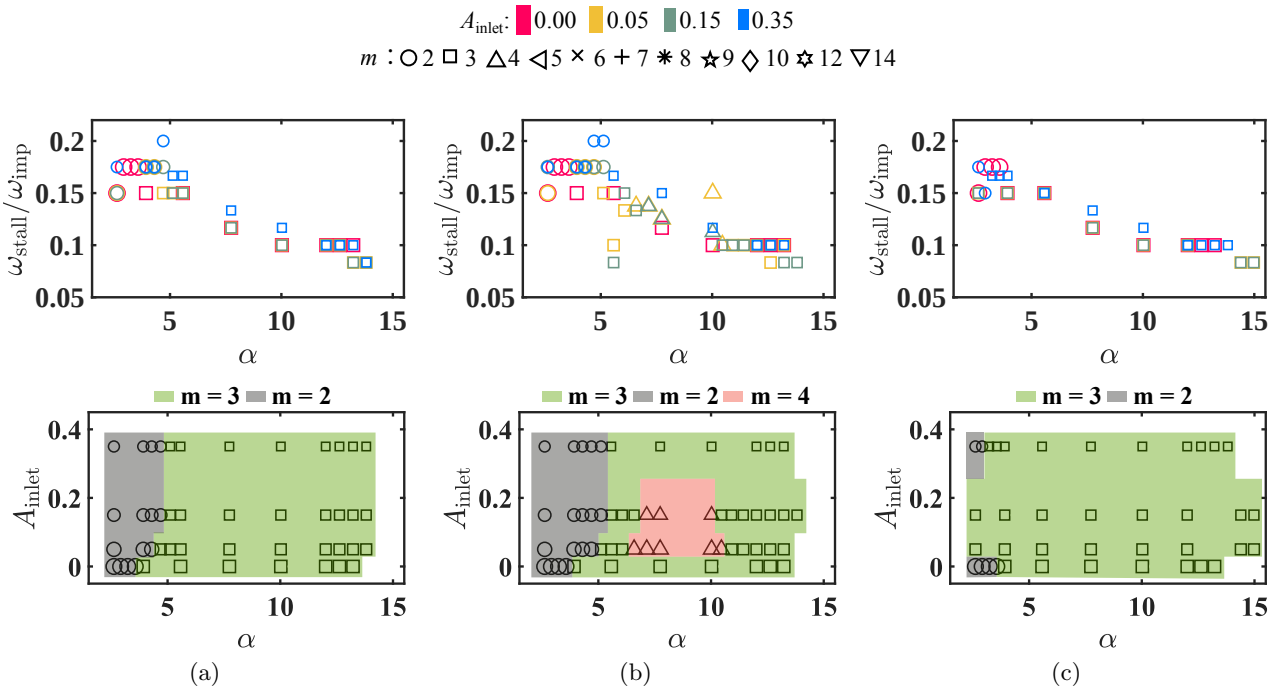

Figure 3.6: Instability characteristics of the flow in the diffuser of radius ratio $\Gamma = 2.00$ with 3 different periodic of inflow Fourier mode m_{F}: (a) $m_{\text{F}} = 7$, (b) $m_{\text{F}} = 5$, (c) $m_{\text{F}} = 3$.

Figure 3.6 depicts the comparison of propagation velocity ω_{stall} and mode diagram of the instability identified for the largest diffuser ($\Gamma = 2.00$) with four different amplitude of the inflow Fourier mode $A_{\text{inlet}} \in \{0, 0.05, 0.15, 0.35\}$ with three different periodic $m_{\text{F}} \in \{7, 5, 3\}$ imposed to the inflow.

Concerning the result with mean inflow ($A_{\text{inlet}} = 0$), the dominant instability mode number is m = 2 (see the grey shadow in the bottom of Fig. 3.6(a-c)) with the inflow angle $\alpha < 3.9°$ (corresponds to the flow rate $Q/Q_{\text{d}} < 0.375$), which show good consistency with the linear stability analysis diagram (see Fig. 3.1). While mode-3 instability is dominant (see blue shadow in the bottom of Fig. 3.6(a-c)) for $\alpha \geq 3.92°$ (corresponds to the flow rate $Q/Q_{\text{d}} \geq 0.375$). As a 7-periodic Fourier mode is imposed on the inflow (see Fig. 3.6(a)), the dominant mode-2 instability spreads slightly towards larger flow angles. However, the inflow Fourier mode does not have any significant impact on the unstable mode. This is due to the amplification mechanism of the perturbation for $\Gamma = 2$. In fact, such a diffuser ratio is mainly destabilized by the deceleration term I_4. Hence, controlling the inlet Fourier mode m_{F}, which would mainly affect the lift-up and reverse lift-up mechanisms, does not have a significant role in this instability as it does not provide any major contribution to I_4. For low aspect ratios $\Gamma \in \{1.25, 1.50\}$, the perturbation growth relates to lift up and reverse lift-up mechanisms for leading to instability, hence the inlet Fourier mode m_{F} provides a significant parameter of control the instability. On the other hand, the modal instability mechanism for large diffusers relies on flow deceleration as the main contribution to the perturbation energy growth. This makes the instability mode almost insensitive to m_{F} for $\Gamma = 2.00$. The m_{F} provides additional shear layers, hence it promotes I_2 and I_3, which are the main destabilizing terms for $\Gamma = 1.25$ and 1.50. Hence, the inlet Fourier wake can select the instability mode only for $\Gamma = 1.25$ and 1.50. For the 5-periodic inflow Fourier mode (see Fig. 3.6(b)), the result does not change significantly compared to the 7-periodic inflow Fourier mode. The only significant difference is that, for $m_{\text{F}} = 5$, the flow can become unstable to m = 4 if the flow angle α is small enough (see results marked in a light red shadow at the bottom of Fig. 3.5(b)). Figure 3.6(c) depicts the results with 3-periodic inflow Fourier mode, we can observe that the range of dominant mode-3 instability extended to smaller and larger flow angles. For this radius ratio Γ, the propagation velocity ω_{stall} is not significantly affected by the inflow Fourier mode regardless of the periodic number m_{F} or amplitude A_{inlet}, and they decrease linearly with increasing inlet angle α.

3.1.3 Reduced-order 3D simulations

The 2D simulation results still have a significant deviation from the results of previous experimental as well as numerical simulation studies of the entire machine since they neglected the boundary layer effect on the flow inside the vaneless diffuser. To better understand the instability mechanism inside

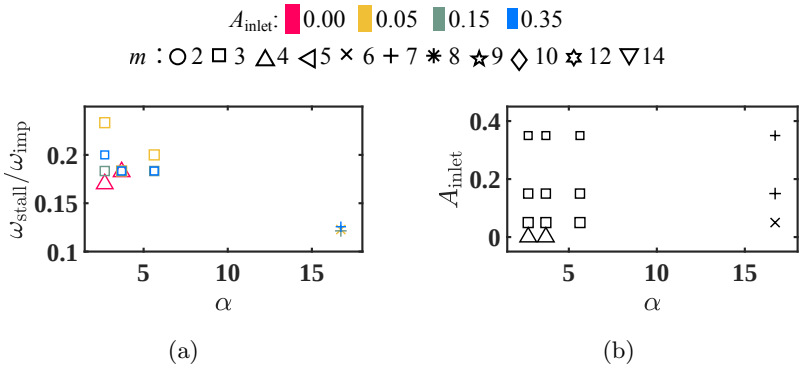

(a) (b)

Figure 3.7: (a) Instability propagation velocity ω_{stall} and (b) mode diagram of the flow in the vaneless diffuser of $\Gamma = 1.50$ with zero-leakage inflow profile with 4 different amplitude A_{F} of inflow Fourier modes.

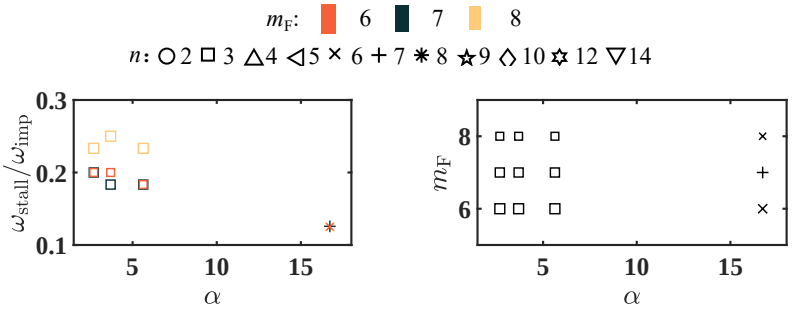

(a) (b)

Figure 3.8: (a) Instability propagation velocity ω_{stall} and (b) mode diagram of the flow in the vaneless diffuser of $\Gamma = 1.50$ with zero-leakage inflow profile with 3 different inflow Fourier mode number with the amplitude $A_{\text{inlet}} = 0.35$.

the vaneless diffuser, numerical simulations for the reduced-order 3D model are carried out. The instability propagation velocity ω_{stall} and mode diagram of three different diffuser radius ratios Γ with three different periods m_{F} and four different amplitudes A_{inlet} of the inflow Fourier modes obtained by the 3D simulations are summarized and discussed in this section. More detailed information including the instability frequency f_{stall} and amplitude A_{p} is summarized in Appendix B.2.

Figure 3.7 depicts the comparison of propagation velocity ω_{stall} and mode diagram of the instability identified for the diffuser with $\Gamma = 1.50$ (consistent with experimental set-up) with mean inlet profile fitted from numerical zero-leakage configuration with four different amplitudes of the Fourier mode $A_{\text{inlet}} \in \{0, 0.05, 0.15, 0.35\}$ and with a seven periodic Fourier mode modulation $m_{\text{F}} = 7$ imposed to the inflow. The 3D flow field is much more complicated compared to the 2D reduced-order simulation results. Concerning the result with mean inflow ($A_{\text{inlet}} = 0.00$), the mode-4 instability is dominant

which is consistent with the 2D simulation (see Fig. 3.5). However such instability only occurs with the flow angle $\alpha < 5.6°$ (corresponds to the flow rate $Q/Q_{\mathrm{d}} = 0.375$). We speculate that this is due to the dissipation induced by the walls and their corresponding boundary layers (not present for the 2D simulations). As the flow angle α increases, the flow field is chaotic under the effect of nonlinear interactions. No other instabilities are found for A = 0 above $Q/Q_{\mathrm{d}} = 0.375$. As a 7-periodic Fourier mode is imposed on the inflow, the previous dominant mode-4 instability is taken over by the mode-3 instability. Besides, another instability at a large flow angle $\alpha = 16.7°$ (corresponds to the flow rate $Q/Q_{\mathrm{d}} = 1.125$) is triggered by the inflow Fourier mode. For the lowest inflow Fourier amplitude $A_{\mathrm{inlet}} = 0.05$, the perturbation is too weak, as a result, a mode 6 instability is triggered. For the other two higher inflow Fourier amplitudes ($A_{\mathrm{inlet}} \in \{0.15, 0.35\}$), the instability wave number at the large flow angle is the same as for the inflow Fourier modes (m = $m_{\mathrm{F}} = 7$). In general, the instability characteristics are less affected by the amplitude A_{inlet} of the inflow Fourier modes m_{F}, the propagation velocity ω_{stall} of the instability are always of the same order, although they vary under different flow conditions.

Figure 3.8 depicts the comparison of instability characteristics identified for the diffuser with $\Gamma = 1.50$ with mean inlet profile fitted from numerical zero-leakage configuration with three different periodic inflow Fourier modes $m_{\mathrm{F}} \in \{6, 7, 8\}$ with the amplitude $A_{\mathrm{inlet}} = 0.35$. The results show that the inflow Fourier mode number m_{F} does not change the low flow rate instability mode number, but significantly changes the mode number of the large flow rate instability.

Figure 3.9 depicts the comparison of instability characteristics identified for the diffuser with $\Gamma = 1.50$ with mean inlet profile fitted from three different numerical configurations with a 7-periodic inflow Fourier mode with the amplitude $A_{\mathrm{inlet}} = 0.35$. The results show that the inflow modulation in the z direction has a significant impact on both the low flow rate and large flow rate instability mode.

Figure 3.10 depicts the comparison of instability characteristics identified for the diffuser with three different radius ratios $\Gamma \in \{1.25, 1.50, 2.00\}$ with mean inlet profile fitted from the zero-leakage numerical configuration with a 7-periodic inflow Fourier mode with the amplitude $A_{\mathrm{inlet}} = 0.35$. The results show that for the shortest diffuser $\Gamma = 1.25$, the flow field is chaotic at low flow angles, only the large flow rate instability exists. For the largest diffuser $\Gamma = 2.00$, the low flow rate instability can be triggered with a larger inflow angle. The low flow rate instability mode number is also different under different flow angles. This further confirms the impact of the boundary layers on the 2D instability

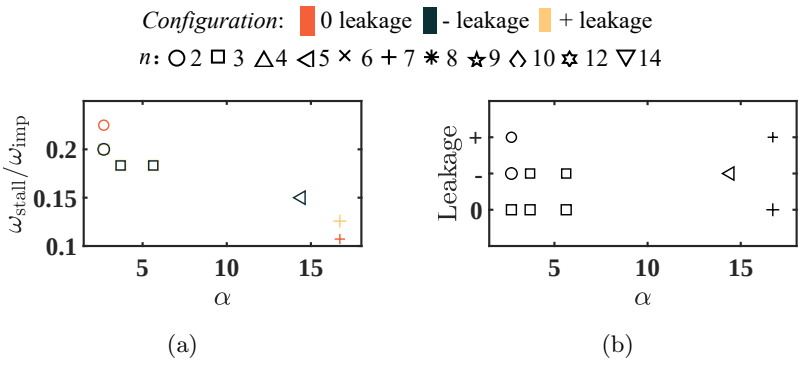

(a) (b)

Figure 3.9: (a) Instability propagation velocity ω_{stall} and (b) mode diagram of the flow in the vaneless diffuser of radius ratio $\Gamma = 1.50$ with 3 different mean inflow profiles with mode-7 inflow Fourier mode with amplitude $A_{\text{inlet}} = 0.35$.

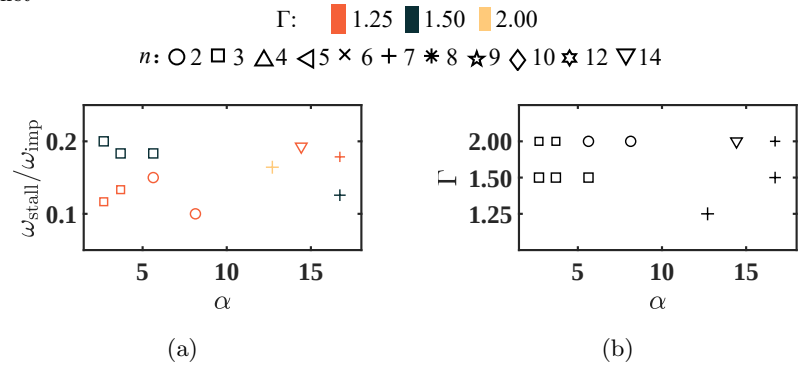

(a) (b)

Figure 3.10: (a) Instability propagation velocity ω_{stall} and (b) mode diagram of the flow in the vaneless diffuser of 3 different diffuser radius ratio Γ with zero-leakage inflow profile with mode-7 inflow Fourier mode with amplitude $A_{\text{inlet}} = 0.35$.

mechanism.

3.1.4 Instabilities in the 2D and 3D reduced-order model for the diffuser

The mechanisms of the instability identified in reduced-order 2D and 3D simulations are discussed in this section. In order to better distinguish the instabilities caused by different mechanisms, we summarize the state of the flow field of our simulation cases in Tabs. 3.4–3.10.

Concerning the flow states of diffusers with different radius ratios ($\Gamma \in \{1.25, 1.50, 2.00\}$) with different inflow Fourier perturbations ($m_{\text{F}} \in \{7, 5, 3\}$, $A_{\text{inlet}} \in \{0, 0.05, 0.15, 0.35\}$) under different flow angles ($\alpha \in [2.5, 16.8]$)obtained by the 2D reduced-order simulations (summarized in Tab. 3.4, Tab. 3.5, and Tab. 3.6), instabilities identified in most cases corroborate the occurrence of a modal linear instability for low flow rates by comparison with the linear stability analysis results (see Fig. 3.1).

Table 3.4: Flow states of the diffuser with radius ratio $\Gamma = 1.25$ with different inflow Fourier perturbations ($m_{\mathrm{F}} \in \{0, 7, 5, 3\}, A_{\mathrm{inlet}} \in \{0, 0.05, 0.15, 0.35\}$) under different flow angles ($\alpha \in [2.5°, 8.6°]$) obtained by 2D reduced-order simulations.

Q/Q_d	0.250	0.3125	0.375	0.4375	0.5	0.5625	0.625	0.6875
α	2.5°	3.1°	3.8°	4.7°	5.9°	7.1°	7.9°	8.6°
$m_{\mathrm{F}} = 0$ $A_{\mathrm{inlet}} = 0.00$	mode-8 mean flow instability	mode-9 mean flow instability	mode-7 mean flow instability	mode-8 mean flow instability	stable	stable	stable	stable
$m_{\mathrm{F}} = 7$ $A_{\mathrm{inlet}} = 0.05$	mode-9 mean flow instability	mode-7 mean flow instability	mode-7 mean flow instability	mode-7 mean flow instability	stable	stable	stable	stable
$m_{\mathrm{F}} = 7$ $A_{\mathrm{inlet}} = 0.15$	mode-12 mean flow instability	mode-7 mean flow instability	mode-7 mean flow instability	mode-7 mean flow instability	mode-7 mean flow instability	stable	stable	stable
$m_{\mathrm{F}} = 7$ $A_{\mathrm{inlet}} = 0.35$	mode-12 mean flow instability	mode-14 mean flow instability	mode-14 mean flow instability	mode-14 mean flow instability	mode-7 mean flow instability	mode-7 mean flow instability	mode-7 mean flow instability	stable
$m_{\mathrm{F}} = 5$ $A_{\mathrm{inlet}} = 0.05$	mode-10 mean flow instability	mode-10 mean flow instability	mode-10 mean flow instability	stable	stable	stable	stable	stable
$m_{\mathrm{F}} = 5$ $A_{\mathrm{inlet}} = 0.15$	mode-10 mean flow instability	mode-10 mean flow instability	mode-10 mean flow instability	mode-10 mean flow instability	stable	stable	stable	stable
$m_{\mathrm{F}} = 5$ $A_{\mathrm{inlet}} = 0.35$	mode-10 mean flow instability	mode-10 mean flow instability	mode-10 mean flow instability	mode-10 mean flow instability	mode-10 mean flow instability	stable	stable	stable
$m_{\mathrm{F}} = 3$ $A_{\mathrm{inlet}} = 0.05$	mode-8 mean flow instability	mode-9 mean flow instability	mode-6 mean flow instability	stable	stable	stable	stable	stable
$m_{\mathrm{F}} = 3$ $A_{\mathrm{inlet}} = 0.15$	mode-9 mean flow instability	mode-9 mean flow instability	mode-9 mean flow instability	stable	stable	stable	stable	stable
$m_{\mathrm{F}} = 3$ $A_{\mathrm{inlet}} = 0.35$	mode-9 mean flow instability	mode-9 mean flow instability	mode-9 mean flow instability	mode-9 mean flow instability	mode-9 mean flow instability	stable	stable	stable

Table 3.5: Flow states of the diffuser with radius ratio $\Gamma = 1.50$ with different inflow Fourier perturbations ($m_{\mathrm{F}} \in \{0, 7, 5, 3\}, A_{\mathrm{inlet}} \in \{0, 0.05, 0.15, 0.35\}$) under different flow angles ($\alpha \in [2.5°, 14.4°]$) obtained by 2D reduced-order simulations.

Q/Q_d	0.250	0.375	0.500	0.625	0.750	0.875	1.000
α	$2.5°$	$3.7°$	$5.6°$	$8.1°$	$10.6°$	$12.7°$	$14.4°$
$m_{\mathrm{F}} = 0$ $A_{\mathrm{inlet}} = 0.00$	mode-3 mean flow instability	mode-4 mean flow instability	mode-4 mean flow instability	mode-5 mean flow instability	stable	stable	stable
$m_{\mathrm{F}} = 7$ $A_{\mathrm{inlet}} = 0.05$	mode-3 mean flow instability	mode-4 mean flow instability	mode-5 mean flow instability	mode-7 mean flow instability	stable	stable	stable
$m_{\mathrm{F}} = 7$ $A_{\mathrm{inlet}} = 0.15$	mode-4 mean flow instability	mode-4 mean flow instability	mode-5 mean flow instability	mode-7 mean flow instability	mode-7 mean flow instability	stable	stable
$m_{\mathrm{F}} = 7$ $A_{\mathrm{inlet}} = 0.35$	mode-4 mean flow instability	mode-4 mean flow instability	mode-4 mean flow instability	mode-4 mean flow instability	mode-7 mean flow instability	mode-7 mean flow instability	stable
$m_{\mathrm{F}} = 5$ $A_{\mathrm{inlet}} = 0.05$	mode-5 mean flow instability	mode-5 mean flow instability	mode-5 mean flow instability	mode-5 mean flow instability	stable	stable	stable
$m_{\mathrm{F}} = 5$ $A_{\mathrm{inlet}} = 0.15$	mode-5 mean flow instability	mode-5 mean flow instability	mode-5 mean flow instability	mode-5 mean flow instability	stable	stable	stable
$m_{\mathrm{F}} = 5$ $A_{\mathrm{inlet}} = 0.35$	mode-5 mean flow instability	mode-5 mean flow instability	mode-5 mean flow instability	mode-5 mean flow instability	mode-5 mean flow instability	stable	stable
$m_{\mathrm{F}} = 3$ $A_{\mathrm{inlet}} = 0.05$	mode-4 mean flow instability	mode-3 mean flow instability	mode-5 mean flow instability	mode-6 mean flow instability	stable	stable	stable
$m_{\mathrm{F}} = 3$ $A_{\mathrm{inlet}} = 0.15$	mode-3 mean flow instability	mode-3 mean flow instability	mode-6 mean flow instability	stable	stable	stable	stable
$m_{\mathrm{F}} = 3$ $A_{\mathrm{inlet}} = 0.35$	mode-3 mean flow instability	mode-3 mean flow instability	mode-6 mean flow instability	mode-6 mean flow instability	stable	stable	stable

Table 3.6: Flow states of the diffuser with radius ratio $\Gamma = 2.00$ with different inflow Fourier perturbations ($m_{\mathrm{F}} \in \{0, 7, 5, 3\}, A_{\mathrm{inlet}} \in \{0, 0.05, 0.15, 0.35\}$) under different flow angles ($\alpha \in [2.6°, 16.8°]$) obtained by 2D reduced-order simulations.

Q/Q_d	0.250	0.375	0.500	0.625	0.750	0.875	1.000	1.125
α	2.6°	3.9°	5.6°	7.7°	10°	12°	14.4°	16.8°
$m_{\mathrm{F}} = 0$ $A_{\mathrm{inlet}} = 0.00$	mode-2 mean flow instability	mode-3 mean flow instability	mode-3 mean flow instability	mode-3 mean flow instability	mode-3 mean flow instability	mode-3 mean flow instability	stable	stable
$m_{\mathrm{F}} = 7$ $A_{\mathrm{inlet}} = 0.05$	mode-2 mean flow instability	mode-2 mean flow instability	mode-3 mean flow instability	mode-3 mean flow instability	mode-3 mean flow instability	mode-3 mean flow instability	stable	stable
$m_{\mathrm{F}} = 7$ $A_{\mathrm{inlet}} = 0.15$	mode-2 mean flow instability	mode-2 mean flow instability	mode-3 mean flow instability	mode-3 mean flow instability	mode-3 mean flow instability	mode-3 mean flow instability	stable	stable
$m_{\mathrm{F}} = 7$ $A_{\mathrm{inlet}} = 0.35$	mode-2 mean flow instability	mode-2 mean flow instability	mode-3 mean flow instability	mode-3 mean flow instability	mode-3 mean flow instability	mode-3 mean flow instability	stable	stable
$m_{\mathrm{F}} = 5$ $A_{\mathrm{inlet}} = 0.05$	mode-2 mean flow instability	mode-2 mean flow instability	mode-3 mean flow instability	mode-4 mean flow instability	mode-4 mean flow instability	mode-3 mean flow instability	stable	stable
$m_{\mathrm{F}} = 5$ $A_{\mathrm{inlet}} = 0.15$	mode-2 mean flow instability	mode-2 mean flow instability	mode-3 mean flow instability	mode-4 mean flow instability	mode-4 mean flow instability	mode-3 mean flow instability	stable	stable
$m_{\mathrm{F}} = 5$ $A_{\mathrm{inlet}} = 0.35$	mode-2 mean flow instability	mode-2 mean flow instability	mode-3 mean flow instability	mode-3 mean flow instability	mode-3 mean flow instability	mode-3 mean flow instability	stable	stable
$m_{\mathrm{F}} = 3$ $A_{\mathrm{inlet}} = 0.05$	mode-3 mean flow instability	mode-3 mean flow instability	mode-3 mean flow instability	mode-3 mean flow instability	mode-3 mean flow instability	mode-3 mean flow instability	mode-3 mean flow instability	stable
$m_{\mathrm{F}} = 3$ $A_{\mathrm{inlet}} = 0.15$	mode-3 mean flow instability	mode-3 mean flow instability	mode-3 mean flow instability	mode-3 mean flow instability	mode-3 mean flow instability	mode-3 mean flow instability	mode-3 mean flow instability	stable
$m_{\mathrm{F}} = 3$ $A_{\mathrm{inlet}} = 0.05$	mode-2 mean flow instability	mode-3 mean flow instability	mode-3 mean flow instability	mode-3 mean flow instability	mode-3 mean flow instability	mode-3 mean flow instability	stable	stable

Table 3.7: Flow states of the diffuser with radius ratio $\Gamma = 1.50$ with zero-leakage inflow with different inflow Fourier perturbations ($m_{\mathrm{F}} = 7, A_{\mathrm{inlet}} \in \{0, 0.05, 0.15, 0.35\}$) under different flow angles ($\alpha \in [2.7°, 19.5°]$) obtained by 3D reduced-order simulations.

Q/Q_d	0.250	0.375	0.500	0.625	0.750	0.875	1.000	1.125	1.250
α	2.7°	3.7°	5.6°	8.1°	10.6°	12.7°	14.4°	16.7°	19.5°
$A_{\mathrm{inlet}} = 0.00$	mode-4 mean flow instability	mode-4 mean flow instability	chaotic	chaotic	stable	chaotic	stable	stable	chaotic
$A_{\mathrm{inlet}} = 0.05$	mode-3 mean flow instability	mode-3 mean flow instability	mode-3 mean flow instability	chaotic	stable	stable	stable	mode-6 jet wake instability	chaotic
$A_{\mathrm{inlet}} = 0.15$	mode-3 mean flow instability	mode-3 mean flow instability	mode-3 mean flow instability	stable	stable	chaotic	chaotic	mode-7 jet wake instability	stable
$A_{\mathrm{inlet}} = 0.35$	mode-3 mean flow instability	mode-3 mean flow instability	mode-3 mean flow instability	chaotic	stable	stable	chaotic	mode-7 jet wake instability	stable

Table 3.8: Flow states of the diffuser with radius ratio $\Gamma = 1.50$ with zero-leakage inflow with different inflow Fourier perturbations ($m_{\mathrm{F}} \in \{6, 7, 8\}, A_{\mathrm{inlet}} \in \{0, 0.05, 0.15, 0.35\}$) under different flow angles ($\alpha \in [2.7°, 19.5°]$) obtained by 3D reduced-order simulations.

Q/Q_d	0.250	0.375	0.500	0.625	0.750	0.875	1.000	1.125	1.250
α	2.7°	3.7°	5.6°	8.1°	10.6°	12.7°	14.4°	16.7°	19.5°
$m_{\mathrm{F}} = 6$	mode-3 mean flow instability	mode-3 mean flow instability	mode-3 mean flow instability	chaotic	stable	stable	chaotic	mode-6 jet wake instability	stable
$m_{\mathrm{F}} = 7$	mode-3 mean flow instability	mode-3 mean flow instability	mode-3 mean flow instability	chaotic	stable	stable	chaotic	mode-7 jet wake instability	stable
$m_{\mathrm{F}} = 8$	mode-3 mean flow instability	mode-3 mean flow instability	mode-3 mean flow instability	chaotic	stable	stable	stable	mode-6 jet wake instability	stable

However, in the case of $\Gamma = 1.25$ and 1.5, a few tested conditions show that the instability can occur at the flow angle α larger than the α_c for $A_{\mathrm{inlet}} > 0.2$ in linear stability analysis. There are

Table 3.9: Flow states of the diffuser with radius ratio $\Gamma = 1.50$ with different inflow profiles (zero-, negative-,and positive-leakage configuration) with different inflow Fourier perturbations ($m_{\mathrm{F}} = 7, A_{\mathrm{inlet}} \in \{0, 0.05, 0.15, 0.35\}$) under different flow angles ($\alpha \in [2.7°, 19.5°]$) obtained by 3D reduced-order simulations.

Q/Q_d	0.250	0.375	0.500	0.625	0.750	0.875	1.000	1.125	1.250
α	2.7°	3.7°	5.6°	8.1°	10.6°	12.7°	14.4°	16.7°	19.5°
0 *leakage*	mode-3 mean flow instability	mode-3 mean flow instability	mode-3 mean flow instability	chaotic	stable	stable	chaotic	mode-7 jet wake instability	stable
− *leakage*	mode-2 mean flow instability	mode-3 mean flow instability	mode-3 mean flow instability	chaotic	stable	chaotic	mode-5 jet wake instability	stable	stable
+ *leakage*	mode-2 mean flow instability	chaotic	chaotic	chaotic	stable	stable	chaotic	mode-7 jet wake instability	stable

Table 3.10: Flow states of diffusers with different radius ratios ($\Gamma =\in \{1.25, 1.50, 2.00\}$) with zero-leakage inflow with different inflow Fourier perturbations ($m_{\mathrm{F}} = 7, A_{\mathrm{inlet}} \in \{0, 0.05, 0.15, 0.35\}$) under different flow angles ($\alpha \in [2.7°, 19.5°]$) obtained by 3D reduced-order simulations.

Q/Q_d	0.250	0.375	0.500	0.625	0.750	0.875	1.000	1.125	1.250
α	2.7°	3.7°	5.6°	8.1°	10.6°	12.7°	14.4°	16.7°	19.5°
$\Gamma = 1.25$	chaotic	stable	stable	stable	chaotic	mode-7 jet wake instability	stable	stable	stable
$\Gamma = 1.50$	mode-3 mean flow instability	mode-3 mean flow instability	mode-3 mean flow instability	chaotic	stable	stable	chaotic	mode-7 jet wake instability	stable
$\Gamma = 2.00$	mode-3 mean flow instability	mode-3 mean flow instability	mode-2 mean flow instability	mode-2 mean flow instability	chaotic	stable	chaotic	mode-7 jet wake instability	stable

currently two hypotheses about such cases: either the inlet Fourier mode m_{F} is responsible for further extending the limits of the modal instability predicted by the LSA, or another instability mechanism is responsible for them. Further investigations are currently in progress and a conclusive statement on such a few cases cannot be done at the moment.

Concerning the comparison of flow states of diffusers with different radius ratios ($\Gamma \in \{1.25, 1.50, 2.00\}$) with different inflow profiles (zero-, negative-, and positive-leakage configuration) with different inflow Fourier perturbations ($m_{\mathrm{F}} \in \{6, 7, 8\}, A_{\mathrm{inlet}} \in \{0, 0.05, 0.15, 0.35\}$) under different flow angles ($\alpha \in [2.7, 19.5]$) obtained by the 3D reduced-order simulations (summarized in Tab. 3.7, Tab. 3.8, Tab. 3.9, and Tab. 3.10), we speculate that due to the dissipation induced by the walls and their corresponding boundary layers (not present for the 2D simulations), the modal linear instability occurs for lower flow rates compared to the 2D linear stability analysis and 2D reduced-order simulation results. Besides, another instability is identified for large flow angles, whose slow rotating pattern is consistent with the rotating instability reported by Ljevar et al., who investigated the core flow in a vaneless diffuser varying the blade jet-to-wake intensity, the number of blades and the outlet-to-inlet diffuser radius ratio. Further considering that our core flow has a blade jet-to-wake angle smaller than the critical angle predicted by Ljevar et al. below which the rotating stall occurs, we infer that the rotating pattern is indeed a rotating jet-wake instability.

In summary, two different instability mechanisms exist in the vaneless diffuser: (1) Core flow instability observed at low flow angles. Such instability relies exclusively on the skewness of the diffuser inflow and does not involve any inhomogeneous forcing in θ. However the wave number can be affected by the inflow Fourier mode m_{F}. (2) Jet-wake instability observed at large flow angles. This instability is strongly affected by the non-homogeneous forcing in $\theta-$ direction and it is observed for the solely 3D model. However, in a previous study, Levjar et al. [26] reported a similar phenomenon for 2D flows with nonmodal inlet wakes. Hence, in future studies, we will investigate the impact of nonmodal inlets (as depicted in Fig. 3.11) also for 2D flows. This will help to clarify if the instability is mainly due to 3D effects or to a 2D mechanism.

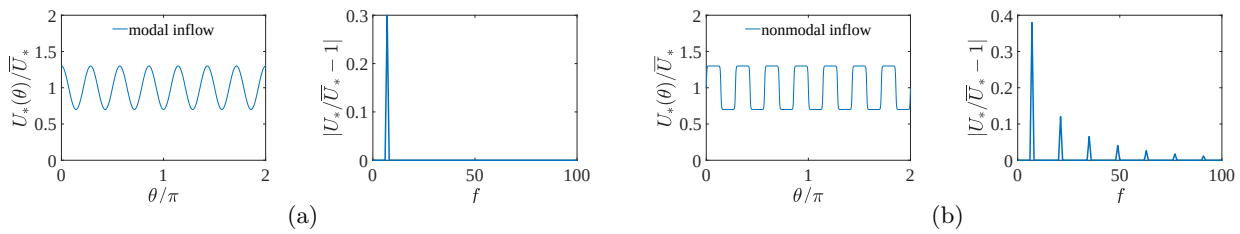

Figure 3.11: Comparison between (a) our modal inflow condition and (b) Ljevar's nonmodal inflow condition.

3.2 Flow field of the entire machine with ideal inflow (zero-leakage case)[B]

To understand the flow in the centrifugal machine, the flow field of the zero leakage case at the design condition obtained from URANS simulations is presented as it represents the simplest scenario where the flow is not influenced by any leakage. The instantaneous static pressure and velocity magnitude distribution on the meridional section ($x = 0$) of the centrifugal machine is shown in Fig. 3.12. Note that in all the following color maps, the velocities and static pressures are nondimensionalized by

$$\hat{U}_* = \frac{U_*}{U_2}, \qquad \hat{P} = \frac{P}{\frac{1}{2}\rho {U_2}^2}, \tag{3.10}$$

where $* \in \{r, \theta, z\}$, and $U_2 = \omega_{\text{imp}} R_2$ is a characteristic velocity in this problem. The airflow is drawn into the machine from the inlet due to the rotating blades. The rotating impeller imparts kinetic energy to the fluid, leading to radially outward movement. The fluid then enters the vaneless diffuser which converts the kinetic energy into pressure energy by slowing down the fluid velocity.

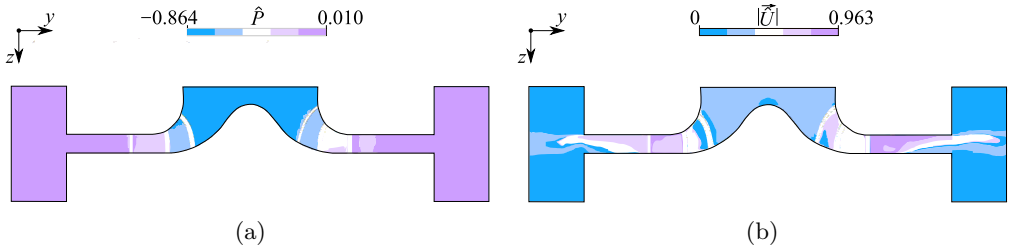

(a) (b)

Figure 3.12: Colour Maps of instantaneous (a) static pressure and (b) velocity magnitude distribution over the meridian section (x = 0) of the pump at the design flow rate $Q/Q_{\text{d}} = 1.00$ obtained by the URANS simulation.

To understand the flow in the vaneless diffuser, the instantaneous flow field of the vaneless diffuser for flow rates ranging from $Q/Q_{\text{d}} = 1.25$ down to $Q/Q_{\text{d}} = 0.25$ is analyzed in this section. Figure 3.13(a–e) depicts the azimuthally-averaged velocity magnitude distribution at the meridian section (top panels) and the instantaneous velocity magnitude distribution at the mid-height of the diffuser (bottom panels) at five flow rates $Q/Q_{\text{d}} \in \{0.25,\ 0.50,\ 0.75,\ 1.00,\ 1.25\}$.

At the largest flow rate $Q/Q_{\text{d}} = 1.25$, the bulk flow in the vaneless diffuser is dominantly influenced by inviscid effects, very similar to the Euler flow solution except for the reverse flow region (see the top panel of Fig. 3.13(a)). The reverse flow region is caused by the non-uniform swirling inflow discharged from the rotating impeller. The vortexes experience obstruction as the incoming jet applies pressure

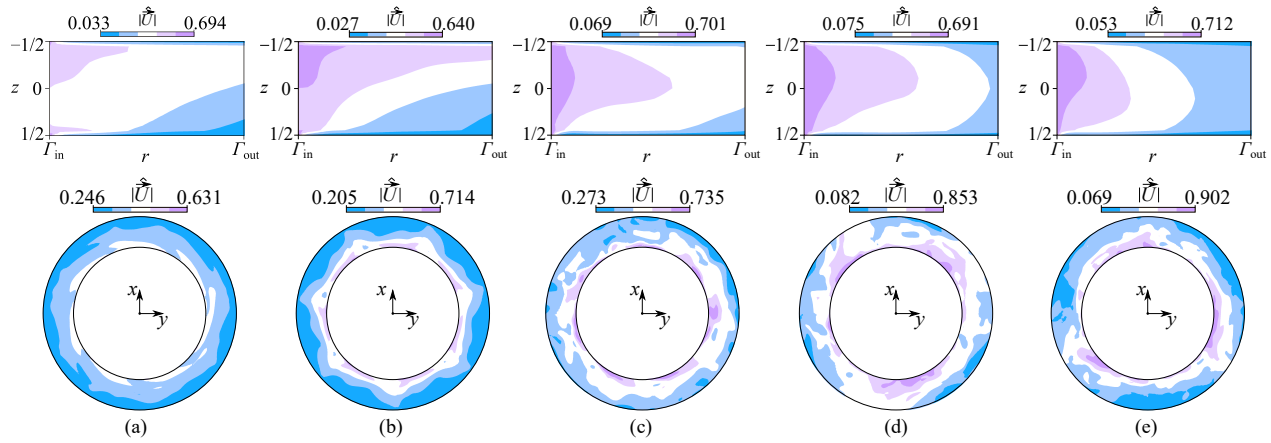

Figure 3.13: Velocity magnitude of the zero-leakage case at the flow rate (a) $Q/Q_{\mathrm{d}} = 1.25$, (b) $Q_d = 1$, (c) $Q/Q_{\mathrm{d}} = 0.75$, (d) $Q/Q_{\mathrm{d}} = 0.50$, and (e) $Q/Q_{\mathrm{d}} = 0.25$. Top panels: Azimuthal arithmetic-average values on the meridian section. Bottom panels: Instantaneous fields at the mid-height of the diffuser.

onto them. For the core flow, a seven-periodic jet-wake pattern can be clearly observed near the diffuser inlet, and the velocity is regularly distributed (see the bottom panel of Fig. 3.13(a)). The flow is inferred to be stabilized by the high mean inflow angle. As the flow rate drops to the design condition $Q/Q_{\mathrm{d}} = 1.00$, a large reverse flow region can be observed on the diffuser hub wall, occupying almost half of the diffuser channel in the $z-$ direction (see the top panel of Fig. 3.13(b)). At the same time, seven-periodic instability patterns corresponding to the number of jet-wake patterns can be captured at the mid-height of the diffuser (see the bottom panel of Fig. 3.13(b)). The instability associated with the jet-wake could be responsible for the large reverse flow region. As the flow rate continues to drop to $Q/Q_{\mathrm{d}} = 0.75$, the influence of the asymmetrically distributed inflow velocity is weakened (see the top panel of Fig. 3.13(c)). No rotating instability is observed as the decrease of the jet-wake intensity led to a stabilization of the flow (see the bottom panel of Fig. 3.13(c)). This is consistent with the interpretation of the rotating instability being responsible for the azimuthally-averaged reverse flow region. As the flow continues to drop and reaches $Q/Q_{\mathrm{d}} = 0.50$, the mean flow inside the vaneless diffuser becomes skewed with flow separation occurring near the diffuser inlet, especially on the hub side (see the top panel of Fig. 3.13(d)). Three rotating stall cells are formed, which can be roughly observed at the mid-height of the diffuser (see the bottom panel of Fig. 3.13(d)). This low-flow rate rotating stall has previously been theoretically, experimentally, and numerically studied by several researchers [10, 40, 18]. Concerning the smallest flow rate $Q/Q_{\mathrm{d}} = 0.25$, the mean flow becomes more

skewed and exhibits an S-shape with reverse flow near the shroud and hub walls close to the vaneless diffuser inlet (see the top panel of Fig. 3.13(e)). The three stall cells can more clearly be identified (see the bottom panel of Fig. 3.13(e)) since the rotating stall became strongly supercritical.

3.2.1 Instability at the design condition

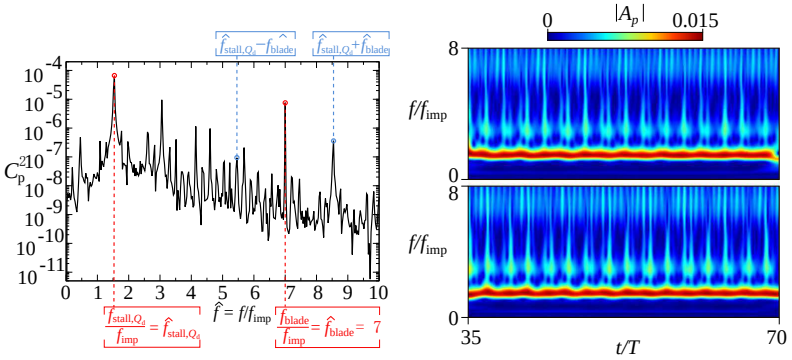

Figure 3.14: (a) Fourier and (b) wavelet analysis of the URANS simulation of the zero-leakage case at the design flow rate Q/Q_d =1.00.

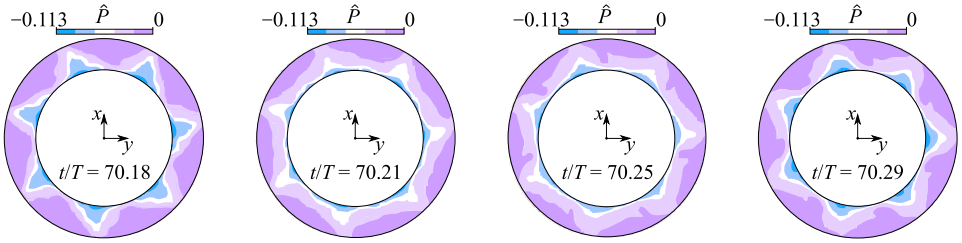

Figure 3.15: Snapshots of the static pressure color map of the zero-leakage case at the design flow rate $Q/Q_d = 1.00$ at different calculation time $t/T \in [70.18,\ 70.29]$

In order to deeper understand the instability characteristics at the design flow rate $Q/Q_d = 1.00$ of the zero-leakage case, a Fourier transform of the cross-power spectrum and a wavelet analysis obtained from two numerical probes in URANS simulation is performed as a complementary analysis.

Concerning the FFT results of the URANS simulation for the zero-leakage case (see Fig. 3.14(a)), the blade-passing-to-impeller-frequency ratio $f_{blade}/f_{imp} = 7$ is prominently evident in FFT results as anticipated, where f_{blade} represents the blade passing frequency and f_{imp} represents the impeller frequency. Besides, a low-frequency ratio $f/f_{imp} = 1.543$ which does not align with any of the sub-/super-harmonics of the impeller or blade passing frequencies is captured, an additional simulation is

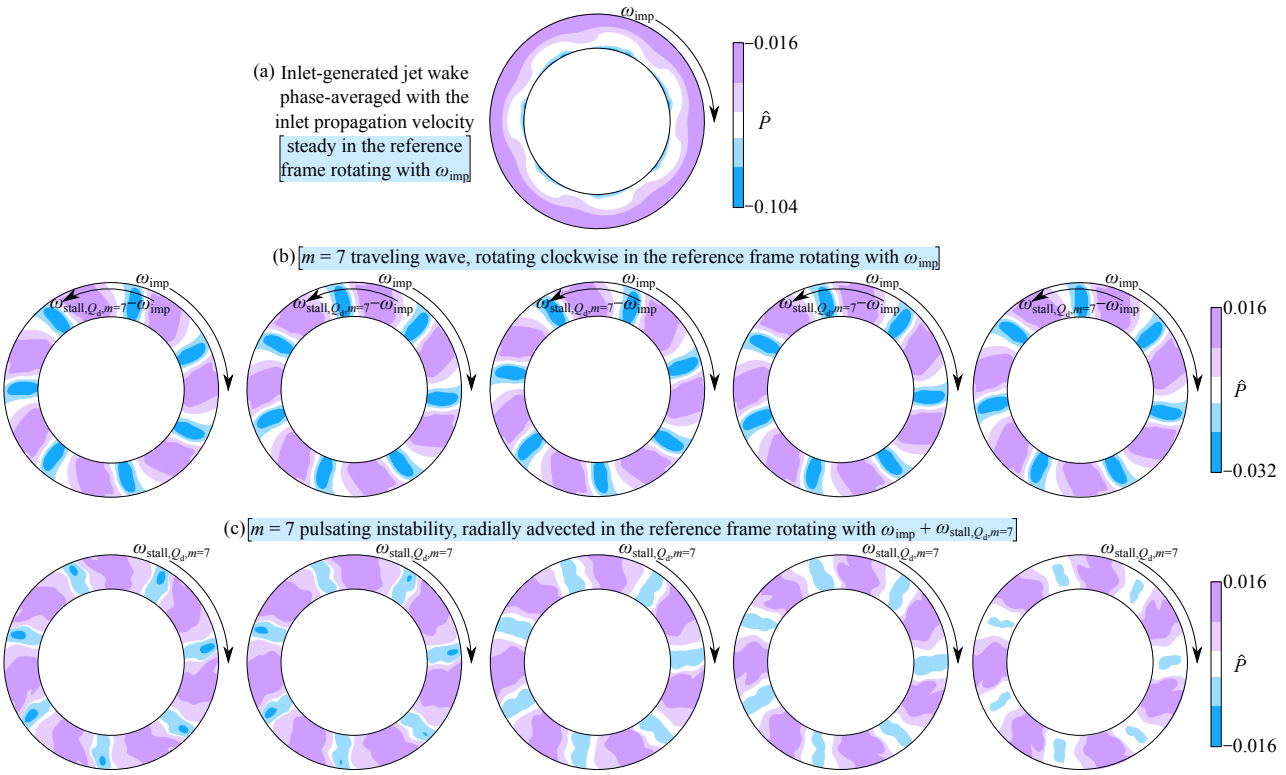

Figure 3.16: (a) Phase-averaged static pressure distribution in a reference frame rotating with the inlet propagation velocity. (b) The traveling wave depicted in the reference frame rotating with ω_{imp} and computed by subtracting the phase-averaged wake (a) from the instantaneous static pressure and phase-averaging with $\omega = \omega_{\mathrm{stall},Q_{\mathrm{d}},m=7}$. (c) Pulsating instability traveling in the reference frame rotating with $\omega_{\mathrm{stall},Q_{\mathrm{d}},m=7}$ and computed with respect to the difference between the phase-averaged wake (a), the traveling wave (b), and the instantaneous static pressure. All figures refer to zero-leakage boundary conditions at the mid-height of the diffuser for $Q/Q_{\mathrm{d}} = 1$.

conducted for one revolution of the impeller to investigate the source of this unanticipated frequency. From a visual inspection of the snapshots of the flow field, we find that the frequency $f/f_{\mathrm{imp}} = 1.543$ is compatible with an instability pattern rotating approximately five times slower than the impeller velocity. To more clearly explain the origin of the incommensurate frequencies observed in FFT results, a detailed quantitative analysis is deemed necessary. Assuming that the frequency of maximum amplitude in FFT is produced by the unexpected rotating pattern, the propagation velocity can then be quantified by $f/f_{\mathrm{imp}} = 1.543$, corresponding to $\omega/\omega_{\mathrm{imp}} = 0.22$. Notably, this propagation velocity aligns with the slower rotating pattern observed in snapshots, which is approximately five times slower than the expected pattern rotating around the blade wake. Ljevar et al. [26] also reported a rotating

instability occurs associated with the inflow jet-wake. By employing a two-dimensional model without considering the boundary layers on the diffuser walls, the rotating instability mode, propagation speed, and critical conditions are found to depend on the blade jet-to-wake intensity, the number of blades, and the outlet-to-inlet diffuser radius ratio of their study. In the case of radius ratio $R_4/R_3 = 1.48$, which is very close to our diffuser, the results provided by Ljevar et al. indicate the presence of either a 6-periodic or a 7-periodic pattern for the rotating instability. This finding aligns with our own observations. Moreover, they reported a propagation velocity of approximately $\omega_{\mathrm{stall},Q_\mathrm{d}}/\omega_{\mathrm{imp}} = 0.3$ for their rotating instability, which is the same order as our observed $\omega/\omega_{\mathrm{imp}} = 0.22$. Although the propagation velocity detected in our study is slightly faster than theirs, the similarity further strengthens the correlation between the two findings. One possible explanation for this deviation is that in our three-dimensional flow configuration, the boundary layer tends to provide resistance against the rotating stall under nominal flow conditions. This resistance can cause a deceleration of the rotating pattern, resulting in a slower propagation velocity compared to the detected value in their study. Furthermore, taking into account the fact that our core flow exhibits a blade jet-to-wake angle that is smaller than the critical angle predicted by Ljevar et al. for the onset of rotating instability, we can conclude that the seven-periodic pattern responsible for the frequency $f/f_{\mathrm{imp}} = f_{\mathrm{stall},Q_\mathrm{d}}/f_{\mathrm{imp}} = 1.543$ is indeed a rotating instability. Other peaks in the FFT results of URANS simulations for the zero leakage case correspond to nonlinear interactions between fundamental frequency or sub-/super-harmonics of them. Regarding the wavelet analysis result (see Fig. 3.14(b)), extra details are revealed, i.e. a strong intermittent phenomenon with a frequency of about $f/f_{\mathrm{imp}} \approx 3$. By more carefully visualizing the flow field (see Fig. 3.15), such a wavelet feature is concluded as a result of the nonlinear interactions between the shear layer of the impeller discharge and the rotating instability, leading to a pulsating higher-order effect appears at the tip of the primary rotating instability pattern mentioned previously. Further evidence of the robustness of this pulsation pattern is provided by Fan et al. [2].

To better visualize the topology of the instability patterns and to quantify more precisely the number of instability patterns, phase-average processing based on the results of the last 120-time steps of the URANS simulation is applied for the unsteady flow field in the vaneless diffuser. Fig. 3.16 shows an overview of the instability scenario for the zero-leakage case at the design flow rate $Q/Q_\mathrm{d} = 1.00$. By phase-averaging the static pressure field at the mid-height of the diffuser in a reference frame rotating with the impeller ω_{imp}, a seven-periodic jet-wake pattern produced by the rotating impeller

can be observed near the diffuser inlet, as anticipated (see Fig. 3.16(a)). By subtracting the primary phase-averaged result from the instantaneous pressure field and performing secondary phase-average processing in a reference frame rotating with $\omega_{\mathrm{stall},Q_\mathrm{d},m=7}$, the topology of the slow seven-periodic rotating instability pattern is more clearly clarified. Such instability pattern travels in the counter-clockwise direction in the reference frame rotating with the impeller ω_{imp} (see arrow $\omega_{\mathrm{stall},Q_\mathrm{d},m=7}-\omega_{\mathrm{imp}}$ in Fig. 3.16(b)), which is consistent with the prediction of Ljevar et al. [26]. By further subtracting the primary and the secondary phase-averaged results from the instantaneous pressure field, a secondary instability is identified as shown in Fig. 3.16(c). The seven-periodic perturbation pattern propagates radially in a reference frame rotating with the primary instability ($\omega_{\mathrm{stall},Q_\mathrm{d},m=7}$). The visualization of the instability pattern further confirms the robustness of the FFT results and the pulsating signal in wavelet analysis. Such a secondary instability is identified for the first time in our centrifugal machine.

3.2.2 Instability at low flow rate condition

In our specific case (radius ratio $\Gamma = 1.50$), the diffuser can be categorized as a "wide" diffuser due to the absence of prominent three-dimensional turbulent boundary layer separations upon a decrease in the flow rate Q, i.e. the boundary layers along the diffuser walls are always thin compared to the diffuser width. Hence the low flow rate rotating stall in our case can be studied as a core-flow instability.

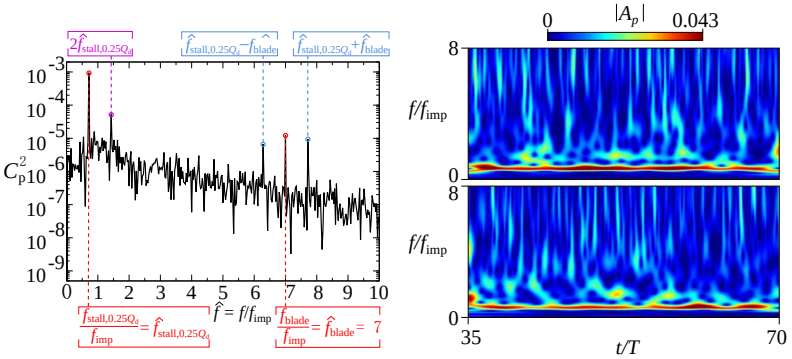

Figure 3.17: (a) Fourier and (b) wavelet analysis of the URANS simulation of the zero-leakage case at the stall condition Q/Q_d =0.25.

Fig. 3.17 shows the FFT and wavelet analysis of the URANS simulations for the zero-leakage case at fully-developed stall condition, i.e. $Q/Q_\mathrm{d} = 0.25$. The blade passing frequency $f_{\mathrm{blade}}/f_{\mathrm{imp}} = 7$ still can be easily identified in FFT (see Fig. 3.17(a)). And it is overcome by a low frequency

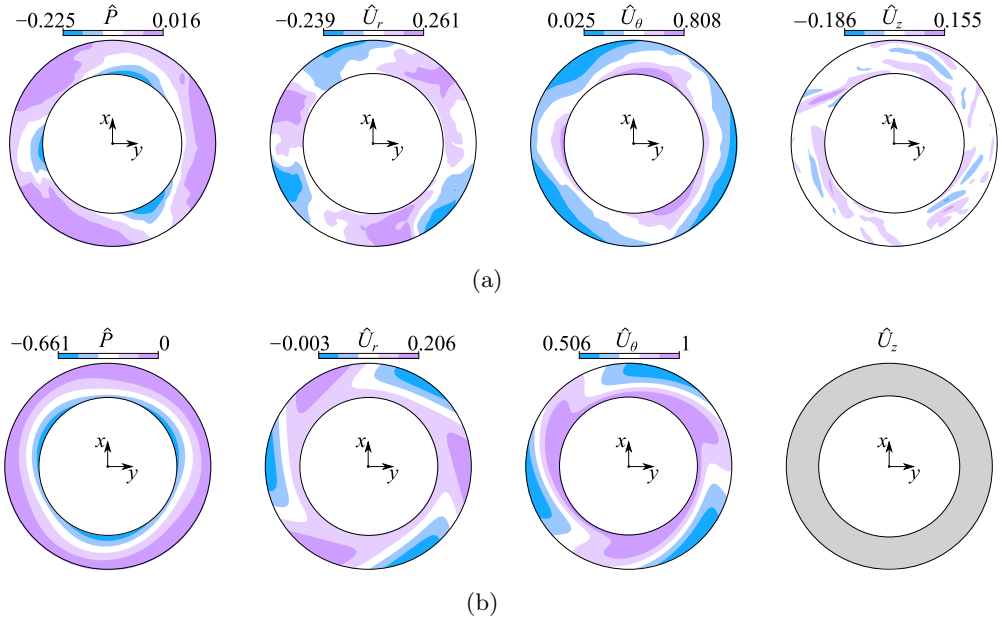

Figure 3.18: Comparison of (a) the phase averaged static pressure, radial velocity, tangential velocity and axial velocity with the instability propagation velocity $\omega_{\text{stall},0.25Q_\text{d}}$ of the zero-leakage case at stall condition $Q/Q_\text{d} = 0.25$ of the URANS simulation, and (b) the flow field calculated by the 2D linear stability model of [1] at the critical condition.

$f_{\text{stall},0.25Q_\text{d}}/f_\text{imp} = 0.714$, which is proven to be the low-flow-rate rotating stall frequency corresponding to a propagation velocity of $\omega_{\text{stall},0.25Q_\text{d}} = 0.238\omega_\text{imp}$. Furthermore, the nonlinear interactions between these two frequencies ($f_{\text{stall},0.25Q_\text{d}} \pm f_\text{imp}$) and the super-harmonic of the instability frequency ($2f_{\text{stall},0.25Q_\text{d}}$) are also captured in the FFT result. Wavelet analysis shows good consistency with the FFT results as shown in Fig. 3.17(b).

By phase averaging the static pressure and three velocity component fields at the mid-height of the diffuser in a reference frame rotating with the $\omega_{\text{stall},0.25Q_\text{d}}$, the structure of the three stall cells are more clearly visualized (see Fig. 3.18(a)). The stall cells consist of two areas displaying radial velocities in opposite directions near the inlet of the diffuser. Between these two regions, there exists a distinct zone characterized by very low tangential velocity. From a qualitative point of view, they have a very good agreement with the critical mode predicted by the two-dimensional linear stability analysis employing the model of Tsujimoto et al. (see Fig. 3.18(b)).

3.3 Parametric study of the entire machine

3.3.1 Effect of the inflow condition on the instability[D]

The leakage between the impeller and the diffuser changes the inflow conditions of the vaneless diffuser and a significant influence on the corresponding bulk flow is therefore expected. The effect of leakage flow on the diffuser at design flow rate $Q = Q_{\mathrm{d}}$ is therefore analyzed in this section.

3.3.1.1 Effect of the inflow condition on the instability at large flow rate

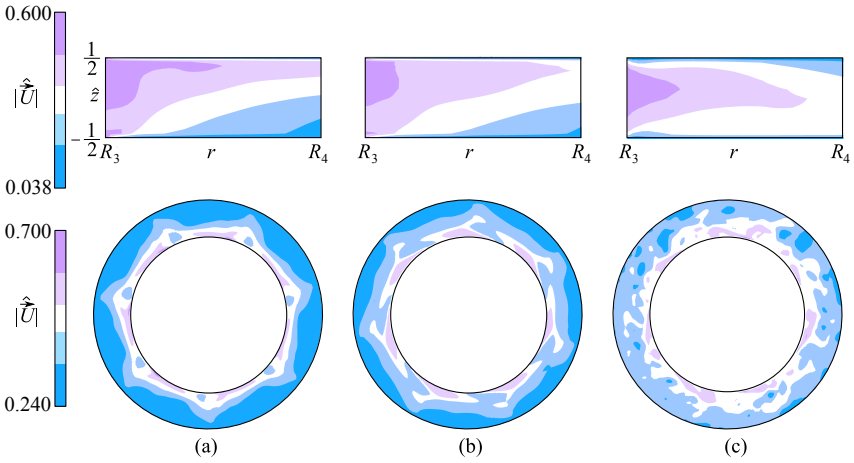

Figure 3.19: Color maps of the instantaneous static pressure, radial velocity, tangential velocity, and axial velocity at the design flow rate $Q/Q_{\mathrm{d}} = 1.00$ for (a) the zero-leakage case ($L/R_2 = 0\%$), (b) the negative-leakage case ($L/R_2 = 1\%$), and (c) the positive-leakage case ($L/R_2 = 1\%$). The upper figures show the azimuth averaged value on the meridian section of the diffuser, the lower figures show the instantaneous value at the mid-height of the diffuser.

The comparison of the flow field within the diffusers for our three different numerical configurations (without leakage: $L/R_2 = 0\%$; with leakage: $L/R_2 = 1\%$) at the design flow rate Q_{d} in terms of the azimuthally-averaged velocity magnitude distribution at the meridian section and the instantaneous velocity magnitude distribution at the mid-height of the vaneless diffuser are presented in Fig 3.19. As already discussed in Section 3.2, the impeller jet-wake and the occurrence of the rotating instability have the most notable effect on the flow field of the zero-leakage case. For the negative-leakage case, the flow field is very similar to the zero-leakage case. Seven-periodic patterns originating from impeller jet-wake and rotating stall (see the bottom panel of Fig 3.19(b)) with an azimuthally-averaged reverse

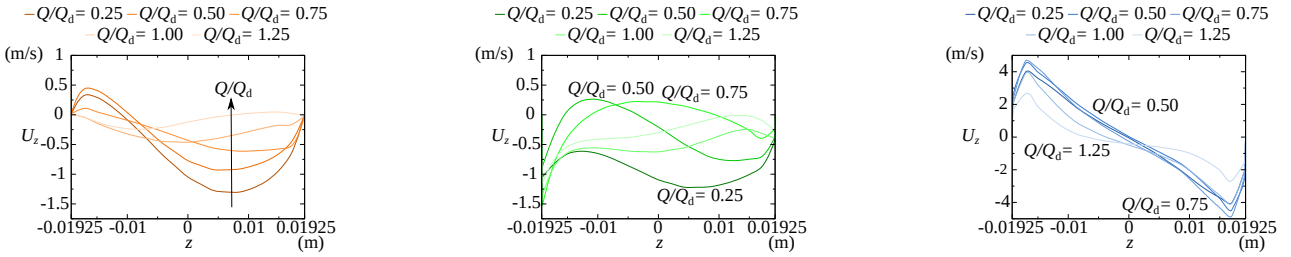

Figure 3.20: Axial velocity profiles at the diffuser inlet of (a) the zero-leakage case ($L/R_2 = 0\%$), (b) the negative-leakage case ($L/R_2 = 1\%$), and (c) the positive-leakage case ($L/R_2 = 1\%$).

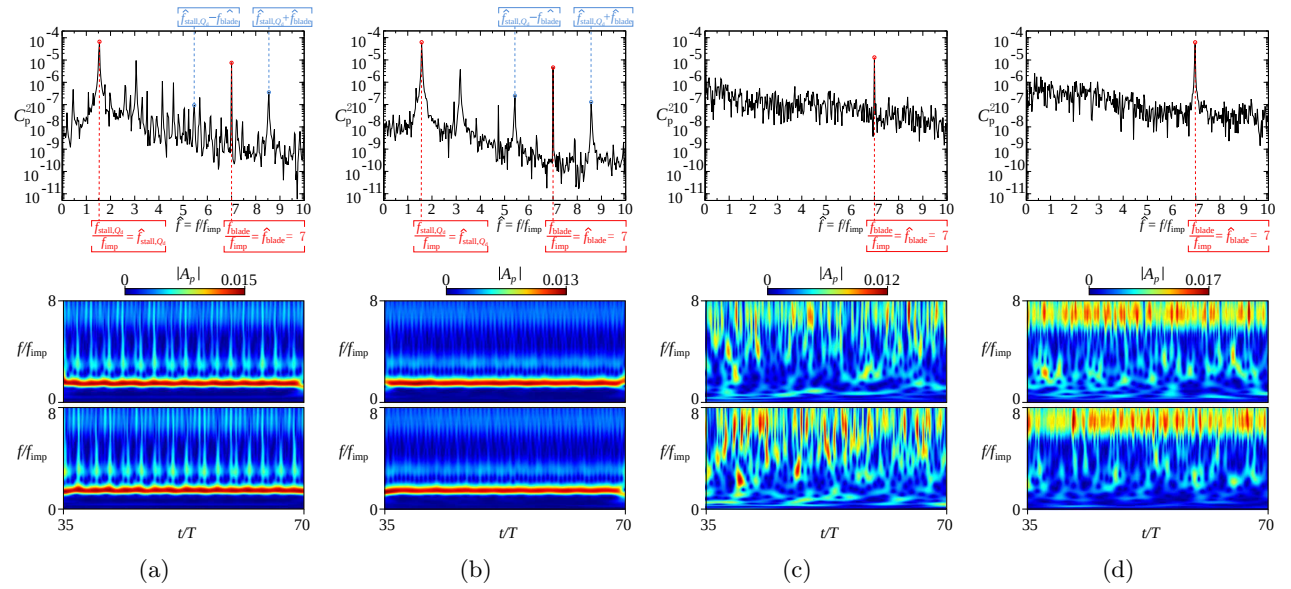

Figure 3.21: Fourier and wavelet analysis of the URANS simulation for (a) the zero-leakage case ($L/R_2 = 0\%$), (b) the negative-leakage case ($L/R_2 = 1\%$), and (c) the positive-leakage case ($L/R_2 = 1\%$), and of (d) the experiment, at the design flow rate $Q/Q_\mathrm{d} = 1.00$.

flow region (see the top panel of Fig 3.19(b)) can be easily discerned. This is anticipated as the flow rate in the diffuser of the negative-leakage case remains unchanged in comparison to the zero-leakage case. Consequently, the inflow conditions at the diffuser exhibit a resemblance to those observed in the zero-leakage scenario. For the positive-leakage case, the seven-periodic jet-wake instability patterns observed in the zero- and negative-leakage cases no longer exist in the positive-leakage case at the design flow rate (see the bottom panel of Fig 3.19(c)). This can be explained as the entrained leakage flow weakens the jet-wake intensity and stabilizes the flow in the diffuser as the effective flow angle increases (see [26]). Hence, the instability that occurs at the design flow rate Q gets suppressed as the critical conditions to trigger the 7-periodic rotating instability are not satisfied. Moreover, the reverse flow region observed in the azimuthally-averaged flow field at the mid-height of the diffuser does not exist anymore (see the top panel of Fig 3.19(c)). This finding provides additional confirmation for the interpretation that the azimuthally-averaged reverse flow region is indeed attributable to the rotating instability occurring at the design flow rate Q_{d}. The significance of the leakage flow effect is further confirmed by the comparison of the axial velocity profiles at the diffuser inlet of three numerical configurations as shown in Fig. 3.20. A detailed qualitative and quantitative analysis of the inflow profiles can be found in our published paper[2].

Figure 3.21 shows the FFT and wavelet analysis for the URANS simulations of three leakage configurations and the experiments at the design condition $Q = Q_{\mathrm{d}}$. Consistent with the qualitative assessment, the rotating instability is indicated for both the zero-leakage and negative-leakage cases (see the top panel of Figs. 3.21(a,b)). The frequency components identified in the FFT analysis for the negative-leakage case are similar to the ones detected from the zero-leakage case. The propagation velocity $\omega_{\mathrm{stall},Q_{\mathrm{d}}}/\omega_{\mathrm{imp}} = 0.22$ obtained from the zero-leakage case undergoes only a slight modification to the negative-leakage condition, changing to $\omega_{\mathrm{stall},Q_{\mathrm{d}}}/\omega_{\mathrm{imp}} = 0.224$. However, the wavelet analysis results show that the strong intermittent phenomenon associated with the secondary instability in the negative-leakage case is not as pronounced as in the zero-leakage case (see the bottom panel of Figs. 3.21(a,b)). This observation suggests that even very subtle variations of the inflow condition can have a substantial impact on secondary instability while having no discernible effect on primary instability. For the positive-leakage case (see Fig. 3.21(c)) only the blade passing frequency can be detected. As anticipated, no rotating instability frequency is found in FFT and wavelet results, which is consistent with the conclusion obtained from the inspection of the instantaneous color maps. This result aligns

well with the experimental result (see Fig. 3.21(d)), as the positive-leakage configuration qualitatively replicates the experimental geometry.

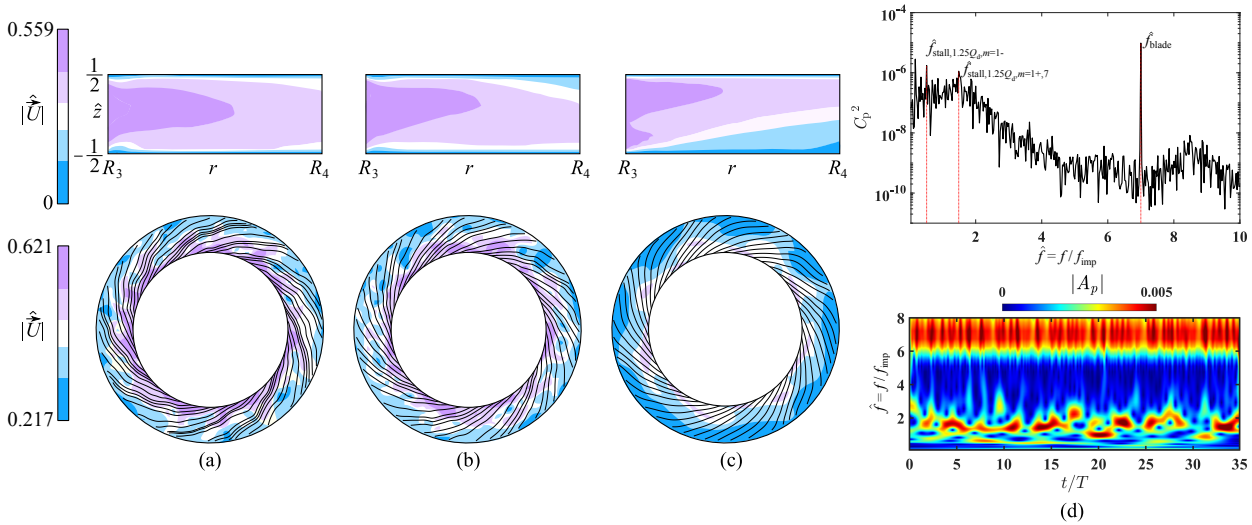

Figure 3.22: Velocity magnitude of the positive-leakage case ($L/R_2 = 1\%$) for (a) $Q/Q_\mathrm{d} = 0.75$, (b) $Q/Q_\mathrm{d} = 1$, and (c) $Q/Q_\mathrm{d} = 1.25$. Top panels: Azimuthal arithmetic-average values on the meridian section. Bottom panels: Instantaneous fields at the mid-height of the diffuser and streamlines (black). (d) Fourier and wavelet analyses of the positive-leakage case for $Q/Q_\mathrm{d} = 1.25$.

As mentioned before, the jet-wake instability at the design condition Q_d is concluded to be suppressed by the leakage flow in the positive-leakage case which weakens the jet-wake intensity. Building upon the previous investigation, we further expand our analysis to explore the instability occurring at flow rates higher and lower than Q_d in the positive-leakage configuration ($L/R_2 = 1\%$). The azimuthal arithmetic-averaged velocity magnitude distribution at the meridian section of the diffuser and the instantaneous velocity magnitude distribution at the mid-height of the diffuser for the positive-leakage case at three different flow rates $Q/Q_\mathrm{d} \in \{0.75,\ 1,\ 1.25\}$ are depicted in Fig. 3.22(a–c). Concerning the flow field of the positive-leakage case at the largest flow rate $Q/Q_\mathrm{d} = 1.25$, the flow feature shows high similarity to the ones observed for the zero-leakage case at the design condition $Q/Q_\mathrm{d} = 1.00$, i.e. 7-periodic flow instability pattern at the mid-height and the massive reverse flow region at the meridional section of the diffuser. As the flow rate decreases to values of $Q/Q_\mathrm{d} = 1.00$ and 0.75, the impact of the leakage flow on the flow field becomes more significant. The inflow velocity distribution became more symmetrical and the boundary layer thickness increased. As a result, the seven-periodic instability pattern observed at $1.25Q_\mathrm{d}$ for the positive leakage case does not exist any-

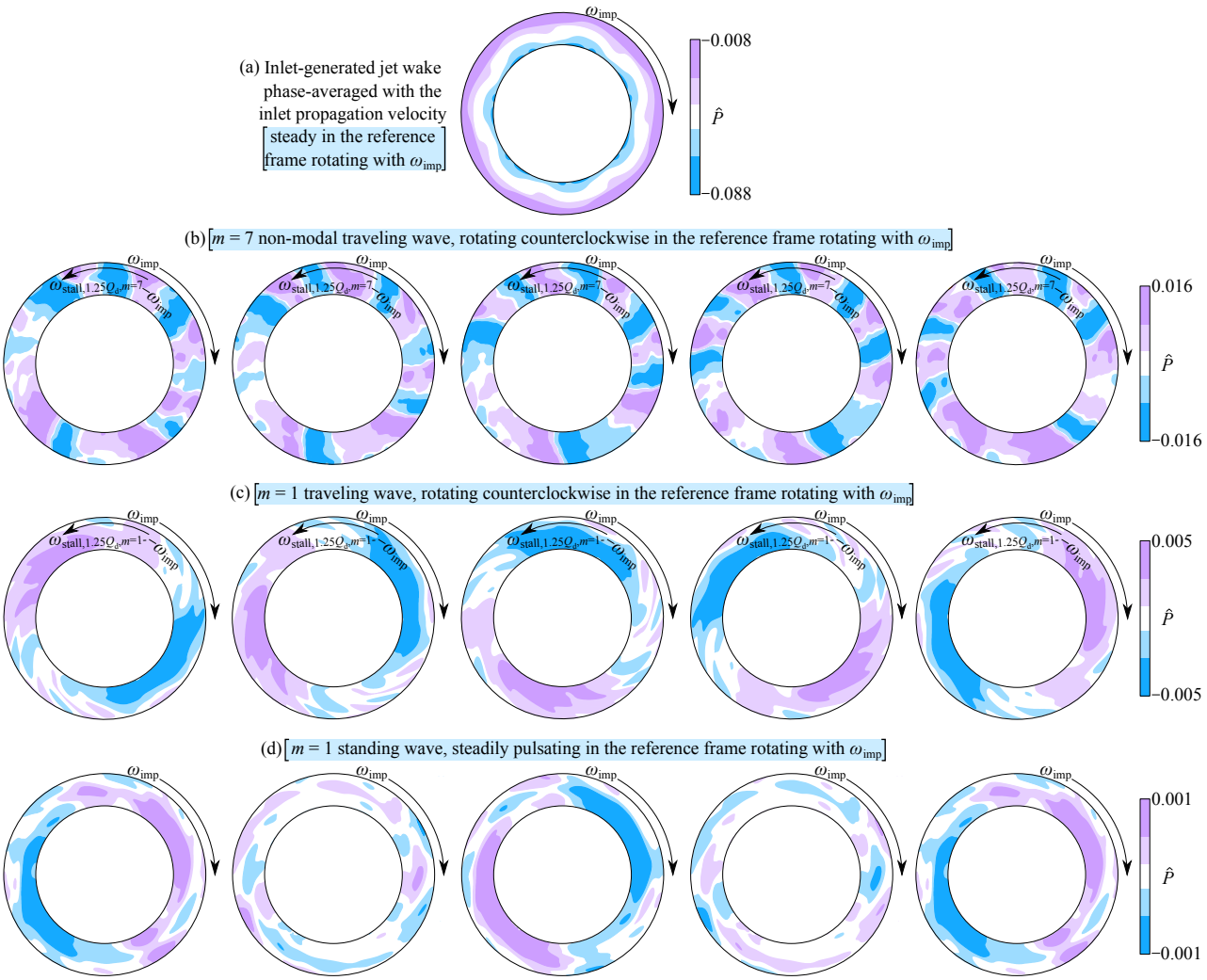

Figure 3.23: (a) Phase-averaged static pressure distribution in a reference frame rotating with the inlet propagation velocity. (b) The traveling non-modal wave of mode $m = 7$ depicted in the reference frame rotating with ω_{imp} and computed by subtracting the phase-averaged wake (a) and the traveling wave (c) to the instantaneous static pressure and phase-averaging with $\omega = \omega_{\text{stall},1.25Q_\text{d},m=7}$. (c) traveling wave of mode $m = 1$ depicted in the reference frame rotating with ω_{imp} and computed by subtracting the phase-averaged wake (a) from the instantaneous static pressure and phase-averaging with $\omega = \omega_{\text{stall},1.25Q_\text{d},m=1}$. (d) Standing wave steady in the reference frame rotating with ω_{imp} and computed with respect to the difference between the phase-averaged wake (a), the traveling wave (c), and the instantaneous static pressure and phase-averaging with $\omega = \omega_{\text{imp}}$. All figures refer to positive-leakage boundary conditions at the mid-height of the diffuser for $Q/Q_\text{d} = 1.25$.

more for $Q/Q_{\mathrm{d}} = 1.00$ and 0.75 (see the bottom panels of Fig. 3.22(a,b). Therefore, we stress again that there is no significant azimuthal-averaged flow separation occurring in the diffuser at large flow rates unless the 7-periodic pattern is present. The suppression of the instability at lower flow rates can be explained by considering that for our positive-leakage case, the jet-wake intensity at the diffuser inlet is weakened by the leakage flow, and the occurrence of the jet-wake instability must shift towards a higher flow rate.

To further confirm such an instability occurring at $1.25Q_{\mathrm{d}}$ of the positive-leakage case, the same quantitative analyses (FFT and wavelet) are performed as depicted in Fig. 3.22(d). The blade passing frequency $f_{\mathrm{blade}}/f_{\mathrm{imp}} = 7$, remains easily detectable in the FFT results. However, despite the clear observation of two-dimensional jet-wake instability patterns in the instantaneous flow field (see Fig. 3.22(c)), no prominent instability frequencies were identified in the FFT analysis. Concerning the wavelet analysis results, several low-frequency components can be observed intermingling during the whole simulation period. This is the reason why there is not a distinct peak corresponding to the instability other than the blade passing frequency in the FFT result. For the positive leakage case, the rotating instability at 1.25Qd is expected to be a non-modal wave rather than a harmonic as in the zero- and negative leakage case, which complicates the identification of rotational instability. Cross-correlation analysis of the two numerical probes is carried out as a complementary study, and several distinct propagation velocities are identified.

By phase-averaging the static pressure field at the mid-height of the diffuser with identified velocities, the frequency $f_{\mathrm{stall},Q_{\mathrm{d}},m=1-}/f_{\mathrm{imp}} = 0.514$ in FFT is identified as a one-periodic rotating pattern with a propagation velocity $\omega_{\mathrm{stall},Q_{\mathrm{d}},m=1-}/\omega_{\mathrm{imp}} = 0.514$. And the frequency $f_{\mathrm{stall},Q_{\mathrm{d}},m=1+,7}/f_{\mathrm{imp}} = 1.486$ in FFT is identified as another one-periodic rotating pattern with a propagation velocity $\omega_{\mathrm{stall},Q_{\mathrm{d}},m=1+}/\omega_{\mathrm{imp}} = 1.486$. At the same time, a third seven-periodic pattern with a propagation velocity $\omega_{\mathrm{stall},Q_{\mathrm{d}},m=7}/\omega_{\mathrm{imp}} = 0.21$ is also identified corresponding to the frequency $\omega_{\mathrm{rot},m=1+}/\omega_{\mathrm{imp}} = 1.486$. The characteristic of the third seven-periodic pattern is very similar to the ones identified from the rotating instability in the zero-leakage case at the design flow rate Q_{d}. Therefore, we can deduce that the two-dimensional jet-wake instability remains present in the positive-leakage case. Furthermore, the interaction between the leakage inflow and this instability results in the emergence of the discussed one-periodic traveling patterns.

Figure. 3.23 shows an overview of the instability scenario for the positive-leakage case at Q/Q_{d}

= 1.25. The seven-periodic jet-wake instability pattern at the mid-height of the diffuser by phase-averaging the static pressure field in a reference frame rotating with the impeller ω_{imp} is depicted in Fig. 3.23(a). By subtracting the primary phase-averaged result from the instantaneous pressure field and performing secondary phase-average processing in a reference frame rotating with $\omega_{\mathrm{stall},Q_{\mathrm{d}},m=1-}$, the one-periodic traveling wave is identified. By further subtracting the primary phase-averaged seven-periodic jet-wake pattern and the secondary phase-averaged one-periodic instability pattern from the instantaneous pressure field and phase-averaging again in a reference frame rotating with $\omega_{\mathrm{stall},Q_{\mathrm{d}},m=1+}$, another weaker one-periodic traveling wave is identified. In fact, the two one-periodic waves propagate in opposite circumferential directions and exhibit identical magnitudes of propagation velocity within a reference frame rotating with ω_{imp}. As a result of the superposition of these two one-periodic waves, a one-periodic traveling wave, and a one-periodic standing wave are formed within the reference frame rotating with ω_{imp}. This explanation sheds light on the primary characteristics introduced by the complex leakage flow within the vaneless diffuser. Additionally, we would like to emphasize that the propagation velocity of the one-periodic patterns is approximately half of the rotational velocity of the impeller. Hence, it is reasonable to assume that the traveling velocity of the one-periodic wave is primarily influenced by the interplay between the leakage flow and, on one hand, the stationary wall of the parallel rings, and on the other hand, the rotating wall of the impeller (rotating at ω_{imp}), which generates a leakage swirl rotating at $\omega_{\mathrm{imp}}/2$. By subtracting the phase-averaged two one-periodic instabilities and the jet-wake patterns from the instantaneous pressure field, and subsequently performing another phase-averaging in a reference frame rotating with $\omega_{\mathrm{stall},Q_{\mathrm{d}},m=7}$, the seven-periodic pattern arising from the jet-wake instability manifests itself as a non-modal wave. The jet-wake instability patterns are qualitatively and quantitatively similar to the one observed in the zero-leakage case (refer to Figs. 3.23(b) and 3.16(b)). However, the secondary instability identified for the zero-leakage case (see Fig. 3.16(c)) does not exist for the positive-leakage case anymore. While the intermittent nonlinear interaction between mode $m = 7$ and modes $m = 1$ results in the observed chaotic dynamics in the wavelet analysis for the positive-leakage case (refer to Fig. 3.22(d)).

To ascertain the critical conditions at which instabilities occur when L/R_2 is set to 1%, we conducted a parametric investigation in terms of the flow rate Q/Q_{d} based on the results of FFTs (see top panel of Fig. 3.24). The results indicate that the jet-wake instability is expected to occur for a critical flow rate $Q_{\mathrm{c}}/Q_{\mathrm{d}} \in [1,\ 1.1]$. Furthermore, the $m = 1$ traveling wave is also evident at $Q_{\mathrm{c}}/Q_{\mathrm{d}} = 1.1$

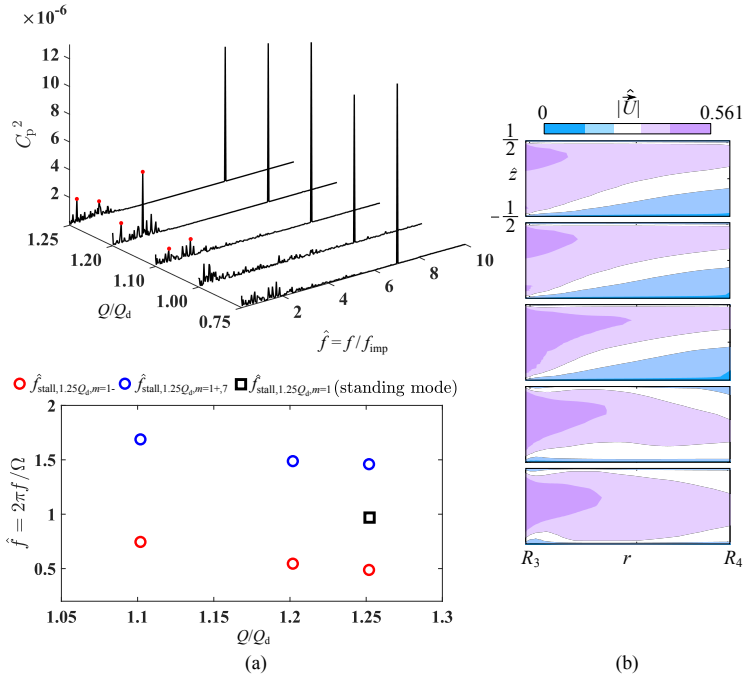

Figure 3.24: (a) Fourier analysis and stability diagram. (b) Azimuthal arithmetic-average velocity fields of the positive-leakage case with the largest leakage size ($L/R_2 = 1\%$) at different flow rates. From top to bottom are $Q/Q_\mathrm{d} = 1.25$, $Q/Q_\mathrm{d} = 1.20$, $Q/Q_\mathrm{d} = 1.10$, $Q/Q_\mathrm{d} = 1.00$, and $Q/Q_\mathrm{d} = 0.75$.

and 1.2. However, the occurrence of the standing wave in the reference frame that rotates with ω_imp is restricted to $Q/Q_\mathrm{d} = 1.25$. This is because the condition $(\hat{f}_{\mathrm{stall},1.25Q_\mathrm{d},m=7} + \hat{f}_{\mathrm{stall},1.25Q_\mathrm{d},m=1-})/2 = 1$ is satisfied only at this particular flow rate. Consequently, this standing wave, observed in the frame of reference synchronized with the inlet frequency, emerges as a consequence of the interaction between the two traveling waves. A visual representation of this scenario is presented in the lower section of Figure 3.24(a). Consequently, this standing wave, observed in the reference frame rotating with the impeller, emerges as a consequence of the interaction between the two traveling waves. A visual representation of this scenario is presented in the bottom panel of Fig. 3.24(a).

To gain insight into the origin of the $m = 1$ traveling wave, we conducted additional simulations, deliberately selecting two different radial gaps between the impeller and the diffuser, i.e. $L/R_2 = 0.33\%$ and 0.66% for flow rate $Q/Q_\mathrm{d} = 1$ and 1.25. The results for $Q/Q_\mathrm{d} = 1$ are illustrated in Fig. 3.25(a,b). In this scenario, the $m = 7$ jet-wake instability persists up to $L/R_2 = 0.66\%$, as corroborated by the corresponding mean flow separation exhibited in Fig. 3.25(b). Therefore, the critical radial gap for $Q/Q_\mathrm{d} = 1$ should be $(L/R_2)_{c,Q/Q_\mathrm{d}=1} \in [0.66,\ 1]\%$ (see bottom panel of Fig. 3.25(a)). Remarkably,

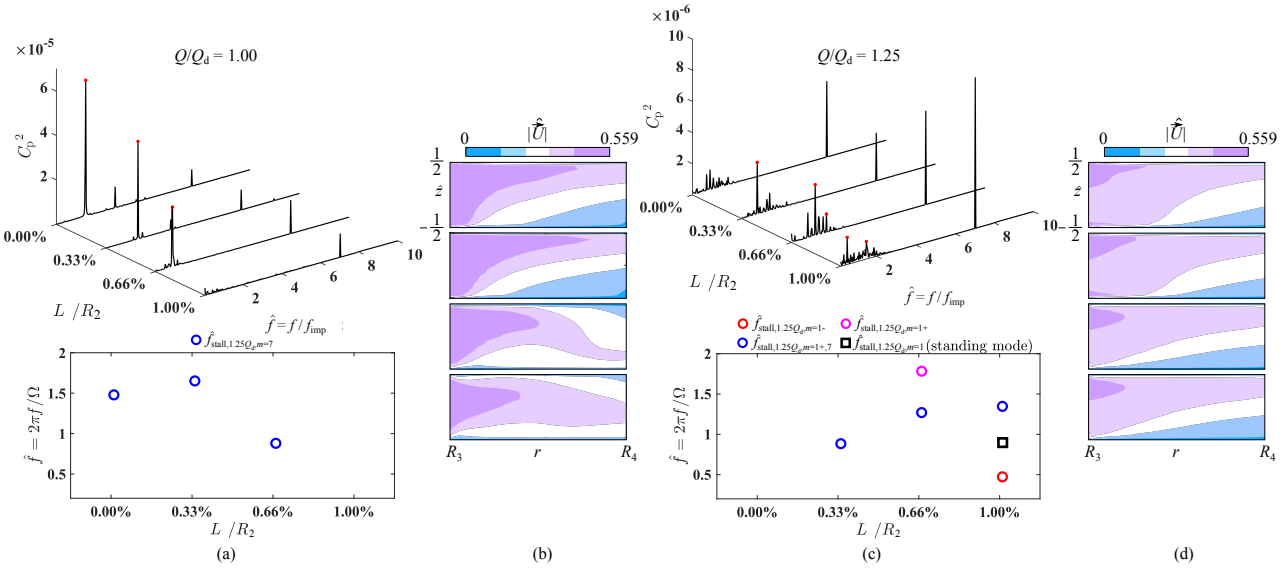

Figure 3.25: (a) Fourier analysis and stability diagram, (b) azimuthal arithmetic-average velocity fields at the meridian section of the diffuser at $Q/Q_\mathrm{d} = 1.00$ and (c) Fourier analysis and stability diagram, (d) azimuthal arithmetic-average velocity fields at $Q/Q_\mathrm{d} = 1.25$ of the positive-leakage case with different leakage size L. (b,d) From top to bottom are $L/R_2 = 0.00\%$, $L/R_2 = 0.33\%$, $L/R_2 = 0.66\%$, and $L/R_2 = 1.00\%$.

none of the simulations conducted at $Q/Q_\mathrm{d} = 1$ reveal any indication of the $m = 1$ traveling wave, as evidenced by the Fourier spectra (see the top panel of Fig. 3.25(a)). This leads us to the conclusion that the presence of the jet-wake instability alone does not necessarily result in the emergence of the $m = 1$ traveling wave as an outcome of its interaction with the leakage flow. If the jet-wake instability is too dominant (as indicated by the amplitudes in the Fourier spectra of Fig. 3.25(a)), the influence of the leakage flow is comparatively weak, preventing the initiation of the $m = 1$ traveling wave. Still, our simulations underscore the significance of the leakage flow, as they reveal that the jet-wake instability transitions from $m = 7$ for $L/R_2 = 0$ and $Q/Q_\mathrm{d} = 1$, to $m = 8$ for $L/R_2 = 0.33\%$, and further to $m = 6$ for $L/R_2 = 0.66\%$ (as depicted in the stability diagram in Fig. 3.25(a)). As previously mentioned, at $Q/Q_\mathrm{d} = 1$, the flow remains stable when $L/R_2 = 1\%$.

As the flow rate increased to $Q/Q_\mathrm{d} = 1.25$, the zero-leakage case ($L/R_2 = 0$) is stabilized, and a bandwidth of frequencies appears in its Fourier spectrum (see Fig. 3.25(c)). This phenomenon is linked to the chaotic dynamics resulting from the interaction between the inflow and the mean-flow separation occurring on the bottom wall (as shown in Fig. 3.25(d) and confirmed through wavelet analysis in

the supplementary material of our previous paper [60]). As the radial gap enlarged, the jet-wake instability became evident at $L/R_2 = 0.33\%$. Thus, the critical gap size for the primary instability at $Q/Q_\mathrm{d} = 1.25$ is $(L/R_2)_{c,1^\circ,Q/Q_\mathrm{d}=1.25} \in [0,\ 0.33]\%$, as depicted in the stability diagram in Fig. 3.25(c). Although the jet-wake instability is less pronounced compared to the situation at $Q/Q_\mathrm{d} = 1$, the radial gap of $L/R_2 = 0.33\%$ is too small to facilitate the generation of the $m = 1$ traveling wave through interaction with the primary instability. On the other hand, when the amplitudes of the jet-wake instability are comparable (as evident in the Fourier spectra in Fig. 3.25(c)), a wider radial gap of $L/R_2 = 0.66\%$ induces a stronger leakage flow, capable of triggering the secondary traveling-wave instability (as indicated by the appearance of the $m = 1$ frequency in the corresponding Fourier spectrum). This effect becomes even more pronounced at $L/R_2 = 1\%$, as the primary instability further reduces its amplitude. Consequently, the critical radial gap for the secondary instability is estimated to be $(L/R_2)_{c,2^\circ,Q/Q_\mathrm{d}=1.25} \in [0.33,\ 0.66]\%$ at $Q/Q_\mathrm{d} = 1.25$. Note that for $L/R_2 = 0.66\%$, the $m = 1$ traveling wave rotates clockwise in a reference frame rotating with the impeller ω_imp. Once again, it is noteworthy that the leakage flow has a significant impact on the dominant mode of the primary instability. This is evident as the jet-wake instability transitions from $m = 6$ for $L/R_2 = 0.33\%$ to $m = 9$ for $L/R_2 = 0.66\%$ and finally to $m = 7$ for $L/R_2 = 1\%$ at $Q/Q_\mathrm{d} = 1.25$ (as illustrated in the stability diagram in Fig. 3.25(c)).

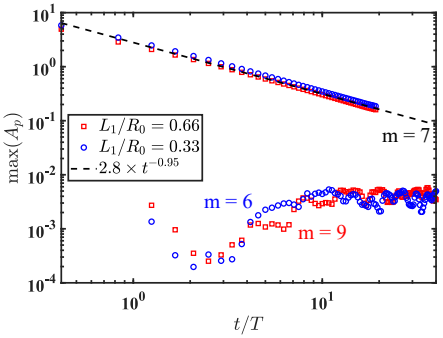

Figure 3.26: Decay upon a sudden reduction of the gap size of the flow instability amplitude ($m = 7$) inherited as initial condition generated for $L/R_2 = 1\%$ and $Q/Q_\mathrm{d} = 1.25$. The lower amplitudes depict the growth of the primary instability amplitude for $L/R_2 = 0.33\%$ ($m = 6$) and 0.66%.($m = 9$)

As the critical mode undergoes changes with variations in the radial gap, we conducted an investigation into flow control for the primary instability by instantly reducing the radial gap. To emulate this scenario in our simulations, we assumed the fully-developed flow condition for $L/R_2 = 1\%$ as

the initial state. Then, we promptly enforced the no-slip condition over one-third ($L/R_2 = 0.33\%$) or two-thirds ($L/R_2 = 0.66\%$) of the radial gap. By monitoring the maximum amplitude of the $m = 7$ mode inherited from the initial $L/R_2 = 1\%$ flow, we observed that the instantaneous reduction of the radial gap resulted in a hyperbolic decay of the large-gap instability pattern, with its amplitude scaling as $\sim (t/T)^{-0.95}$ (see Fig. 3.26(a)).

This rapid decay of the large leakage flow allowed us to uncover the growth of the most critical mode associated with the $m = 6$ and $m = 9$ jet-wake instability for $L/R_2 = 0.33\%$ and $L/R_2 = 0.66\%$, respectively. We accomplished this by conducting a wavelet analysis and retaining only the frequencies $f/f_{\text{imp}} \in [0, 4]$, encompassing a range twice as wide as expected for the instability. The maximum amplitudes extracted from this analysis are presented in Fig. 3.26. These findings indicate that the growth of the jet-wake instability is a phenomenon that triggers non-linear interactions during the perturbation development. Moreover, the non-modal nature of the instability is confirmed by the non-orthogonality in the amplification of perturbation energy.

3.3.1.2 Effect of the inflow condition on the instability at small flow rate

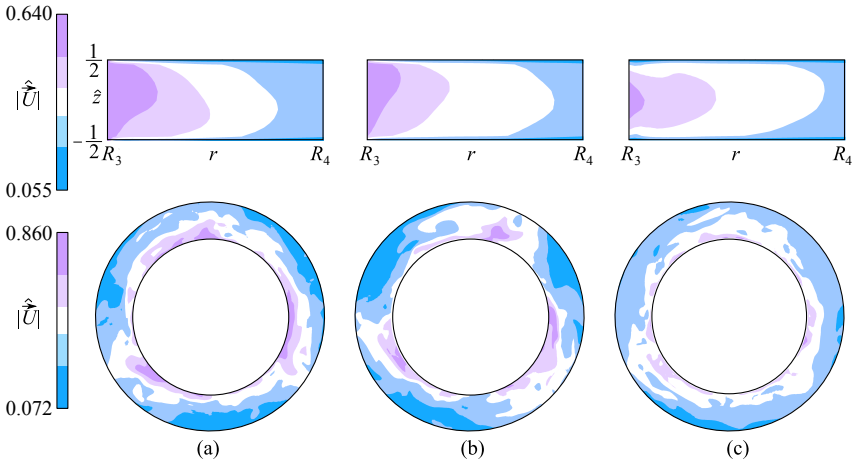

Figure 3.27: Color maps of the instantaneous static pressure, radial velocity, tangential velocity, and axial velocity at the design flow rate $Q/Q_{\text{d}} = 1.00$ for (a) the zero-leakage case, (b) the negative-leakage case, and (c) the positive-leakage case. The upper figures show the azimuth averaged value on the meridian section of the diffuser, the lower figures show the instantaneous value at the mid-height of the diffuser.

Figure 3.30 shows the comparison of the flow field within the diffusers for our three different nu-

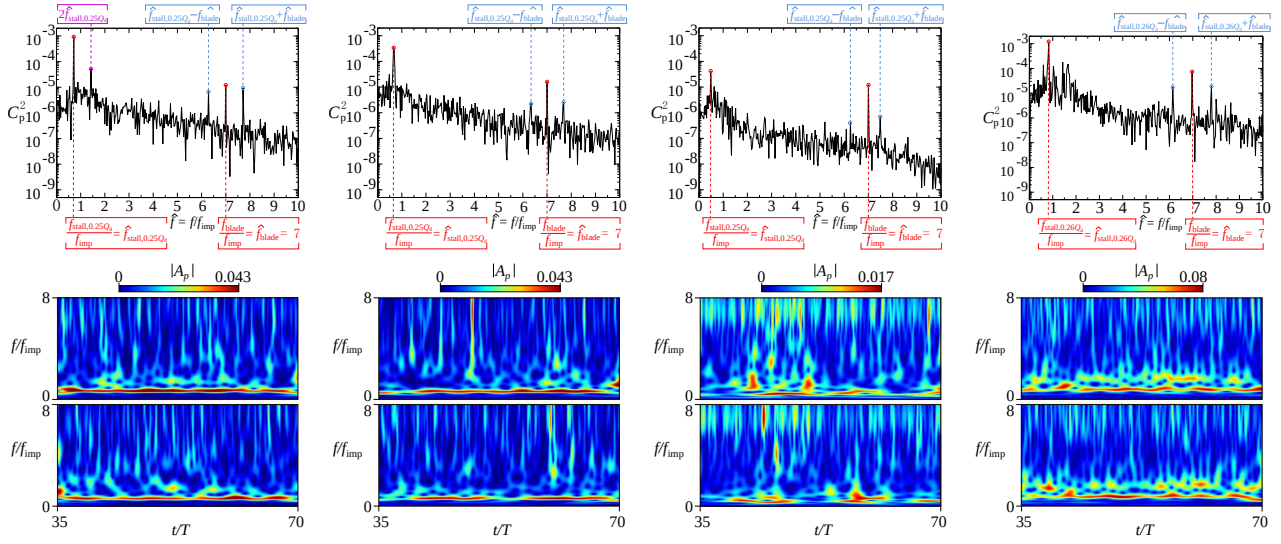

Figure 3.28: Fourier and wavelet analysis of the URANS simulation for (a) the zero-leakage case, (b) the negative-leakage case, and (c) the positive-leakage case, and of (d) the experiment, at the stall condition $Q/Q_\mathrm{d} = 0.25$.

merical configurations at the fully-developed stall condition $Q/Q_\mathrm{d} = 0.25$ in terms of the azimuthally-averaged velocity magnitude distribution at the meridian section and the instantaneous velocity magnitude distribution at the mid-height of the vaneless. In all three numerical configurations, three rotating stall cells can be observed. However, the flow field of the positive-leakage case (see Fig. 3.30(c)) exhibits an intricate nature compared to the other two cases.

Figure 3.28 shows the comparison of the FFT and wavelet analysis for the three URANS simulations and experiments at the fully-developed stall condition. The blade passing frequency, rotating stall frequency, and nonlinear interactions between them were easily captured both by the FFT and wavelet analysis for the zero- and negative-leakage cases. And the rotating stall frequencies of these two leakage configurations are very close. For the positive-leakage case (Fig. 3.28(c)), the FFT result exhibits similar qualitative characteristics, but the wavelet analysis reveals a notable distinction when comparing to the zero- and negative-leakage cases (refer to Fig. 3.28(a–d)) under the effect of leakage flow. In the numerical configuration, the leakage from the impeller to the diffuser is more pronounced compared to the experimental setup. The leakage flow, which rotates with the impeller walls, enters the diffuser at the impeller frequency f_imp. This leads to nonlinear interactions with the blade passing frequency f_blade and the rotating stall frequency $f_{\mathrm{stall},0.25Q_\mathrm{d}}$, resulting in a more intricate flow field.

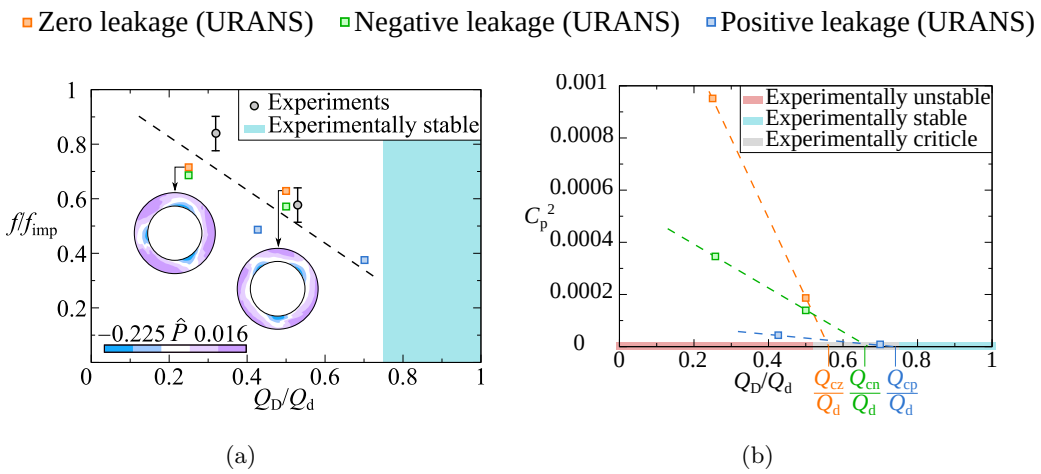

(a) (b)

Figure 3.29: (a) Rotating stall frequency and (b) amplitude analysis at small flow rates ($Q/Q_d = 0.50$ and 0.25).Flow angle of the core flow versus rotating stall propagation velocity at small flow rates ($Q/Q_d = 0.50$ and 0.25).

Table 3.11: Propagation velocity of the rotating instability obtained by the FFT at the stall condition $Q/Q_d = 0.25$.

Case	Zero-leakage (URANS)	Negative-leakage (URANS)	Positive-leakage (URANS)	Positive-leakage (Experiment)	2D linear model (Tsujimoto)
$\frac{f_{stall,0.25Q_d}}{f_{imp}}$	0.714	0.686	0.486	0.840	0.867
$\frac{\omega_{stall,0.25Q_d}}{\omega_{imp}}$	0.238	0.228	0.162	0.280	0.289

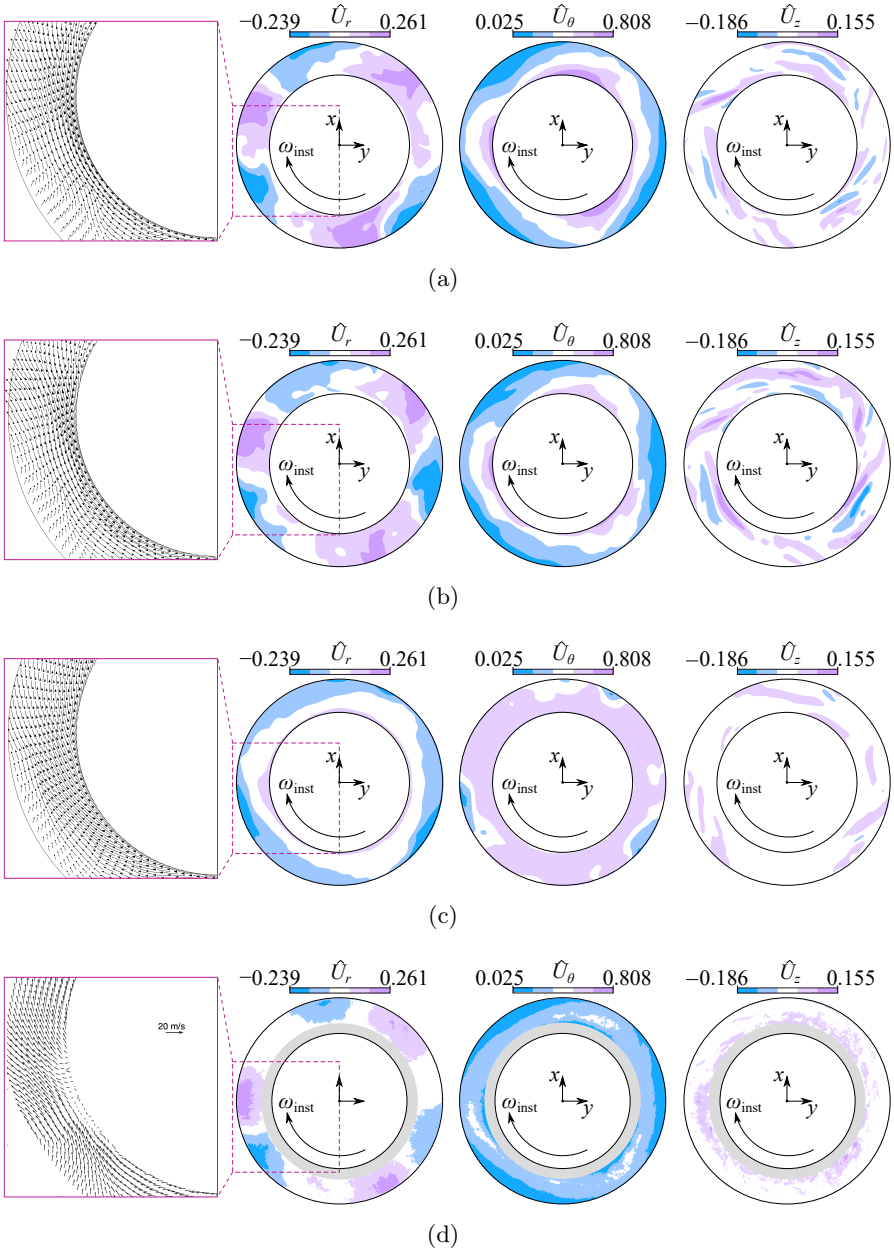

Figure 3.30: Phase averaged velocity vectors and color maps of radial, tangential, and axial velocity at the mid-height of the diffuser based on the instability propagation speed $\omega_{\text{stall},0.25Q_\text{d}}$ at the stall condition $Q/Q_\text{d} = 0.25$ for (a) the zero-leakage case, (b) the positive-leakage case, (c) the negative-leakage case, and (d) the PIV measurement results. The grey region close to the diffuser inlet is not accessible to PIV because of laser reflection on the impeller blades. The measurements near its edge are therefore to be considered affected by a significant error bar.

The numerical and experimental results obtained from the FFTs are summarized in Tab. 3.11. It can be observed that the identified stall propagation velocity $\omega_{\text{stall},0.25Q_\text{d}}$ is consistent with the experimental value across the various cases. However, it is worth noting that the frequency of the rotating instability is highly susceptible to changes in the leakage flow. In order to demonstrate this phenomenon, Fig. 3.29 illustrates the variation of rotating stall frequencies (Fig. 3.29(a)) and amplitudes (Fig. 3.29(b)) extracted from both simulations and experiments. These values are plotted against the effective diffuser flow rate Q_D, which has been normalized to the nominal flow rate Q_d/Q_d after accounting for the leakage flow.

The rotating stall frequency $f_{\text{stall},0.25Q_\text{d}}/f_\text{imp}$ decreases with increasing effective diffuser flow Q following the equation $f_{\text{stall},0.25Q_\text{d}}/f_\text{imp} \approx \alpha + \beta Q_\text{D}$, where $\alpha = 0.9689$ and $\beta = -0.8189$ are fitting coefficients that approximate at leading order the change of frequency with Q_D for all the numerical configurations. By considering a linear process, the critical diffuser flow rate can be estimated for the rotating stall instability, as discussed in our published paper [2]. Based on this, we can infer that the square of the perturbation amplitude, denoted as C_p^2, scales with the deviation of Q_D from the critical flow rate $Q_\text{D,c}$, i.e. $C_p^2 \sim (Q_\text{D} - Q_\text{D,c})$. By extracting C_p^2 from the FFT for $Q/Q_\text{d} = 0.25$ and 0.5, the critical flow rate $Q_\text{D,c}$ can be estimated through linear extrapolation until C_p^2 reaches zero. This is illustrated by the dashed lines in Fig. 3.29(b). Fig. 3.29(b) depicts the critical flow rates estimated for our three different numerical configurations. All results fall within the experimental range $Q_\text{D,c} \in [0.55,\ 0.7]$ measured by looking for local recirculation regions, as reported by [61] in the very first publication on the present centrifugal machine model.

Figure 3.30 illustrates the comparison of the phase-averaged flow field of the three numerical configurations and the PIV experiment in a reference frame rotating with the rotating stall propagation velocity. Three stall cells are easily observed for the zero- and negative-leakage cases, and they qualitatively and quantitatively well compare in terms of the velocity field with the PIV experimental measurements for $Q = 0.26Q_\text{d}$ (Fig. 3.30(d), ([10])). Due to the positive leakage case (Fig. 3.30(c)) considering an effective flow of $Q_\text{D} = 0.43Q_\text{d}$, the phase-averaged flow field is not comparable to other cases.

3.3.2 Effect of the diffuser radial aspect ratio on the instability[E]

The main focus of this section is to examine how the instability characteristics of the flow in the vaneless diffuser are affected by the radial aspect ratio Γ, with $\Gamma \in \{1.25,\ 1.5,\ 2\}$.

3.3.2.1 Effect of the radius ratio on the instability at large flow rate

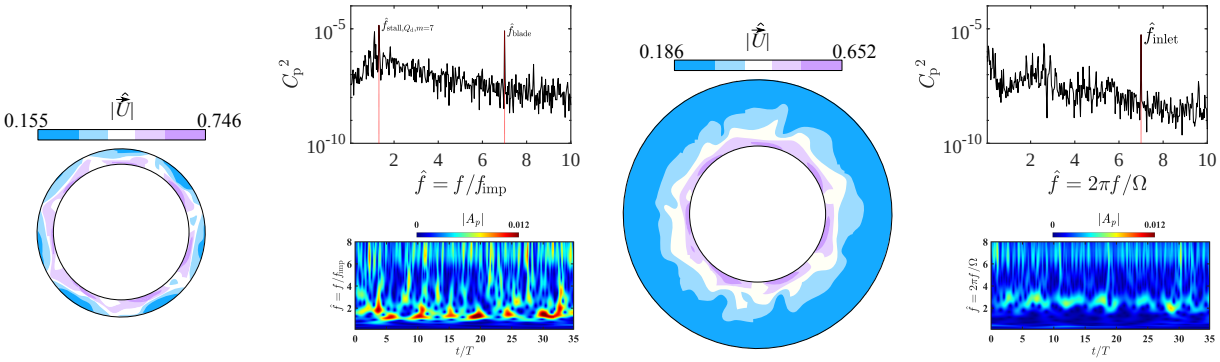

(a) (b)

Figure 3.31: Color maps of instantaneous velocity magnitude distribution at the mid-height of the diffusers and Fourier and wavelet analysis results for diffusers with different radial aspect ratios: (a) $\Gamma = 1.25$, (b) $\Gamma = 2.00$. All figures refer to the zero-leakage inflow for $Q/Q_{\text{d}} = 1.00$

To study the effect of the radial aspect ratio Γ on the 2D jet-wake instability occurring at large flow rates ($Q/Q_{\text{d}} \gtrsim 1.00$), the instantaneous velocity field at the mid-height of the diffuser for the zero-leakage case at the design flow rate $Q/Q_{\text{d}} = 1$ with radial aspect ratio $\Gamma = 1.25$ and $\Gamma = 2.00$ are presented in Fig. 3.31(a). The results show that jet-wake patterns corresponding to seven impeller blades are observed near the diffuser inlet for both radial aspect ratios Γ. Besides, a seven-periodic instability pattern can be roughly observed for $\Gamma = 1.25$ (see the top panel of Fig. 3.31(a)) which is consistent with the result for $\Gamma = 1.50$ as discussed previously. As the radial aspect ratio increases to $\Gamma = 2.00$, the outflow moves farther away, leading to the dominance of non-linear effects caused by the interactions of radial diffuser boundary layers. Consequently, a complex chaotic regime emerges (as depicted in the bottom panel of Fig. 3.31(a)), replacing the previously observed quasi-periodic instability pattern seen in the other two smaller radial aspect ratios.

The FFT and wavelet analysis results are depicted in the right panel of Fig. 3.31(a) to further understand the underlying mechanisms of the instabilities. For $\Gamma = 1.25$, the blade passing frequency

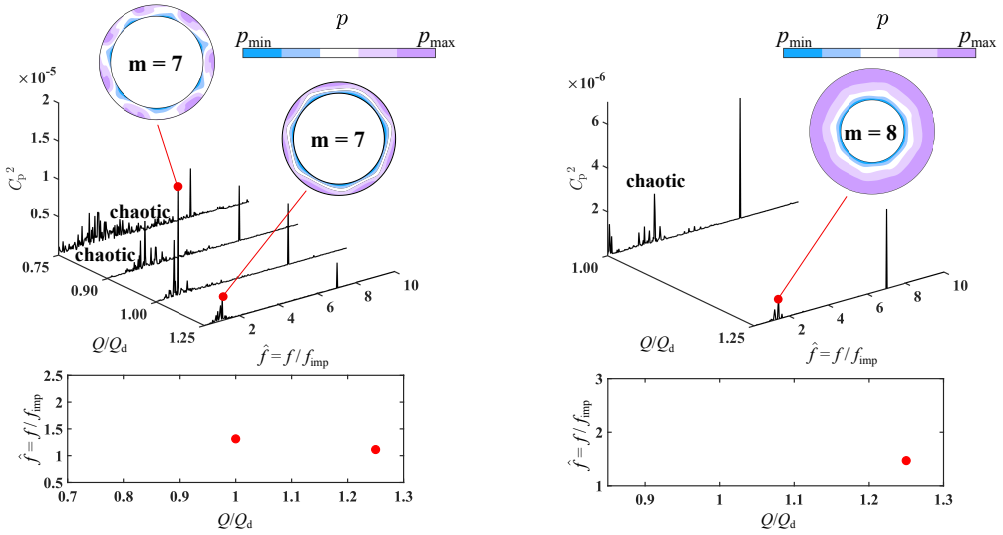

(a) $\Gamma = 1.25$ (b) $\Gamma = 2$

Figure 3.32: Fourier analysis and stability diagram near design flow rate for (a) $\Gamma = 1.25$ and (b) $\Gamma = 2$ with zero-leakage inflow. The identified instabilities are pictured phase averaging the URANS in a reference frame rotating with the instability propagation velocity.

$f_{\text{blade}}/f_{\text{imp}} = 7$ and the two-dimensional jet-wake instability frequency $f_{\text{stall},Q_\text{d},m=7}/f_{\text{imp}} = 1.314$ can be easily detected both in FFT and wavelet results. By subtracting the phase-averaged seven-periodic jet-wake pattern in a reference frame rotating with impeller ω_{imp}, and phase-average again in a reference frame rotating with $\omega_{\text{stall},Q_\text{d},m=7} = 0.188$, seven-periodic jet-wake instability pattern consistent with the prediction made by Ljevar et al. [26] can be observed (see supplementary video of our previous paper [62] at `https://github.com/fromano88/CentrifugalPump.git`). Such instability is traced back to the frequency $f_{\text{stall},Q_\text{d},m=7}/f_{\text{imp}} = 1.314$ observed in the FFT and wavelet analysis and consistent with the primary instability of Γ =1.50 which is thoroughly analyzed, propagating in the counterclockwise direction (see arrow $\omega_{\text{stall},Q_\text{d},m=7} - \omega_{\text{imp}}$ on Fig. 3.16(b)) in a reference frame rotating with ω_{imp}. However, the secondary instability resulting from nonlinear interactions between the primary instability and the shear layer of the inlet jet wave detected for Γ =1.50 does not exist for Γ =1.25 anymore. This is because a Γ =1.25 radial diffuser is too short to allow strong nonlinear interaction.

Concerning the FFT results for $\Gamma = 2.00$, only the blade passing frequency $f_{\text{blade}}/\omega_{\text{imp}} = 7$ is prominent (see the right panel of Fig. 3.31(b)). Besides, a relatively wide population of bandwidths

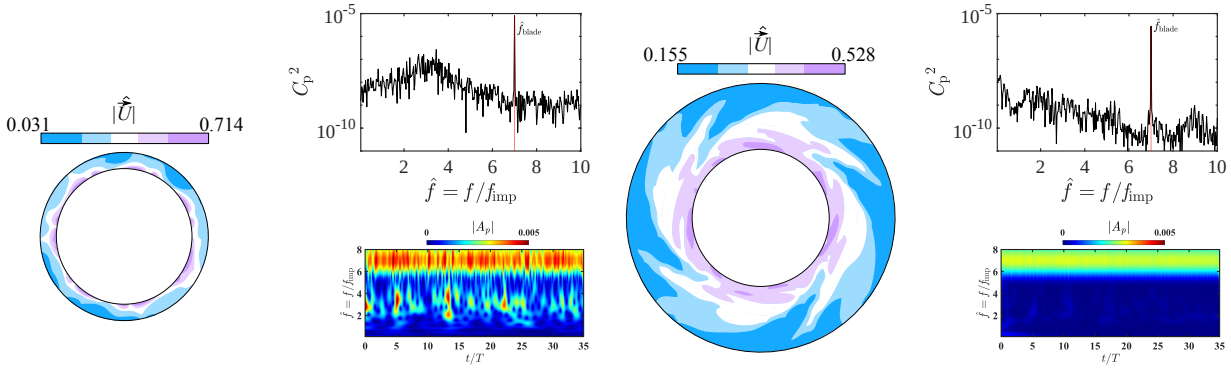

(a) (b)

Figure 3.33: Color maps of instantaneous velocity magnitude distribution at the mid-height of the diffusers and Fourier and wavelet analysis results for diffusers with different radial aspect ratios: (a) $\Gamma = 1.25$, (b) $\Gamma = 2.00$. All figures refer to the positive-leakage inflow for $Q/Q_{\text{d}} = 1.25$

between 2 and 3 times the impeller frequency f_{inlet} can be observed in FFT as well as in wavelet analysis. Such complex chaotic dynamics are attributed to non-linear interactions. Ramping up the flow rate to $Q/Q_{\text{d}} = 1.25$, we observe the emergence of an 8-periodic jet-wake instability pattern for $\Gamma = 2$, as illustrated in Fig. 3.32(b). The stability boundaries for $\Gamma = 1.25$ and 2 are also detailed in Fig. 3.32, where FFT analysis reveals that the jet-wake instability occurs when the flow rate Q/Q_{d} exceeds a critical value $Q_{\text{c}}^{\text{jet-wake}}/Q_{\text{d}}$ for the large-flow-rate instability. For $\Gamma = 1.25$, the critical value $\alpha_c^{\text{jet-wake}} \in [0.9,\ 1]$, and for $\Gamma = 2$ the critical value shifts to $\alpha_c^{\text{jet-wake}} \in [1,\ 1.25]$. From a qualitative standpoint, it can be concluded that the flow dynamics are significantly affected by the radius ratio Γ of the radial rings. This effect is evident as it suppresses the primary instability, even for the zero-leakage case.

As discussed before, the jet-wake instability is supposed to occur at higher flow rates for the positive-leakage case. Therefore, the flow field of the positive-leakage case at $1.25Q_{\text{d}}$ with different radius ratios are compared and discussed. For $\Gamma = 1.25$, it is challenging to clearly identify the instability pattern, unlike the situation observed in the zero-leakage case (see Fig. 3.33(a). Consequently, only the blade passing frequency $f_{\text{blade}}/\omega_{\text{imp}} = 7$ can be clearly detected in FFT and wavelet analysis. By subtracting the primary phase-averaged flow in the reference frame rotating with ω_{imp} from the instantaneous pressure field, the remaining flow field is chaotic for $\Gamma = 1.25$. The observed phenomenon indicates that even the primary instability can be suppressed by a positive leakage flow in a short vaneless diffuser (see Fig. 3.34(a) for $Q/Q_{\text{d}} = 1$ and 1.25). This differs from the findings for $\Gamma = 1.5$

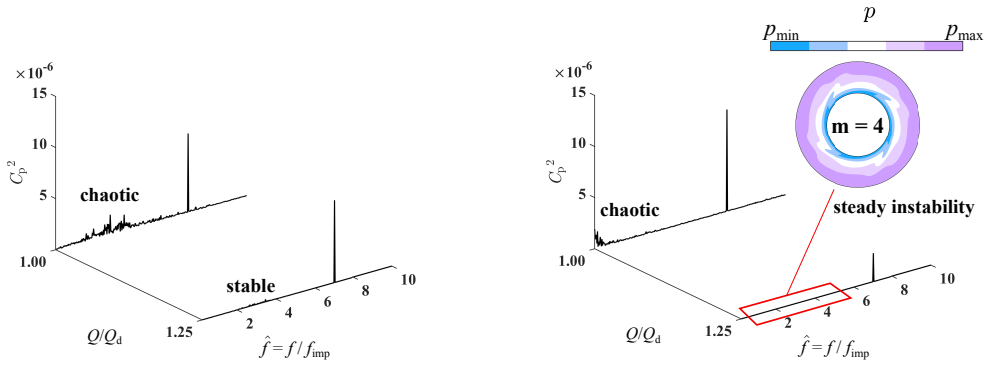

(a) $\Gamma = 1.25$ (b) $\Gamma = 2$

Figure 3.34: Fourier analysis and stability diagram near design flow rate for (a) $\Gamma = 1.25$ and (b) $\Gamma = 2$ with positive-leakage inflow. The identified instability for $\Gamma = 2$ is pictured phase averaging the URANS in a steady reference frame.

even from a qualitative point of view, where leakage only affects the secondary instability.

For the positive-leakage case with $\Gamma = 2.00$, an unexpected four-periodic pattern was observed in the snapshot (see the left panel of Fig. 3.33(a)). However, no additional frequencies could be identified in addition to the blade passing frequency $f_{\text{blade}}/\omega_{\text{imp}} = 7$ by the FFT and wavelet analyses. By performing phase-averaging of the flow field in a stationary reference frame, following the subtraction of the primary phase-averaged flow from the instantaneous pressure field in a reference frame rotating with ω_{imp}, the presence of a four-periodic spiraling mode as the instability is confirmed (see supplementary video of our previous paper [62] at `https://github.com/fromano88/CentrifugalPump.git`). The energy production of such instability is concentrated in the region of the interaction between the boundary layers of two parallel plates (not shown). The reason behind this observation is easily comprehensible when considering that the positive-leakage flow leads to the thickening of the boundary layers, thereby facilitating their interaction. This interaction, in turn, gives rise to a Kelvin-Helmholtz instability responsible for the spiraling pattern. In contrast, the zero-leakage case did not exhibit this instability as the boundary layers were too thin to promote such phenomena. It is worth noting that this instability phenomenon occurring in the vaneless diffuser is being reported for the first time in this study.

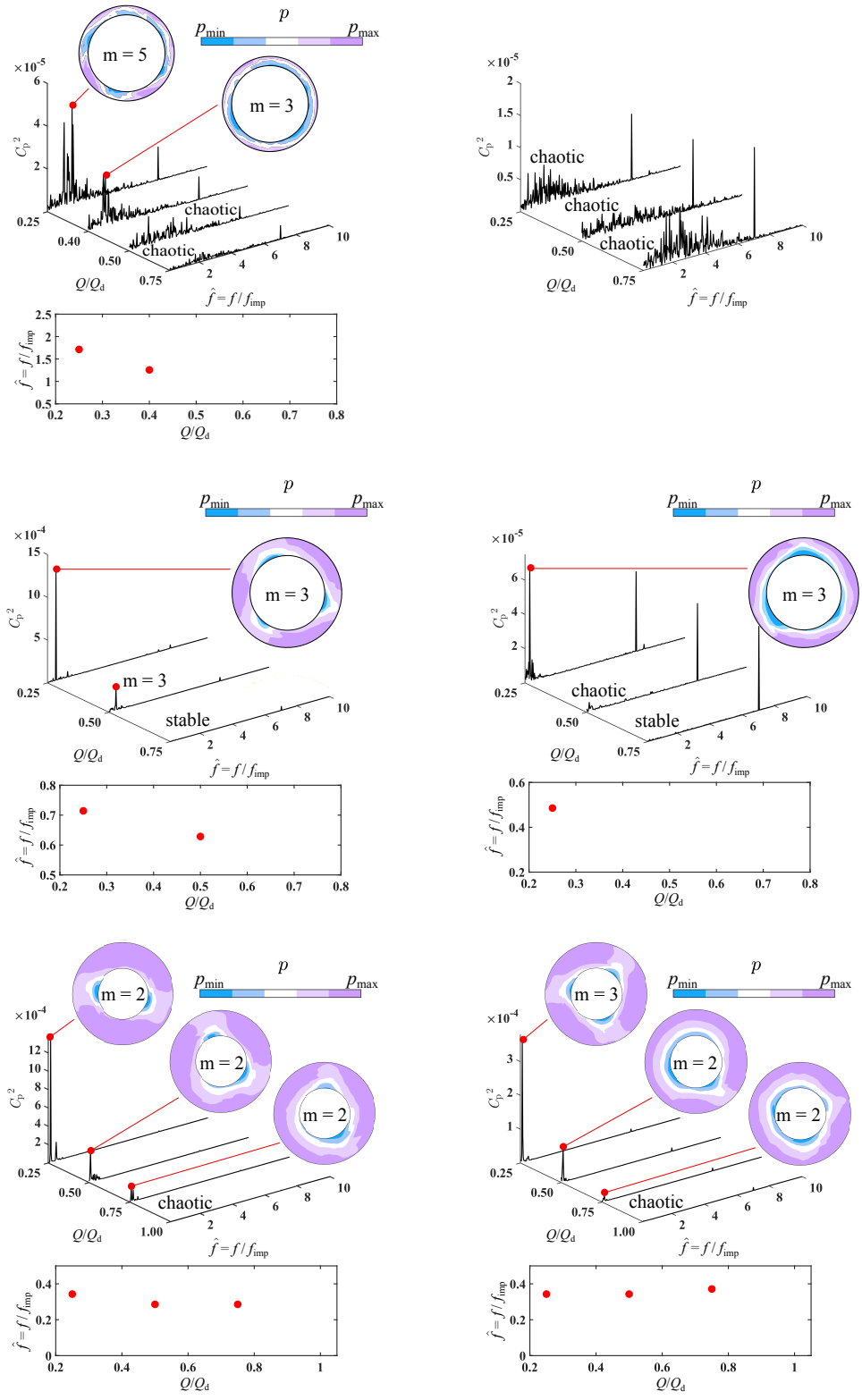

(a) zero-leakage inflow (b) positive-leakage inflow

Figure 3.35: Fourier analysis and stability diagram at low flow rates for $\Gamma = 1.25$ (top), $\Gamma = 1.5$ (middle), and $\Gamma = 2$ (bottom) with (a) zero-leakage and (b) positive-leakage inflow. The identified instabilities are pictured phase averaging the URANS in a reference frame rotating with the instability propagation velocity.

3.3.2.2 Effect of the radius ratio on the instability at low flow rate

Finally, the impact of the radial aspect ratio Γ on the instability occurring at low flow rates is examined. The instability characteristics for the zero-leakage case at $0.25Q_\mathrm{d}$ with different Γ are summarized firstly. For $\Gamma = 1.25$, four stall cells with a frequency $f_{\mathrm{stall},0.25Q_\mathrm{d},m=4}/f_\mathrm{imp} = 1.229$ are detected, rotating with an angular velocity $\omega_{\mathrm{stall},0.25Q_\mathrm{d},m=4}/\omega_\mathrm{imp} = 0.22$. For $\Gamma = 1.50$, three stall cells with a frequency $f_{\mathrm{stall},0.25Q_\mathrm{d},m=3}/f_\mathrm{imp} = 0.714$ are detected, rotating with an angular velocity $\omega_{\mathrm{stall},0.25Q_\mathrm{d},m=3}/\omega_\mathrm{imp} = 0.238$. For $\Gamma = 2.00$, two stall cells with a frequency $f_{\mathrm{stall},0.25Q_\mathrm{d},m=2}/f_\mathrm{imp} = 0.343$ are detected, rotating with an angular velocity $\omega_{\mathrm{stall},0.25Q_\mathrm{d},m=2}/\omega_\mathrm{imp} = 0.172$. These instabilities are considered to be mean core flow instabilities and are effectively captured by the model proposed by Tsujimoto *et al.* [1], as further demonstrated in the study by Fan *et al.* [2]. The stability diagrams for the three radius ratios were reconstructed by FFT (see Fig. 3.35) and the critical flow rate $Q_\mathrm{c}^{\mathrm{core-flow}}/Q_\mathrm{d}$ (the mean-core-flow instability occurs below this value) was determined. For $\Gamma = 1.25$ $Q_\mathrm{c}^{\mathrm{core-flow}}/Q_\mathrm{d} \in [0.4,\ 0.5]$, while for $\Gamma = 1.5$ $Q_\mathrm{c}^{\mathrm{core-flow}}/Q_\mathrm{d} \in [0.5,\ 0.75]$, and for $\Gamma = 2$ $Q_\mathrm{c}^{\mathrm{core-flow}}/Q_\mathrm{d} \in [0.75,\ 1]$ under zero-leakage inflow conditions (see Fig. 3.35(a)).

For the positive-leakage case, the entrained leakage flow still significantly affected the flow field for $\Gamma = 1.25$ at the low flow rate $0.25Q_\mathrm{d}$. The instability is suppressed resulting in a highly chaotic dynamic flow (see top panel in Fig. 3.35(b)). For $\Gamma = 1.50$, no qualitative difference is observed compared to the zero-leakage case. Three stall cells with a frequency $f_{\mathrm{stall},0.25Q_\mathrm{d},m=3}/f_\mathrm{imp} = 0.486$ are dected, rotating with an angular velocity $\omega_{\mathrm{stall},0.25Q_\mathrm{d},m=3}/\omega_\mathrm{imp} = 0.162$. However, when comparing the amplitudes of the FFTs, an evident quantitative difference is observed (see Fig. 3.35). This indicates that the leakage flow strongly reduced the amplitude of the core flow instability. Besides, the critical flow rate $Q_\mathrm{c}^{\mathrm{core-flow}}/Q_\mathrm{d}$ falls within the range of $Q_\mathrm{c}^{\mathrm{core-flow}}/Q_\mathrm{d} \in [0.25,\ 0.5]$ for $\Gamma = 1.5$ with positive-leakage inflow. For $\Gamma = 2.00$, three stall cells with a frequency $f_{\mathrm{stall},0.25Q_\mathrm{d},m=3}/f_\mathrm{imp} = 0.343$ are detected, rotating with an angular velocity $\omega_{\mathrm{stall},0.25Q_\mathrm{d},m=3}/\omega_\mathrm{imp} = 0.114$, which is qualitatively different from the zero-leakage case (three stall cells). The disparity observed can be elucidated by the linear stability analysis of the mean core flow model presented by Tsujimoto *et al.* [1]. In our previous publication [2], it was expounded that the modes $m = 2$, 3, and 4 all exhibit supercritical behavior at $Q/Q_\mathrm{d} = 0.25$. Once again, it is evident that the quantitative influence of the positive-leakage inflow condition on the instability amplitude is substantial, as seen by comparing the FFTs for $\Gamma = 2$ under zero-leakage (see Fig. 3.35(a)) and positive-leakage (see Fig. 3.35(b)) inflows conditions. The critical

flow rate Q_{c} remain within the range of $Q_{\mathrm{c}}^{\mathrm{core-flow}}/Q_{\mathrm{d}} \in [0.75,\ 1]$ for $\Gamma = 2$ under positive-leakage inflow conditions.

Chapter 4

Conclusions and future works

Contents

4.1 Conclusions

The flow field in a centrifugal pump was thoroughly investigated by combining theoretical modeling, URANS simulations, and experiments. An in-depth theoretical analysis has been carried out to shed some light on the mechanisms at the core of this instability. Employing the two-dimensional, inviscid model of Tsujimoto et al. [1], we demonstrated that the inception of the rotating stall is predicted by linear stability analysis, assuming that the flow is homogeneous in θ. However the 2D linear approach is unable to determine the dominant mode, and the non-linear interaction between different modes is also unsolved. Furthermore, by carrying out an energy budget analysis on the critical perturbation, we demonstrated for the first time that the low-flow rate instability is produced by the contribution of lift-up and flow deceleration mechanisms; moreover, we ruled out the hypothesis of a centrifugal-type mechanism as an origin for the rotating stall.

To understand the effect of inflow modulation in θ on the instability and the non-linear interaction between different instability modes, a 2D reduced-order simulation which considers a Fourier mode imposed to the inflow is performed. The results show good consistency with the 2D linear approach. The instabilities are all consistent with the 2D mean flow linear instability. At the same time, the inflow Fourier mode used to model the impeller wake can trigger some other unstable modes. However, whether these instabilities still result from the same mechanisms is not clear, more in-depth numerical studies need to be carried out to understand this.

Furthermore, to study the boundary layer effect on the instabilities, a reduced-order 3D model is also simulated. To obtain more realistic diffuser inlet boundary conditions, a modeling method is developed by fitting the diffuser inflow velocity derived from numerical simulations of the entire machine. The classic fitting methods used to approximate inflow profiles by algebraic polynomials or Gaussian functions are observed to introduce numerical artifacts that can significantly affect the flow and therefore its stability. The multi-stage scale-matching fitting approach developed in this study is designed as a robust successive-order approximation of the inflow conditions, which allows us to precisely predict the flow instability occurring in the pump diffuser. Two different instability mechanisms are derived from this stage, one is the low-flow rate mean flow instability which can be correctly predicted by the 2D linear stability analysis, and another one is associated with the jet-wake inflow. For the latter one, the instability mechanism has been traced back to the two-dimensional jet-

wake instability reported by Ljevar et al., verifying that we get a parametric onset of the instability as well as a wave number consistent with their predictions. This is the first time such an unexpected rotating instability is reported to occur in a 3D vaneless diffuser at a large flow rate $Q > Q_{\mathrm{D}}$.

Finally, the 3D simulation for the entire pump is carried out. The leakage effect produced by a radial gap between the impeller and the vaneless diffuser is first investigated. Hence, three geometries have been considered: (i) a zero-leakage case (ideal case commonly simulated in the literature), a positive-leakage case (corresponding to our experimental facility), and (iii) a negative-leakage case (most commonly employed in industrial applications). The numerical simulations have first been validated by comparing them with corresponding experiments. The URANS-predicted pump and diffuser performances are in very good agreement with the experimental measurements, with a maximum error of about 5% observed for the zero- and positive-leakage cases. Moreover, the onset and features of the low-flow rate rotating stall observed in the experiments have been reproduced by our URANS simulations. The validated numerical tool has, therefore, been used to investigate more in-depth the rotating instabilities occurring in the vaneless diffuser for the three aforementioned configurations, taking the ideal case (i.e., the zero-leakage case) as a reference.

The 3D entire pump simulation result shows that the large flow rate jet-wake instability which we identified in the reduced-order 3D simulation still exists in the real pump model. Such rotating instability has a major impact on the mean flow, and it is responsible for a large separation region on the diffuser hub. As a result, the diffuser performance significantly degrades. Moreover, by means of dedicated wavelet analysis, we identified a secondary instability pulsating in the reference frame of the primary rotating stall and migrating from the shear layer of the impeller wake to the diffuser outlet. To the best of the authors' knowledge, this secondary instability has been reported in our study for the first time in a vaneless diffuser of a centrifugal pump. The same rotating stall has been found for the negative-leakage case at the design flow rate; however, the disturbance due to the entrainment of the leakage flow was strong enough to almost totally disrupt the secondary instability, even if a clear signature of it remains in the wavelet analysis. On the contrary, when a positive-leakage case is considered, the modification to the jet-wake angle brings the flow into the stable regime, and no rotating stall is observed. This is in agreement with the prediction of the two-dimensional model of Ljevar et al., and it is confirmed by our experiments. A corresponding suppression of the separation region over the diffuser hub is observed, leading to a significant increase in the diffuser performance

(also confirmed by our experiments). This leads to the conclusion that even small radial gaps between the impeller and the diffuser, as the 1% gap we consider, can significantly affect the flow as also pointed out in other studies of turbomachinery configurations, and they must be included in the pump design when numerical shape optimization is performed.

Moreover, we found the mean flow instability for $\mathrm{Q} < 0.65 Q_{\mathrm{d}}$. This low-flow rate rotating stall has been previously reported in the literature by several authors (see, e.g., Dazin et al. [39, 10]), and a good agreement is found also in terms of the instability onset (Barrand et al. reports an onset at $\mathrm{Q} = 0.6 Q_{\mathrm{d}}$). The rotating stall has been characterized numerically for our three leakage configurations, and good qualitative and quantitative agreement was demonstrated in comparison with the PIV measurements reported in the literature and with the FFT and wavelet analysis performed in our experiments. Furthermore, by arbitrarily scaling the critical perturbation and superposing it to the basic state of Tsujimoto's model, it has been shown a remarkably good agreement with our URANS phase-averaged results for supercritical conditions. This supports the conclusion that the rotating stall emerges from a core-flow instability, and it does not get significantly influenced by the presence of the turbulent boundary layers on the shroud and on the hub of the diffuser. We point out that, even though both the rotating stalls are core flow instabilities, they are essentially different because the low-flow rate stall does not require a jet-wake inflow, but it rather relies on the skewness of the flow at the diffuser inlet.

To study the effect of the radial aspect ratio Γ on the instability characteristics, the radial aspect ratio varies in the range $\Gamma \in \{1.25, 1.5, 2\}$ and adjusting the constant cross-sectional aspect ratio as $\Lambda = 2(\Gamma - 1) \times 3.325$. For $\Gamma = 1.50$, we first reported that the jet-wake instability occurs at a large flow rate ($Q/Q_{\mathrm{d}} \gtrsim 1$) triggering a secondary instability. For the zero-leakage case (idealized inflow conditions), the primary 7-periodic instability pattern is there for $\Gamma = 1.25$. However, the secondary pulsating instability detected for $\Gamma = 1.5$ does not occur for $\Gamma = 1.25$. As the radial aspect ratio Γ increases to $\Gamma = 2$, non-linear effects take over and a complex chaotic regime hinders the quasi-periodic pattern observed with the other two smaller radial aspect ratios. For the positive-leakage inflow, the flow field for $\Gamma = 1.25$ is always chaotic under the effect of leakage flow. As Γ increased to $\Gamma = 1.5$, we found the 7-periodic jet-wake instability patterns as observed for zero-leakage case. Additionally, two 1-periodic instability patterns propagate with the same propagation velocity but in opposite directions in a reference frame rotating with Ω, owing to the leakage flow (see Fan *et al.* [60]). For $\Gamma = 2$, a 4-

periodic steady Kelvin-Helmholtz instability is reported for the first time. Concerning the well-known low-flow-rate ($Q/Q_d \lesssim 0.65$) mean core-flow instability, its characteristics are significantly affected by the radius aspect ratio Γ, especially in terms of the wave number, that passes from 4 to 3 and then to 2 for $\Gamma = 1.25$, 1.5, and 2, respectively. Besides, the instability mode number and propagation velocity are also found to be very sensitive to the inlet leakage flow for $\Gamma = 2$. For short diffusers ($\Gamma = 1.25$), they are more stable than other diffusers which is well agreed with the linear stability analysis results. Moreover, the leakage flow results in an increment of the inlet flow angle. Hence, the instability is entirely suppressed.

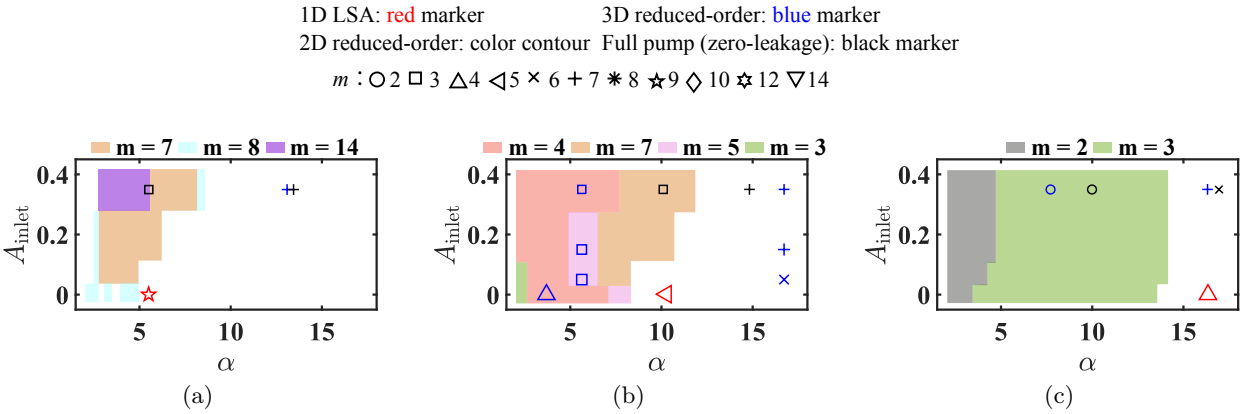

Figure 4.1: Instability characteristics of the flow in the diffuser obtained by different approaches for 3 different radius ratios: (a) $\Gamma = 1.25$, (b) $\Gamma = 1.50$, (c) $\Gamma = 2.00$.

To support the conclusions, we further summarize a part of our results in Fig. 4.1 that depicts the stability boundaries in the parametric space, highlighting the nature of the instabilities identified by different approaches.

4.2 Future works

Various avenues for furthering the research work developed in this manuscript are detailed below. First, it will be interesting to perform numerical simulations for the reduced-order 2D and 3D models with new inflow boundary conditions, e.g. nonmodal inlet wakes employed by Levjar et al. [26]. This can help to further understand how the inlet boundary condition can affect the instability and clarify if the instability is mainly due to 3D effects or to a 2D mechanism. Then, a further inspection of the Kelvin-Helmholtz instability observed in the 3D simulation results with $\Gamma = 2.00$ could confirm

the supposed instability mechanism. Then, we can characterize the components of the energy budget leading to a transfer of energy from the two-dimensional basic state to the jet-wake perturbation. Finally, several upgrades to the test bench can be proposed. The first one could be the test of diffusers with different radius ratios to confirm the numerical results. The second one could be to modify the inlet leakage condition. A last modification could be the installation of an inlet flow control valve. This will allow us to make more continuous experimental measurements and more qualitative and quantitative comparisons between experimental and numerical results.

Bibliography

[1] Y. Tsujimoto, Y. Yoshida, Y. Mori, Study of vaneless diffuser rotating stall based on two-dimensional inviscid flow analysis, Journal of Fluids Engineering 118 (1) (1996) 123–127.

[2] M. Fan, A. Dazin, G. Bois, F. Romanò, Effect of inlet leakage flow on the instability in a radial vaneless diffuser, Physics of Fluids 35(1) (2023) 014105.

[3] S.-M. Diga, N. Diga, P.-M. Mircea, M.-S. Nicolae, I. Mircea, Modern aspects of analysis of the efficient operation of the centrifugal pumps within the hydropower facilities with pumped storage, in: 2023 13th International Symposium on Advanced Topics in Electrical Engineering (ATEE), IEEE, 2023, pp. 1–4.

[4] A. Bednarz, K. Kabalyk, R. Jakubowski, R. Bartłomowicz, Numerical study on sensitivity of turbofan engine performance to blade count of centrifugal compressor impeller, Energies 16 (14) (2023) 5251.

[5] M. Jabłońska, W. Jurczak, D. Ozimina, M. Adamiak, Increasing the operational reliability of a ship by using a composite impeller in the event of hydrophore pump failure., Maintenance & Reliability/Eksploatacja i Niezawodnosc 25 (1) (2023).

[6] V. Almeida, G. Dei Agnoli, O. Pinheiro, F. Feitosa, Analysis of high frequency noise sources on air conditioning variable speed compressors, in: INTER-NOISE and NOISE-CON Congress and Conference Proceedings, Vol. 265, Institute of Noise Control Engineering, 2023, pp. 32–43.

[7] L. Mongeau, D. Thompson, D. McLaughlin, Sound generation by rotating stall in centrifugal turbomachines, Journal of Sound and Vibration 163 (1) (1993) 1–30.

[8] P. Silvestri, S. Marelli, V. Usai, Experimental investigation on the vibrational and fluid dynamics behaviour of a turbocharger compressor in the transition to surge operation, in: E3S Web of Conferences, Vol. 414, EDP Sciences, 2023, p. 02016.

[9] Z. Zhao, W. Song, Y. Jin, L. He, Numerical study on flow stall and kinetic energy conversion of low-specific-speed centrifugal pump, Physics of Fluids 35 (4) (2023).

[10] A. Dazin, G. Cavazzini, G. Pavesi, P. Dupont, S. Coudert, G. Ardizzon, G. Caignaert, G. Bois, High-speed stereoscopic piv study of rotating instabilities in a radial vaneless diffuser, Experiments in fluids 51 (2011) 83–93.

[11] E. G. Ferrara, Characterization of vaneless diffuser rotating stall on centrifugal compressors for industrial applications, Ph.D. thesis, University of Florence, Florence, Italy (2013).

[12] S. Li, G. Yu, J. Chen, X. Gui, Y. Chang, C. Han, W. Zhu, J. Yin, Y. Zhang, Aerodynamic design and experimental study of small flow rate centrifugal compressor, in: Journal of Physics: Conference Series, Vol. 2551, IOP Publishing, 2023, p. 012024.

[13] E. Sundström, Flow instabilities in centrifugal compressors at low mass flow rate, Ph.D. thesis, Kungliga Tekniska högskolan (2017).

[14] J. T. Gravdahl, Modeling and control of surge and rotating stall in compressors, Ph.D. thesis, Norwegian University of Science and Technology, Trondheim, Norway (1998).

[15] J. J. N. Everitt, Investigation of stall inception in centrifugal compressors using isolated diffuser simulations, Ph.D. thesis, Massachusetts Institute of Technology (2010).

[16] H. Mohtar, Increasing surge margin of turbocharger centrifugal compressor automotive application, Ph.D. thesis, Ecole Centrale de Nantes (ECN) (2010).

[17] A. Engeda, Experimental and numerical investigation of the performance of a 240 kw centrifugal compressor with different diffusers, Experimental thermal and fluid Science 28 (1) (2003) 55–72.

[18] Y. Heng, A. Dazin, M. N. Ouarzazi, Q. Si, A study of rotating stall in a vaneless diffuser of radial flow pump, Journal of Hydraulic Research 56 (4) (2018) 494–504.

[19] W. Jansen, Rotating stall in a radial vaneless diffuser, Journal of Fluids Engineering 86 (4) (1964) 750–758.

[20] Y. Senoo, Y. Kinoshita, Influence of inlet flow conditions and geometries of centrifugal vaneless diffusers on critical flow angle for reverse flow, Journal of Fluids Engineering 99 (1) (1977) 98–102.

[21] Y. Senoo, Y. Kinoshita, M. Ishida, Asymmetric flow in vaneless diffusers of centrifugal blowers, Journal of Fluids Engineering 99 (1) (1977) 104–111.

[22] P. Frigne, R. Van den Braembussche, A theoretical model for rotating stall in the vaneless diffuser of a centrifugal compressor, journal of engineering for gas turbines and power 107 (2) (1985) 507–513.

[23] H.-S. Dou, S. Mizuki, Analysis of the flow in vaneless diffusers with large width-to-radius ratios, Journal of Turbomachinery 120 (1) (1998) 193–201.

[24] A. Abdelhamid, W. Colwill, J. Barrows, Experimental investigation of unsteady phenomena in vaneless radial diffusers, journal of engineering for gas turbines and power 101 (1) (1979) 52–59.

[25] F. Moore, Theory of finite disturbances in a centrifugal compression system with a vaneless radial diffuser, in: Turbo Expo: Power for Land, Sea, and Air, Vol. 78989, American Society of Mechanical Engineers, 1991, p. V001T01A030.

[26] S. Ljevar, H. De Lange, A. Van Steenhoven, Two-dimensional rotating stall analysis in a wide vaneless diffuser, International journal of rotating machinery 2006 (2006).

[27] E. Maskell, Flow separation in three dimensions, RAE Report No. Aero 2565 (1955).

[28] A. Abdelhamid, Effects of vaneiess diffuser geometry on flow instability in centrifugal compression systems, in: Turbo Expo: Power for Land, Sea, and Air, Vol. 79610, American Society of Mechanical Engineers, 1981, p. V001T03A008.

[29] H. Tsurusaki, K. IMAICHI, R. MIYAKE, A study on the rotating stall in vaneless diffusers of centrifugal fans (1st report, rotational speeds of stall cells, critical inlet flow angle): fluids engineering, JSME international journal 30 (260) (1987) 279–287.

[30] G. Ferrara, L. Ferrari, L. Baldassarre, Rotating stall in centrifugal compressor vaneless diffuser: experimental analysis of geometrical parameters influence on phenomenon evolution, International Journal of Rotating Machinery 10 (6) (2004) 433–442.

[31] M. Ötügen, R. So, B. Hwang, Diffuser stall and rotating zones of separated boundary layer, Experiments in Fluids 6 (1988) 521–533.

[32] M. Ishida, D. Sakaguchi, H. Ueki, Suppression of rotating stall by wall roughness control in vaneless diffusers of centrifugal blowers, Journal of Turbomachinery 123 (1) (2001) 64–72.

[33] Y. Zhu, S. Sjolander, Effect of geometry on the performance of radial vaneless diffusers, Journal of Turbomachinery 109 (4) (1987) 550–556.

[34] Y. Yoshida, Y. Murakami, Y. Tsujimoto, H. Tsurusaki, Rotating stalls in centrifugal-impeller/vaned diffuser systems; 1st report, experiment. enshin haneguruma-vane tsuki diffuser kei ni shojiru senkai shissoku; dai ippo, jikken, Nippon Kikai Gakkai Ronbunshu, B Hen (Transactions of the Japan Society of Mechanical Engineers, Part B);(Japan) 56 (530) (1990).

[35] T. Sano, Y. Yoshida, Y. Tsujimoto, Y. Nakamura, T. Matsushima, Numerical study of rotating stall in a pump vaned diffuser, Journal of Fluids Engineering 124 (2) (2002) 363–370.

[36] S. SUZUKI, Y. UGAI, H. HARADA, Noise characteristics in partial discharge of centrifugal fans: 1st report, low-frequency noise due to the rotating stall, Bulletin of JSME 21 (154) (1978) 689–696.

[37] G. Caignaert, B. Desmet, D. Stevenaert, Experimental investigations on the flow in the impeller of a centrifugal fan, in: Turbo Expo: Power for Land, Sea, and Air, Vol. 79566, American Society of Mechanical Engineers, 1982, p. V001T01A013.

[38] A. Cellai, G. Ferrara, L. Ferrari, C. Mengoni, L. Baldassarre, Experimental investigation and characterization of the rotating stall in a high pressure centrifugal compressor: Part iii—influence of diffuser geometry on stall inception and performance (2nd impeller tested), in: Turbo Expo: Power for Land, Sea, and Air, Vol. 36894, 2003, pp. 711–719.

[39] A. Dazin, O. Coutier-Delgosha, P. Dupont, S. Coudert, G. Caignaert, G. Bois, Rotating instability in the vaneless diffuser of a radial flow pump, Journal of Thermal Science 17 (2008) 368–374.

[40] G. Pavesi, A. Dazin, G. Cavazzini, G. Caignaert, G. Bois, G. Ardizzon, Experimental and numerical investigation of unforced unsteadiness in a vaneless radial diffuser, in: Proceedings of 12th European Conference on Turbomachinery Fluid dynamics & Thermodynamics, EUROTURBO, 2011, pp. ETC2011–262.

[41] Y. G. Heng, A. Dazin, M. N. Ouarzazi, Linear stability analysis of rotating stall in a wide vaneless diffuser, in: 12th European Conference on Turbomachinery Fluid Dynamics and Thermodynamics, ETC, 2017, pp. ETC2017–301.

[42] D. Sakaguchi, M. Ishida, H. Ueki, Z. Sun, Suppression of rotating stall in vaneless diffuser by wall roughness control, Nihon Kikai Gakkai Ronbunshu, B Hen/Transactions of the Japan Society of Mechanical Engineers, Part B 66 (648) (2000) 2101–2108.

[43] S. A. Ahmed, Control of stall in a radial diffuser using rough surfaces, Canadian Aeronautics and Space Journal 54 (1) (2008) 9–15.

[44] J. Kurokawa, S. L. Saha, J. Matsui, T. Kitahora, Passive control of rotating stall in a parallel-wall vaneless diffuser by radial grooves, Journal of Fluids Engineering 122 (1) (2000) 90–96.

[45] C. Gao, C. Gu, T. Wang, B. Yang, Passive control of rotating stall in vaneless diffuser with radial grooves: detailed numerical study, in: Turbo Expo: Power for Land, Sea, and Air, Vol. 48883, 2009, pp. 1225–1233.

[46] H. Tsurusaki, T. Kinoshita, Flow control of rotating stall in a radial vaneless diffuser, Journal of Fluids Engineering 123 (2) (2001) 281–286.

[47] M. Fan, A. Dazin, F. Romano, G. Bois, Effect of leakage on the performance of the vaneless diffuser of a centrifugal pump model, Conference on Modelling Fluid Flow (CMFF'22), Budapest, Hungary (2022) 51–58.

[48] G. Wuibaut, G. Bois, P. Dupont, G. Caignaert, M. Stanislas, PIV Measurements in the Impeller and the Vaneless Diffuser of a Radial Flow Pump in Design and Off-Design Operating Conditions, Journal of Fluids Engineering 124 (3) (2002) 791–797.

[49] L. Gibson, L. Galloway, S. Spence, Assessment of turbulence model predictions for a centrifugal compressor simulation, Journal of the Global Power and Propulsion Society 1 (2017) 142–156.

[50] I. Chalghoum, H. Kanfoudi, S. Elaoud, M. Akrout, R. Zgolli, Numerical modeling of the flow inside a centrifugal pump: Influence of impeller–volute interaction on velocity and pressure fields, Arabian journal for science and engineering 41(11) (2016) 4463–4476.

[51] O. Borm, H. P. Kau, Unsteady aerodynamics of a centrifugal compressor stage: Validation of two different cfd solvers, In Turbo Expo: Power for Land, Sea, and Air 44748 (2012) 2753–2764.

[52] J. H. Kim, J. H. Choi, K. Y. Kim, Design optimization of a centrifugal compressor impeller using radial basis neural network method, In Turbo Expo: Power for Land, Sea, and Air 48883 (2009) 443–451.

[53] M. Asuaje, F. Bakir, S. Kouidri, F. Kenyery, R. Rey, Numerical modelization of the flow in centrifugal pump: volute influence in velocity and pressure fields, International journal of rotating machinery 3 (2005) 244–255.

[54] F. R. Menter, Ten years of industrial experience with the sst turbulence model, Turbulence, heat and mass transfer 4 (2003) 625–632.

[55] F. Cenci, A. L. C. Fujarra, Urans simulation: Numerical study of flow around a two-dimensional circular cylinder, Proceedings of the XXXVIII Iberian Latin-American Congress on Computational Methods in Engineering (2017).

[56] S. K. PERAVALI, Investigation of effective wake scaling for unconventional propellers, Gothenburg: Chalmers University of Technology (2015).

[57] C. Hu, C. Yang, X. Shi, R. Zou, L. Liu, H. Chen, Investigation of rotating stall in radial vaneless diffusers with asymmetric inflow, Aerospace Science and Technology 96 (2020) 105546.

[58] M. Fan, A. Dazin, G. Bois, F. Romanò, Instabilities identification based on a new centrifugal 3d impeller outflow model, Aerospace Science and Technology (2023) 108466.

[59] F. Romanò, Stability of generalized kolmogorov flow in a channel, Physics of Fluids 33 (2) (2021) 024106.

[60] M. Fan, A. Dazin, G. Bois, F. Romanò, Instabilities in a turbulent swirling source flow between parallel rings, Physics of Fluids 35(10) (2023) 101701.

[61] J. Barrand, G. Caignaert, R. Canavelis, Experimental determination of the reverse flow onset in a centrifugal impeller., In Proceedings of the 1st International Pump Symposium. Turbomachinery Laboratories, Department of Mechanical Engineering, Texas A&M University. (1984).

[62] M. Fan, A. Dazin, G. Bois, F. Romanò, Effect of radius ratio on the instabilities in a turbulent swirling source flow between parallel rings, European Journal of Mechanics - B/Fluids (under review) (09 2023).

Appendix A

Turbulence model independence analysis

The appropriate selection of turbulence model is crucial, therefore four turbulence models available in OpenFOAM (standard $k-\epsilon$, realizable $k-\epsilon$, standard $k-\omega$, and $k-\omega$ SST models) are here evaluated. As our study focuses on the boundary layers of the vaneless diffuser, we have excluded the standard $k-\epsilon$ model because it requires $y^+ > 30$, which would result in the entire boundary layer on the parallel plates being included within a single computational cell, causing over-diffused boundary layers. Therefore, the evaluation of turbulence models is limited to three options: the realizable $k-\epsilon$, the standard $k-\omega$, and the $k-\omega$ SST models.

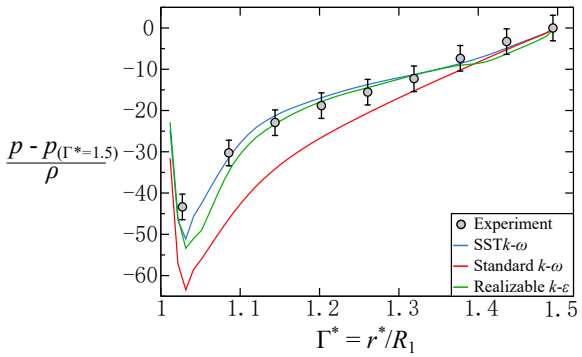

Figure A.1: Azimuthally-averaged pressure rise measured at the top ring along the radial coordinate $\Gamma^* = r^* - R_1$, where r^* is a dimensional quantity. The experimental measurements of [2] are depicted by the gray bullets and the corresponding error bars. The numerical results are shown in red ($k-\omega$), blue ($k-\omega$ SST), and green (realizable $k-\epsilon$). The simulations refer to $\alpha_Q = 1$ for the realistic inflow conditions.

Fig. A.1 depicts a comparison between the experimental measurements from Fan et al. [2] and the corresponding azimuthally-averaged static pressure p obtained from numerical simulations for the positive-leakage case with the three turbulence models mentioned earlier. The measurements

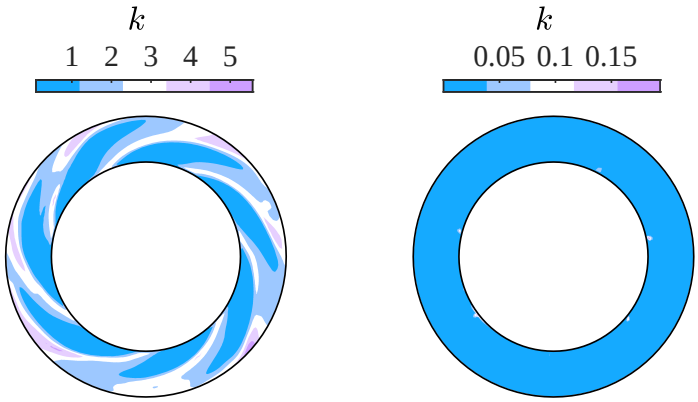

(a) (b)

Figure A.2: Turbulent kinetic energy at mid-height produced by the $k-\omega$ SST (a), and the realizable $k-\epsilon$ (b) models at $\alpha_Q = 1$ for the realistic case.

were taken along the shroud wall of the diffuser at the design flow rate Q_d. The results show that the standard $k-\omega$ model over-predicts the average pressure drop at the diffuser inlet and the radial pressure gradient throughout the diffuser. In view of the adverse pressure gradient being an important feature of the flow in the diffuser, the standard $k-\omega$ model is not suitable for our URANS simulation. On the other hand, both the realizable $k-\epsilon$ and $k-\omega$ SST models give comparable results that agree well with the experimental measurements.

As the standard $k-\omega$ model is excluded, a comparison of the turbulent kinetic energy k at the mid-height of the diffusers is compared between the $k-\omega$ SST and realizable $k-\epsilon$ model as shown in Fig. A.2. The results show that the realizable $k-\epsilon$ model does not work well, even at the diffuser inlet, where the inflow condition ought to produce the highest k. In fact, the realizable $k-\epsilon$ model predicts k at a very low level. On the other hand, the results obtained from the $k-\omega$ SST model are coherent, in agreement with the anticipated seven-jet wake introduced at the diffuser inlet.

Appendix B

Instability characteristics obtained from reduced-order models

B.1 Instability characteristics obtained from 2D reduced-order model

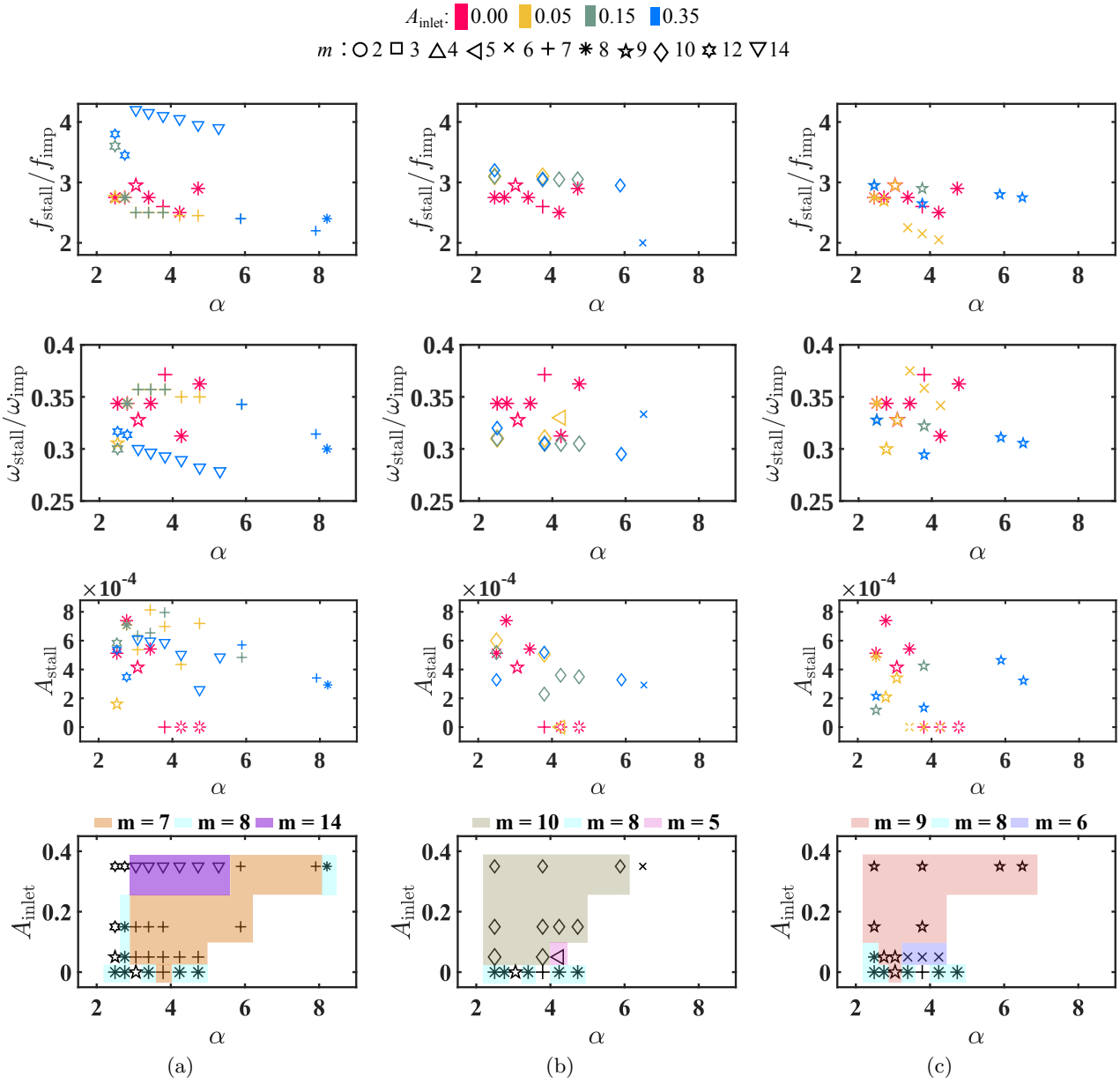

Figure B.1: Instability characteristics of the flow in the diffuser of radius ratio $\Gamma = 1.25$ with 3 different periodic of inflow Fourier mode m_{F}: (a) $m_{\text{F}} = 7$, (b) $m_{\text{F}} = 5$, (c) $m_{\text{F}} = 3$.

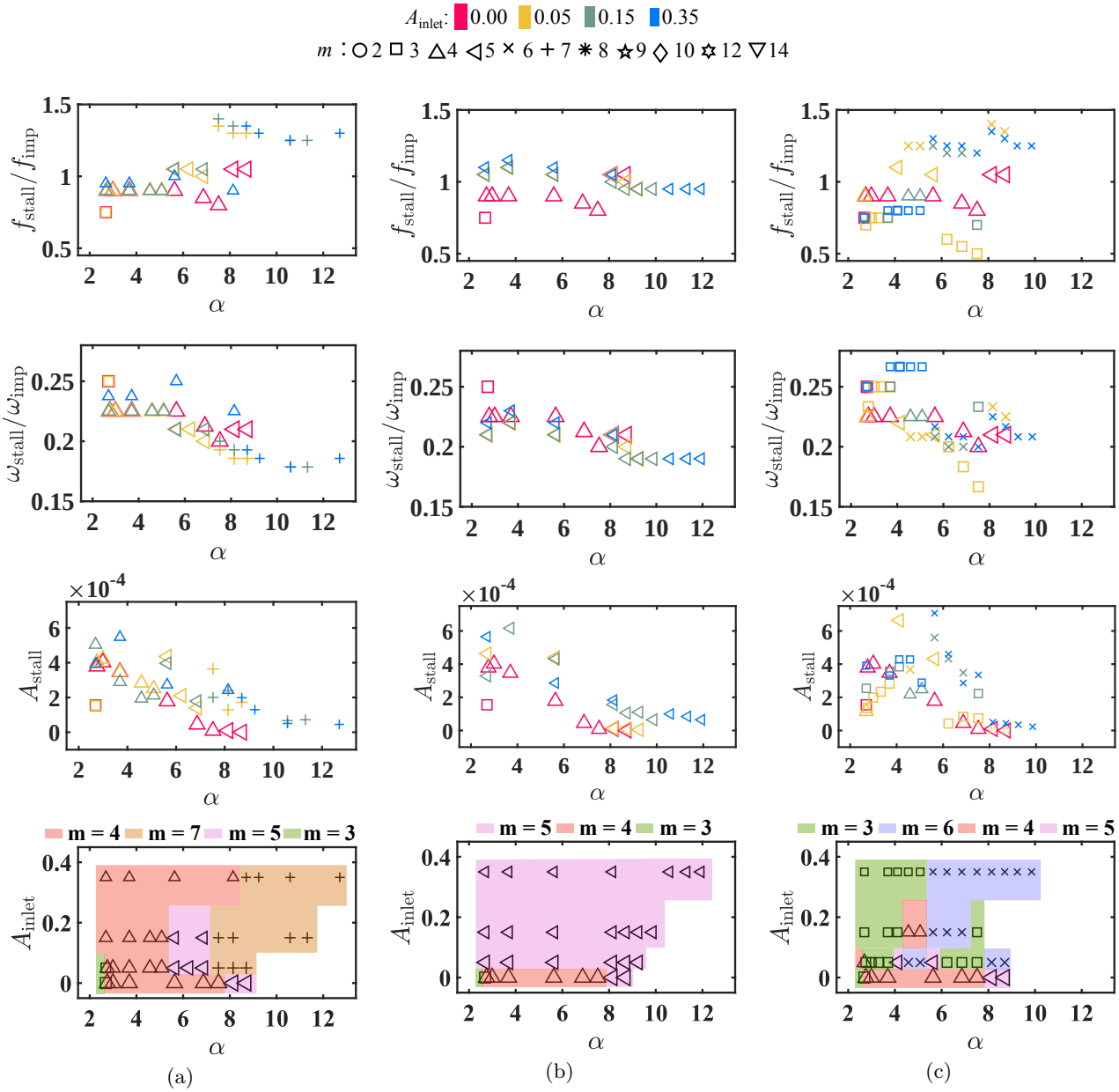

Figure B.2: Instability characteristics of the flow in the diffuser of radius ratio $\Gamma = 1.50$ with 3 different periodic of inflow Fourier mode m_F: (a) $m_F = 7$, (b) $m_F = 5$, (c) $m_F = 3$.

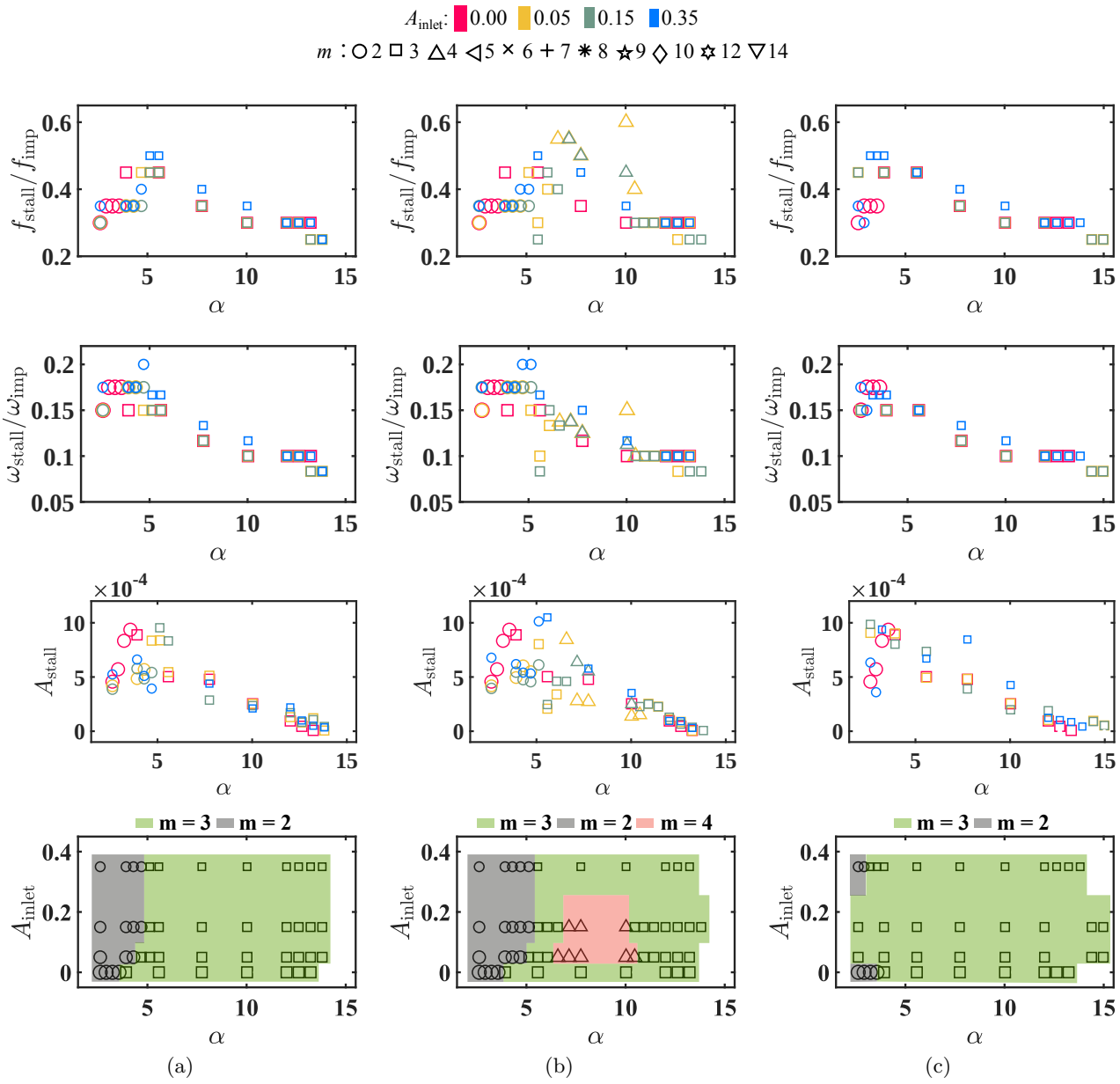

Figure B.3: Instability characteristics of the flow in the diffuser of radius ratio $\Gamma = 2.00$ with 3 different periodic of inflow Fourier mode m_{F}: (a) $m_{\text{F}} = 7$, (b) $m_{\text{F}} = 5$, (c) $m_{\text{F}} = 3$.

B.2 Instability characteristics obtained from 3D reduced-order model

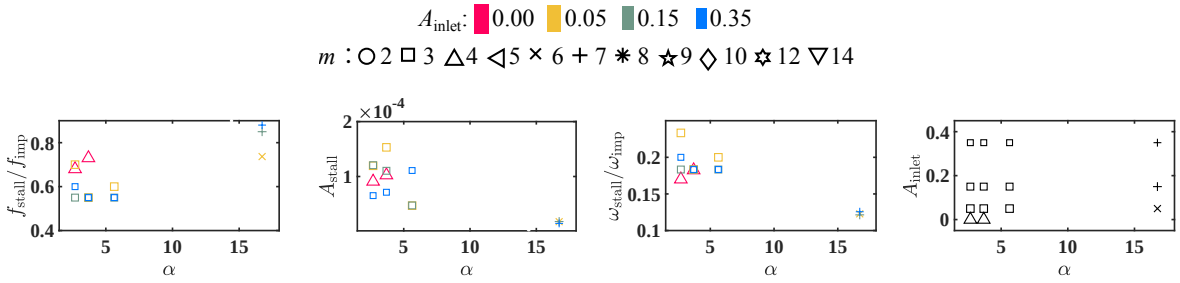

(a) (b) (c) (d)

Figure B.4: (a) Instability frequency f_{stall}, (b) amplitudes A_{stall}, (c) propagation velocity ω_{stall}, and (d) mode map of the flow in the vaneless diffuser of $\Gamma = 1.50$ with zero-leakage inflow profile with 4 different amplitude A_{F} of inflow Fourier modes.

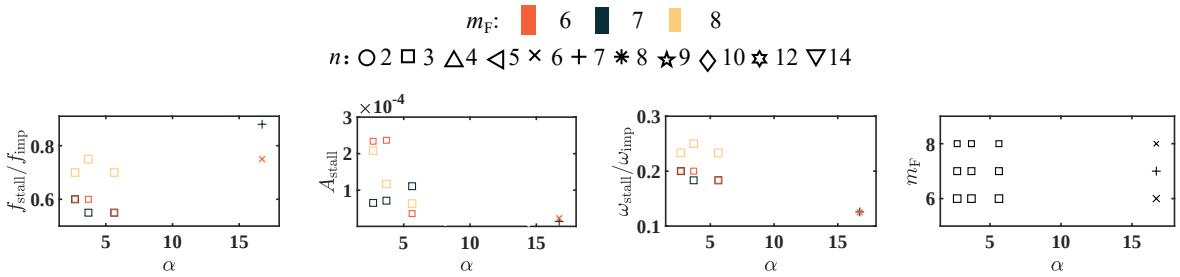

(a) (b) (c) (d)

Figure B.5: (a) Instability frequency f_{stall}, (b) amplitude A_{stall}, (c) propagation velocity ω_{stall}, and (d) mode map of the flow in the vaneless diffuser of $\Gamma = 1.50$ with zero-leakage inflow profile with 3 different inflow Fourier mode number with the amplitude $A_{\text{inlet}} = 0.35$.

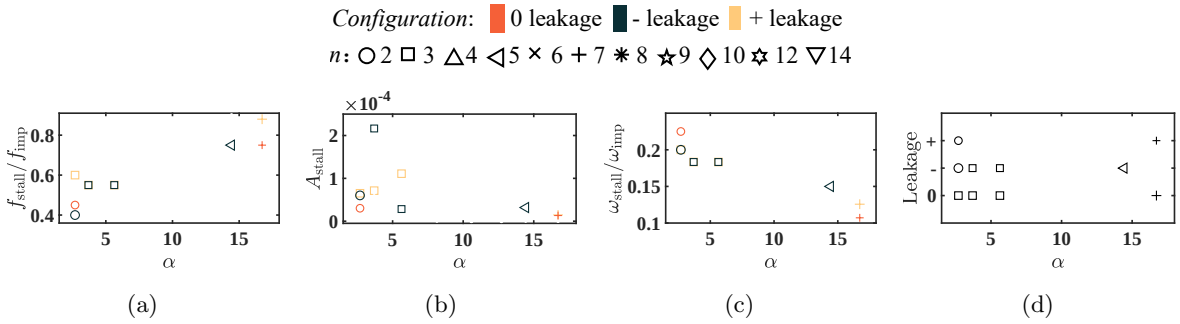

Figure B.6: (a) Instability frequency f_{stall}, (b) amplitude A_{stall}, (c) propagation velocity ω_{stall}, and (d) mode map of the flow in the vaneless diffuser of radius ratio $\Gamma = 1.50$ with 3 different mean inflow profiles with mode-7 inflow Fourier mode with amplitude $A_{\text{inlet}} = 0.35$.

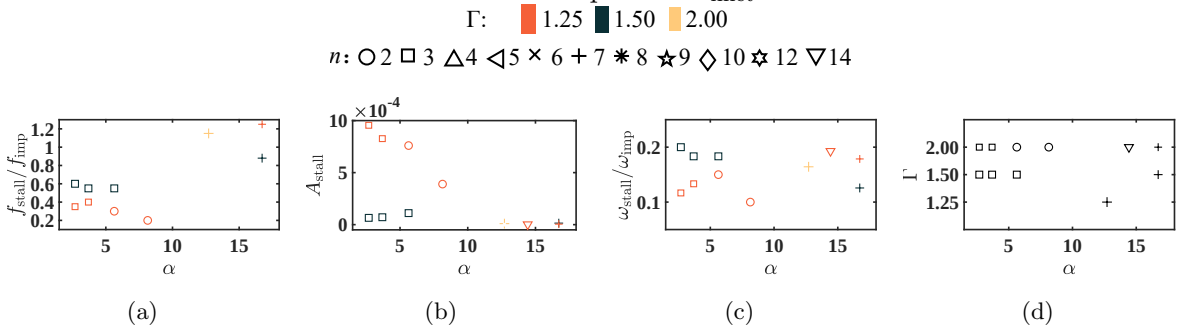

Figure B.7: (a) Instability frequency f_{stall}, (b) amplitude A_{stall}, (c) propagation velocity ω_{stall}, and (d) mode map of the flow in the vaneless diffuser of 3 different diffuser radius ratio Γ with zero-leakage inflow profile with mode-7 inflow Fourier mode with amplitude $A_{\text{inlet}} = 0.35$.

Appendix C

Appended papers

C.1 Paper A

"Effect of leakage on the performance of the vaneless diffuser of a centrifugal pump model",

M. Fan, A. Dazin, F. Romanò, G. Bois,

CMFF'22 (2022), 51–58.

Conference on Modelling Fluid Flow (CMFF'22)
The 18th International Conference on Fluid Flow Technologies
Budapest, Hungary, August 30-September 2, 2022

EFFECT OF LEAKAGE ON THE PERFORMANCE OF THE VANELESS DIFFUSER OF A CENTRIFUGAL PUMP MODEL

Meng FAN[1], Antoine DAZIN[1], Francesco ROMANO[1], Gérard BOIS[1]

[1] Univ. Lille, CNRS, ONERA, Arts et Métiers Institute of Technology, Centrale Lille, UMR 9014-LMFL-Laboratoire de Mécanique des Fluides de Lille - Kampé de Fériet, F-59000, Lille, France

ABSTRACT

An analysis of a pump vaneless diffuser model is presented with a particular focus on the leakage effect between the impeller outlet and diffuser inlet section. RANS and URANS simulations are conducted for three different leakage configurations. The $k-\omega$ SST turbulence model is used, carrying out the simulation by the open-source software OpenFOAM. Results obtained for each numerical configuration are analyzed and discussed. Comparison with experimental results corresponding to one of the tested configurations is also presented. They show that the leakage flow slightly influences the overall pump performance and more specifically the vaneless diffuser one. When considering the real flow rate obtained by CFD, including leakage effects, comparison with the experimental results get closer both for the overall pump and for the vaneless diffuser performances. A special focus on the instability onset in the vaneless diffuser is also proposed for each leakage configuration which leads to selecting the best way to reproduce experimental behavior from an adequate CFD approach and correct boundary conditions.

Keywords: numerical simulation, performance, instability

NOMENCLATURE

δ	$[-]$	relative error
Δp	$[Pa]$	pressure difference
ν_T	$[-]$	eddy viscosity
ω_{imp}	$[rad/s]$	angular velocity
ρ	$[kg/m^3]$	air density
b	$[m]$	diffuser width
H_b	$[m]$	outflow domain height
L	$[m]$	radial gap value
N	$[rpm]$	rotational speed
p	$[Pa]$	static pressure
Q	$[m^3/s]$	pump flow rate
Q_d	$[m^3/s]$	pump design flow rate
R	$[m]$	radius
Re	$[-]$	pump Reynolds number
Z	$[-]$	number of blades

Subscripts

1	impeller inlet
2	impeller outlet
3	diffuser inlet
4	diffuser outlet
C	centrifugal pump
D	diffuser
$D1$-$D9$	related to the nine evenly distributed probes along the radial direction over the shroud side of the diffuser
I	impeller
$S1$-$S4$	related to the probes placed at $\theta = 0,\ \pi/2,\ \pi,\ 3\pi/2$ on the inlet pipe

1. INTRODUCTION

Centrifugal pumps are widely used in many domains such as irrigation, water supply, cooling systems, and pumping stations. However, the operating range of pumps is affected by the occurrence of unstable phenomena. Among them, rotating stall can affect the vaneless diffuser of the pump when operating at a partial flow rate. This has been already described and analyzed by several authors in radial flow pumps and compressors like Jansen et al. [1, 2], Senoo et al. [3], Fringe et al. [4], and Sundström et al. [5]. Even if this phenomenon is now well described, the effect of the leakage flow at diffuser inlet on the rotating stall onset and dynamic has never been investigated. Detailed information on the pump model geometry can be found in Wuibaut et al. [6]. This model set-up uses air as working fluid and its dimensions are determined using similarity laws parameters, i.e same specific speed and specific radius of the initial pump working with water. To get a sufficiently high pump Reynolds number value of $Re = \omega_{imp} R^2/\nu = 5.48 \times 10^5$, based on the impeller outlet radius and a rated angular speed of $\omega_{imp} = 125$ rad/s, the air pump model's main dimensions are listed in table 1.

The present case study has been experimentally

SHF impeller characteristics	
Tip intlet radius	$R_1 = 141.1$mm
Outlet radius (experiment)	$R_2 = 256.6$mm
Outlet radius (simulations)	$R_2 = 257.5$mm
Outlet width	$b_2 = 38.5$mm
Number of blades	$Z = 7$
Outlet blade angle	β_{2c} =22.5°
Design flowrate(1200 rpm)	$Q_d = 0.236\text{m}^3/\text{s}$
Reynolds number	$Re = {R_2}^2\omega_{imp}/\nu$
($Q/Q_d = 1.0$, $N = 1200$ rpm)	$= 5.52\times10^5$
Vaneless diffuser characteristics	
Inlet radius (experiment)	$R_3 = 257.1$mm
Inlet radius (case A)	$R_3 = 257.5$mm
Inlet radius (case B and C)	$R_3 = 260.075$mm
Outlet radius	$R_4 = 385.5$mm
Constant width	$b_3 = 38.5$mm

Table 1. Main geometrical characteristics of the impeller and diffuser

and analytically investigated in previous works by Dazin et al. [7, 8], and by Heng et al. [9, 10] and [11], even though the effects of the leakage flow have been neglected. Some attempts to include leakage effects in CFD investigation have been presented by Dupont et al. [12] and Pavesi et al. [13] to partially explain overall mean performance discrepancies between experiments and numerical results, but with a vaned diffuser configuration. In the present paper, three different leakage configurations are numerically analyzed using RANS and URANS approaches and compared with experimental performance results on the whole pump and the vaneless diffuser itself. The limitations of the numerical methods employed on this pump model are pointed out combined with the effects of each leakage configuration.

2. METHODOLOGY

2.1. Computational Domain

The three different tested configurations are shown in figure 1. They are respectively called "case A", "case B", and "case C".

- Case A corresponds to a simplified configuration for which there is no leak between the impeller and the vaneless diffuser (see fig. 1 (a)).

- Case B corresponds to a usual pump configuration that allows leakage flow from outlet to inlet sections of the impeller. Consequently, a radial gap $L = R_3 - R_2$ is introduced as shown in fig. 1 (b).

- Case C, given in fig. 1 (c), is quite close to the experimental set-up with the same value of the radial gap value L. The inlet axial gap that separates the inlet tube and the rotating impeller is neglected.

The overall CFD domains include the inlet pump pipe domain (radius R_1 and pipe lenght $10R_1$). The outlet pump domain that is represented by an external cylinder of height H_b and external radius R_b. An outflow box dimension of $H_b/b_3 = 15$ and outlet radius $R_b/R_3 = 3$, is placed after the diffuser outlet section.

2.2. Problem Formulation and Mesh

The flow in a centrifugal pump is incompressible and three-dimensional. Turbulence, rotation of the impeller, the shape of the blades, centrifugal force, and Coriolis force lead to complex flow phenomena in the centrifugal pump. In this study, the flow in the pump is described by the Reynolds averaged Navier-Stokes equations, either in steady (RANS) or unsteady (URANS) form. The URANS equations are

$$\frac{\partial(\mathbf{u})}{\partial t} + (\mathbf{u}\cdot\nabla)\mathbf{u} + \nabla p = \nabla\cdot(2\nu\mathbf{S} - \boldsymbol{\tau}), \quad \nabla\cdot\mathbf{u} = 0, \quad (1)$$

where $\mathbf{u} = \mathbf{u}(\mathbf{x}, t)$ denotes the mean part of the velocity vector, $\mathbf{u} = (u_1, u_2, u_3)$, $p = p(\mathbf{x}, t)$ denotes the mean part of the kinematic pressure, ν is the constant kinematic viscosity, $\mathbf{x}$ is the position vector, t denotes time, $\mathbf{S} = \frac{1}{2}(\nabla\mathbf{u} + \nabla^T\mathbf{u})$ is the mean rate of the strain tensor with the components

$$S_{ij} = \frac{1}{2}\left(\frac{\partial u_i}{\partial x_j} + \frac{\partial u_j}{\partial x_i}\right), \quad (2)$$

and $\boldsymbol{\tau}$ is the Reynolds stress tensor.

For the (U)RANS simulation, the Reynolds stress tensor is modeled by an eddy-viscosity approach containing two conservation equations for the turbulent properties ϕ. Depending on the model type, the placeholder ϕ can be the turbulent kinetic energy k, the turbulent dissipation ϵ or the turbulent specific dissipation rate ω, respectively:

$$\frac{\partial(\phi)}{\partial t} + (\mathbf{u}\cdot\nabla)\phi = P_\phi + \nabla\cdot(D_\phi\nabla\phi) + E_\phi. \quad (3)$$

Different turbulence models contain the terms for production P, diffusion D, and dissipation E. The eddy viscosity ν_T can be deduced from the calculated turbulence quantities as $\nu_T \sim k^2/\epsilon$ or $\nu_T \sim k/\omega$ [14]. The shear-stress transport $k-\omega$ SST turbulent model is used to simulate the turbulent flow in this study.

The computational mesh for the whole domain is multi-block-structured and has several refinement zones to capture the flow field in detail in areas of interest. The mesh is finest near the walls and is gradually coarser further away from the walls. The finer block-structured mesh of the short inlet pipe, impeller, and vaneless diffuser regions with a zoomed view of the refined zones in the impeller and diffuser domain is illustrated in fig. 2 (a) and fig. 2 (b). While a coarser mesh is used in the long inlet pipe and the outflow box regions. In the model scale, the numerical simulations have y+ values of approximately 1 near the walls in the short inlet pipe, impeller, and diffuser regions. The corresponding y+ value near

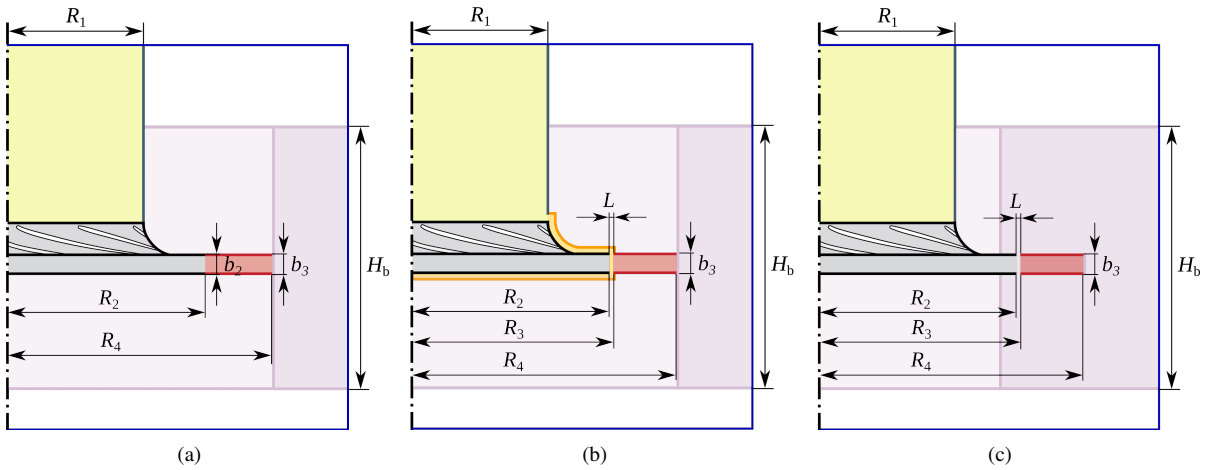

Figure 1. Schematic of the (a) case A, (b) case B, and (c) case C of the centrifugal pump.

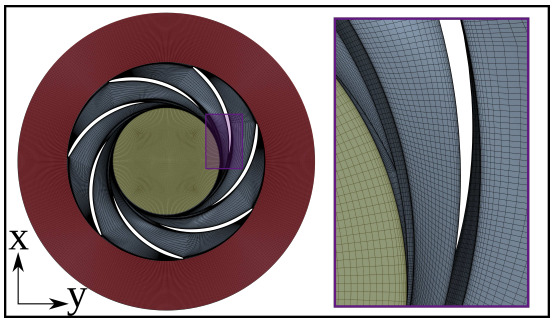

(a)

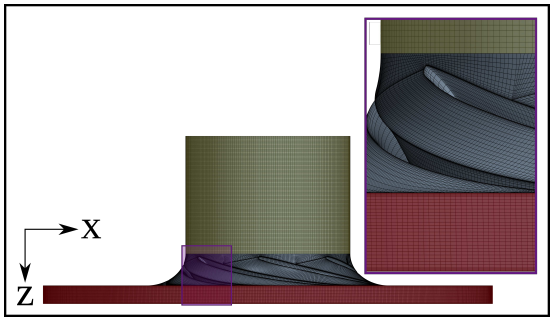

(b)

Figure 2. Top (a) and side (b) view of a typical mesh of case A employed for carrying out the three-dimensional URANS simulations.

the long pipe wall is less than 10 since the mesh for this region is coarser. The mesh is generated by the commercial software ANSYS ICEM CFD and then converted to the format that OpenFoam uses based on the mesh converter library `fluent3DmesToFoam`.

A grid number independence verification was carried out with four schemes. As shown in tab. 2, the predicted performance of the pump at the design condition with different grid resolutions are compared. The relative error of the predicted pump performance increases with the increase of grids sizes and then decreased to 0.93%. Therefore, a total mesh number of

Case	Grid number	PSI	δ
1	617691	0.3843	1.75%
2	1118819	0.3864	2.30%
3	2316400	0.3742	0.93%
4	5406783	0.3777	–

Table 2. Grid independence verification data. δ is the relative error computed with respect to the finest grid, i.e. $\delta = |\mathrm{PSI}_{\mathrm{Case\ 4}} - \mathrm{PSI}_{\mathrm{Case}\ *}|/|\mathrm{PSI}_{\mathrm{Case\ 4}}|$, where the asterisk denotes either Case 1, 2 or 3.

2.3 million for the numerical domain were selected.

2.3. Numerics in OpenFOAM

All the numerical simulations were carried out using the open-source software OpenFOAM. The solver `simpleFoam` which enables the addition of MRF (Multiple Reference Frame) zones is applied for RANS simulations. While a transient solver `pimpleFoam` with dynamic mesh handling is applied for URANS simulations. In this simulation work, the temporal discretization term makes use of a second-order `backward` differencing scheme, named backward. The gradient term was discretized using the discretization method `Gauss` with linear interpolation where the discretization scheme is `Gauss` means gaussian interpolation of second order. The momentum divergence term was discretized using the second-order `linearUpwind` scheme, which is a blend of linear and upwind schemes. The linear scheme is used for `Interpolation` terms, where Gauss linear corrected scheme is used for Laplacian terms.

A Dirichlet type boundary condition named `flowRateInletVelocity` is chosen for the inlet boundary condition. We specify the inlet velocity corresponding to a pre-set value of inlet flow rate Q. And the static pressure $p = 0$ Pa is set for the outlet. The noslip wall boundary is used for fixed walls, and the `rotatingWallVelocity` boundary condi-

tion which specifies a rotational velocity is used for rotating walls.

To exclude the startup phase of the flow from the simulations, the RANS simulation results are used as initial values for URANS. The rotational speed was chosen as 125 rad/s and a time step was chosen as Δt, corresponding to 0.5° of the impeller revolution. The simulation results lead to an averaged Courant number for the whole domain of 0.0075 at the design flow rate. For RANS simulations, 10000-time steps were simulated. For URANS simulations, 70 rotating revolutions were simulated and all the results presented in this paper are corresponding to the last time step.

2.4. Experimental Set-ups

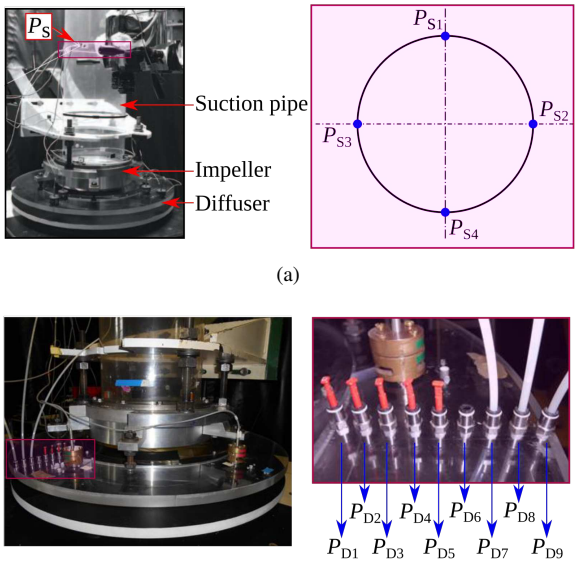

Figure 3. (a) Static pressure taps' locations at the pump inlet pipe. (b) Wall static pressure taps and microphones' locations installed on the vaneless diffuser.

The experimental set-up is briefly described here and is shown on fig. 3. It includes the transparent inlet pipe, the radial impeller, and the vaneless diffuser. The inlet pipe length is equivalent to the one of the numerical inlet domain. A set of replaceable diaphragms (with different inlet diameters), placed in a tank located before the inlet pipe section, are used to adjust the flow rate Q. No volute exists downstream the vaneless diffuser to ensure axisymmetric outlet boundary conditions corresponding to atmospheric pressure. To obtain diffuser pressure recovery, the set-up is equipped with nine steady wall pressure taps along with the diffuser shroud (equally spaced from R = 264 mm to 384 mm). The corresponding measurement uncertainty is evaluated at ± 2 Pa. Several flow rates values between Q/Q_d = 0.26 and 1.53 are chosen for a fixed rotational speed of N = 1200 rpm. Q_d denotes the design flow rate.

3. RESULTS

3.1. Pump Performance

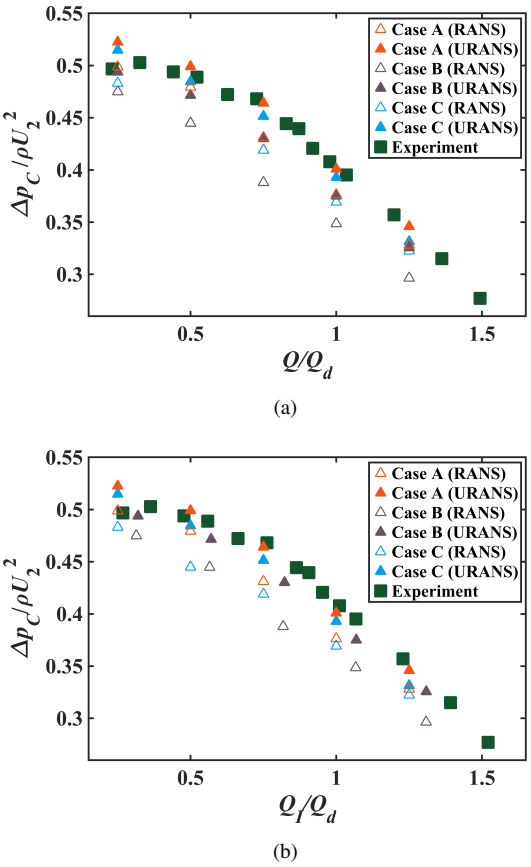

Figure 4. (a) Overall pump performance versus reduced pump flow rate Q. (b) Overall pump performance versus reduced impeller flow rate Q_I. Δp_C denotes the static pressure difference between the inlet and the outlet sections of the centrifugal pump; ρ denotes the density of the air.

The pump performance curves obtained by the RANS and URANS simulations are compared with the experimental results as shown in fig. 4 (a). As expected, the URANS simulation results are in better agreement with the experimental ones, as they captured the slowest scales of the time-dependent dynamics. Looking at the results of the three different configurations, the performance curve of case C, which is the same geometrical configuration as the experimental set-up, is the closest to the experimental results over the whole operating range. The performance curve of case A is slightly above the experimental results. Most of the experimental results are between the numerical results of cases A and C. Concerning case B, the pressure difference between the impeller outlet and inlet section leads to a leakage flow going out at the impeller-diffuser radial gap, feeding back the impeller inlet plane. This results in an increment of the flow rate in the impeller. Besides, an approximated flow leakage value is estimated through the inlet axial gap in front of

the impeller as already proposed by Heng [11], who modify the experimental impeller flow rate Q_I which is slightly larger than Q. This effect is taken into account and the corrected performance curves of case C and experiment, based on the impact of the flow rate increment in the impeller, are plotted in fig. 4 (b). The corresponding simulation results of case C get closer to the experimental ones.

3.2. Impeller Performance

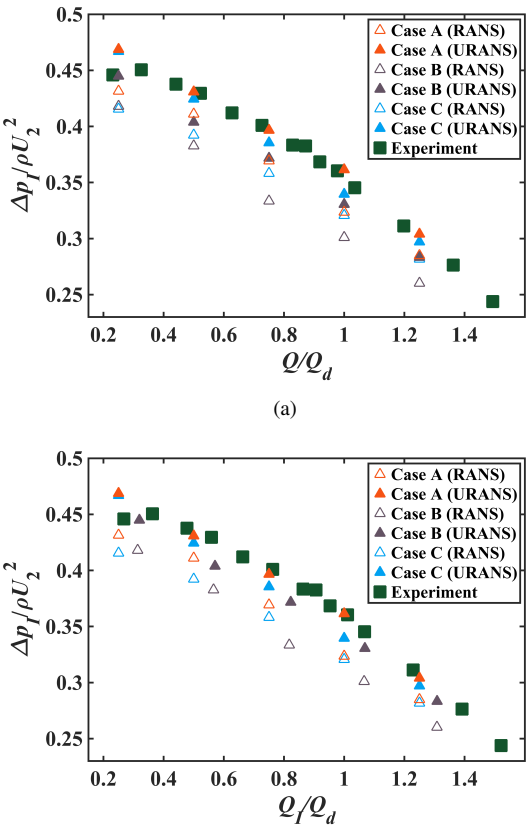

Figure 5. (a) Impeller performance versus reduced pump flow rate Q. (b) Impeller performance versus the reduced impeller flow rate Q_I. Δp_I denotes the static pressure difference between the inlet and the outlet impeller sections.

Fig. 5 (a) shows the impeller performance curve obtained with the RANS and URANS approaches. The impeller performance curves are very similar to the whole pump performance curves with the same trend. However, the simulation results of the impeller performance are closer to the experimental results of the whole pump performance. This means that the pump performance is mainly dominated by the impeller performance. The shifted impeller performance curves, based on the flow rate correction method mentioned before, are shown in fig. 5 (b). The corrected results show that excepting a flow rate change, the leakage flow does not have a big impact on the impeller performances.

3.3. Diffuser Performance

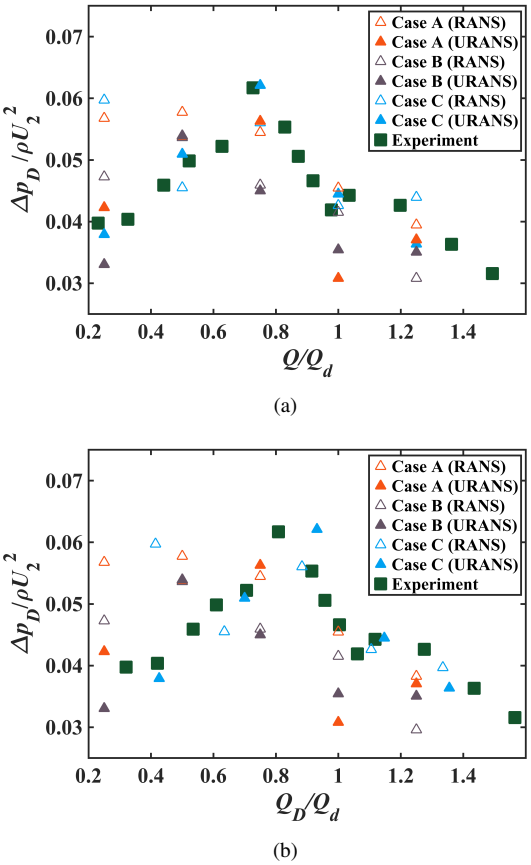

Figure 6. (a) Diffuser pressure recovery versus reduced pump flow rate Q. (b) Diffuser pressure recovery versus reduced diffuser flow rate Q_D. Δp_D denotes the static pressure difference between the inlet and the outlet sections of the vaneless diffuser.

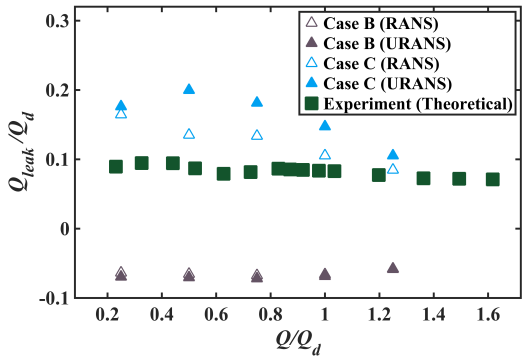

Figure 7. Plotting of the leakage flow rates Q_{leak} versus the flow rate of the pump Q.

Fig. 6 (a) shows the comparison of the diffuser performance obtained by the RANS and URANS simulations for several flow rate Q values. Both the RANS and URANS simulation results look acceptable under large flow rates. The real flow rate inside the diffuser Q_D is higher than the flow rate Q used

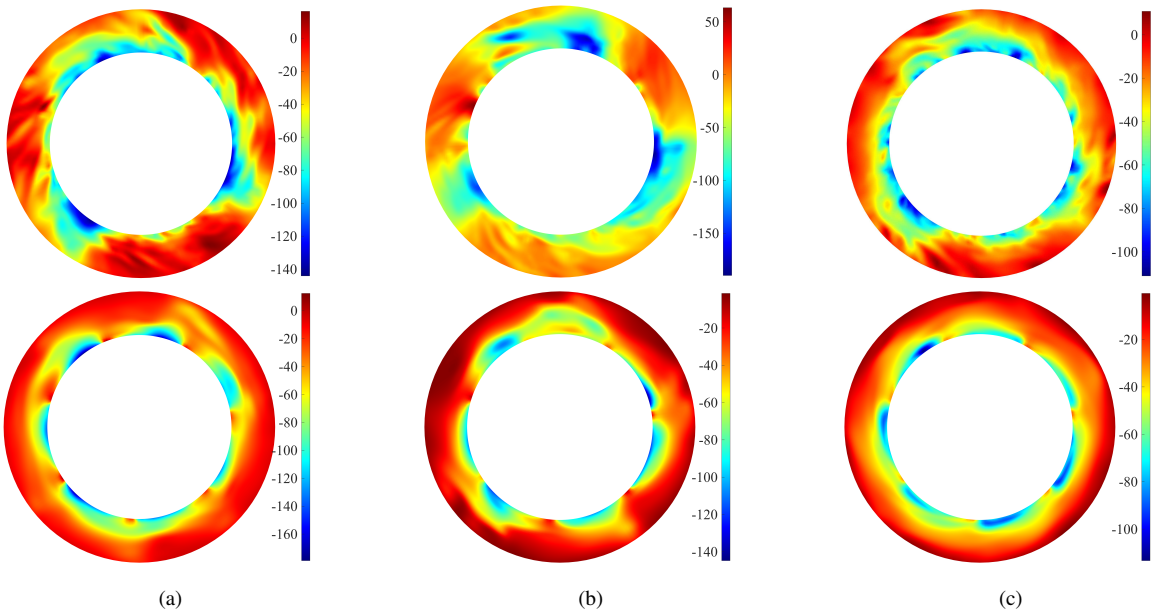

Figure 8. Instantaneous color maps of the static pressure p (pa) at the mid-height of the diffuser at the flow rate $Q/Q_d = 0.25$ obtained by the URANS (top figures) and RANS (bottom figures) for: (a) case A, (b) case B, and (c) case C.

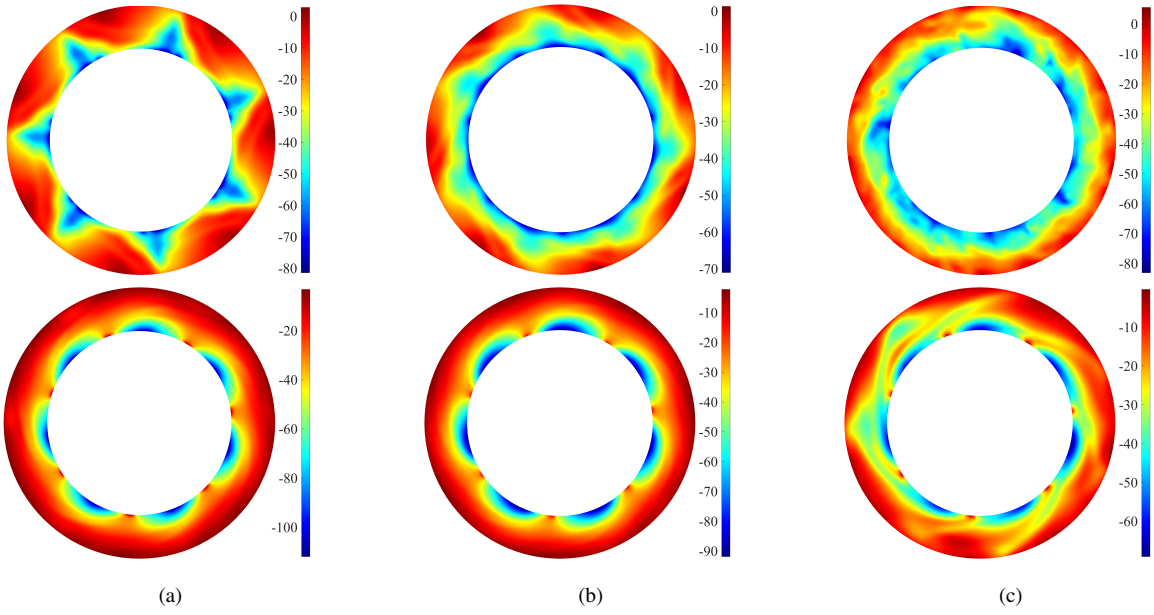

Figure 9. Instantaneous color maps of the static pressure p (pa) at the mid-height of the diffuser at the flow rate $0Q/Q_d = 1.00$ obtained by the URANS (top figures) and RANS (bottom figures) for: (a) case A, (b) case B, and (c) case C.

on fig. 6 (a). The corresponding flow rate increment, obtained by the numerical simulations in the vaneless diffuser, is due to the leakage caused by the pressure difference between the diffuser inlet and the atmospheric pressure. Fig. 7 gives the estimated leakage flow rate ratio that was first obtained from experiments by Heng et al. [9, 10, 11] and the one obtained from CFD. The diffuser performance curves are consequently shifted as plotted on the fig. 6 (b); it shows that simulation results obtained for case C are now in a better agreement with the experimental results.

However at the smallest flow rate, the RANS simulation results are very different compared with the URANS results. This is due to the rotating stall phenomena occurring in the vaneless diffuser that was already detected in previous works. Such an instability cannot be captured properly by the steady calculations. This can be seen on fig. 8 (a), 8 (b)

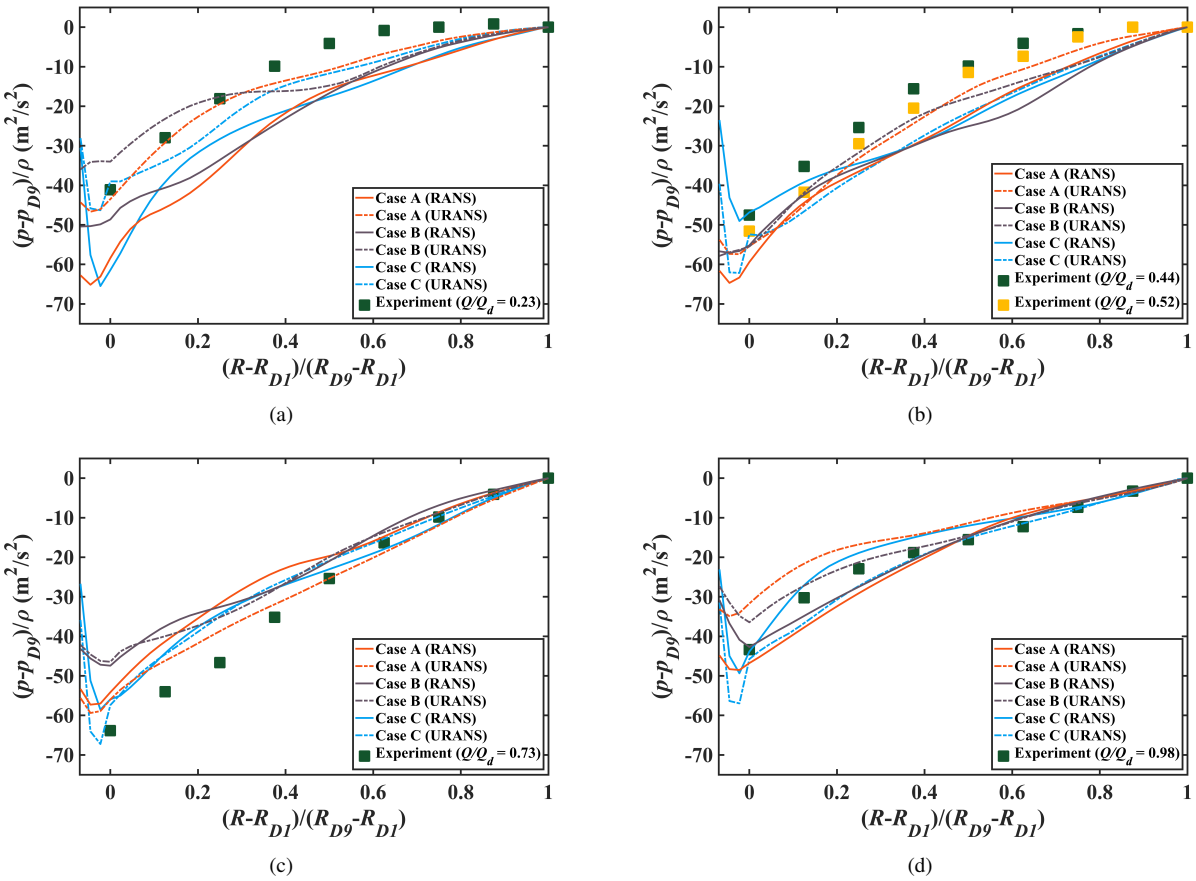

Figure 10. Diffuser radial pressure recovery distributions for different flow rates. (a) $Q/Q_d = 0.25$**, (b)** $Q/Q_d = 0.50$**, (c)** $Q/Q_d = 0.75$**, (d)** $Q/Q_d = 1.00$**.**

and 8 (c). They show the static pressure maps at mid height section between hub to shroud obtained by the numerical simulations for $Q/Q_d = 0.25$, using URANS (top figures) and RANS (bottom figures) for each three cases A, B and C respectively. Three stall cells can be observed very clearly in the case A and case B of the URANS results which well corresponds to the PIV study carried out by Dazin in 2011 [8] in previous investigations.

For the cases A and B at the design flow rate $Q/Q_d = 1.00$, the numerical diffuser performance is still very different from the experiment. This is due to another instability developing at the design flow rate and enhancing the impeller wake inside the diffuser (see fig. 9). A peculiar seven-periodic pattern is observed in the vaneless diffuser far from the diffuser inlet for case A and case B looking at the URANS results. Such instability is normally tamed down by the leakage flow in case C, which results in better performance close to design conditions. As the RANS simulations cannot capture the time dependent instability for case A and case B at the design flow rate, they over-predict the diffuser performance.

The radial distributions of the pressure recovery are plotted in fig. 10, for all three configuration cases (A, B and C) at four different flow rates. The non-dimensional radial position equals zero at the first radial location of the experimental wall pressure tap in the vaneless diffuser $D1$. The negative radial value corresponds to the region where strong jet and wake mixture usually occurs just after the impeller outlet section. This is the reason why URANS results can better capture the corresponding large local pressure losses corresponding to negative pressure recovery with large gradients.

For $Q/Q_d = 0.25$ (fig. 10 (a)), the RANS simulation cannot correctly predict the diffuser pressure recovery owing to the rotating stall. As the flow rate increases, for $Q/Q_d = 0.50$ to $Q/Q_d = 0.75$ (respectively fig. 10 (b) and fig. 10 (c)), both URANS and RANS simulation results are a good agreement with the experiments.

At the design flow rate $Q/Q_d = 1.00$ (fig. 10 (d)), an important difference can be observed between the RANS and URANS simulations. This is attributed to the instability development that was previously pointed out in the previous section for case A and B.

4. CONCLUSIONS

Performances on a pump model using air as working fluid is numerically and experimentally investigated with a focus on the vaneless diffuser characteristics. Three different geometrical configurations have been tested for the RANS and URANS

simulations for the analysis of the leakage effects and make more precise comparisons with experimental results.

The leakage flow can significantly affect the flow characteristics depending on the volume flow rate at the impeller inlet. The simulation results show little influence of the leakage on the global performance and impeller performance, but show a significant impact on the diffuser behavior.

When correctly taking the local leakage effects into account:

- The comparisons between numerical predictions and experiments are significantly improved. URANS approach is always better than RANS one, mainly for the vaneless diffuser performance analysis.
- For off-design low flow rates, like for Q/Q_d = 0.25, three-stall-cells structures can be observed for the configuration that corresponds to the experimental one. Moreover, a different instability is observed to develop at the design flow rate $Q/Q_d = 1.00$. A more precise analysis of such a complex phenomenon will be performed in future works.

ACKNOWLEDGEMENTS

We kindly acknowledge the GENCI (grand équipement national de calcul intensif) for the numerical resources granted to conduct this study under the project A0102A01741. Furthermore, we appreciate the support of the China Scholarship Council for the doctoral students of M. Fan (CSC student number 201908320328).

REFERENCES

[1] Jansen, W., 1964, "Rotating Stall In a Radial Vaneless Diffuser", *Journal of Basic Engineering-Transactions of the ASME*, Vol. 86(4), pp. 750–758.

[2] Jansen, W., 1964, "Steady Fluid Flow in A Radial Vaneless Diffuser", *Journal of Basic Engineering-Transactions of the ASME*, Vol. 86(3), pp. 607–617.

[3] Senoo, Y., and Kinoshita, Y., 1977, "Influence of Inlet Flow Conditions and Geometries of Centrifugal Vaneless Diffusers on Critical Flow Angle for Reverse Flow", *ASME Journal of Fluids Engineering*, Vol. 99(1), pp. 98–103.

[4] Frigne, P., and Van Den Braembussche, R., 1984, "A Theoretical Model for Rotating Stall In the Vaneless Diffuser of A Centrifugal Compressor", *Journal of Engineering for Gas Turbines and Power*, Vol. 106, pp. 468–474.

[5] Sundström, E., Mihăescu, M., Giachi, M., Belardini, E., and Michelassi, V., 2017, "Analysis of Vaneless Diffuser Stall Instability in A Centrifugal Compressor.", *International Journal of Turbomachinery, Propulsion and Power*, Vol. 2(4), p. 19.

[6] Wuibaut, G., Dupont, P., Caignaert, G., and Stanislas, M., 2000, "Experimental Analysis of Velocities in the Outlet Part of A Radial Flow Pump Impeller and the Vaneless Diffuser using Particle Image Velocimetry", *Proceedings of the XX IAHR Symposium (Charlotte USA)*, Charlotte, USA, pp. 6–9.

[7] Dazin, A., Coutier-Delgosha, O., Dupont, P., Coudert, S., Caignaert, G., and Bois, G., 2008, "Rotating Instability in the Vaneless Diffuser of A Radial Flow Pump", *Journal of Thermal Science*, Vol. 17, pp. 368–374.

[8] Dazin, A., 2011, "High-speed Stereoscopic PIV Study of Rotating Instabilities in A Radial Vaneless Diffuser", *Experiments in Fluids*, Vol. 51, pp. 83–93.

[9] Heng, Y. G., Dazin, A., Ouarzazi, M. N., and Si, Q. R., 2016, "Experimental Study and Theoretical Analysis of the Rotating Stall in a Vaneless Diffuser of Radial Flow Pump", *IOP Conference Series: Earth and Environmental Science*, Vol. 49, p. 032006.

[10] Heng, Y. G., Dazin, A., and Ouarzazi, M. N., 2017, "Linear Stability Analysis of Rotating Stall in A Wide Vaneless Diffuser", *Proceedings of 12th European Conference on Turbomachinery Fluid dynamics & Thermodynamics*, Stockholm, Sweden, Vol. EUROPEAN TURBOMACHINERY SOCIETY, pp. ETC2017–301.

[11] Heng, Y. G., Dazin, A., Ouarzazi, M. N., and Si, Q. R., 2018, "A Study of Rotating Stall in A Vaneless Diffuser of Radial Flow Pump", *Journal of Hydraulic Research*, Vol. 56(4), pp. 494–504.

[12] Dupont, P., Bayeul-Laine, A. C., Dazin, A., and Bois, G., 2014, "Leakage Flow Simulation in A Specific Pump Model", *IOP Conference Series: Earth and Environmental Science*, Montreal, Canada, Vol. 22, pp. 1–10.

[13] Pavesi, G., Dazin, A., Cavazzini, G., Caignaert, G., Bois, G., and Guido, A., 2011, "Experimental and Numerical Investigation of Unforced unsteadiness in a Vaneless Radial Diffuser", *9th european conference on turbomachinery-fluid dynamics and thermodynamics*, Istanbul, Turkey, pp. 625–636.

[14] Kratzsch, C., Timmel, K., Eckert, S., and Schwarze, R., 2015, "URANS Simulation of Continuous Casting Mold Flow: Assessment of Revised Turbulence Models", *Steel Research International*, Vol. 86(4), pp. 400–410.

Appended papers

C.2 Paper B

"Effect of inlet leakage flow on the instability in a radial vaneless diffuser",
M. Fan, A. Dazin, G. Bois, F. Romanò,
Phys. Fluids, 35(1) (2023), 014105.

Physics of Fluids

RESEARCH ARTICLE | JANUARY 10 2023

Effect of inlet leakage flow on the instability in a radial vaneless diffuser

M. Fan ; A. Dazin ; G. Bois ; F. Romanò

Physics of Fluids 35, 014105 (2023)
https://doi.org/10.1063/5.0133948

Physics of Fluids ARTICLE scitation.org/journal/phf

Effect of inlet leakage flow on the instability in a radial vaneless diffuser

Cite as: Phys. Fluids **35**, 014105 (2023); doi: 10.1063/5.0133948
Submitted: 7 November 2022 · Accepted: 19 December 2022 ·
Published Online: 10 January 2023

M. Fan,[a] A. Dazin, G. Bois, and F. Romanò

AFFILIATIONS

Univ. Lille, CNRS, ONERA, Arts et Métiers Institute of Technology, Centrale Lille, UMR 9014-LMFL-Laboratoire de Mécanique des Fluides de Lille-Kampé de Fériet, F-59000 Lille, France

[a]Author to whom correspondence should be addressed: meng.fan@ensam.eu

ABSTRACT

The internal flow structures in a vaneless diffuser of a radial pump are experimentally and numerically investigated. Numerical simulations are used for investigating the prominent features of the fluid flow in the vaneless diffuser upon a change of the flow rate and of the impeller-to-diffuser radial gap. Comparisons between experimental and numerical results on the overall pump and diffuser performances are presented and discussed. The influence of inlet diffuser leakages on the development of flow instabilities is specifically addressed, owing to the remarkable impact that a small impeller-to-diffuser radial gap can have on the diffuser flow. Highlights on the rotating instabilities in terms of stall cell number and propagation velocity at design and off-design conditions are the main focus of this study and will be investigated using the numerical and experimental results post-processed by fast Fourier transform and wavelet analysis.

I. INTRODUCTION

The pressure recovery in radial compressors or pump vaneless diffusers is often subject to performance limitations. This is typical of compressors or pumps operating at partial flow rates, i.e., at flow rates lower than the design flow rate. Such limitations are induced by flow separation phenomena usually classified in singular and ordinary flow separations as reported by Japikse.[1] The former, on the one hand, occurs because a too-large mean deceleration is produced by the vaneless diffuser. The latter, on the other hand, is more common due to the local overturning of the streamlines close to the wall.

The local decrease in kinetic energy is the main cause of separation as explained by several authors (see, e.g., Ref. 2). Both types of performance limitations refer to static stall configurations that occur in a specific fixed location in the machine. However, they may initiate peculiar rotating instabilities that, in vaneless diffusers, are commonly termed rotating stall in order to point out the dynamic character of the stall.

Dynamic stall is an important subject, far more difficult to report on than static stall. Dynamic stall patterns are, in fact, not fixed in a given reference frame as it happens for the static stall. Indeed, they rotate in the machine system at some fraction of the machine's rotational speed. Such dynamic conditions can exist in different components in all kinds of turbomachines, depending on the specific speed and design. However, in radial flow machines (pumps, fans, and compressors), they are mostly observed in configurations for which the machine is equipped with a vaneless diffuser, which turns out to be the most sensitive component with respect to such instabilities. They are crucial to control or avoid as they can induce vibrations and initiate or amplify surge conditions for the whole machine system.

Based on Jansen's work, two papers from Senoo and Kinoshita[3] and Senoo *et al.*[4] critically evaluated the conditions for the onset of reverse flow in a vaneless diffuser. In their first reference, Abdelhamid *et al.*[5] have reported dynamic measurements in a vaneless diffuser that helped unravel the underlying physics of dynamic stall phenomena. They observed that the dynamic stall condition develops in a gradual manner in the diffuser space as the machine flow rate is decreased. Their work was extended, considering the diffuser geometry variations.[6] These unforced rotating instabilities have been theoretically investigated using two different approaches: a 3D wall boundary layer stability analysis[7] and a two-dimensional inviscid approach only assuming a core-flow region in the vaneless diffuser hub-to-shroud sections[8,9] in the case of wide diffuser ratios, i.e., for diffusers whose ratio between the height (b_2) and the outlet-to-inlet diffuser radius difference ($R_4 - R_3$) is $\Gamma = (R_4 - R_3)/b_2 \lesssim \mathcal{O}(1)$.

The results show that the stability limit for wide vaneless diffusers can be expressed in terms of the critical flow angle at the diffuser inlet. The critical flow angle is also found to depend on the diffuser radius ratio as well as on the number of stall cells. In accordance with the core-flow assumption, the effect of the wall boundary layers is found

to be negligible. However, it is expected that by including the wall boundary layer effects into the 2D inviscid model developed by Tsujimoto *et al.*,[8] the characteristics of the most-dangerous mode predicted by their two-dimensional model may change, certainly in terms of the detailed unstable pattern and potentially either in terms of the number of stall cells or of their propagation speed, if not of the onset of instability only expressed by the critical flow angle. Within similar two-dimensional working hypotheses, an additional study presented by Ljevar *et al.*[10] also suggests that the usual jet and wakepattern delivered by impellers has no influence on the development of these rotating instabilities at low flow rates.

In a previous study, an identification of the instabilities developing in the radial vaneless diffuser of interest for our study has been performed numerically and experimentally by Pavesi *et al.*[11] for two partial flow rates. Depending on the operating conditions, Pavesi *et al.*[11] identified either a rotating stall in the form of a single mode or two competing modes leading to an intermittency phenomenon (see also Dazin[12]). It is, however, still unclear if a specific mechanism is responsible for driving the switch from one mode to the other one, or if the phase space of the unstable flows at low flow rates is chaotically arranged around two connected attractors (the two modes). In the latter case, no specific mechanism would be required to switch from one mode to another, and the intermittency would be the result of an enhanced sensitivity of the system to small perturbations near saddle or hyperbolic points in phase space. Additionally, Pavesi *et al.*[11] reported that to capture correctly the instability, it was necessary to include in the simulations the effect of the leakage flow occurring between the diffuser and the runner, even for small impeller-to-diffuser radial gaps. The instability, thus, seems to be very sensitive to the diffuser inlet flow conditions.

For the present paper, the same pump model of Pavesi *et al.*[11] is investigated experimentally, and three conceptually complementary leakage flow configurations are considered numerically, either (i) sealing the impeller-to-diffuser gap (zero-leakage case), (ii) leaving a radial gap open to the surroundings from which air can flow inside the diffuser (positive-leakage case), or (iii) including a fixed carter that connects the diffuser inlet to the section just before the impeller inlet leaking air from the diffuser to the impeller inlet (negative-leakage case) through a small radial gap. The key point of this work is to study the rotating instability inside the vaneless diffuser, as even small radial gaps between the impeller and the diffuser can significantly affect the flow. In addition, we will consider the hypothesis of a centrifugal-type mechanism as an origin for the rotating stall and discuss the low-flow rate instability in terms of the lift-up and flow deceleration mechanisms.

The paper is, therefore, structured as follows: Sec. II introduces the experimental apparatus and measuring techniques, Sec. III defines the mathematical model of the incompressible flow and presents the discretization employed to numerically solve the Navier–Stokes system. The results of the Unsteady Reynolds-Averaged Navier–Stokes (URANS) simulations are presented in Sec. IV, and, finally, in Sec. V, the results are summarized and conclusions are drawn.

II. EXPERIMENTAL APPARATUS AND PROCEDURE

A. Experimental apparatus

The experimental vaneless diffuser test case corresponds to the so-called Société Hydrotechnique de France (SHF) pump, which is an enlarged air model (impeller with diffuser and no volute) specifically built to allow experimental optical access for unsteady flow analysis with well-defined constant outlet pressure boundary conditions as already presented by Dazin[12] and Wuibaut *et al.*[13] Such an experimental test rig includes a radial impeller coupled with a vaneless diffuser, as shown in Fig. 1(a). The main parameters of the radial impeller and vaneless diffuser are given in Table I.

This arrangement allows for positive-leakage flow entering the vaneless diffuser inlet because of the radial gap between the outlet rotating impeller section and the fixed inlet diffuser one. This leakage flow configuration is representative of radial ventilation and extraction devices, whose outlet static pressure is at atmospheric conditions. Thus, all local static pressures inside the whole pump are always below the atmospheric pressure. The main difference with conventional radial pump designs is that they usually make use of a carter connecting the diffuser inlet and the inlet-pipe outlet, therefore providing a casing to the impeller. Hence, differently from our experimental setup, for conventional radial pumps, part of the outflow rate at the impeller outlet returns to the impeller inlet driven by the pressure gradient. This corresponds to a negative-leakage flow for the diffuser and is generally represented by the so-called pump volumetric efficiency, expressing that the outlet pump flow rate is lower than the impeller flow rate.

B. Measuring techniques

Our experimental setup is equipped with nine steady pressure taps, which are flush-mounted on the diffuser wall along a radial line. The probes are equally spaced from $r = 264$ to $r = 384$ mm [see Fig. 1(b)].

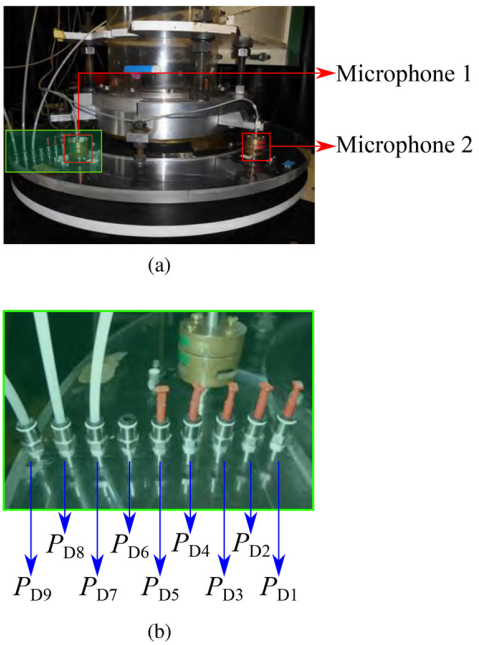

FIG. 1. Experimental setups of the centrifugal pump with (a) two microphones mounted on it, and (b) zoom-in view of nine static pressure taps installed on the vaneless diffuser [green rectangle in (a)].

TABLE I. Main geometrical characteristics of the impeller and diffuser model.

SHF impeller characteristics		
R_1	Tip inlet radius	141.1 mm
R_2	Outlet radius	257.5 mm
b_2	Outlet width	38.5 mm
Z	Number of blades	7
β_{2c}	Outlet blade angle	22.5°
K	Mean blade thickness	9 mm
Q_d	Design flow rate (1200 rpm)	0.236 m^3/s
$Re = R_2{}^2\omega_{imp}/\nu$	Reynolds number, ($Q/Q_d = 1.0$, $N = 1200$ rpm)	5.52×10^5
Vaneless diffuser characteristics		
R_3	Inlet radius (zero-leakage)	257.5 mm
	Inlet radius (negative-leakage)	260.075 mm
	Inlet radius (positive-leakage)	260.075 mm
R_4	Outlet radius	385.5 mm
b_3	Constant width	38.5 mm

Therefore, the diffuser performance is characterized based on the pressure recovery from the inlet to the outlet of the diffuser. The uncertainty of these measurements is estimated to be ±2 Pa. To ensure stable pump inlet flow condition, a tank, equipped with a honeycomb flow straightener, was placed in front of the suction pipe. A set of changeable diaphragms (with different inlet diameters) is available to be installed at the tank inlet in order to adjust the flow rate Q.

Two Brüel & Kjaer (Nærum, Denmark) condenser microphones (type 4135) were used to measure the unsteady pressure fluctuation. They are flush-mounted at the same radial location, i.e., at $r = 320$ mm, on the diffuser wall but with an angular shift of $\Delta\theta = 60°$. This allows us to detect the instabilities occurring in the vaneless diffuser and characterize their propagation velocity. The measurement uncertainty for these probes is less than 1%. The data were acquired by LMS Test Xpress (SIEMENS, Munich, Germany) for the total time of 600 s sampled with the frequency of 4096 Hz.

The experiments were performed in the air for a wide range of flow rate ratios relative to design condition $Q/Q_d \in [0.26, 1.53]$, where Q and Q_d denote the actual and the design flow rates measured at the inlet pipe at constant rotating speed $N = 1200$ rpm (i.e., $\omega_{imp} = 125$ rad/s). More details of this experimental test rig can be found in previous studies presented by Dazin[12] and Dazin *et al.*[14] that operate the same apparatus. We further stress that, due to the leakage effects, the flow rate of the diffuser and of the impeller may differ from Q as they require the evaluation of the leakage flow at the impeller and diffuser inlet. More details about such corrections are discussed in Sec. IV.

III. COMPUTATIONAL PROCEDURE

A. Computational domain

Figure 2(a) depicts the computational domain consisting of an inlet pipe (blue), the pump impeller (gray), the diffuser (violet), and a radial outflow box (dark pink) introduced at the outlet of the diffuser in order to avoid enforcing the outflow boundary conditions too close to the pump. The geometry of the numerical model matches the experimental setup (Fig. 1) characterized in Table I. The inlet boundary conditions are set at the top of the circular straight pipe (inlet pipe), whose length H_c is equal to ten times of the impeller tip inlet radius R_1. The outlet conditions are given at the boundaries of the outflow box (dark pink) of height H_b and radius R_4, where $H_b/b_3 = 15$ and $R_4/R_3 = 3$. In order to investigate the effect of the leakage flow on the radial diffuser flow, three conceptually different leakage configurations are numerically simulated. They are termed zero-, negative-, and positive-leakage case as they refer to the leakage flow entering the diffuser.

1. Zero-leakage

Zero-leakage corresponds to a simplified configuration, for which there is no leak between the impeller and the vaneless diffuser as the

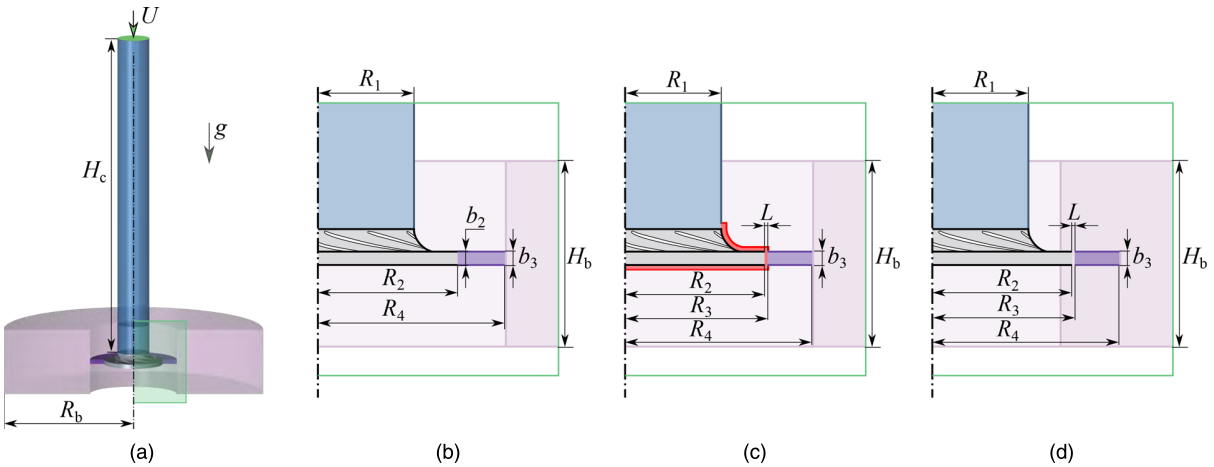

FIG. 2. Schematic of (a) the entire computational domain for the radial flow pump and zoom-in view for the three configurations: (b) zero-, (c) negative-, and (d) positive-leakage case.

radial gap between impeller and diffuser is set to zero [see Fig. 2(b)]. Also, between the inlet-pipe outlet and the impeller inlet, we consider no axial gaps.

2. Negative-leakage

Negative-leakage corresponds to a usual pump configuration that allows leakage flow from outlet to inlet sections of the impeller, thanks to the casing around the impeller. Consequently, a radial gap $L = R_3 - R_2$ is introduced as shown in Fig. 2(c). The distance from the casing wall to the impeller is constantly equal to the gap width L.

3. Positive-leakage

Positive-leakage shown in Fig. 2(d) qualitatively reproduces the experimental geometry in the corresponding numerical simulations. Note that the experimental radial gap (1 mm) and the numerical one (3 mm) are different. In our numerical simulations, the radial gap between the impeller and the diffuser is enlarged on purpose to clearly highlight the influence of the positive-leakage flow. The axial gap between the inlet-pipe outlet and the impeller inlet is neglected. All the comparisons between experiments and numerical performance are considered for the positive-leakage case, employed for discussion and validation of our numerics.

B. Governing equations

The incompressible viscous fluid flow in a radial pump is formulated by employing the Unsteady Reynolds-Averaged Navier–Stokes (URANS) equations,

$$\frac{\partial \vec{U}}{\partial t} + (\vec{U}\cdot\nabla)\vec{U} + \nabla P = \nabla\cdot(2\nu\vec{\bar{S}} - \vec{\tau}), \quad \nabla\cdot\vec{U} = 0, \tag{1}$$

where $\vec{U} = \vec{U}(\vec{x};\, t) = (U_1, U_2, U_3)$ denotes the mean part of the velocity vector, $(\vec{x};\, t) = (x_1, x_2, x_3;\, t)$ are the spatial and temporal coordinates, $P = P(\vec{x}, t)$ is the mean pressure field, ν is the kinematic viscosity, $\vec{\bar{S}} = \frac{1}{2}(\nabla\vec{U} + \nabla^T\vec{U})$ is the mean rate of the strain tensor, $\vec{\tau}$ is the Reynolds stress tensor, and ν_T is the turbulent viscosity (see Wilcox[15] and Sváček *et al.*[16] for details).

As the main focus of this study is on the fully developed instabilities, the initial startup of the pump is skipped by initializing all the URANS simulations out of a corresponding steady simulation (RANS). Since the frequencies of the stall phenomena of interest in this study are lower than the rotational speed of the impeller, a long physical simulation time t_{fin} is required to resolve the low-frequency range. Therefore, $t_{\text{fin}} = 70T$, where T is the one impeller revolution period, was set for all URANS simulations to make sure that all the results presented hereinafter are at fully developed conditions. All the following results are, therefore, presented at $t = t_{\text{fin}}$, and all the phase-averaged results employed to characterize rotating patterns are produced advancing the simulation starting from $t = t_{\text{fin}}$.

C. Turbulence modeling

The shear-stress transport (SST) $k-\omega$ turbulence model is used to model the Reynolds stress tensor because it accounts for the transport of the principal turbulent shear stress. Such a feature makes the $k-\omega$ SST model a suitable choice for the centrifugal pump over both the standard $k-\varepsilon$ and the realizable $k-\varepsilon$ models. Other modifications to the standard $k-\omega$ SST model have been proposed in the literature[17] to include a cross-diffusion term in the $\omega-$ equation and a blending function to ensure that the model equations behave appropriately in the near-wall and far-field zones.[18] In this study, we employ one of such modified $k-\omega$ SST models, following the formulation of Menter.[19] It is known that turbulence models based on the Boussinesq hypothesis can face modeling issues when attempting to solve for rapidly rotating flows with strongly curved streamlines. The model we selected has been proven to have a reasonably stable, robust, and time-efficient capability to predict global performance and capture the key flow features in centrifugal pump simulations.[20] This is also confirmed by several examples[21–24] in the literature and validated by experiments.

The corresponding turbulent kinetic energy k equation is given by

$$\frac{\partial k}{\partial t} + (\vec{u}\cdot\nabla)k = P_k - \beta^*\omega k + \nabla\cdot[(\nu + \sigma_k\nu_T)\nabla k], \tag{2}$$

and for turbulence-specific dissipation rate ω, it yields

$$\frac{\partial \omega}{\partial t} + (\vec{u}\cdot\nabla)\omega = \alpha S^2 - \beta\omega^2 + \nabla\cdot[(\nu + \sigma_\omega\nu_T)\nabla\omega] + 2(1-F_1)\frac{\sigma_{\omega2}}{\omega}\nabla k\cdot\nabla\omega, \tag{3}$$

where the production term P_k is given by

$$P_k = \nu_T\vec{\bar{S}}(u) : \vec{\bar{S}}(u), \tag{4}$$

and the blending function F_1 is defined by

$$F_1 = \tanh\left\{\left\{\min\left[\max\left(\frac{2\sqrt{k}}{\beta^*\omega y}, \frac{500\nu}{y^2\omega}\right), \frac{4\rho\sigma_{\omega2}k}{CD_{k\omega}y^2}\right]\right\}^4\right\}, \tag{5}$$

where $CD_{k\omega} = \max\left(2\rho\sigma_{\omega2}\frac{1}{\omega}\nabla k\cdot\nabla\omega, 10^{-10}\right)$ and y is the normal distance to the nearest wall. Finally, the turbulent eddy viscosity is defined as

$$\nu_T = \frac{\alpha_1 k}{\max(\alpha_1\omega, SF_2)}, \tag{6}$$

where F_2 is a second blending function

$$F_2 = \tan\left[\left[\max\left(\frac{2\sqrt{k}}{\beta^*\omega y}, \frac{500\nu}{y^2\omega}\right)\right]^2\right]. \tag{7}$$

Further details of the modeling techniques and the constants $(\beta, \beta^*, \sigma_k, \sigma_{\omega2}, \alpha_\omega)$ of this model can be found in Menter.[19]

D. Mesh and time step

Hexahedral cells are chosen for meshing, which is proven to be less costly and less diffusive than tetrahedral cells, especially at the boundary layer. The commercial software ANSYS ICEM-CFD is used for generating the mesh. The multi-block structure used in ICEM-CFD makes the mesh generation flexible and accurate. The inlet pipe (of height $H_c = 20R_1$) is split into two parts, one of which is long enough before the impeller to stabilize the inlet flow, while the second short part of the inlet pipe (of height $\frac{1}{10}H_c$) shares an interface with the

impeller. The grid in the short part of the inlet pipe, impeller, and vaneless diffuser regions is finer as shown in Fig. 3. The grid used in the long part of the inlet pipe and the outflow radial box regions is coarser as these parts of the computational domain are included solely to avoid enforcing inlet and outlet boundary conditions too close to the impeller and the diffuser, respectively. Once the mesh is generated, the mesh converter `fluent3DmeshToFoam` is used to convert the mesh into the format in use by OpenFOAM. The postulated mathematical problem is solved by the open-source software OpenFOAM, and details of the OpenFOAM solvers we used can be found in Appendix A.

In the near-wall regions, the mesh is refined using an expansion ratio of 1.5. Thus, the values y^+ are kept at approximately $y^+ \approx 1$ near the walls in the short inlet pipe, impeller, and diffuser regions. The corresponding y^+ value is less than $y^+ < 10$ near the long pipe wall as a coarser mesh is used for this region. The Menter $k-\omega$ SST model used in the current study has an accurate and robust near-wall treatment. Referring to the near-wall grid density, this model can automatically shift from a low-Re formulation to wall functions.[17,25] This allows us to use the correct range of y^+. Based on a grid number independence verification, a total mesh number of 2.3 M finite volumes was selected for the following numerical simulations; more details are given in Appendix B.

In order to assure the required numerical accuracy and to limit the total computational cost, a time step Δt, corresponding to $\Delta\theta = 0.5^\circ$ of the runner revolution, i.e., $\Delta t = \Delta\theta/(2\pi\omega_{\text{imp}}) \times 2\pi/180^\circ$, was selected. This is in agreement with several literature studies[26] that suggest $\Delta\theta \leq 1^\circ$. Our choice for the Δt leads to a characteristic Courant number of $C = |U|\frac{\Delta t}{\Delta x} \approx 0.05$, where Δx is the local mesh size. This value is estimated for the cells in the bulk region of the diffuser, which is the major focus of this study. Its estimate is based on the theoretical value of the diffuser inlet velocity and the length scale resulting from the volume of the mesh elements. By *a posteriori* computation of the Courant number, all our simulations at the nominal flow rate are carried out with an averaged Courant number for the whole domain of $\bar{C} = 0.0075$.

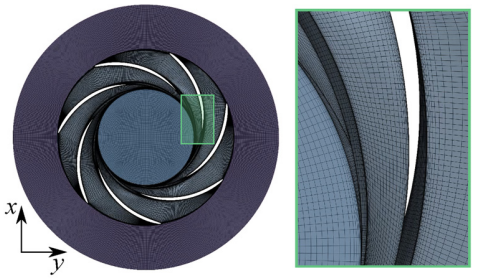

(a) Top view

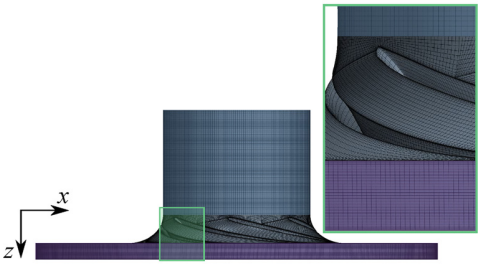

(b) Side view

FIG. 3. Top (a) and side (b) view of a typical mesh of the zero-leakage case used in URANS simulations. (The right part of each figure is a zoom-in view of the green rectangle region marked in the left part.)

E. Boundary conditions

Dirichlet, Neumann, or mixed conditions are set at the boundaries of the computational domain. The inlet velocity is specified by a Dirichlet boundary condition termed `flowRateInletVelocity` in OpenFOAM, which prescribes an inlet velocity corresponding to a pre-set value of the inlet flow rate Q. For fixed walls, the no-slip boundary condition is employed (`noSplip` in OpenFOAM), whereas the option `rotatingWallVelocity` is used for the rotating walls in order to specify the constant rotation rate of the impeller. The `inletOutlet` routine of OpenFOAM is employed with the static pressure $P = 0$ Pa at the outflow box set a boundary condition that enforces: (i) a Neumann-type zero-gradient boundary condition for the velocity field if the fluid flows out of the computational domain and (ii) a Dirichlet-type boundary condition if the velocity field in the domain would require a fluid inflow, which is obtained by extrapolation from the bulk.[27] Distinct mesh zones are coupled at their interfaces using the coupling condition `cyclicAMI`, which applies to the interfaces between (i) the inlet pipe and impeller, (ii) impeller and diffuser, and (iii) diffuser and outflow box. All the OpenFOAM routines used to model the boundary conditions are summarized in Table II.

The inlet value for the turbulent kinetic energy k_{in} is estimated by

$$k_{\text{in}} = \frac{3}{2}(I|u_{\text{ref}}|)^2, \tag{8}$$

where u_{ref} is a reference velocity given by the radial velocity at the suction pipe inlet and I is the turbulence intensity defined by

$$I = 0.16(Re)^{-\frac{1}{8}}. \tag{9}$$

The turbulent specific dissipation rate ω_{in} is calculated as

$$\omega_{\text{in}} = \frac{k_{\text{in}}^{0.5}}{C_\mu^{0.25} l}, \tag{10}$$

where C_μ is a constant equal to 0.09 and l is a reference length scale, i.e., the inlet pipe diameter in our simulations. Along the walls, we set

$$k_{\text{wall}} = 0, \quad \omega_{\text{wall}} = \frac{60\nu}{0.075 y_1^2}, \tag{11}$$

where the subscript "wall" denotes the boundary condition for the turbulence model at the pump walls and y_1 is the distance from the first cell center to the closest wall.[28]

IV. RESULTS

A. Comparison of the overall performance

The performance of the pump, encompassing the impeller and the diffuser, as well as the diffuser performance evaluated in terms of static pressure rise are obtained from the URANS simulations and compared with the experimental results, respectively, in

TABLE II. Boundary condition types used in OpenFOAM v1912.

Boundary surface	p	U	k	ω
Inlet	`zeroGradient`	`flowRateInletVelocity`	`fixedValue`	`fixedValue`
Outlet	`fixedValue`	`inletOutlet`	`inletOutlet`	`inletOutlet`
Interfaces	`cyclicAMI`	`cyclicAMI`	`cyclicAMI`	`cyclicAMI`
Fixed walls	`zeroGradient`	`noSlip`	`fixedValue`	`omegaWallFunction`
Rotating walls	`zeroGradient`	`rotatingWallVelocity`	`fixedValue`	`omegaWallFunction`

Figs. 4(a) and 4(b). Note that the volumetric flow rate Q is measured far upstream of the pump inlet, i.e., at the upstream section of the inlet pipe. The performance curve of the positive-leakage case, which is the closest configuration to the experimental setup, approaches the experimental ones the most over the whole operating range. The performance curve of the zero-leakage case is slightly above the experimental results, while the performance for the negative-leakage case lies below. Most of the experimental results are between the numerical results of the zero- and positive-leakage case, with a maximum deviation of about 5% for both cases. This is expected as the effective leakage flow of the experiments is within the positive- and the zero-leakage cases simulated by URANS. Concerning the negative-leakage case, the pressure difference between the impeller outlet and the impeller inlet section leads to a leakage flow going out at the impeller–diffuser radial gap, feeding back to the impeller inlet plane. This results in an increment of the flow rate in the impeller, leading to a larger deviation in the pump performance curve when comparing the negative-leakage case and the experimental results. Due to the presence of experimental positive inlet leakage, the flow rate inside the vaneless diffuser Q_D is bigger than the actual Q value, which is close to the impeller flow rate Q_I. Figure 5 depicts the estimated leakage flow rate ratio proposed by Heng *et al.*,[9] Heng *et al.*,[29,30] and the one obtained from our URANS simulations. The numerical positive-leakage value is about three times bigger than the experimental one, which is in accordance with the gap ratio that has been chosen to be three times bigger than in the experiments for our URANS simulations. This effect is taken into account, and the corrected performance curves based on the flow rate increment in the impeller are plotted in Fig. 6(a). The corresponding simulation results of negative-leakage get closer to the experimental ones taking into account such a correction.

The diffuser performance is shown in Fig. 4(b). With the same consideration on the leakage effect proposed above, the results of the positive-leakage case are in better agreement with the experimental data as shown in Fig. 6(b). To investigate more in-depth the diffuser behavior with three different geometries and to better compare the experiment and numerical simulation results, the diffuser pressure recovery curves at the design flow rate $Q/Q_d = 1.00$ and under fully developed low-flow rate rotating stall conditions at $Q/Q_d = 0.25$ are plotted in Fig. 7. The URANS simulations well predict the experimental diffuser performance.

B. Flow configuration of the zero-leakage case

The flow field obtained from URANS simulations of the zero-leakage case at the design flow rate is first presented in this section since it corresponds to the simplest case without the influence of the leakage flow. Note that in all the following color maps, the velocities and static pressures are nondimensionalized by

$$\hat{U}_* = \frac{U_*}{U_2}, \quad \hat{P} = \frac{P}{\frac{1}{2}\rho U_2{}^2}, \tag{12}$$

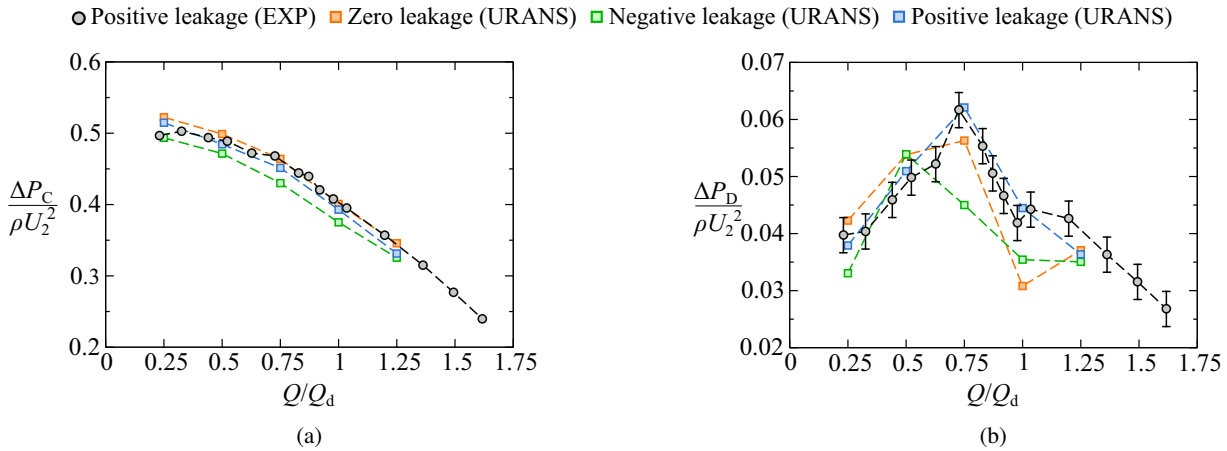

FIG. 4. Performance curves of the (a) pump and the (b) diffuser for three different geometries obtained from experimental and URANS numerical simulation results.

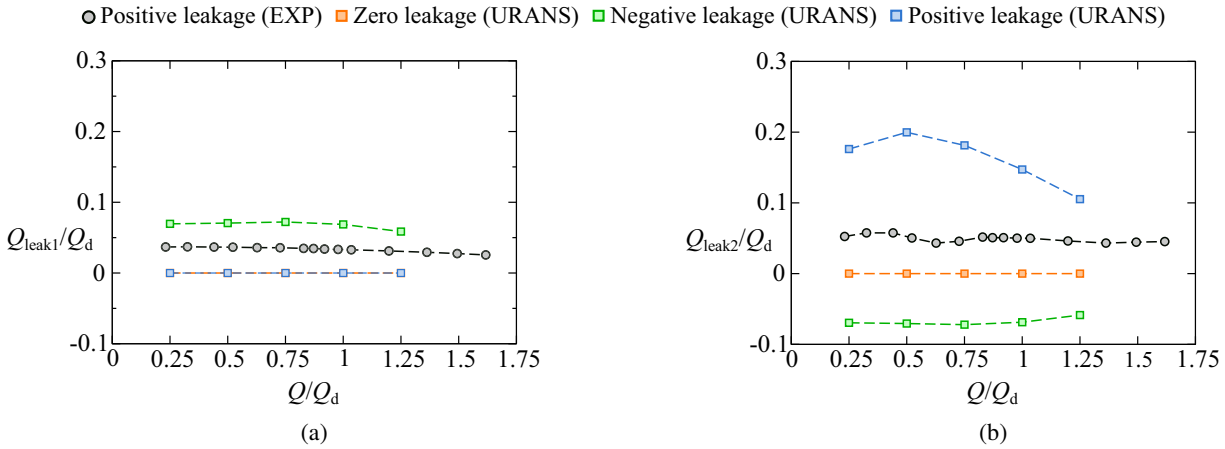

FIG. 5. (a) Inlet-impeller leakage flow rate Q_{leak1} and (b) impeller-diffuser leakage flow rate Q_{leak2} vs the flow rate of the pump Q.

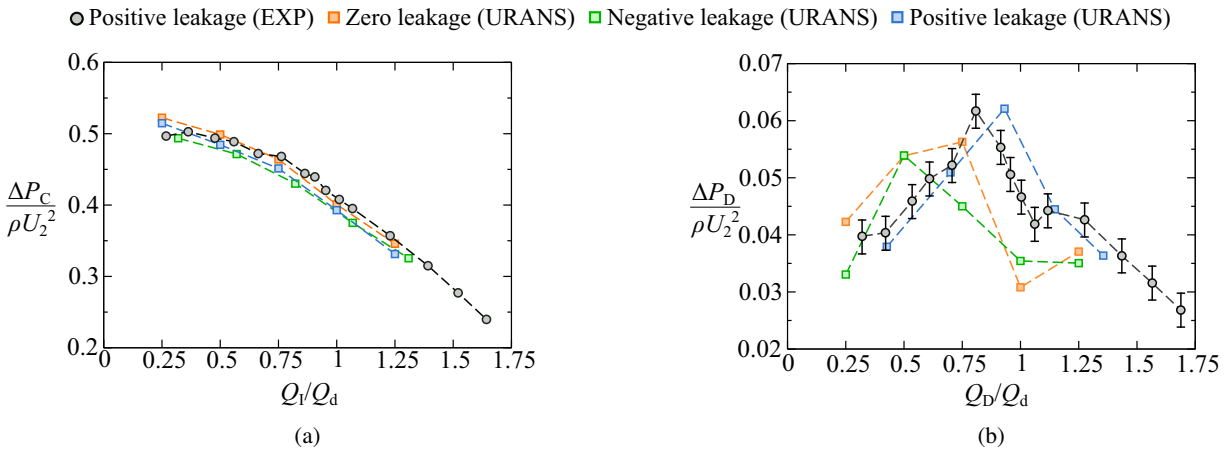

FIG. 6. Corrected performance curves of the (a) pump and the (b) diffuser for three different geometries obtained from experimental and URANS numerical simulation results.

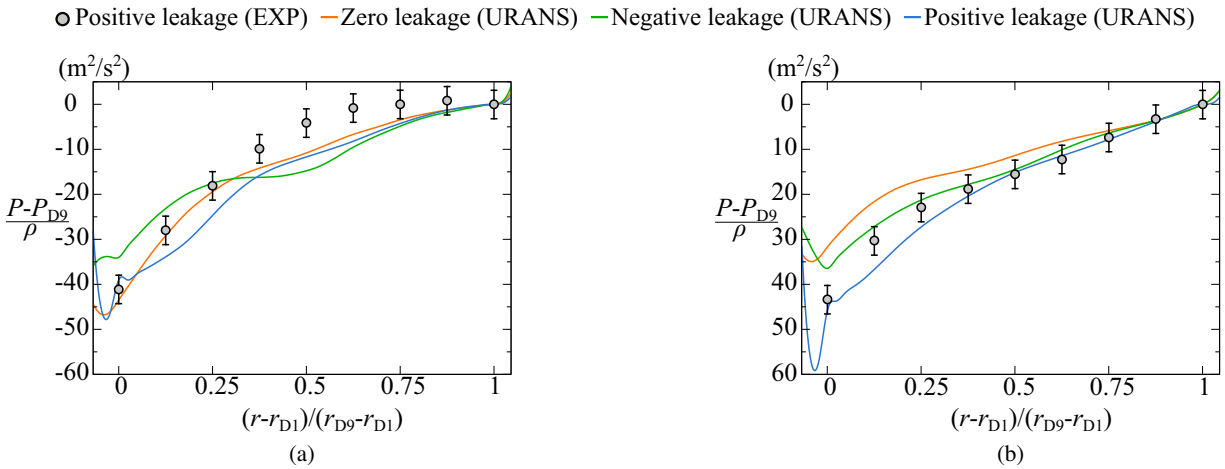

FIG. 7. Diffuser pressure recovery curves of three different geometries at the (a) design condition $Q/Q_d = 1.00$ and (b) stall condition $Q/Q_d = 0.25$.

where $* \in \{r, \theta, z\}$ and $U_2 = \omega_{imp} R_2$ is a characteristic velocity in this problem.

Figure 8 depicts the instantaneous static pressure and velocity magnitude over the meridian plane ($x = 0$). The static pressure distribution shown in Fig. 9(a) depicts the seven-periodic pattern in accordance with the impeller blade number. Hub to shroud pressure remains almost constant for a given radial and tangential location. Owing to the presence of the no-slip boundary condition over the rotating walls, the instantaneous velocity field differs from hub to shroud, as shown in Fig. 9(b). A bigger velocity magnitude is observed close to the shroud section, which corresponds to the combined effects of the meridian impeller shape and the hub diffuser limiting the deceleration as already observed in previous research papers.[11]

C. Instability at the design flow rate

1. Instability characteristics of the zero-leakage case

To investigate more in-depth the flow field at the design flow rate $Q/Q_d = 1.00$, the azimuthal arithmetic-averaged color maps at the meridian section of the diffuser and the instantaneous color maps at three different heights of the diffuser are plotted in Fig. 10 for the static pressure and the three different velocity components of the zero-leakage case. Under the influence of the non-uniform swirling inflow coming from the rotating impeller, a pronounced flow separation and a significant reverse flow can be detected close to the hub side starting from the diffuser inlet and growing further in the entire diffuser hub area [Fig. 10(a)]. The seven-periodic flow pattern is observed very clearly in all color maps, especially in the static pressure and the radial velocity field at different heights of the diffuser [Figs. 10(b)–10(d)]. The reverse flow area observed in Fig. 10(a) further reinforces the radial velocity component due to blockage effects.

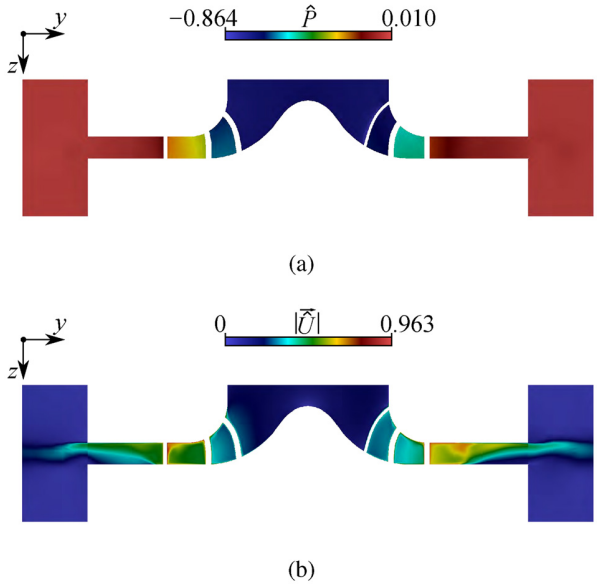

FIG. 8. Color maps of instantaneous (a) static pressure and (b) velocity magnitude distribution over the meridian section ($x = 0$) of the pump at the design flow rate $Q/Q_d = 1.00$ obtained by the URANS simulation.

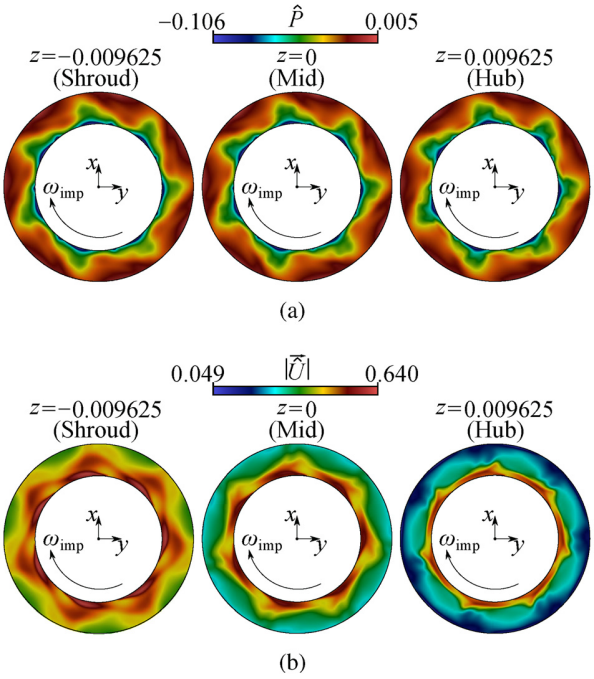

FIG. 9. Color maps of instantaneous (a) static pressure and (b) velocity magnitude distribution over three different heights of the diffuser at the design flow rate $Q/Q_d = 1.00$ obtained by the URANS simulation.

A complementary analysis is carried out using a Fourier decomposition of the cross-power spectrum using the URANS simulation results from two numerical probes located at the mid-radial distance of the diffuser shroud wall. These two numerical probes have an angular phase shift of 60°. In fact, the analysis of the cross-power spectra of two pressure probes located at the same radius but at two different angular positions enables the detection of rotating phenomena[31,32] and gives their characteristics in terms of a number of cells and propagation velocity. The cross-power spectrum of the zero-leakage case is shown in Fig. 11(a). The blade-passing-to-impeller-frequency ratio $f_{blade}/f_{imp} = 7$ can be observed very clearly as expected, where f_{blade} and f_{imp} denote the blade passing and the impeller frequency, respectively. Another frequency is detected corresponding to $f/f_{imp} = 1.543$. As this frequency is not compatible with any of the super-/sub-harmonics of the impeller or blade-passing frequencies, respectively, the flow was simulated for one additional impeller revolution in order to inspect the origin of such an unexpected frequency. The video of the corresponding velocity magnitude is given as supplementary material. By visual inspection of the video, we figured out that the frequency $\tilde{f}/f_{imp} = 1.543$ is compatible with a rotating pattern having a propagation velocity that is approximately estimated to be about five times slower than the impeller velocity. Moreover, the amplitude of the rotating pattern is also consistent with the amplitude of the cross-power spectra of the two probe signals in the vaneless diffuser.

A more quantitative analysis was, therefore, required to further clarify the origin of the incommensurate frequencies in the FFT. As the highest amplitude of the cross-power spectrum is produced by such an unexpected rotating pattern, the rotational velocity can

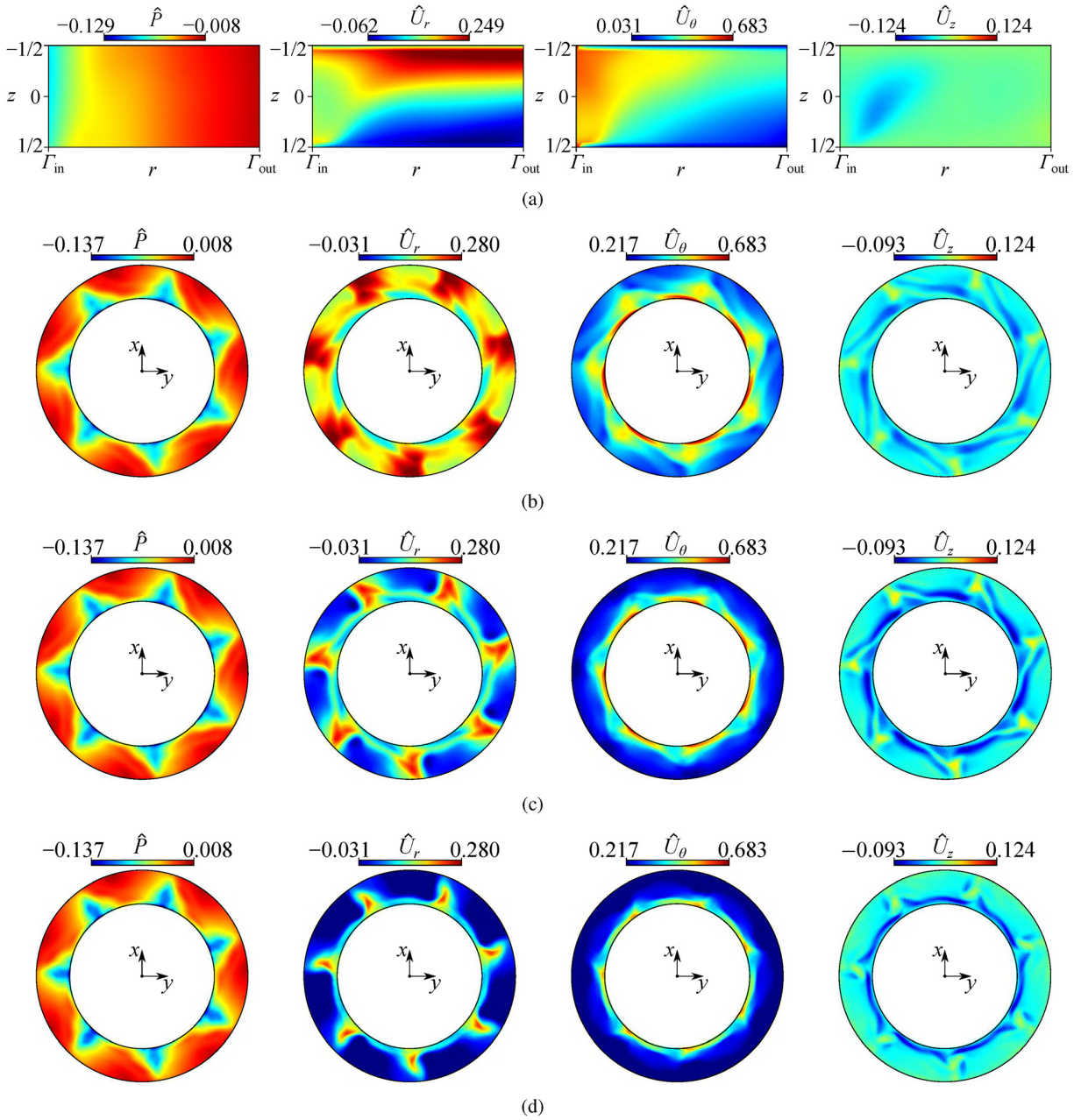

FIG. 10. Color maps (from left to the right side) of instantaneous static pressure, radial velocity, tangential velocity, and axial velocity distribution at (a) the meridian section of the pump (azimuth arithmetic average values), (b) shroud side, (c) mid-height, and (d) hub side of the diffuser at the design flow rate $Q/Q_d = 1.00$ of the zero-leakage case obtained by the URANS simulation.

be quantified by $\tilde{f}/f_{imp} = 1.543$, corresponding to $\tilde{\omega}/\omega_{imp} = 0.22$. This propagation velocity is, therefore, consistent with the about-five-times-slower pattern rotating around the blade wake observed in the video. The slow rotating pattern is moreover consistent with the rotating instability reported by Ljevar *et al.*,[10] who investigated the core flow in a vaneless diffuser varying the blade jet-to-wake intensity, the number of blades and the outlet-to-inlet diffuser radius ratio. By employing a two-dimensional model, hence neglecting the boundary layers on the hub and the shroud, they report a rotating instability whose mode, propagation speed, and critical conditions depend on the three parameters of their study. For $R_4/R_3 = 1.48$ corresponding to our diffuser, their data lead to either a six- or a seven-periodic pattern

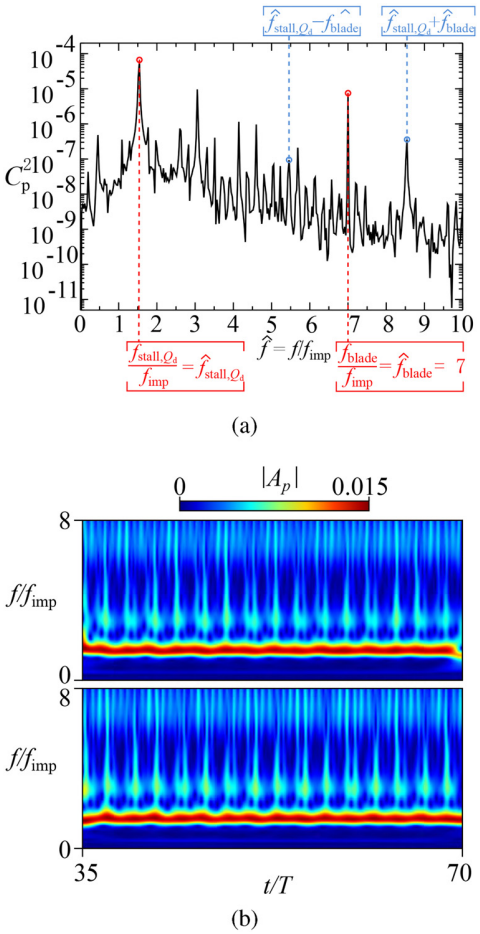

FIG. 11. (a) Fourier and (b) wavelet analyses of the URANS simulation of the zero-leakage case at the design flow rate $Q/Q_d = 1.00$.

for the rotating instability, which is consistent with our observations. Moreover, the propagation velocity of their rotating stall is about $\omega_{\mathrm{stall},Q_d}/\omega_{\mathrm{imp}} = 0.3$, which is of the same order of our $\tilde{\omega}/\omega_{\mathrm{imp}} = 0.22$ even if slightly faster. This can be explained by considering that in our three-dimensional flow, the boundary layer tends to oppose resistance to the rotating stall at nominal flow conditions, resulting in a slowed-down rotating pattern. Further considering that our core flow has a blade jet-to-wake angle smaller than the critical angle predicted by Ljevar *et al.*[10] below which the rotating stall occurs, we infer that the rotating pattern producing the frequency $\tilde{f}/f_{\mathrm{imp}} = f_{\mathrm{stall},Q_d}/f_{\mathrm{imp}} = 1.543$ is, indeed, a rotating instability.

The other peaks of the power spectrum correspond to sub-/super-harmonics of the fundamental frequencies or nonlinear interactions among them. Further quantification of this complex flow topology is investigated by two independent wavelet analyses carried out for the two probe signals used for the cross-power spectrum [see Fig. 11(b)]. Both wavelet analyses reveal extra details. In fact, in addition to the blade passing $f_{\mathrm{blade}}/f_{\mathrm{imp}} = 7$ and the rotating instability frequency $f_{\mathrm{stall},Q_d}/f_{imp} = 1.543$ detected by Fourier analysis, we also observe an intermittent phenomenon whose frequency of about $f/f_{\mathrm{imp}} \approx 3$. Because of the nonlinear interactions between the rotating stall and the shear layer of the impeller discharge, a pulsating high-order effect emerges at the cusps of the slow rotating flow pattern. This is depicted in the four snapshots shown in Fig. 12 for one pulsating frequency, i.e., for $t/T \in [70.18, 70.29]$. The robustness of such a pulsating pattern is demonstrated by the identification of the corresponding wavelet features for more than the last 40 revolutions of the impeller, and the corresponding breathing pattern is well depicted in the wavelet analysis [Fig. 11(b)] for the last 35 revolutions.

To further quantify the number of stall cells and visualize their topology, the unsteady flow field associated with the rotating instability is phase-averaged. The corresponding color maps are produced with 120-time steps of the last revolution for two rotating reference frames. Figure 13(a) shows the averaged flow field in a reference frame rotating with the impeller. A mode-7 jet-wake flow rotating with the impeller can be observed near the diffuser inlet as expected. In addition, Fig. 13(b) shows the averaged flow field in a reference frame rotating with the propagation velocity of the instability. Another seven-periodic pattern can be observed, consistently with the prediction of Ljevar *et al.*[10] Therefore, two different kinds of azimuthally traveling patterns exist at the same time at the design flow rate $Q = Q_d$ for the zero-leakage case. The first one is expected to correspond to the classical jet-wake pattern, while the second one is consistent with the literature and found for the first time in our pump. Moreover, subtracting the phase-averaged jet-wake pattern from the total flow, Fig. 13(c) demonstrates that the pulsating mode observed in Fig. 11(c) is azimuthally stationary in a reference frame rotating with $\omega_{\mathrm{stall},Q_d}$, and it is produced near the boundary of the jet wake and advected downstream toward the outlet of the diffuser. To the best of the authors' knowledge, this secondary instability has never been reported in the literature.

The leakage between the impeller and the diffuser changes the inflow conditions of the vaneless diffuser, and a significant influence on the corresponding bulk flow is, therefore, expected. The effect of leakage flow on the diffuser at design flow rate $Q = Q_d$ is, therefore, analyzed in this section, considering the azimuthally averaged color maps at the meridian section and the instantaneous color maps at the mid-height section in the vaneless diffuser for our three numerical configurations. For the zero-leakage case [see the Appendix C (a)], the flow field is most significantly influenced by the impeller jet wake and the emerging of the rotating stall described in Sec. IV C 1. For the negative-leakage case [see the Appendix C (b)], the flow rate in the diffuser does not change significantly, which means that the inflow conditions at the diffuser resemble the ones observed for the zero-leakage case. The flow field in the negative-leakage case is, therefore, found to be similar to the corresponding one for the zero-leakage case, where seven-periodic patterns (both from the impeller jet wake and from the rotating stall) can clearly be identified. For the positive-leakage case [see the Appendix C (c)], on the other hand, the leakage flow entering the diffuser from the hub and the shroud side is stronger and has a stabilizing effect on the periodic pattern of the jet wake as the effective flow angle increased (see Ljevar *et al.*[10]). This leads to a more symmetrical azimuthally averaged velocity distribution in z and to a more complicated and less symmetrical core flow at the midplane. The increased significance of the leakage flow for the positive-leakage case is further confirmed in Fig. 14 that depicts the axial velocity profile at the diffuser inlet for all three pump configurations. The zero- and negative-leakage cases have very similar axial

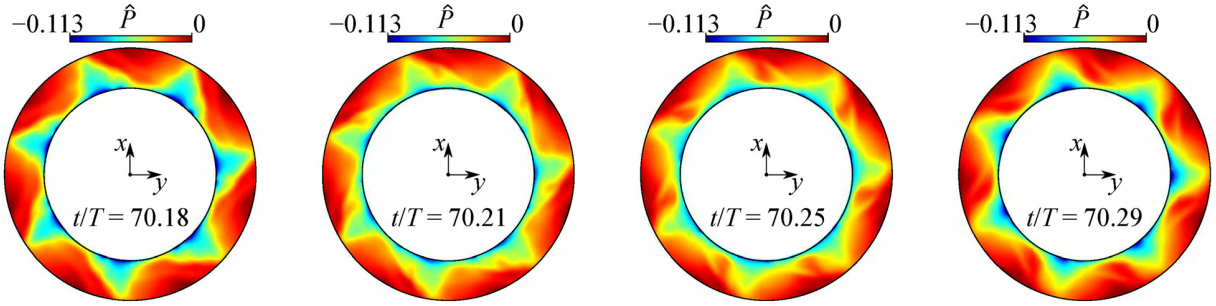

FIG. 12. Snapshots of the static pressure color map of the zero-leakage case at the design flow rate $Q/Q_d = 1.00$ at different calculation time $t/T \in [70.18, 70.29]$.

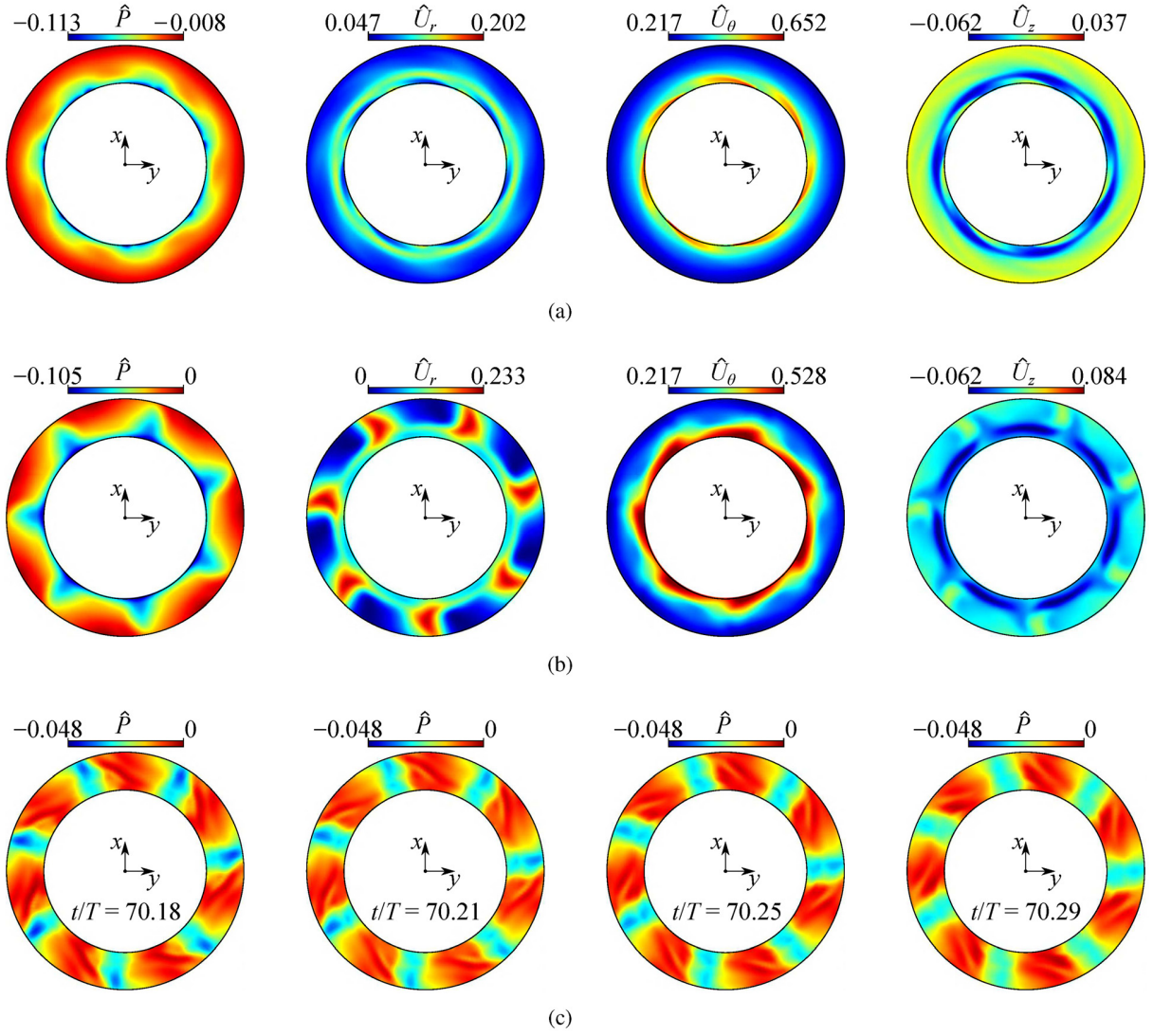

FIG. 13. Phase-averaged color maps of the static pressure, radial velocity, tangential velocity, and axial velocity with (a) the impeller rotating velocity ω_{imp}, and (b) the instability propagation velocity ω_{stall,Q_d} of the zero-leakage case at design condition $Q/Q_d = 1.00$, and (c) the snapshots of the static pressure field subtracted the phase-averaged flow with ω_{imp} for $t/T \in [70.18, 70.29]$.

velocity profiles, whose maximum absolute values at the design flow rate are about 2% to 5% of the maximum tangential velocity of the jet wake. On the other hand, the positive-leakage case has an axial velocity, whose maximum values are about 20% of $\max(U_\theta)$. This explains how the far more significant values of U_z for the positive-leakage case at the diffuser inlet are capable of remarkably perturbing the blade's wake. As the jet-wake flow at the diffuser entrained air through the radial gap (positive-leakage flow), the critical conditions needed to trigger the seven-periodic rotating stall are not met. This explains why the seven-periodic pattern far from the diffuser inlet is not observed in the instantaneous flow fields of the core flow for the positive-leakage case. In fact, the seven-periodic pattern due to the rotating stall detected by visual inspection of the core-flow videos for the zero- and negative-leakage cases can no longer be found in the positive-leakage case.

A more quantitative analysis was, therefore, carried out to further substantiate the interpretation of the qualitative evidence derived by visual inspection of the core-flow videos. Figure 15 presents the comparison of the FFT and wavelet analysis for the URANS simulations and the experiments at the design flow rate $Q = Q_d$. In agreement with the qualitative inspection, a rotating instability is signaled for zero- and negative-leakage case [see Figs. 15(a) and 15(b)]. For the negative-leakage case [Fig. 15(b)], the frequency components are similar to the ones detected for the zero-leakage case. However, the secondary instability leading to a pulsating flow traveling with the primary rotating stall instability is not as clear in the wavelet analysis as it was for the zero-leakage case. This leads to conclude that even a small leakage flow may significantly impact the secondary instability. On the other hand, such a small leakage does not remarkably affect the primary instability. This is confirmed by Table III that reports the primary rotating instability characteristics for all our cases. The propagation velocity $\omega_{\text{stall},Q_d}/\omega_{\text{imp}} = 0.22$ measured for the numerical simulations in the zero-leakage case gets only slightly modified by the negative-leakage, passing to $\omega_{\text{stall},Q_d}/\omega_{\text{imp}} = 0.224$. For the positive-leakage case [Fig. 15(c)], only the blade-passing frequency can be observed. This is in good agreement with experiments [Fig. 15(d)] as they are produced in a similar positive-leakage configuration. As anticipated by inspecting the core-flow videos, no rotating stall frequency is found in the Fourier spectrum of the positive-leakage cases [URANS simulations, Fig. 15(c), and experiments, Fig. 15(d)].

Figure 16 shows the comparison of the phase-averaged flow field in a reference frame rotating with the impeller at ω_{imp}. The color maps for the three different geometries show that the seven-periodic jet-wake pattern near the diffuser inlet always exists in the phase-average flow, even for the positive-leakage flow whose instantaneous flow field did not clearly show the jet-wake periodic pattern. The jet-wake pattern found by phase averaging is consistent with the Fourier analysis, thanks to which the blade-passing frequency could be identified in the frequency spectrum. As the propagation velocity of the rotating stall does not significantly change with the leakage flow, Fig. 17 shows the comparison of the phase-averaged flow field in a reference frame rotating with $\omega_{\text{stall},Q_d} = 0.22\omega_{\text{imp}}$. For the zero- and the negative-leakage cases, the corresponding seven-periodic pattern of the rotating stall is found far from the diffuser inlet. On the other hand, for the positive-leakage case, this kind of instability does not occur, hence no major non-zero modal coherence is found in the respective phase-average core flow rotating with $\omega_{\text{stall},Q_d} = 0.22\omega_{\text{imp}}$. This observation is consistent with the corresponding FFT and wavelet analysis.

D. Effect of the flow rate on the flow field for the zero-leakage case

1. Flow field analysis

To understand how the flow in the vaneless diffuser is affected by the flow rate Q, we vary the inflow conditions at the inlet pipe ranging from $Q/Q_d = 1.25$ down to $Q/Q_d = 0.25$. The azimuthally averaged color maps at the meridian section (Fig. 18) and the instantaneous color maps of the mid-height of the diffuser (Fig. 19) are depicted for five flow rates $Q/Q_d \in [0.25,\ 1.25]$ with $\Delta Q/Q_d = 0.25$, where ΔQ is the increment in the flow rate at the inlet pipe. The static pressure and the three velocity components are also analyzed separately to better distinguish the flow structures within the velocity field.

Looking at Fig. 18(a), the plot of the radial velocity at the largest flow rate ($Q/Q_d = 1.25$) indicates that the bulk flow in the diffuser passage is dominated by inviscid effects. Indeed, it well resemble an Euler-flow solution except for the azimuthally averaged reverse flow region (blue area in U_r). Under the influence of the non-uniform swirling inflow coming from the rotating impeller, the incoming jet forces the blockage of the vortexes, which are pushed toward the diffuser outlet and confined near the walls. Flow separation and reverse flow occur up to a large extent near the outlet of the hub (not shown). The color maps at the mid-height of the diffuser [Fig. 19(a)] show that the velocity and the pressure are regularly distributed, and the main flow streamline is a nearly logarithmic spiral curve. In addition, the jet-wake pattern can be clearly observed in the color map of the static pressure distribution with seven high-pressure peaks. In these flow conditions, the increase in the mean flow angle is responsible for the

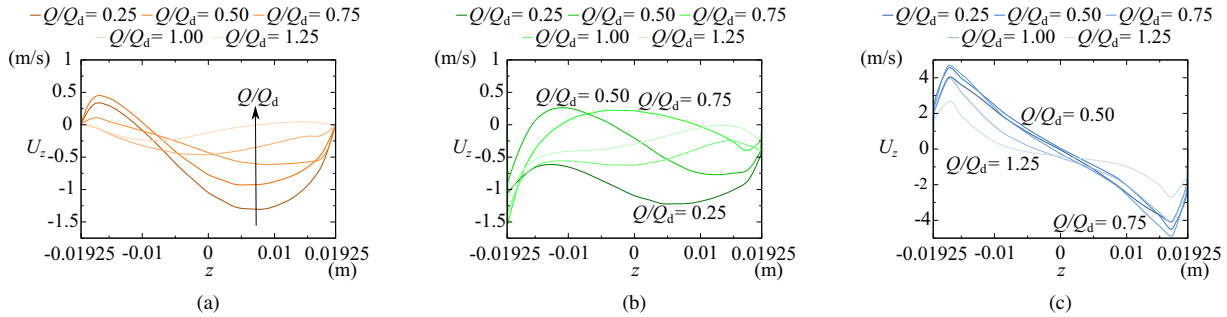

FIG. 14. Axial velocity profiles at the diffuser inlet of (a) the zero-leakage case, (b) the negative-leakage case, and (c) the positive-leakage case.

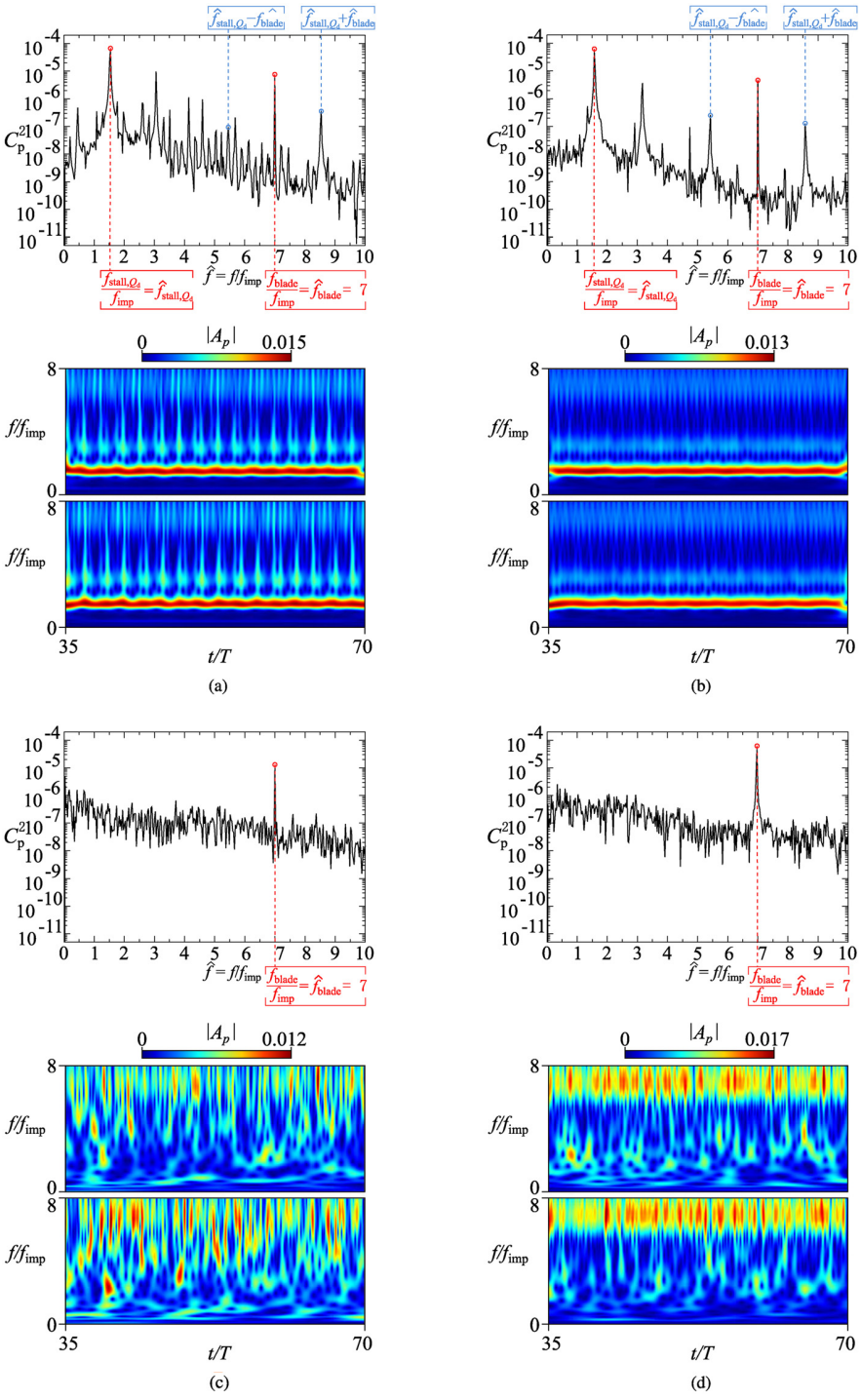

FIG. 15. Fourier and wavelet analyses of the URANS simulation for (a) the zero-leakage case, (b) the negative-leakage case, and (c) the positive-leakage case, and of (d) the experiment, at the design flow rate $Q/Q_d = 1.00$.

stabilization of the flow [see Fig. 9(a) of Ljevar *et al.*[10]], and no jet-wake-induced rotating instability was observed.

As the flow rate decreases down to the design flow rate, i.e., for $Q/Q_d = 1.00$, Fig. 18(b) shows that the reverse flow region becomes surface-filling over the hub [see blue zone in U_r, Fig. 18(b)], occupying almost half of the diffuser passage in the z-direction. We recall that a core-flow rotating instability has been identified for the $Q/Q_d = 1.00$ design flow rate (see Sec. IV C 1). The massive reverse flow is due to the

TABLE III. Propagation velocity of the rotating instability obtained by the cross correlation analysis at the design flow rate $Q/Q_d = 1.00$.

Case	Zero-leakage (URANS)	Negative-leakage (URANS)	Positive-leakage (URANS and Exp)
$f_{stall,Q_d}/f_{imp}$	1.543	1.571	...
$\omega_{stall,Q_d}/\omega_{imp}$	0.220	0.224	...

significant pressure and velocity magnitude of the rotating stall at the design flow rate. In fact, the same mean flow separation is observed for the negative-leakage case, where the rotating stall has been identified [see Appendix C (b)]. On the other hand, no rotating stall instability has been found for the positive-leakage case at the design flow rate, and the reverse flow region is almost absent in the azimuthally average flow [see Appendix C (c)]. Consistently, we further recall that no massive flow separation has been observed for $Q/Q_d = 1.25$ in the zero-leakage flow [see Fig. 19(a)] as the rotating stall does not occur. These points toward a clear indication that the rotating stall phenomenon described in Sec. IV C 1 is responsible for the distinct massive azimuthally averaged reverse flow region observed in the diffuser. This is consistent with the observations of Ljevar *et al.*[10] (see Figs. 3 and 4 of their paper).

As the flow rate further decreases to $Q/Q_d = 0.75$, Fig. 18(c) shows that the influence of the asymmetrically distributed inflow velocity weakened. This is consistent with the interpretation of the rotating stall being responsible of the azimuthally averaged reverse flow region. In fact, for $Q/Q_d = 0.75$, no rotating stall is observed as the decrease in the jet-wake intensity led to a stabilization of the flow. This is demonstrated in Fig. 19(c), whose color maps at the mid-height of the diffuser show that the seven-periodic rotating instability pattern disappeared [cf. with the rotating stall observed at the design flow rate $Q/Q_d = 1.00$, Fig. 19(b)]. Owing to the mass conservation law and the friction loss, the radial velocity tends to decrease along the diffuser radius, although it increases near the inlet under the effect of the increased boundary layer thickness. Azimuthally averaged flow separation and reverse flow regions can be observed near the shroud and hub walls.

Upon a decrease in the flow rate down to $Q/Q_d = 0.5$, a stronger flow separation occurs especially near the diffuser inlet of the hub side. Moreover, the mean flow inside the vaneless diffuser becomes more skewed [see Fig. 18(d)], and several backflow regions can be observed near the diffuser outlet [see Fig. 19(d)]. Three rotating stall cells are apparent, especially considering the pressure and the azimuthal flow fields at midplane [see leftmost and second-right panels in Fig. 19(d)]. This rotating instability has previously been reported by several authors who investigated it numerically and experimentally.[11,12,30] The associated azimuthally averaged reverse flow regions are not as evident as for the rotating stall at the design flow rate [cf. Figs. 18(b) and 18(d)]. We speculate that this is due to the weaker energy transfer from the jet-wake to the rotating stall upon a decrease in the flow rate.

For the lowest flow rate $Q/Q_d = 0.25$, Fig. 18(e) shows that the high-radial velocity region moved toward the diffuser inlet, and the mean flow near the diffuser inlet tends to exhibit a clearer S-shape with reverse flow near the shroud and hub walls close to the vaneless diffuser inlet. As the flow rate decreased, the rotating stall became more supercritical, and the mode-3 patter can more clearly be distinguished. In fact, three rotating stall cells composed of a core of outward radial velocity followed by a zone of inward radial velocity are quite well identifiable in

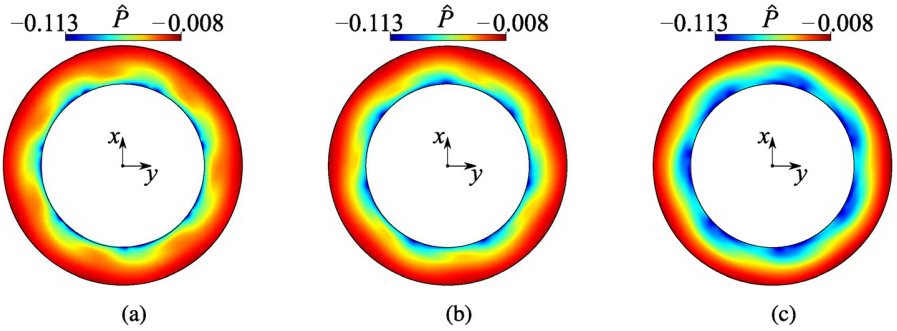

FIG. 16. Color maps of phase-averaged static pressure at the mid-height of the diffuser based on the impeller rotating speed ω_{imp} at the design flow rate $Q/Q_d = 1.00$ for (a) the zero-leakage case, (b) the negative-leakage case, and (c) the positive-leakage case.

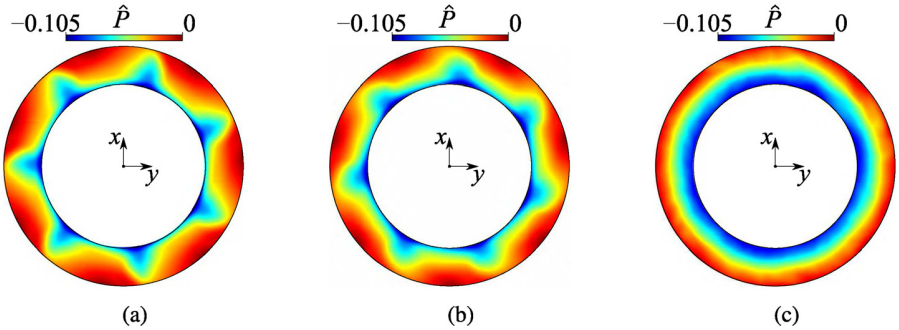

FIG. 17. Color maps of phase-averaged static pressure at the mid-height of the diffuser based on the instability propagation speed ω_{ins} at the design flow rate $Q/Q_d = 1.00$ for (a) the zero-leakage case, (b) the negative-leakage case, and (c) the positive-leakage case.

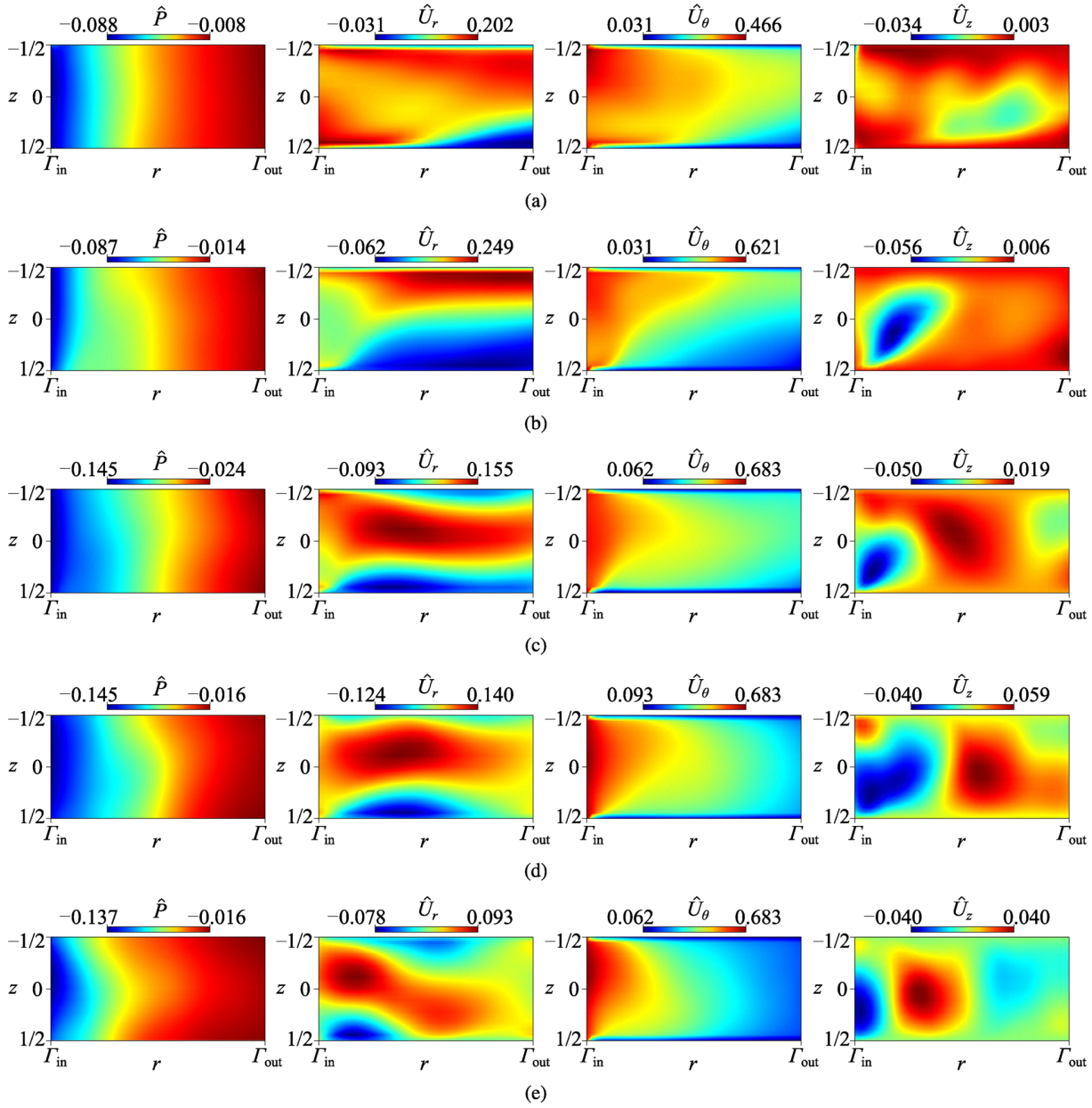

FIG. 18. Color maps of the azimuth averaged instantaneous static pressure, radial velocity, tangential velocity, and axial velocity at the meridian section of the diffuser at the flow rate (a) $Q/Q_d = 1.25$, (b) $Q_d = 1$, (c) $Q/Q_d = 0.75$, (d) $Q/Q_d = 0.50$, and (e) $Q/Q_d = 0.25$.

the color maps at the mid-height of the diffuser [see Fig. 19(e)]. The core flow changes are associated with the wake-jets coming out of the impeller discharge. Moreover, the streamlines inside the vaneless diffuser are strongly distorted and are far from the ideal logarithmic spiral curve, especially in the area corresponding to the low-velocity regions. These same observations are reported in the literature and are in significant agreement with the PIV visualizations performed for the same type of vaneless diffusers.[12]

E. Rotating stall at the smallest flow rates

1. Instability mechanism

At large-enough flow rates, if the rotating stall does not occur (see, e.g., $Q/Q_d = 1.25$ and $Q/Q_d = 0.75$ for the zero-leakage case), the core flow away from the walls experiences a quasi-two-dimensional development from the diffuser inlet to the outlet, and the flow streamlines follow a nearly logarithmic spiral curve. Upon a decrease in the

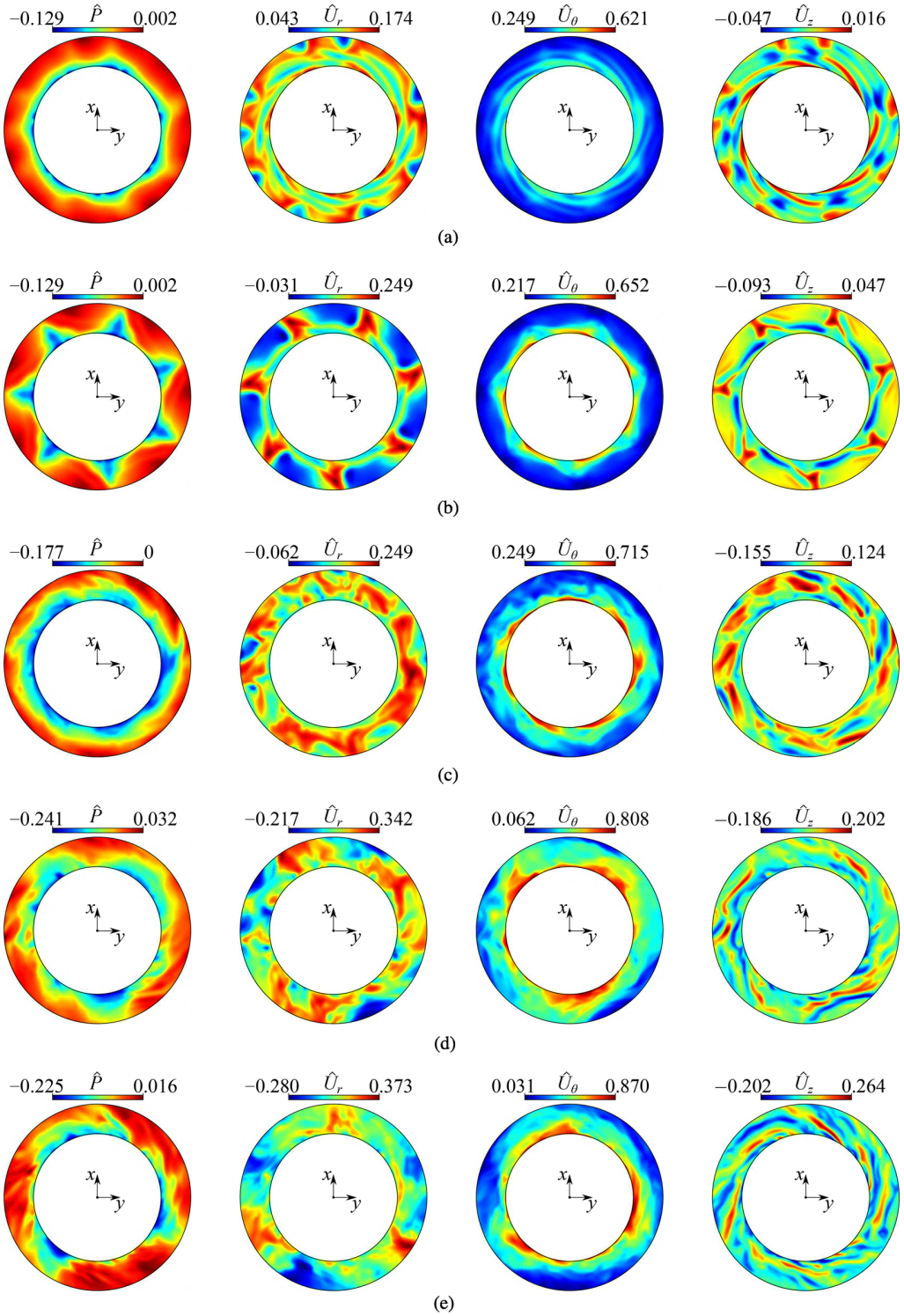

FIG. 19. Color maps of instantaneous static pressure, radial velocity, tangential velocity, and axial velocity at the mid-height of the diffuser at the flow rate (a) $Q/Q_d = 1.25$, (b) Q_d, (c) $Q/Q_d = 0.75$, (d) $Q/Q_d = 0.50$, and (e) $Q/Q_d = 0.25$.

flow rate, the rotating stall at low design flow rates can, therefore, be studied as a core-flow instability if the boundary layers along the shroud and the hub of the vaneless diffuser are thin. This is the case of so-called "wide" diffusers. We stress that the two-dimensional core instability argument holds if the turbulent boundary layers on the diffuser walls do not exhibit significant three-dimensional features leading to flow separations that may occur owing to the high adverse pressure gradient produced by the radial increase in the diffuser section in the $(\phi, z)-$ plane when moving from inlet to outlet.

Under the hypothesis of a two-dimensional core-flow mechanism, we employ the analytical model of Tsujimoto *et al.*[8] in order to characterize the components of the energy budget leading to a transfer of energy from the two-dimensional basic state to the two-dimensional most-dangerous infinitesimal perturbation. This linear stability analysis has successfully predicted the mode-3 instability observed in Heng *et al.*[9] and Heng *et al.*[29,30] [see Figs. 19(d) and 19(e)], and it will further help to clarify the origin of the rotating stall at low flow rates. We, however, anticipate that the corresponding low-flow rate rotating stall is somehow simpler than the rotating stall observed at the design flow rate for the zero- and the negative-leakage flow. In fact, in the latter case, the rotating instability is strongly affected by the non-homogeneous forcing in the θ-direction. On the contrary, at low flow rates, the mechanism proposed by Tsujimoto *et al.*[8] relies exclusively on the skewness of the diffuser inflow and does not involve any inhomogeneous forcing in θ. In fact, the analytical model of Tsujimoto *et al.*[8] considers an infinite number of blades, hence a uniform inflow in θ, which is solely characterized by its jet-wake angle.

For the model of Tsujimoto *et al.*,[8] several assumptions were made:

- a two-dimensional incompressible and inviscid flow is considered,
- the boundary conditions are axisymmetric, i.e., uniform static pressure at diffuser outlet and imposed velocity magnitude and flow angle at inlet,
- the flow field is described as a superposition of a steady basic state and an infinitesimal rotating perturbation determined by linear stability analysis.

Within such assumptions, the basic state streamlines in the vaneless diffuser are logarithmic spirals from diffuser inlet to outlet. Hence, the basic state solution is essentially one-dimensional as it is invariant to rotation along the logarithmic spiral. Non-dimensionalizing by using the quantities R_3, $(2\pi R_3^2)/Q$, $Q/2\pi R_3$, and $\rho Q^2/(2\pi R_3)^2$ to scale length, time, velocity, and pressure, respectively, the basic state velocity $\vec{U}_0 = (U_{0,r}, U_{0,\theta})$ and pressure P_0 read

$$\begin{aligned} U_{0,r} &= \frac{1}{r}, \\ U_{0,\theta} &= \frac{\mu}{r}, \\ P_0 &= -\frac{1}{2}(1+\mu^2)\left(\frac{1}{r^2}+\frac{1}{R^2}\right), \end{aligned} \tag{13}$$

where $\mu = U_{0,\theta}/U_{0,r}|_{r=1}$ and $1 < r < R = R_4/R_3$. We further remark that such a basic state is irrotational, i.e., $\nabla \times \vec{U}_0 = 0$. Carrying out a linear stability analysis, the total flow in the vaneless diffuser results from the sum of the basic state and the infinitesimal perturbation (prime sign),

$$\begin{aligned} U_r &= U_{0,r}(r) + u'_r(r,\theta,t), \\ U_\theta &= U_{0,\theta}(r) + u'_\theta(r,\theta,t), \\ P &= P_0(r) + p'(r,\theta,t), \end{aligned} \tag{14}$$

where $\vec{u}' \ll \vec{U}_0$ and $p' \ll P_0$. As the basic state is steady and homogeneous in θ, the ansatz for the infinitesimal perturbation is

$$\{u'_r, u'_\theta, p'\}(r,\theta,t) = \{\tilde{u}_r, \tilde{u}_\theta, \tilde{p}\}(r) e^{i\xi t - im\theta}, \tag{15}$$

where m is the wavenumber, i.e., the number of rotating stall cells. The complex frequency ξ could be divided in a real χ and complex σ part, i.e., $\xi = \chi - i\sigma$. The real part χ is the angular frequency, while σ is the growth rate of the instability. The flow is unstable (stable) when $\sigma > 0$ ($\sigma < 0$), and the mathematical problem is closed by enforcing the boundary conditions proposed by Tsujimoto *et al.*,[8]

$$r = 1 : \tilde{u}_r = \tilde{u}_\theta = 0; \quad r = R : \tilde{p} = 0. \tag{16}$$

The neutral stability modes are then obtained by setting $\sigma = 0$, fixing m, and following the algorithm proposed by Heng *et al.*,[9] which makes use of a shooting method for approaching the analytical solution by successive iterations.

An *a posteriori* analysis of the kinetic energy transferred between the basic state and the critical mode is here employed to identify the physical mechanisms leading to the flow instability and to validate the overall energy conservation of our neutral mode. To that end, we numerically evaluate all terms of the inviscid Reynolds–Orr-equation,

$$\frac{dE^{kin}}{dt} = \sum_{k=1}^{4} \int_V I'_k dV + K^{out}, \tag{17}$$

where E_{kin} is the total kinetic energy, I'_k is the kinetic energy densities resulting from the nonlinear term of the incompressible Euler equations, and

$$K^{\text{out}} = -\frac{1}{2}\int_S U_{0,r} u'^2_r S^{\text{out}} \tag{18}$$

is the transport of perturbation energy through the outlet surface S^{out}. Since $\tilde{u} = 0$ at the inlet, no perturbation energy is advected into the system from upstream. Moreover, the work done by pressure forces does not contribute to the energy budget as we assume that the pressure perturbations vanish at the outlet (i.e., $\tilde{p} = 0$ at $r = R$). To ease the interpretation of the energy budget, the local energy production rates are decomposed along the streamline coordinates of the basic state, i.e.,

$$\vec{u}' = \vec{u}'_\parallel + \vec{u}'_\perp, \tag{19}$$

where $\vec{u}'_\parallel$ is the perturbation component projected along the basic state streamlines, while $\vec{u}'_\perp = \vec{u}' - \vec{u}'_\parallel$ is the normal component. The corresponding energy density terms I'_k read

$$\begin{aligned} \sum_{k=1}^{4} I'_k = -\Big[&\vec{u}'_\perp \cdot (\vec{u}'_\perp \cdot \nabla \vec{U}_0) + \vec{u}'_\parallel \cdot (\vec{u}'_\perp \cdot \nabla \vec{U}_0) + \vec{u}'_\perp \cdot (\vec{u}'_\parallel \cdot \nabla \vec{U}_0) \\ &+ \vec{u}'_\parallel \cdot (\vec{u}'_\parallel \cdot \nabla \vec{U}_0)\Big], \end{aligned} \tag{20}$$

where k numbers all terms on the right-hand side consecutively. The sign of the integrands I'_k determines whether the local energy transfer acts as a destabilizing (positive) or a stabilizing (negative) contribution.

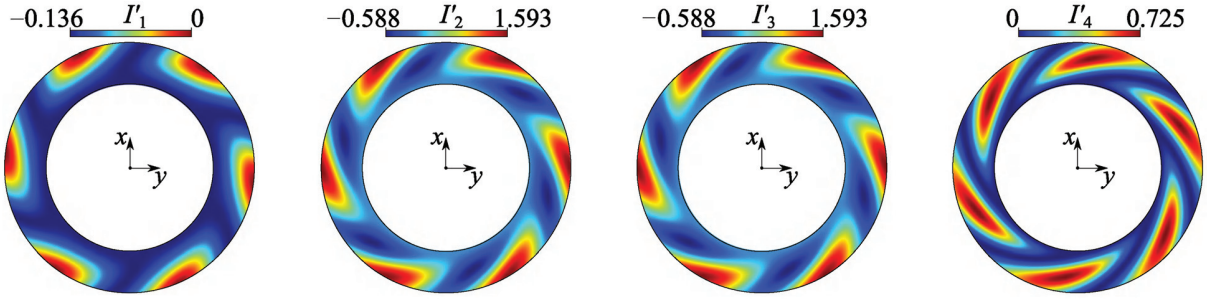

FIG. 20. Color maps of normalized local energy-transfer terms.

If the rate of change of the kinetic energy $\frac{dE^{kin}}{dt}$ is positive, the basic flow is unstable and vice versa. Hence, the energy budget is also used to verify the linear stability results because the rate of change of the kinetic energy must vanish for the neutral modes, i.e.,

$$\left.\frac{dE^{kin}}{dt}\right|_{\sigma=0} = 0. \tag{21}$$

In our computations, such a condition is verified at the fifth digit; hence, we can consider our computation of the neutral mode validated.

The scalar field of the energy production rates in the bulk is given in Fig. 20 for the critical modes, i.e., for $m = 3$. As they result from the energy density of the perturbation (hence they involve the square of the perturbation velocity), their wavenumber is twice the perturbation m. Figure 20 clearly identifies a mode-3 critical perturbation, in agreement with what already reported in the mid-height colormaps for our URANS simulations. Moreover, the spiraling character of the I'_k fields is characteristic of a rotating instability, hence of rotating stall. We anticipate, however, that we find that the critical propagation velocity obtained by the model of Tsujimoto *et al.*,[8] $\chi = 0.289$, is larger compared to our URANS simulations. This is expected because the two-dimensional model of Tsujimoto does not account for the resistance due to the hub and shroud wall.

To complement the qualitative interpretation done so far relying on the scalar fields of I'_k, Fig. 21 reports the total energy budget. Our results show that $\int_V I_2' dV$, $\int_V I_3' dV$, and $\int_V I_4' dV$ are contributing to the destabilization of the basic state, with $\int_V I_4' dV$ being slightly dominant in magnitude. On the other hand, $\int_V I_1' dV$ has a minor stabilizing effect, while most of the energy produced by $\int_V I_2' dV$, $\int_V I_3' dV$, and $\int_V I_4' dV$ is transported outside of the diffuser leading to a high-magnitude, negative K^{out}. There are, therefore, two mechanisms contributing to the instability of the diffuser basic state:

1. The lift-up mechanism, which describes how the basic flow momentum is transported in normal direction to the basic state streamlines by $\vec{u}'_\perp \cdot \nabla \vec{U}_0$ and feeds back on the parallel component of the critical perturbation $\vec{u}'_\parallel$. This is represented by the $I'_2 = -\vec{u}'_\parallel \cdot (\vec{u}'_\perp \cdot \nabla \vec{U}_0)$, which, in our flow, coincides with the I'_3, as also depicted in Fig. 20.
2. The strong streamwise deceleration due to the radial increase of the diffuser cross section. This is always a destabilizing effect because I'_4 has a quadratic term in $\vec{u}_\parallel$, hence its sign is solely determined by the gradient of the basic flow momentum transported along the streamlines. A decrease of basic state momentum leads to a positive contribution of $I'_4 = -\vec{u}'_\parallel \cdot (\vec{u}'_\parallel \cdot \nabla \vec{U}_0)$, therefore to a transfer of energy from the basic state to the perturbation.

The lift-up effect is a typical destabilization mechanism proper of shear flows, and in our case, it plays a significant role because the basic state streamlines are logarithmic spirals; hence, a fluid element would be subject to a shear if displaced in the cross-stream direction. On the other hand, the streamwise deceleration is a destabilizing mechanism dominant in all the diffusers and jet flows. It seems, therefore, that centrifugal instabilities do not play any significant role within the model framework. To confirm it, we apply the criterion by Sipp and Jacquin[33] that identifies the necessary condition to admit centrifugal instabilities for inviscid, incompressible, two-dimensional planar flows in rotating systems. Their criterion generalized the Rayleigh criterion by considering the local algebraic radius of curvature $\ddot{R}$ at a given point of a basic state streamline,

$$\ddot{R} = \frac{|\vec{U}_0|^3}{(\nabla \psi_0) \cdot [\vec{U}_0 \cdot \nabla \vec{U}_0]}, \tag{22}$$

where ψ_0 is the basic state stream function. The criterion of Sipp and Jacquin[33] is defined on the following quantity:

$$\delta = 2\left(\frac{|\vec{U}_0|}{\ddot{R}} + \Omega\right)(\nabla \times \vec{U}_0 + 2\Omega), \tag{23}$$

where Ω denotes the rotation rate of the coordinate system, i.e., $\Omega = 0$ in our case. According to Sipp and Jacquin,[33] the flow is unstable if there exists ψ_0 such as $\max_{\psi_0}(\delta) < 0$. Reworking our basic steady, the terms entering the local algebraic radius of curvature can be computed as

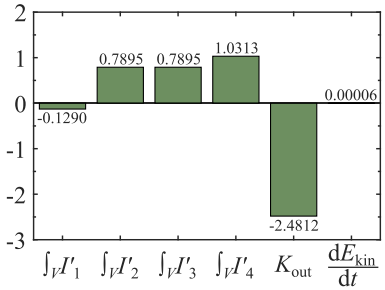

FIG. 21. Integral energy budget.

$$U_{0,r} = \frac{1}{r}\frac{\partial \psi_0}{\partial \theta}, \quad U_{0,\theta} = -\frac{\partial \psi_0}{\partial r}, \tag{24}$$

then, it yields

$$\nabla \psi_0 = \left[\frac{\partial \psi_0}{\partial r} \quad \frac{1}{r}\frac{\partial \psi_0}{\partial \theta}\right] = \left[-U_{0,\theta}\, U_{0,r}\right] = \left[-\frac{\mu}{r} \quad \frac{1}{r}\right], \tag{25}$$

and we can calculate

$$(\nabla \psi_0)\cdot\left[\vec{U}_0 \cdot \nabla \vec{U}_0\right] = \left[-\frac{\mu}{r} \quad \frac{1}{r}\right]\cdot\begin{bmatrix} U_{0,r}\dfrac{\partial U_{0,r}}{\partial r} - \dfrac{U_{0,\theta}^2}{r} \\ U_{0,r}\dfrac{\partial U_{0,\theta}}{\partial r} + \dfrac{U_{0,r}U_{0,\theta}}{r}\end{bmatrix}$$

$$= \frac{\mu}{r^4}(1+\mu^2). \tag{26}$$

Finally, $|\vec{U}_0|^3 = \frac{1}{r^3}(\mu^2+1)^{\frac{3}{2}}$, and it yields

$$\ddot{R} = \frac{r}{\mu}\sqrt{\mu^2+1}. \tag{27}$$

Hence, the final form of δ reads

$$\delta = \frac{2\mu \nabla \times \vec{U}_0}{r^2}, \tag{28}$$

since our basic state is irrotational, i.e., $\nabla \times \vec{U}_0 = 0$, the flow is always neutrally stable to the centrifugal instability. This means that the necessary condition to attribute the instability to a Rayleigh centrifugal-type mechanism is not met under the simplifying hypotheses of the model of Tsujimoto *et al.*[8]; hence our instability is not centrifugal.

Considering that $|U_z| \ll |U_r|, |U_\theta|$ in our URANS simulations, the two-dimensional criterion of Sipp and Jacquin[33] is applied to the mid-height diffuser flow of our full-pump results. The low-flow rate rotating stall is expected to occur at $Q \approx 0.6Q_d$;[34] hence, we computed δ and the in-plane streamlines at $z=0$ for $Q/Q_d = 0.5$ [Fig. 22(a)] and 0.75 [Fig. 22(b)]. As all the in-plane streamlines (black lines) pass through regions of positive δ (gray zones), none of them verifies the necessary condition $\max_{\psi_0}\delta < 0$ to admit the centrifugal instability as a destabilizing mechanism. We consider this as a heuristic indication that the rigorous proof derived for the Tsujimoto's model can be generalized to the three-dimensional diffuser flow.

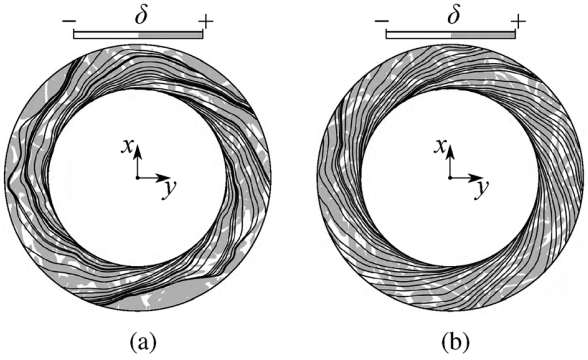

FIG. 22. Numerically calculated δ at the mid-height ($z=0$) of the diffuser at the flow rate (a) $Q/Q_d = 0.50$, and (b) $Q/Q_d = 0.75$ obtained from the URANS simulation. The black lines denote the in-plane streamlines at $z=0$.

2. Rotating stall characteristics of the zero-leakage case

To capture and visualize the unsteady flow field associated with the rotating stall at low flow rates, Fig. 23 shows the FFT and wavelet analysis of the URANS simulations for the zero-leakage case at fully developed stall conditions for $Q/Q_d = 0.25$. The frequency associated with the low-flow rate rotating stall $f_{\text{stall},0.25Q_d}/f_{\text{imp}} = 0.714$ and the blade-passing frequency $f_{\text{blade}}/f_{\text{imp}} = 7$ can be identified very clearly as shown in Fig. 23(a). The FFT identifies, therefore, the propagation velocity of the stall cells $\omega_{\text{stall},0.25Q_d} = 0.238\omega_{\text{imp}}$. Moreover, the nonlinear interaction between such two frequencies is also observed in the FFT at $f_{\text{stall},0.25Q_d} + f_{\text{imp}}$. The rotating stall frequency can also be clearly identified by the wavelet analysis as shown in Fig. 23(b).

Figure 24 shows the phase-averaged color maps with 120-time steps of the last revolution at the mid-height of the diffuser in a reference frame rotating with the rotating stall propagation velocity $\omega_{\text{stall},0.25Q_d}$. Three cells are clearly identified (top), and they qualitatively well compared with the critical mode predicted by linear stability analysis within the model of Tsujimoto (bottom). They are composed

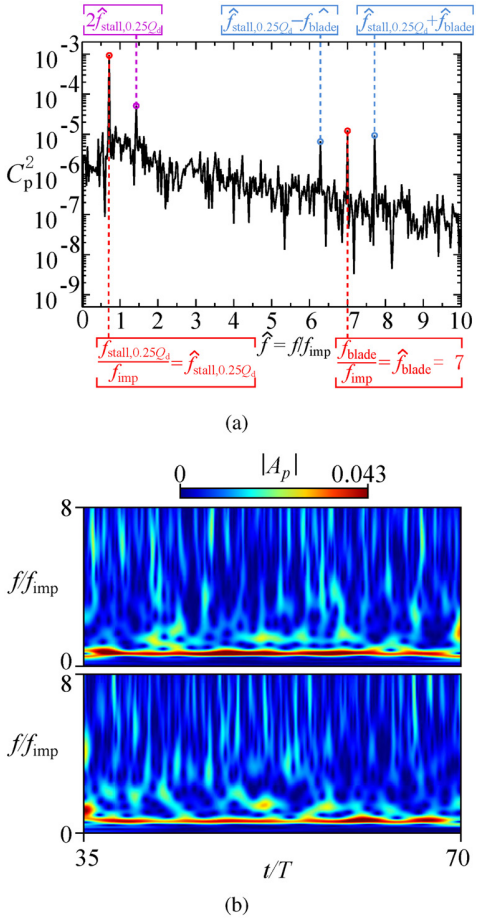

FIG. 23. (a) Fourier and (b) wavelet analyses of the URANS simulation of the zero-leakage case at the stall condition $Q/Q_d = 0.25$.

of two regions of inward and outward radial velocities located near the diffuser inlet, and between these two regions, a zone with negative tangential velocity is identified.

3. Comparison of different cases at low-flow rate stall conditions

Numerical simulations at fully developed stall conditions will be compared for the three different pump geometries of interest in this study. Figure 25 presents the comparison of the Fourier and wavelet analysis for the URANS simulations and experiments at $Q/Q_d = 0.25$. For the zero-leakage case [Fig. 25(a)], the rotating stall instability frequency was captured both by the Fourier and wavelet analysis as described before. This is also the case for the negative-leakage case [Fig. 25(b)], whose instability frequency is similar to the ones found for the zero-leakage case. For the positive-leakage case [Fig. 25(c)], the leakage flow has a significant impact on the rotating stall characteristics in the vaneless diffuser. The FFTs are qualitatively similar, but the wavelet analysis demonstrates a significant difference with respect to the zero- and negative-leakage cases [Figs. 25(a)–25(d)]. In the URANS simulations for the positive-leakage case at $Q/Q_d = 0.25$, the impeller–diffuser leakage is larger than in the experiments, and the leakage flow (rotating with the impeller walls) enters the diffuser with the impeller frequency f_{imp}, resulting in nonlinear interactions with the blade-passing frequency f_{blade} and the rotating stall frequency $f_{stall,0.25Q_d}$, triggering a more complicated flow field.

Table IV summarizes the numerical and experimental results derived from the corresponding FFTs. One can observe that the stall propagation velocity $\omega_{stall,0.25Q_d}$ identified in the different cases is compatible with the experimental one. However, the rotating instability frequency is very sensitive to the leakage flow. To illustrate this effect, Fig. 26 depicts the change of the rotating stall frequencies [Fig. 26(a)] and amplitudes [Fig. 26(b)] extracted from all simulations and experiments plotted against the effective diffuser flow rate Q_D/Q_d (corrected taking into account the leakage flow) normalized to the nominal flow rate Q_d. The instability frequency decreases upon an increase in the effective diffuser flow rate and $f_{stall,0.25Q_d}/f_{imp} \approx \alpha + \beta Q_D$, where $\alpha = 0.9689$ and $\beta = -0.8189$ are fitting coefficients that approximate at leading order the change of frequency with Q_D for all the pump configurations considered in this study. The critical diffuser flow rate can be estimated, assuming that the rotating stall instability is strongly driven by a linear process as described in Sec. IV E 1. This brings to assume that the square of the perturbation amplitude scales with the deviation of Q_D from the critical flow rate $Q_{D,c}$, i.e., $C_p^2 \sim (Q_D - Q_{D,c})$. Extracting C_p^2 from the FFT for $Q/Q_d = 0.25$ and 0.5, $Q_{D,c}$ can be approximated by linear extrapolation up to $C_p^2 = 0$, as shown by the dashed lines in Fig. 26(b). Three values of $Q_{D,c}$ are found, one per each leakage configuration considered, i.e., zero-, negative-, and positive-leakage. The critical values numerically estimated by our URANS all fall within the experimental range $Q_{D,c} \in [0.55, 0.7]$ measured by looking for local recirculation regions, as reported by Barrand *et al.*[34] in the very first publication on the present

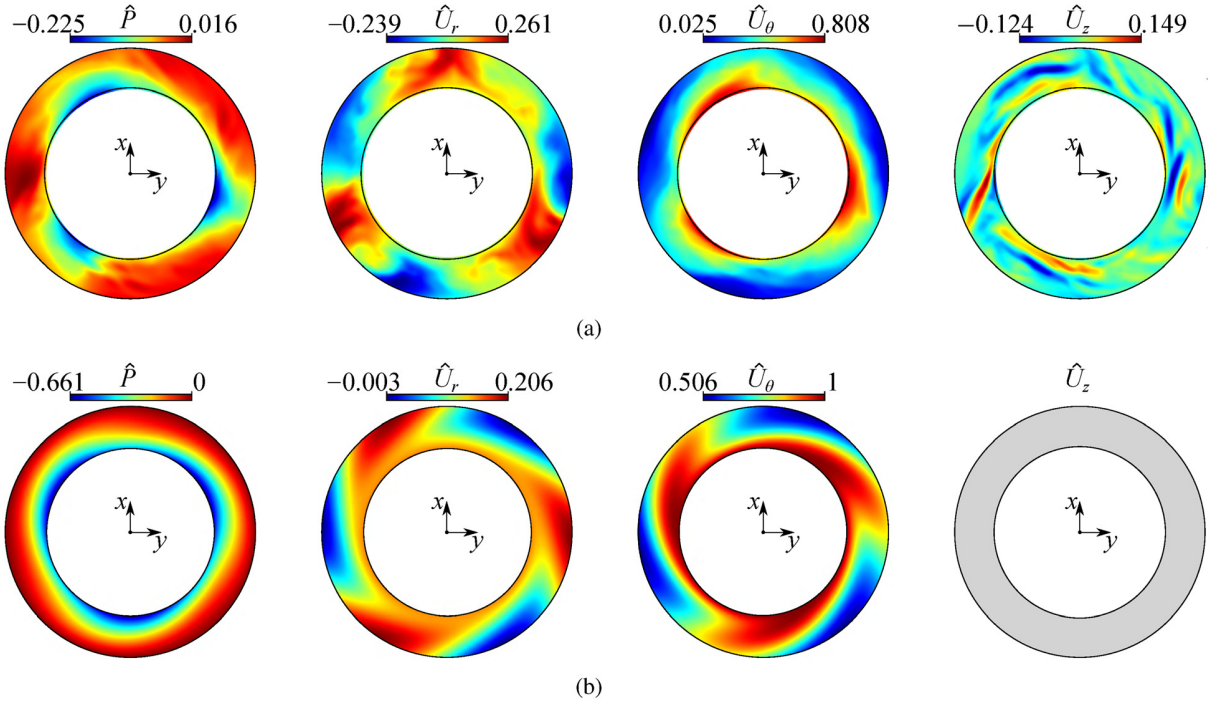

FIG. 24. Comparison of (a) the phase-averaged static pressure, radial velocity, tangential velocity, and axial velocity with the instability propagation velocity $\omega_{stall,0.25Q_d}$ of the zero-leakage case at stall condition $Q/Q_d = 0.25$ of the URANS simulation, and (b) the flow field calculated by the 2D linear stability model of Tsujimoto *et al.*[8] at the critical condition.

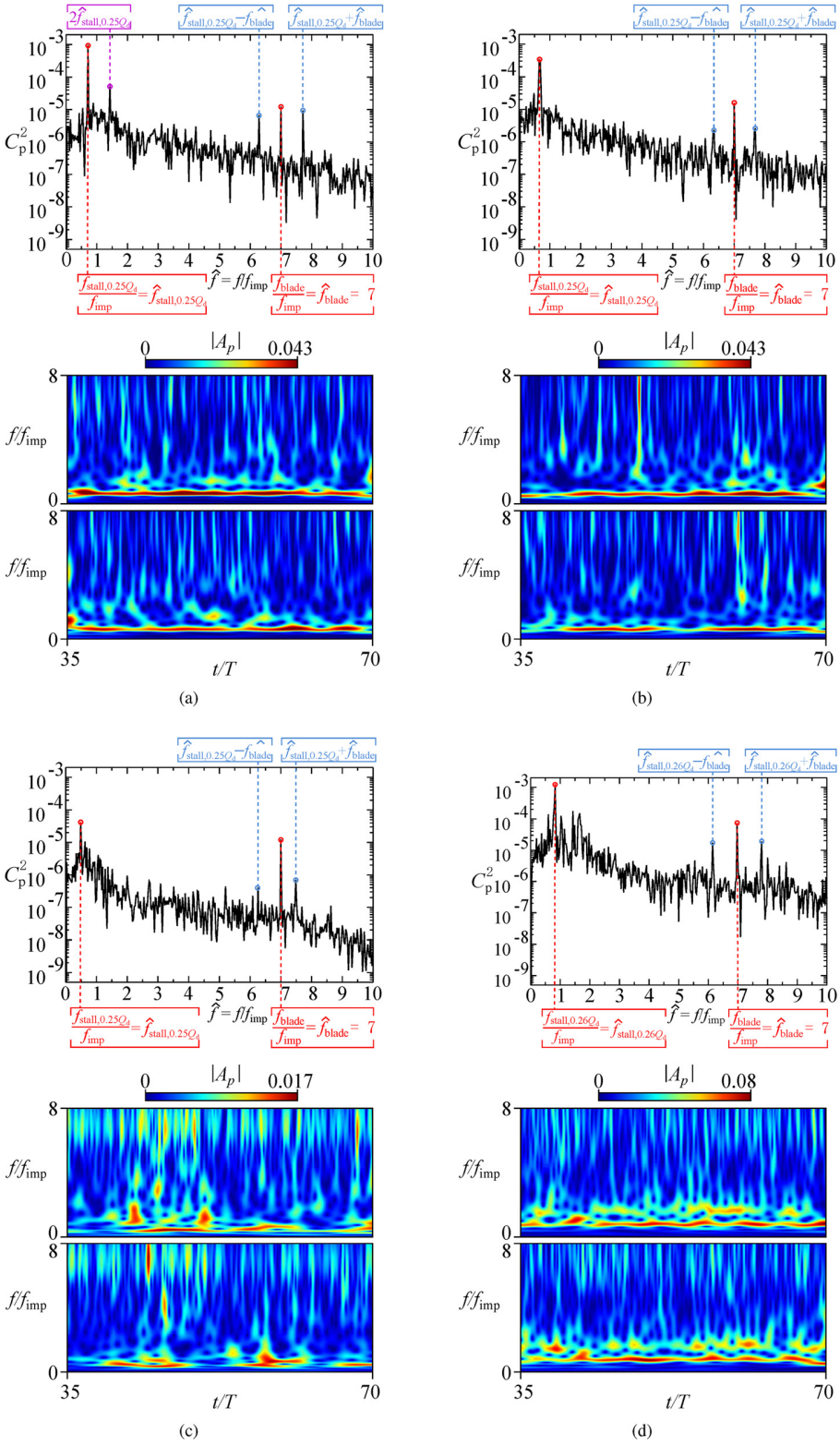

FIG. 25. Fourier and wavelet analyses of the URANS simulation for (a) the zero-leakage case, (b) the negative-leakage case, and (c) the positive-leakage case, and of (d) the experiment, at the stall condition $Q/Q_d = 0.25$.

TABLE IV. Propagation velocity of the rotating instability obtained by the FFT at the stall condition $Q/Q_d = 0.25$.

Case	Zero-leakage (URANS)	Negative-leakage (URANS)	Positive-leakage (URANS)	Positive-leakage (Experiment)	2D linear model (Tsujimoto)
$f_{stall,0.25Q_d}/f_{imp}$	0.714	0.686	0.486	0.840	0.867
$\omega_{stall,0.25Q_d}/\omega_{imp}$	0.238	0.228	0.162	0.280	0.289

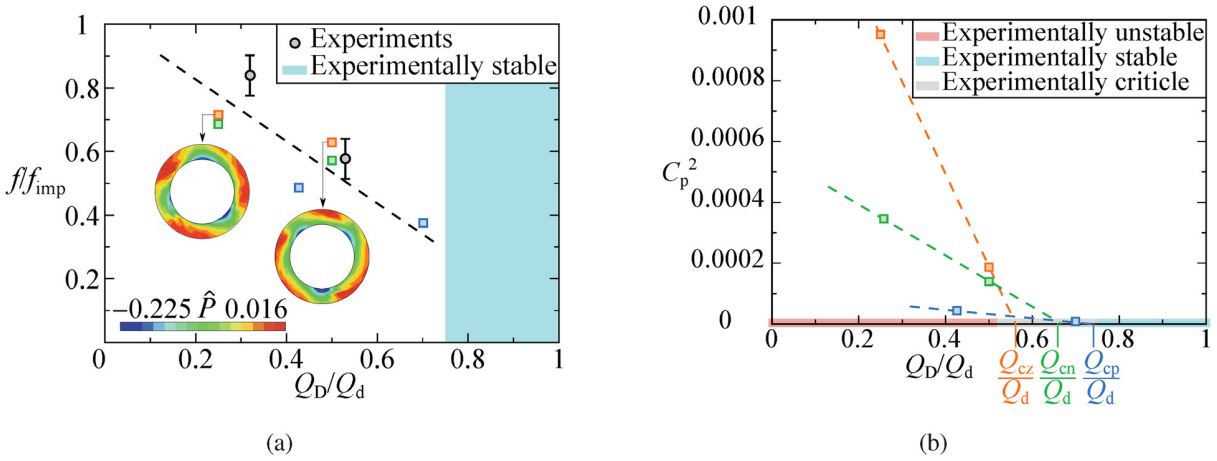

FIG. 26. (a) Rotating stall frequency and (b) amplitude analysis at small flow rates ($Q/Q_d = 0.50$ and 0.25).

pump model. The good agreement between numerics and experiments on the critical onset is depicted in Fig. 26(b).

Figure 27 depicts the normalized rotation frequency of the rotating stall resulting from the URANS simulations and Tsujimoto's model. The comparison between these data demonstrates that the critical angle α_c predicted by Tsujimoto's model (magenta triangle) is in good agreement with the α of the closest-to-critical rotating stall conditions we found, i.e., $\alpha_c \approx \alpha(Q/Q_d = 0.5, \text{positive} - \text{leakage case})$. We, however, remark that the simplified model of Tsujimoto significantly overpredicts the critical propagation velocity by about a factor of 3.

Figure 28 shows the comparison of the phase-averaged flow field in a reference frame rotating with the rotating stall propagation velocity. According to Fig. 26, the experimental PIV measurements for $Q = 0.26Q_d$ [Fig. 28(d), Ref. 12] are best compared with the phase-averaged flow field for the zero- and negative-leakage cases [$Q = 0.25Q_d$, Figs. 28(a) and 28(b)]. As the positive-leakage case [Fig. 28(c)] considers an effective flow rate of $Q_D = 0.43Q_d$, the phase-averaged rotating stall is not comparable to the other cases, which have the same nominal flow rate $Q = 0.25Q_d$. Three stall cells are identified in the phase-averaged URANS for the zero- and negative-leakage cases, and they qualitatively and quantitatively well compare in terms of the velocity field with the PIV experimental measurements.

V. SUMMARY AND CONCLUSIONS

The flow field in a centrifugal pump was thoroughly investigated by combining URANS simulations, theoretical modeling, and experiments. Among the major focuses of this study is the investigation of the leakage effect produced by a radial gap between the impeller and the vaneless diffuser. Hence, three geometries have been considered: (i) a zero-leakage case (ideal case commonly simulated in the literature), a positive-leakage case (corresponding to our experimental facility), and (iii) a negative-leakage case (most commonly employed in industrial applications).

The numerical simulations have first been validated by comparing them with corresponding experiments. The URANS-predicted pump and diffuser performances are in very good agreement with the experimental measurements, with a maximum error of about 5% observed for the zero- and positive-leakage cases. Moreover, the onset

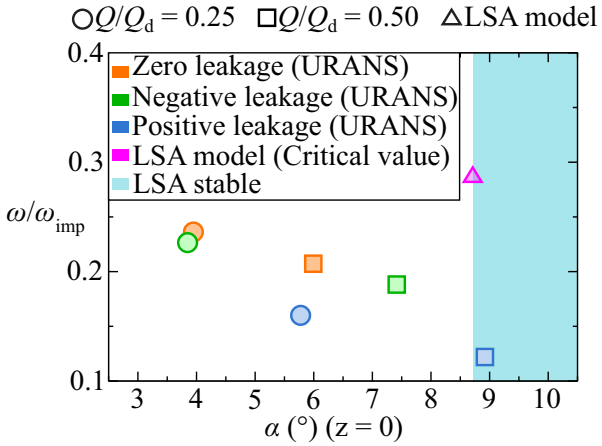

FIG. 27. Flow angle of the core flow vs rotating stall propagation velocity at small flow rates ($Q/Q_d = 0.50$ and 0.25).

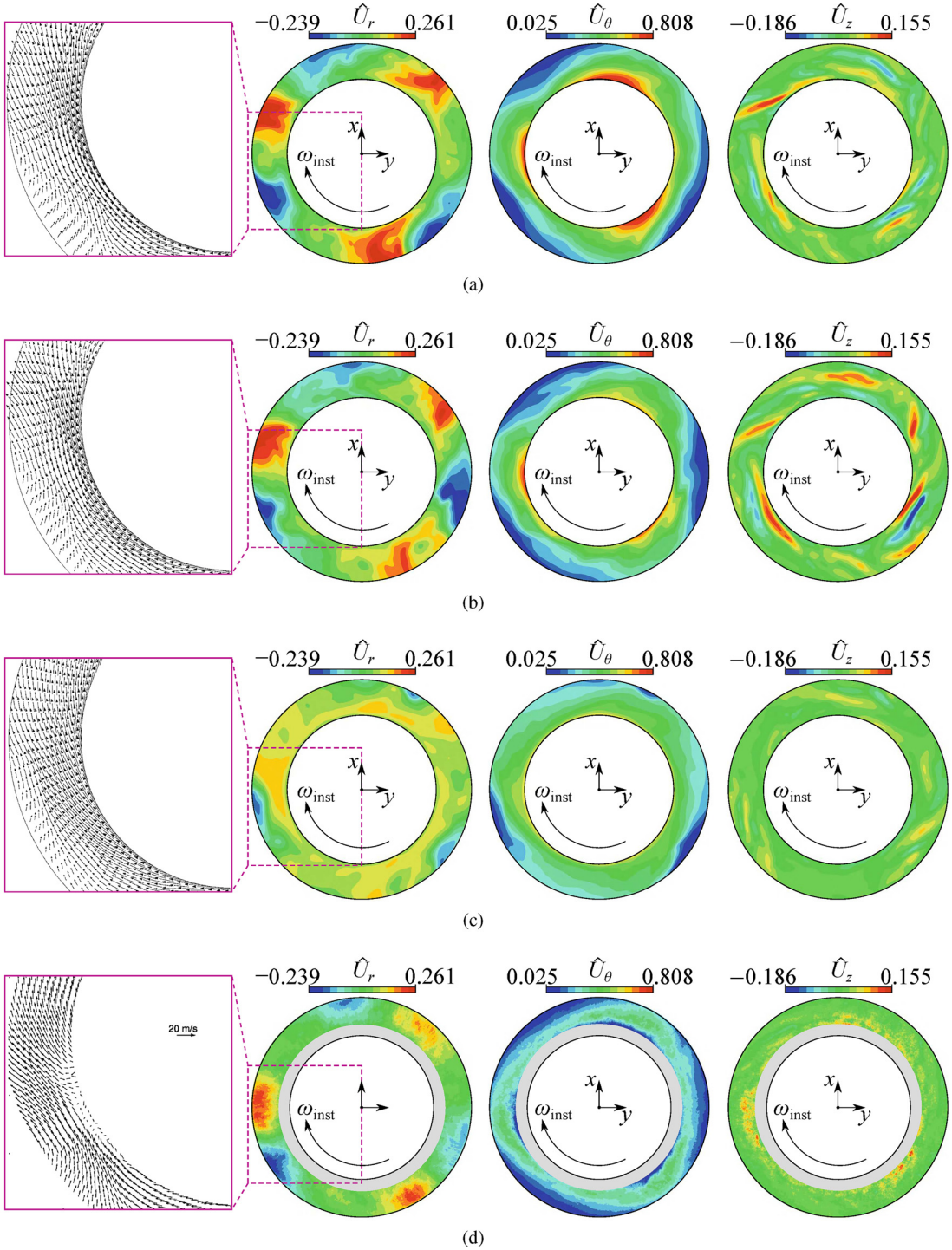

FIG. 28. Phase-averaged velocity vectors and color maps of radial, tangential, and axial velocity at the mid-height of the diffuser based on the instability propagation speed $\omega_{stall,0.25Q_d}$ at the stall condition $Q/Q_d = 0.25$ for (a) the zero-leakage case, (b) the positive-leakage case, (c) the negative-leakage case, and (d) the PIV measurement results. The gray region close to the diffuser inlet is not accessible to PIV because of laser reflection on the impeller blades. The measurements near its edge are, therefore, to be considered affected by a significant error bar.

and features of the low-flow rate rotating stall observed in the experiments have well been reproduced by our URANS simulations. The validated numerical tool has, therefore, been used to investigate more in-depth the rotating instabilities occurring in the vaneless diffuser for the three aforementioned configurations, taking the ideal case (i.e., the zero-leakage case) as a reference.

We identified, for the first time in this centrifugal pump, an unexpected rotating instability occurring in the vaneless diffuser at design flow rate $Q = Q_d$. This rotating stall has a major impact on the mean flow, and it is responsible for a large separation region on the diffuser hub. As a result, the diffuser performance significantly degrades. The instability mechanism has been traced back to the two-dimensional jet-wake instability reported by Ljevar *et al.*,[10] verifying that we get a parametric onset of the instability as well as a wavenumber consistent with their predictions.

Moreover, by means of dedicated wavelet analysis, we identified a secondary instability pulsating in the reference frame of the primary rotating stall and migrating from the shear layer of the impeller wake to the diffuser outlet. To the best of the authors' knowledge, this secondary instability has been reported in our study for the first time. The same rotating stall has been found for the negative-leakage case at the design flow rate; however, the disturbance due to the entrainment of the leakage flow was strong enough to almost totally disrupt the secondary instability, even if a clear signature of it remains in the wavelet analysis. On the contrary, when a positive-leakage case is considered, the modification to the jet-wake angle brings the flow into the stable regime and no rotating stall is observed. This is in agreement with the prediction of the two-dimensional model of Ljevar *et al.*,[10] and it is confirmed by our experiments. A corresponding suppression of the separation region over the diffuser hub is observed, leading to a significant increase in the diffuser performance (also confirmed by our experiments). This leads to the remarkable conclusion that even small radial gaps between the impeller and the diffuser, as the 1% gap we consider, can significantly affect the flow, and they must be included in the pump design when numerical shape optimization is performed.

By varying the flow rate from $Q = 1.25Q_d$ down to $Q = 0.25Q_d$, we bracketed the design flow rate instability to the range above $Q > 0.75Q_d$ and below $Q < 1.25Q_d$. Moreover, we found another rotating instability for $Q < 0.65Q_d$. This low-flow rate rotating stall has been previously reported in the literature by several authors (see, e.g., Dazin[12]), and a good agreement is found also in terms of the instability onset (Barrand *et al.*[34] report an onset at $Q \approx 0.6Q_d$). The rotating stall has been characterized numerically for our three leakage configurations, and good qualitative and quantitative agreement were demonstrated in comparison with the PIV measurements reported in the literature and with the FFT and wavelet analysis performed on our experiments.

An in-depth theoretical analysis has been carried out to shed some light on the mechanisms at the core of this instability. Employing the two-dimensional, inviscid model of Tsujimoto *et al.*,[8] we demonstrated that a consistent $m = 3$ critical mode is predicted by linear stability analysis, assuming that the flow is homogeneous in θ. Furthermore, by arbitrary scaling the critical perturbation and superposing it to the basic state of Tsujimoto's model, it has been shown a remarkably good agreement with our URANS phase-averaged results for supercritical conditions. This supports the conclusion that the rotating stall emerges from a core-flow instability, and it does not get significantly influenced by the presence of the turbulent boundary layers on the shroud and on the hub of the diffuser.

We point out that, even though both the rotating stalls are core-flow instabilities, they are essentially different because the low-flow rate stall does not require a jet-wake inflow, but it rather relies on the skewness of the flow at the diffuser inlet. Finally, by carrying out an energy budget analysis on the critical perturbation, we demonstrated for the first time that the low-flow rate instability is produced by the contribution of lift-up and flow deceleration mechanisms; moreover, we ruled out the hypothesis of a centrifugal-type mechanism as an origin for the rotating stall.

ACKNOWLEDGMENTS

We kindly acknowledge the GENCI (Grand Equipement National de Calcul Intensif) for the numerical resources granted to conduct this study under Project No. A0102A01741. Furthermore, we appreciate the support of the China Scholarship Council for the doctoral students of M. Fan (CSC student No. 201908320328).

AUTHOR DECLARATIONS

Conflict of Interest

The authors have no conflicts to disclose.

Author Contributions

Meng Fan: Data curation (lead); Investigation (equal); Methodology (equal); Software (lead); Visualization (lead); Writing – original draft (equal); Writing – review & editing (equal). **Antoine Dazin:** Conceptualization (equal); Data curation (equal); Investigation (equal); Resources (equal); Supervision (equal); Writing – original draft (equal); Writing – review & editing (equal). **Gérard Bois:** Conceptualization (equal); Investigation (equal); Supervision (equal); Writing – original draft (equal); Writing – review & editing (equal). **Francesco Romanò:** Conceptualization (equal); Data curation (equal); Investigation (equal); Methodology (equal); Software (supporting); Supervision (equal); Writing – original draft (equal); Writing – review & editing (equal).

DATA AVAILABILITY

The data that support the findings of this study are available from the corresponding author upon reasonable request.

APPENDIX A: OPENFOAM SOLVERS

The open-source software OpenFOAM v1912 has been used to carry out all the numerical simulations of this study. An overview of the applied algorithms and discretization schemes used in our numerical simulations is shown in Table V. For the RANS simulations, the solver `simpleFoam` is employed, making use of Multiple Reference Frames (MRFs) to deal with fixed and rotating boundaries (matched using a mixing plane technique[35]), while the transient solver `pimpleFoam` was used for the URANS simulations, employing a dynamic mesh to handle the pump without using a mixing plane.[36]

To solve the discretized systems, the option `smoothSolver` was used along with the linear solver `GaussSeidel smoother` for velocity and all transported variables. For pressure, the GAMG solver (Geometric agglomerated algebraic multigrid solver) was employed

together with the linear solver `symGaussSeidel smoother`.[37,38] The pressure–velocity coupling is taken care of by the OpenFOAM Rhie–Chow interpolation[39] in combination with the Semi-Implicit Method for Pressure Linked Equations (SIMPLE) algorithm for steady calculations, whereas the Pressure-Implicit Method for Pressure Linked Equations (PIMPLE) algorithm is used for the URANS. The latter is a combination of the Pressure-Implicit with Splitting of Operators (PISO) and the SIMPLE algorithms allowing for larger time steps[38,40] than the standard PISO algorithm. The PIMPLE algorithm is set to operate with three inner loops: one nonorthogonal and two outer corrector loops. The under-relaxation factors of pressure, momentum, turbulent kinetic energy, and turbulent dissipation rate for RANS simulation are set to 0.4, 0.6, 0.3, and 0.3, respectively. For the URANS simulation, the under-relaxation factors of momentum, turbulent kinetic energy, and turbulent dissipation rate are set to 0.7.

The temporal discretization terms are discretized using a second-order backward differentiation scheme (`backward` option in OpenFOAM). For the gradient terms, the discretization scheme employs a second-order discretization with Gaussian interpolation (option `Gauss` in OpenFOAM), while linear interpolation is employed to consistently reconstruct the flow inside the finite volumes. The divergence term in the projected momentum equation is discretized using a second-order upwind scheme (`linearUpwind` in OpenFOAM), which is a blend of linear and upwind schemes. The Gauss linear corrected scheme is used for the Laplacian terms, and a linear interpolation is employed for reconstructing velocity and pressures in the finite volume cells from their face fluxes. Finally, for the RANS simulations, the steady state is assumed to be converged if the residuals of mass, momentum, and turbulence properties become smaller than 5×10^{-4}.

APPENDIX B: MESH INDEPENDENCE ANALYSIS

A grid number independence verification was carried out with four grids. Table VI shows the comparison of the predicted mass-weighted average static pressure difference between the pipe inlet and the diffuser outlet (PSI) of the centrifugal pump at the design condition with different grid resolutions. The relative error of the predicted pump performance increases with the increase in the grid size passing from 618k cells (grid 1) to $\approx 1.1 \times 10^6$ cells (grid 2) and then decreased to 0.93% for 2.3×10^6 cells (grid 3). Therefore, a total mesh number of 2.3×10^6 finite volumes was selected for the numerical simulations.

APPENDIX C: FLOW FIELD DETAILS FOR $Q/Q_d = 1$

Color maps of the instantaneous static pressure, radial velocity, tangential velocity, and axial velocity at the design flow rate $Q/Q_d = 1.00$ for (a) the zero-leakage case, (b) the negative-leakage case, and (c) the positive-leakage case. The upper figures show the azimuth averaged value on the meridian section of the diffuser, the lower figures show the instantaneous value at the mid-height of the diffuser.

TABLE V. Numerical methods and schemes employed in OpenFOAM v1912.

Types	RANS	URANS
Numerical method		
Solver	simpleFoam	pimpleFoam
Pressure–velocity coupling	SIMPLE	PISO
Matrices-solver	p: `GAME`; U, k, ω: `smoothSolver`	p: `GAME`; U, k, ω: `smoothSolver`
Relaxation factor	$p : 0.5;\ U : 0.8;$ $k, \omega : 0.7$	$U, k, \omega : 0.7$
Discretization scheme		
Time		`backward`
Gradient		`Gauss linear`
Divergence	`Gauss linear` `Upwind`	`Gauss linear` `Upwind`
Laplacian	`Gauss linear corrected`	`Gauss linear corrected`
Interpolation	`Linear`	`Linear`

TABLE VI. Grid independence verification data. δ is the relative error computed with respect to the finest grid, i.e., $\delta = |\mathrm{PSI}_{\mathrm{Case\,4}} - \mathrm{PSI}_{\mathrm{Case}*}|/|\mathrm{PSI}_{\mathrm{Case\,4}}|$, where PSI denotes the mass-weighted average static pressure difference between the pipe inlet and the diffuser outlet, the number denotes either grid 1, 2, or 3.

	Cells number						
Grid No.	Inlet pipe	Impeller	Diffuser	Outflow box	Total	PSI	δ
1	113 155	267 008	145 728	91 800	617 691	0.3843	1.75%
2	238 853	493 920	210 600	175 446	1 118 819	0.3864	2.30%
3	406 462	1 051 176	590 976	267 786	2 316 400	0.3742	0.93%
4	1 218 825	2 456 160	1 379 448	352 350	5 406 783	0.3777	⋯

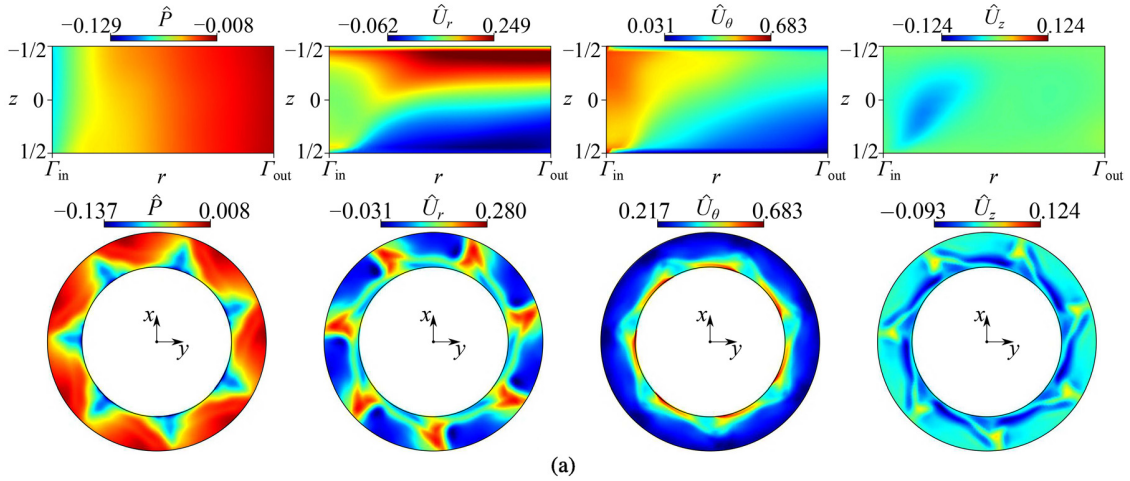

(a)

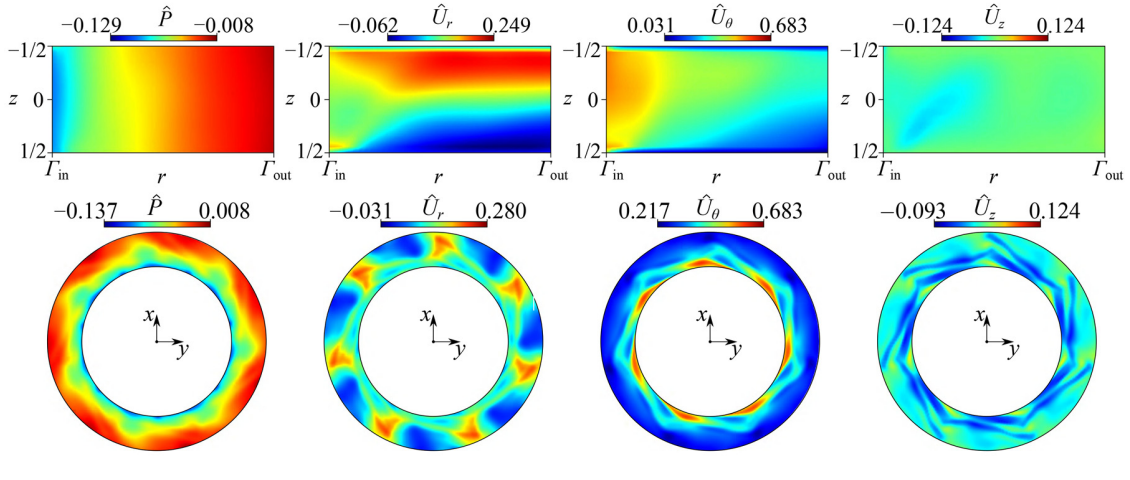

(b)

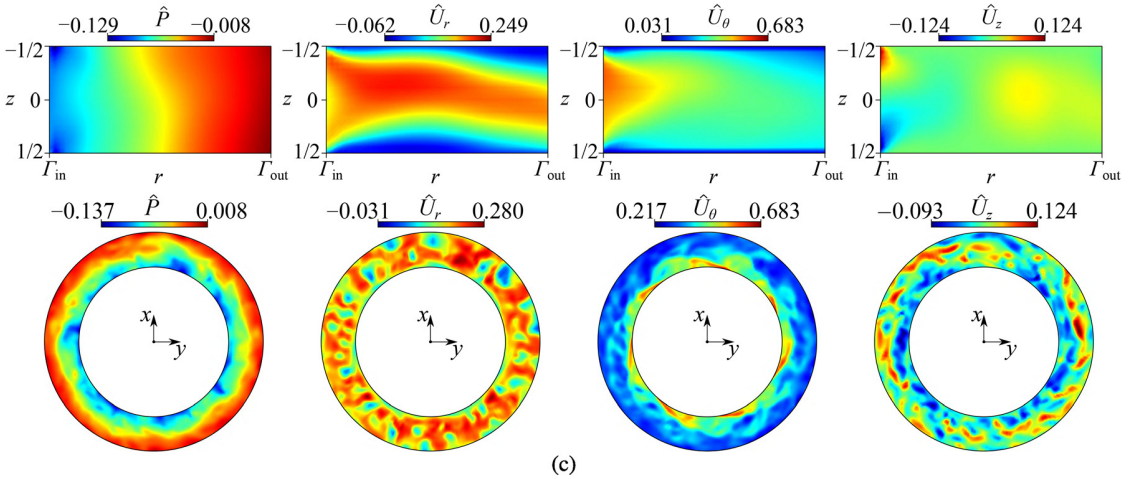

(c)

REFERENCES

[1]D. Japikse, "Stall, stage stall, and surge," in *Proceedings of the Tenth Turbomachinery Symposium* (Texas A&M University, Turbomachinery Laboratories, 1981).
[2]W. Jansen, "Rotating stall in a radial vaneless diffuser," J. Basic Eng. **86**, 750–758 (1964).
[3]Y. Senoo and Y. Kinoshita, "Influence of inlet flow conditions and geometries of centrifugal vaneless diffusers on critical flow angle for reverse flow," J. Fluids Eng. **99**(1), 98–102 (1977).
[4]Y. Senoo, Y. Kinoshita, and M. Ishida, "Asymmetric flow in vaneless diffusers of centrifugal blowers," J. Fluids Eng. **99**(1), 104–114 (1977).
[5]A. N. Abdelhamid, W. H. Colwill, and J. F. Barrows, "Experimental investigation of unsteady phenomena in vaneless radial diffusers," J. Eng. Power **101**, 52–59 (1979).
[6]A. N. Abdelhamid, "Effects of vaneless diffuser geometry on flow instability in centrifugal compression systems," Turbo Expo **79610**, V001T03A008 (1981).
[7]P. Frigne and R. van den Braembussche, "A theoretical model for rotating stall in the vaneless diffuser of a centrifugal compressor," J. Eng. Gas Turbines Power **107**, 507–513 (1985).
[8]Y. Tsujimoto, Y. Yoshida, and Y. Mori, "Study of vaneless diffuser rotating stall based on two-dimensional inviscid flow analysis," J. Fluids Eng. **118**, 123–127 (1996).
[9]Y. Heng, A. Dazin, and M. Ouarzazi, "Linear stability analysis of rotating stall in a wide vaneless diffuser," in 12th European Conference on Turbomachinery Fluid Dynamics and Thermodynamics, ETC 2017 (2017).
[10]S. Ljevar, H. C. de Lange, and A. A. van Steenhoven, "Two-dimensional rotating stall analysis in a wide vaneless diffuser," Int. J. Rotating Mach. **2006**, 1–11.
[11]G. Pavesi, A. Dazin, G. Cavazzini, G. Caignaert, G. Bois, and G. Ardizzon, "Experimental and numerical investigation of unforced unsteadiness in a vaneless radial diffuser," in 9th European Conference on Turbomachinery: Fluid Dynamics and Thermodynamics, ETC 2011-Conference Proceedings (2011), Vol. 1.
[12]A. Dazin, "High-speed stereoscopic PIV study of rotating instabilities in a radial vaneless diffuser," Exp. Fluids **51**, 83–93 (2011).
[13]G. Wuibaut, G. Bois, P. Dupont, G. Caignaert, and M. Stanislas, "PIV measurements in the impeller and the vaneless diffuser of a radial flow pump in design and off-design operating conditions," J. Fluids Eng. **124**, 791–797 (2002).
[14]A. Dazin, O. Coutier-Delgosha, P. Dupont, S. Coudert, G. Caignaert, and G. Bois, "Rotating instability in the vaneless diffuser of a radial flow pump," J. Therm. Sci. **17**(4), 368–374 (2008).
[15]D. C. Wilcox, *Turbulence Modeling for CFD* (DCW Industries, 1993).
[16]P. Sváček, P. Louda, and K. Kozel, "On numerical simulation of three-dimensional flow problems by finite element and finite volume techniques," J. Comput. Appl. Math. **270**, 451–461 (2014).
[17]F. R. Menter, J. C. Ferreira, T. Esch, and B. Konno, "The SST turbulence model with improved wall treatment for heat transfer predictions in gas turbines," in Gas Turbine Congress (International) Proceedings, Tokyo (2003).
[18]M. Rahman, "Numerical investigation of unsteady flow past a circular cylinder using 2D finite volume method," J. Nav. Archit. Mar. Eng. **4**(1), 27–42 (2007).
[19]F. R. Menter, "Ten years of industrial experience with the SST turbulence model," Turbul., Heat Mass Transfer **4**(1), 625–632 (2003).
[20]L. Gibson, L. Galloway, and S. Spence, "Assessment of turbulence model predictions for a centrifugal compressor simulation," J. Global Power Propul. Soc. **1**, 142–156 (2017).
[21]I. Chalghoum, H. Kanfoudi, S. Elaoud, M. Akrout, and R. Zgolli, "Numerical modeling of the flow inside a centrifugal pump: Influence of impeller–volute interaction on velocity and pressure fields," Arabian J. Sci. Eng. **41**(11), 4463–4476 (2016).
[22]O. Borm and H. P. Kau, "Unsteady aerodynamics of a centrifugal compressor stage: Validation of two different CFD solvers," Turbo Expo **44748**, 2753–2764 (2012).
[23]J. H. Kim, J. H. Choi, and K. Y. Kim, "Design optimization of a centrifugal compressor impeller using radial basis neural network method," Turbo Expo **48883**, 443–451 (2009).
[24]M. Asuaje, F. Bakir, S. Kouidri, F. Kenyery, and R. Rey, "Numerical modelization of the flow in centrifugal pump: Volute influence in velocity and pressure fields," Int. J. Rotating Mach. **3**, 244–255 (2005).
[25]M. Invigorito, D. Cardillo, and G. Ranuzzi, "Application of OpenFOAM for rocket design," in *9th OpenFOAM Workshop* (OpenFOAM, 2003), pp. 1–15.
[26]C. Hu, "Investigation of rotating stall in radial vaneless diffusers with asymmetric inflow," Aerosp. Sci. Technol. **96**, 105546 (2020).
[27]M. Šourek and M. Isoz, "DEM-CFD study of flow in a random packed bed," in Conference Topical Problems of Fluid Mechanics (2018).
[28]F. Cenci and A. L. C. Fujarra, "URANS simulation: Numerical study of flow around a two-dimensional circular cylinder," in Proceedings of the XXXVIII Iberian Latin-American Congress on Computational Methods in Engineering (2017).
[29]Y. G. Heng, A. Dazin, M. N. Ouarzazi, and Q. R. Si, "Experimental study and theoretical analysis of the rotating stall in a vaneless diffuser of radial flow pump," IOP Conf. Ser. **49**, 032006 (2016).
[30]Y. G. Heng, A. Dazin, M. N. Ouarzazi, and Q. R. Si, "A study of rotating stall in a vaneless diffuser of radial flow pump," J. Hydraul. Res. **56**(4), 494–504 (2018).
[31]S. Suzuki, U. Yoshio, and H. Hideomi, "Noise characteristics in partial discharge of centrifugal fans: 1st report, low-frequency noise due to the rotating stall," Bull. JSME **21**(154), 689–696 (1978).
[32]G. Caignaert, B. Desmet, and D. Stevenaert, "Experimental investigations on the flow in the impeller of a centrifugal fan," Turbo Expo **79566**, V001T01A013 (1982).
[33]D. Sipp and L. Jacquin, "Three-dimensional centrifugal-type instabilities of two-dimensional flows in rotating systems," Phys. Fluids **12**(7), 1740–1748 (2000).
[34]J. Barrand, G. Caignaert, and R. Canavelis, "Experimental determination of the reverse flow onset in a centrifugal impeller," in *Proceedings of the 1st International Pump Symposium* (Turbomachinery Laboratories, Department of Mechanical Engineering, Texas A&M University, 1984).
[35]D. Wilhelm, "Rotating flow simulations with OpenFOAM," Int. J. Aeronaut. Sci. Aerosp. Res. **1**, 1 (2015).
[36]D. Živković, "Simulacija promjene opterećenja Francisove hidrauličke turbine," Ph.D. thesis (University of Zagreb, Zagreb, 2016).
[37]T. Behrens, "OpenFOAM's basic solvers for linear systems of equations," Technical Report No. 1802 (Department of Applied Mechanics, Chalmers, 2009).
[38]C. J. Greenshields, *OpenFOAM User Guide* (The OpenFOAM Foundation, 2020).
[39]H. Jasak, "Error analysis and estimation for the finite volume method with applications to fluid flows," Ph.D. thesis (University of London, London, 1996).
[40]T. Uroić, "Implicitly coupled finite volume algorithms," Ph.D. thesis (University of Zagreb, Zagreb, 2019).

Appended papers

C.3 Paper C

"Instabilities identification based on a new centrifugal 3D impeller outflow model",

M. Fan, A. Dazin, G. Bois, F. Romanò,

Aerosp. Sci. Technol (2023), 108466.

Aerospace Science and Technology 140 (2023) 108466

Contents lists available at ScienceDirect

Aerospace Science and Technology

journal homepage: www.elsevier.com/locate/aescte

Instabilities identification based on a new centrifugal 3D impeller outflow model

Meng Fan *, Antoine Dazin, Gérard Bois, Francesco Romanò

Univ. Lille, CNRS, ONERA, Arts et Métiers Institute of Technology, Centrale Lille, UMR 9014-LMFL-Laboratoire de Mécanique des Fluides de Lille - Kampé de Fériet, Av. Paul Langevin, Villeneuve-d'Ascq, Lille, F-59000, Hauts de France, France

ARTICLE INFO

Article history:
Received 2 February 2023
Received in revised form 31 May 2023
Accepted 16 June 2023
Available online 22 June 2023
Communicated by Damiano Casalino

Keywords:
Instabilities
Vaneless diffuser
Scale-matching fit
3D modelization
Inflow velocity profiles

ABSTRACT

Previous research works have shown that the inflow boundary conditions have a significant effect on the behavior of diffusers in a centrifugal machine. To better understand the vaneless diffuser instability mechanism and save computing resources, several numerical works are planned to be conducted for the solely vaneless diffuser, excluding the rest of the centrifugal machine from the flow domain to simulate. Previous reduced-order models used either two-dimensional approaches that focused exclusively on the core-flow instability or three-dimensional models tested for a few inflow conditions. To obtain the more realistic diffuser inlet boundary conditions, a modeling method is here developed by fitting the diffuser inflow velocity derived from numerical simulations of the entire machine. The classic fitting methods used to approximate inflow profiles by algebraic polynomials or Gaussian functions are observed to introduce numerical artifacts that significantly affect the flow and therefore its stability. The multi-stage scale-matching fitting approach developed in this study is designed as a robust successive-order approximation of the inflow conditions. Our objective is to demonstrate its robust capability of taking into account the main physical features of the inlet velocity profiles, which, in turn, allows us to significantly improve the prediction of the flow instability occurring in the pump diffuser. Firstly, the RANS and URANS simulations of the entire machine are carried out by OpenFOAM using the $k-\omega$ SST turbulence model. The simulation results show that the RANS simulation is efficient in correctly capturing the diffuser inlet velocity profile except for developed stall conditions. The RANS simulations are carried out for cases with three different kinds of leakage configurations between the impeller and the diffuser. For each case, five flow rates were simulated to get the basic data for fitting the inlet profiles for a total of 125 simulations. The diffuser inlet velocity profiles are averaged in the azimuthal direction and fitted such to obtain an explicit function for the azimuthally-averaged velocity profile that varies with the flow rate Q. The fitting results are very close to the original data, and using our fits to predict the diffuser flow instabilities we show that our modeling approach compares well against the URANS simulations of the whole machine.

1. Introduction

The vaneless diffuser of any radial, mixed flow compressor or pumps acts to properly reduce the mean flow velocity and gain static pressure along its path. As for two-dimensional parallel wall diffusers, too rapid a diffusion process leads to important flow separations, whereas too low a diffusion rate increases the friction losses due to excessive flow path length of the mean flow. Large or uncontrolled diffusion limits diffuser performances and induces stall with specific unsteady phenomena that have been explained and described by several authors like Jansen [1] and Japikse [2].

For a constant vaneless diffuser width, the mean streamline path length is directly related to the evolution of the absolute flow angle α between the mean absolute velocity and the tangential direction. The diffuser inlet flow angle value depends on initial asymmetric velocity components delivered by the impeller, the values of which depend on the compressor Reynolds number, March number, impeller design, and more specifically specific speed. The prediction of the diffuser "inlet critical mean flow an-

* Corresponding author.
E-mail address: meng.fan@ensam.eu (M. Fan).

https://doi.org/10.1016/j.ast.2023.108466
1270-9638/

gle" for which stall may occur is the main parameter research target that has been investigated in past decades. The vaneless diffuser stall mechanism has indeed been studied by many researchers. Most analytical models are based on two different approaches:

1. Boundary layer momentum integral equation to relate rotating stall with radial reverse flow inside the boundary layer (see Jansen [1], Senoo & Kinoshita [3], and Frigne & Van den Braembussche [4]),
2. Inviscid core flow instability analysis (see Tsujimoto et al. [5], Abdelhamid [6], Moore [7], and Ljevar et al. [8]).

Both situations can be found in radial fans, centrifugal pumps, industrial compressors, and aerospace applications for air-breathing engines, airplane conditioning units, or cryogenic rocket multi-stage pumps, depending on design-specific speeds. Diffusers with a large aspect ratio (defined as $\chi = b_3/(R_4 - R_3)$, where R_3 denote the diffuser inlet radius, R_4 denote the diffuser outlet radius, and b_3 denotes the diffuser constant width) and a small aspect ratio respond differently to variations of a given parameter. Most of the relevant experimental and numerical contributions can be found in the review section performed by Gao et al. [9]. They performed a statistical analysis of the geometrical effects on the rotating stall. They confirm that the critical flow angle value mainly depends on the diffuser geometry and more specifically the diffuser aspect ratio and the radius ratio (defined as $\Gamma = R_4/R_3$). The stall cell number and location also depend on diffuser geometry and flow parameters. In their conclusion, Gao et al. [9] suggest the possible existence of two mechanisms that could be responsible for the occurrence of instability in the impeller and diffuser combinations. Dou & Mizuki [10] and Abdelhamid [6] try to combine the above two approaches and concluded that stall mechanisms were different for the narrow diffusers and wide diffusers. However, no one can clearly define the frontier between narrow and wide diffusers.

This reinforces the idea of paying attention to more detailed inlet boundary conditions at the impeller outlet plane including non-uniform flow. In this respect, an interesting sensitivity analysis has been recently presented by Hu et al. [11] using four typical asymmetric inlet radial flow conditions associated with a constant tangential velocity component in the core region as the initial condition for the diffuser. This study was conducted for three different diffuser aspect ratios below 0.14 (which is despite everything being considered as a relatively small value) but only for one flow coefficient corresponding to a core flow angle close to 20 degrees.

The present paper deals with a higher diffuser constant aspect ratio of about 0.3 combined with a radius ratio of about 1.50. The complete 3D velocity profile at the impeller outlet section is taken as initial conditions at the diffuser inlet section using a fitting technique described in detail. It better describes the real radial and tangential asymmetric inflow conditions compared with the simplified one adopted by Hu et al. [11]. The radius ratio has been enlarged compared with the optimal value to favor the instabilities development. Several experimental investigations on the whole model including a shrouded impeller and diffuser have been already presented in several papers listed in the next section. This study aims to develop and validate a low-computationally-intensive approach that relies on a reduced-order diffuser inflow model. Compared with a fully 3D URANS one, our method could better suit future diffuser designs and fundamental studies with respect to unsteady modes occurring in vaneless diffusers.

Fitting techniques are widely used to provide boundary conditions for reduced-order model simulations. Emvin et al. [12] developed a simple approach for a diffuser simulation using a momentum method for approximation of the inlet velocity. All the inlet jets are replaced by the momentum and mass boundary conditions over the diffuser plate. Such a momentum method is suitable for coarse meshes and cannot accurately reproduce some of the mean inflow features of the diffuser inlet profile such as the boundary layers for the mean flow and the swirl. Deng et al. [13] performed the momentum equation discretization for the first cell adjacent to the diffuser. Their velocity algebraic equation is expressed as a diffuser-related term and a diffuser-nonrelated term. Based on the analysis of the diffuser-related term, a total-flux momentum method helps minimize the computational error and reduces the effort required to determine an optimal grid. Other reduced-order models used either two-dimensional approaches that focused exclusively on the core-flow instability [5,8] or three-dimensional models tested for a few inflow conditions [11]. The multi-stage fitting approach we propose in this study is intended to provide inflow conditions for the diffuser regardless of the local computational grid. To do so, we develop a multi-stage fitting method that focuses on one specific scale per fitting stage and then matches them in a final fitting step that returns the fitted velocity profile in analytical explicit form. This approach allows us to introduce the theoretical local scaling at the boundary layers, which inherently separates the boundary layer scale from the bulk flow. This could be of help for future analyses that will attempt to use asymptotic matching and can compare the theoretical prediction with our fitting coefficients. None of the previous techniques adopted a scale-matching-like approach for their fitting. This is the original contribution of our fitting technique and it does not suffer from spurious oscillations typical of classic fitting methods. Having a multi-stage fitting approach allows for building a model capable of identifying successive approximations of the inflow condition. Once again, this follows the typical logic used in asymptotic theory and helps identify and interpret the effects that determine the velocity inlet profile.

This paper is structured as follows: Section 2 defines the mathematical model, assuming low Mach number conditions (incompressible flow), Sec. 3 presents the discretization employed to numerically solve the Navier–Stokes system, Sec. 4 explains the method to approximate the azimuthally averaged vaneless diffuser inlet velocity profiles as explicit functions of the flow rate Q. The results including the fitted velocity profiles and the numerical simulations based on the fitted profiles as inlet boundary conditions are presented and tested in Sec. 5. Finally, in Sec. 6 the results are summarized, discussed, and conclusions are drawn.

2. Methodology

2.1. Geometry model

The study investigates the effect of leakage flow between the impeller and diffuser on incompressible airflow in a radial flow machine. The entire computational domain which includes the inlet pipe (yellow), the centrifugal impeller (gray), the vaneless diffuser (dark green), and a radial outflow box (light green) is depicted in Fig. 1. The outflow box is placed at the outlet of the diffuser to prevent the outflow boundary conditions from being applied too close to the centrifugal machine. The numerical model used in the study reproduces the geometry and flow conditions of our experimental set-up described in detail in Appendix B. The main parameters of the radial impeller

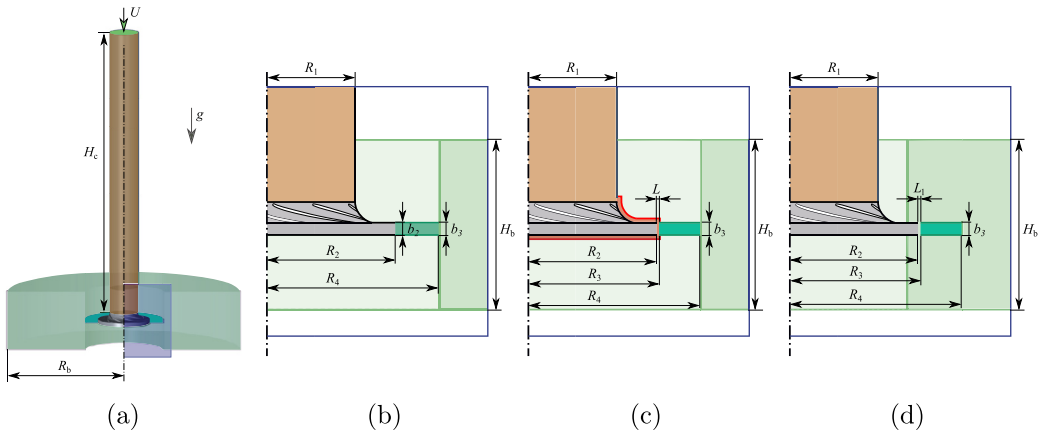

Fig. 1. Schematic of (a) the entire computational domain for the radial flow machine and the zoom-in view of the three computational configurations: (b) zero-, (c) negative-, and (d) positive-leakage case. (For interpretation of the colors in the figure(s), the reader is referred to the web version of this article.)

Table 1
Main geometrical characteristics of the impeller and diffuser model. The CAD of the impeller is uploaded on https://github.com/fromano88/CentrifugalPump.git.

Impeller characteristics		
R_1	Tip inlet radius (shroud side)	141.1 mm
R_{1h}	Tip inlet radius (hub side)	96.9 mm
R_2	Outlet radius	257.5 mm
b_2	Outlet width	38.5 mm
Z	Number of blades	7
β_{2c}	Outlet blade angle	22.5°
K	Mean blade thickness	9 mm
R_{c1}	Casing inlet radius (negative-leakage case)	143.675 mm
R_{c2}	Casing outlet radius (negative-leakage case)	260.075 mm
Q_d	Design flowrate (1200 rpm)	0.236 m^3/s
$Re = {R_2}^2\omega_{imp}/\nu$	Reynolds number	5.52×10^5
$Ma = R_2\omega_{imp}/c$	Mach number (Q/Q_d = 1.0, ω = 125 rad/s)	0.095
Diffuser characteristics		
R_3	Inlet radius (zero-leakage case)	257.5 mm
	Inlet radius (negative-leakage case)	260.075 mm
	Inlet radius (positive-leakage case)	260.075 mm
R_4	Outlet radius	385.5 mm
b_3	Constant width	38.5 mm
Γ	Radius ratio	≈1.50
χ	Aspect ratio	≈0.3
α_m	Inlet mean flow angle (Q/Q_d = 1.0)	≈14°

and vaneless diffuser are provided in Table 1. Three different leakage configurations are simulated in the study, referred to as zero-, negative-, and positive-leakage cases, depending on the direction of the leakage flow entering the diffuser:

Zero-leakage: corresponds to a simplified configuration. The radial gap between the impeller and the vaneless diffuser is set to zero, which means there is no leakage between the two components (see Fig. 1(b)). Also, there are no axial gaps between the inlet-pipe outlet and the impeller inlet, ensuring no leakage in this area;

Negative-leakage: corresponds to a usual centrifugal machine configuration, there is a small gap between the impeller and the vaneless diffuser, which allows for leakage flow from the outlet to inlet sections of the impeller. Consequently, a radial gap $L = R_3 - R_2$ is introduced in Fig. 1(c); Furthermore, a casing of height L is added to prevent leakage flows.

Positive-leakage: qualitatively reproduced the experimental geometry in the corresponding numerical simulations (see Fig. 1(d)). The axial gap between the outlet of the inlet pipe and the inlet of the impeller is not taken into consideration. All the comparisons between experiments and numerical performance are considered for the positive-leakage case, employed for validation of our numerics.

The inlet boundary condition is defined at the entrance of the circular pipe that connects to the impeller. The height of the pipe H is 10 times the impeller tip inlet radius R_1. A radial outflow box (dark pink) is introduced at the outlet of the diffuser to prevent the outflow boundary conditions from being applied too close to the machine. The height of this box H_b is 15 times its width b_3 and its radius R_4 is three times the radius of the diffuser outlet R_3.

2.2. Problem fomulations

In the computational domain of our problem, the mass, momentum and energy conservation equations are solved in the form of steady (RANS) and unsteady Reynolds-averaged Navier–Stokes (URANS) equations. The URANS equations are

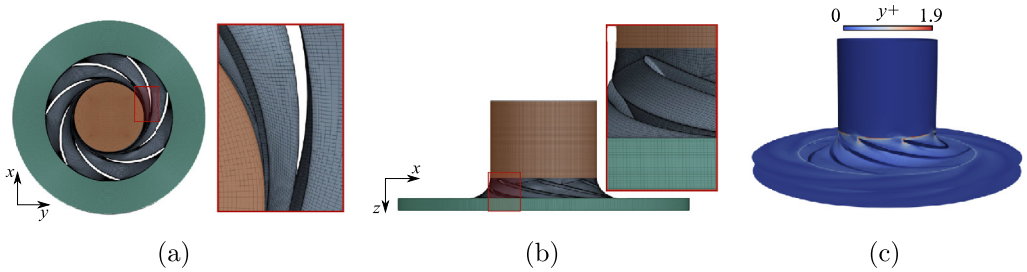

Fig. 2. Top view (a) and side view (b) of a typical mesh of the zero-leakage case used to perform the three-dimensional numerical simulations, and (c) an example of the y^+ distribution on the walls.

$$\frac{\partial \vec{U}}{\partial t} + (\vec{U} \cdot \nabla)\vec{U} + \nabla P = \nabla \cdot (2\nu \vec{\vec{S}} - \vec{\vec{\tau}}), \quad \nabla \cdot \vec{U} = 0, \tag{1}$$

where $\vec{U} = \vec{U}(\vec{x};\ t) = (U_1, U_2, U_3)$ denotes the mean part of the velocity vector, $P(\vec{x}; t)$ is the mean pressure divided by the fluid density, ν is the constant kinematic viscosity, $\vec{x}$ is the position vector, t denotes the time, $\vec{\vec{S}} = \frac{1}{2}(\nabla \vec{U} + \nabla^T \vec{U})$ is the mean rate of the strain tensor, and $\vec{\vec{\tau}}$ is the Reynolds stress tensor. The values of the Reynolds stress in the (U)RANS equations are computed by the SST $k-\omega$ turbulence model which is commonly employed for dealing with turbomachines. This model has shown the capability to capture the key flow features at the core of our study [14,15]. Detailed information about the turbulence model is given by Menter [16].

3. Computational setup

3.1. Mesh generation

Hexahedral cells are a popular choice for meshing in computational fluid dynamics (CFD) simulations because they are less costly and less diffusive compared with tetrahedral cells, particularly near the boundary layers. ANSYS ICEM-CFD is a commercial software that is utilized for creating meshes. The multi-block structure used in ICEM-CFD allows for flexibility and accuracy in the mesh generation process. A mesh with 2.3 million finite volumes was chosen for RANS and URANS simulations of the whole machine after conducting a grid-independent verification using four grids (details in Appendix C). Meanwhile, to ensure the accuracy of the boundary layer calculation, three different boundary layer meshes are tested (details in Appendix C). The mesh we chose in the near-wall regions is refined with an expansion ratio of 1.5 as shown in Fig. 2(a–b) to keep the y^+ values close to 1 on the walls in the inlet pipe, impeller, and vaneless diffuser domains (see Fig. 2(c)). The sole areas where the y^+ is of order 1 (still lower than 2) are at the leading edges of the impeller blades, where the flow curvature is too high to attempt a localized refinement without incurring excessive grid stretching. We further stress that in the areas of interest, hence all over the diffuser walls and the rest of the impeller blades, our y^+ is below 1.

The mesh is then converted to a format readable by OpenFOAM using the converter, `fluent3DmesToFoam`. The same mesh excluding the impeller and inlet pipe regions are used for the simulation of the sole diffuser in our latter work. Besides, to better carry out the fitting work of the velocity profiles presented in the following sections, additional RANS simulations with the 5.4M cells mesh were carried out to assure a sufficient amount of cells along the diffuser height direction.

3.2. Numerical method

In this work, the Mach number $Ma = R_2\omega_{\text{imp}}/c$ = 0.095 $\ll$ 0.3, where ω_{imp} is the rotation rate of the impeller and c = 340 m/s the speed of sound. More details on the local distribution of the Mach number across the starting phase from rest and under fully-developed conditions are given in Appendix A. The incompressible Navier-Stokes equations were solved using the $k-\omega$ SST turbulence model in OpenFOAM v1912 based on a turbulence model independence analysis (details in Appendix D). The high-order advection scheme and second-order backward Euler transient scheme were employed. The selected solvers are `pimpleFoam` and `simpleFoam` for transient and steady incompressible flows, respectively. The discretization is based on a finite volume approach, where both the convective and the diffusive terms are approximated by second-order centered schemes. A second-order Crank-Nicolson method [17] is used for time integration. The transient solver makes use of the solution algorithm PIMPLE, a cross-over merging the PISO and SIMPLE algorithms. For steady simulations, we use the algorithm SIMPLE. A generalized geometric-algebraic multi-grid (GAMG) method with a tolerance of 10^{-7} is used to solve the linear system for the pressure equations. Boundary conditions are implemented using the standard OpenFOAM capabilities, while the outflow boundaries use the `inletOutlet` boundary type.

The inlet velocity corresponding to a pre-set value of inlet flow rate Q is specified using a Dirichlet type boundary condition named `flowRateInletVelocity`, and the static pressure p = 0 Pa is set for the outlet at the outflow contours far away from the diffuser outlet. The `noslip` wall boundary is applied to fixed walls, and the `rotatingWallVelocity` boundary condition which specifies a rotational velocity is used for rotating walls.

The initial boundary conditions used for URANS simulation were taken from the RANS simulation results in order to disregard the flow's startup phase in the simulation. The rotational speed was set as 125 rad/s and the time step Δt, corresponds to 0.5° of the impeller revolution. The simulation results give a mean Courant number for the whole domain of $\overline{C} = 0.0075$ at the design condition. RANS simulations were run for ten thousand time steps to ensure convergence of the SIMPLE algorithm. URANS simulations were run for 70 revolutions of the impeller, and all URANS results presented in the paper are either from the last time step or a phase average of the last impeller revolution. For more details of the numerical settings, refer to Fan et al. [14].

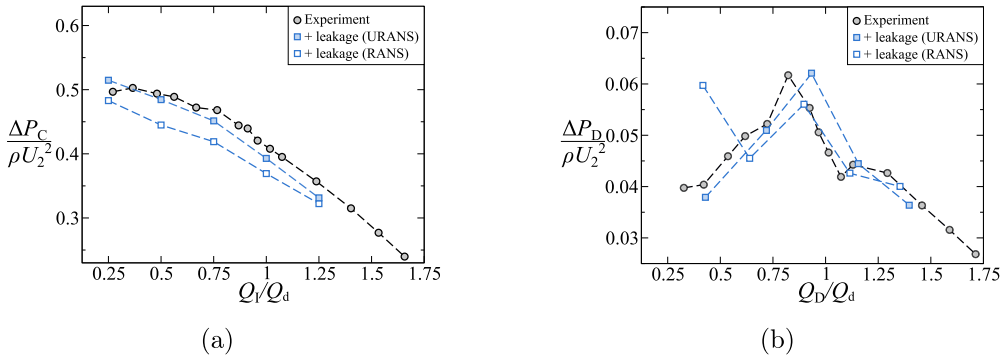

Fig. 3. Performance curves of (a) entire machine and (b) diffuser for the positive-leakage case obtained from experimental and numerical simulation results.

3.3. Validation of the numerical method

As an extended study that originated in the LMFL laboratory. A detailed experimental database is available to the authors thanks to our previous studies [15] and is here used for the validation of numerical results. The numerical results of the positive-leakage case using 2.3M cells mesh are firstly validated against the experimental results since this geometrical configuration of our simulations is the closest to the experimental set-up. The performance of the entire machine, encompassing the impeller and the diffuser, as well as the performance of the sole diffuser evaluated in terms of static pressure rise obtained from the RANS and URANS simulations are compared with the experimental results respectively in Fig. 3(a,b). Note that Q_I and Q_D denote the volume flow rate of the impeller and the one of the vaneless diffuser respectively, which takes the leakage flow effect into account (see Fan [15]). As expected, the entire machine performance obtained from the URANS simulation better agrees with the experimental results (see Fig. 3(a)), as they capture the slowest time scales of the flow dynamics. Concerning the diffuser performance (see Fig. 3(b)), the results of both the RANS and the URANS simulations are acceptable at large flow rates. But at the smallest flow rate, the RANS simulation results are very different from the URANS and experimental results. This is result from the rotating stall phenomena occurring in the vaneless diffuser which can not be captured by the steady-state calculations (for more details, we refer to Fan et al. [14]).

Fig. 4 shows the comparison of the radial, tangential, and axial velocity profile with the impeller rotational speed $\omega_{imp} = 125$ rad/s and the diffuser radius ratio $\Gamma = 1.50$ obtained by RANS with 2.3M cells and 5.4M cells and URANS with 2.3M cells at the flow rate $Q/Q_d = 1.25,\ 1.00,\ 0.75,\ 0.50$, and 0.25. Note that in all the color maps of this study, the velocities U_*, static pressures P, and z coordinates are nondimensionalized by

$$\hat{U}_* = \frac{U_*}{U_2}, \qquad \hat{P} = \frac{P}{\frac{1}{2}\rho {U_2}^2}, \qquad \hat{z} = \frac{z}{b_3} \tag{2}$$

where $* \in \{r, \theta, z\}$, $U_2 = \omega_{imp} R_2$ is a characteristic velocity in this problem, and b_3 is the constant diffuser width. It can be observed that at the large flow rate, the profiles obtained from the RANS simulation are very close to the URANS ones. With the decrease in the flow rate, the deviation between the RANS and URANS increases. This is because the RANS simulation can not capture the rotating instability that occurs in the vaneless diffuser at such low flow rates, hence it further confirms our interpretation of the deviation of the entire machine performance predicted by RANS simulations. Fig. 4 also demonstrates that the profiles obtained by the RANS simulation with 2.3M and 5M cells show good convergence.

4. Fitting the boundary condition at the diffuser inlet

In order to model the diffuser inflow, a parametric fitting protocol will be employed, based on three underlying assumptions:

- The fitting protocol assumes that the inlet flow conditions of the vaneless diffuser can be extracted from solely tangentially averaged RANS simulation results for several flow rates.
- It is implicitly assumed that no mutual interactions are present between an impeller and the vaneless diffuser as far as rotating instabilities are concerned. This is further motivated by the study of flow instabilities [14], whose mechanism is related to the flow behavior solely inside the diffuser itself.
- The three velocity components at the impeller outlet will be fitted with explicit analytical functions.

The validation of the numerical results to fit has been recently published by Fan et al. [14] and is based on the comparisons between fully 3D URANS simulations and experimental results. In Fan et al. [14], a detailed analysis of the effect of inlet boundary conditions on the instability patterns, including leakages between the impeller-diffuser gap, has been carried out. Building on the fitting developed in this study, we will be capable of further controlling the diffuser inflow and perturb it ad hoc to study the effect of first harmonic modulations on the mean inflow obtained via the fit.

4.1. Model simplification

A simplified simulation approach is proposed here to allow for a parametric investigation of the flow in the vaneless diffuser at an affordable computational cost. Fig. 5(a) depicts the three-dimensional computational domain of the simplified model: the inlet pipe

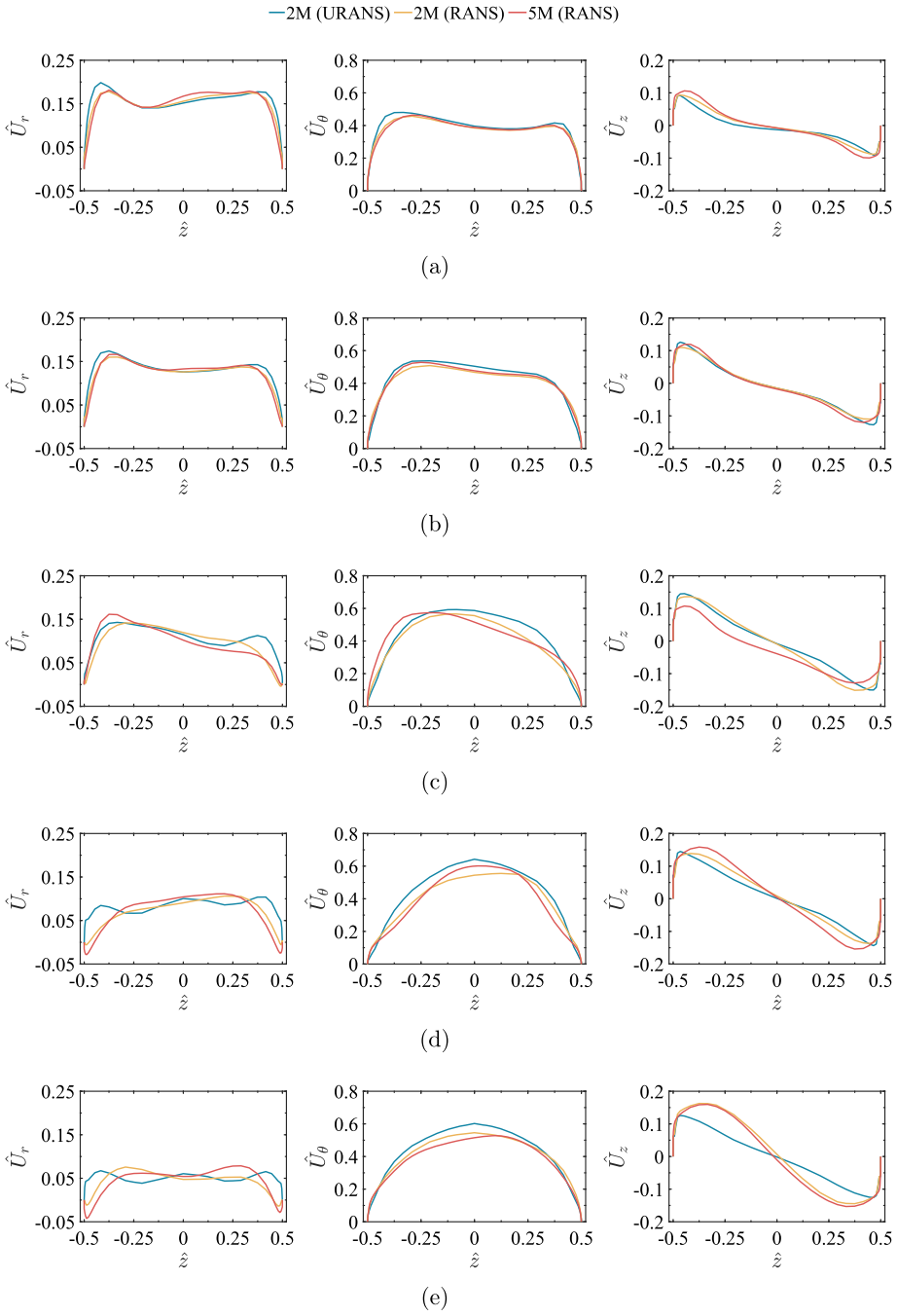

Fig. 4. Comparison of the diffuser inlet radial, tangential, and axial velocity profile with the rotational speed $\omega_{\text{imp}} = 125$ rad/s and the diffuser radius ratio $\Gamma = 1.50$ obtained from RANS with 2 million mesh and 5 million mesh and URANS at five different flow rates: (a) $Q/Q_d = 1.25$, (b) $Q/Q_d = 1.00$, (c) $Q/Q_d = 0.75$, (d) $Q/Q_d = 0.50$, and (e) $Q/Q_d = 0.25$.

and the rotating impeller have been removed, and only the vaneless diffuser and the outflow box are simulated. To reproduce the inlet boundary conditions, the diffuser inlet velocity profile is fitted as a function of the flow rate $\hat{Q} = Q/Q_d$, using the RANS simulation results as a fitting database. We start by fitting the flow profiles azimuthally averaged at the diffuser inlet. To fit the z-dependent inlet velocity profile $\vec{U}(z)$, the full range $z \in [-h/2, h/2]$ is subdivided into two boundary layer regions and a bulk flow region (see Fig. 5(b)). The two boundary regions are fitted with a power-law function, and their thickness δ_i is numerically determined by finding the length that allows fitting the boundary layer at best. The velocity component $U_*(z)$, where $*$ denotes the r, θ, and z direction, is approximated by dedicated functional dependencies within each region according to

$$\text{Boundary region 1,} \qquad z \in [z_{\min}, z_{\min} + \delta_1]: \quad U_* \approx a_{*0} \left(\frac{h}{2} + z \right)^{a_{*1}}, \tag{3a}$$

$$\text{Boundary region 2,} \qquad z \in [z_{\max} - \delta_2, z_{\max}]: \quad U_* \approx b_{*0} \left(\frac{h}{2} - z \right)^{b_{*1}}, \tag{3b}$$

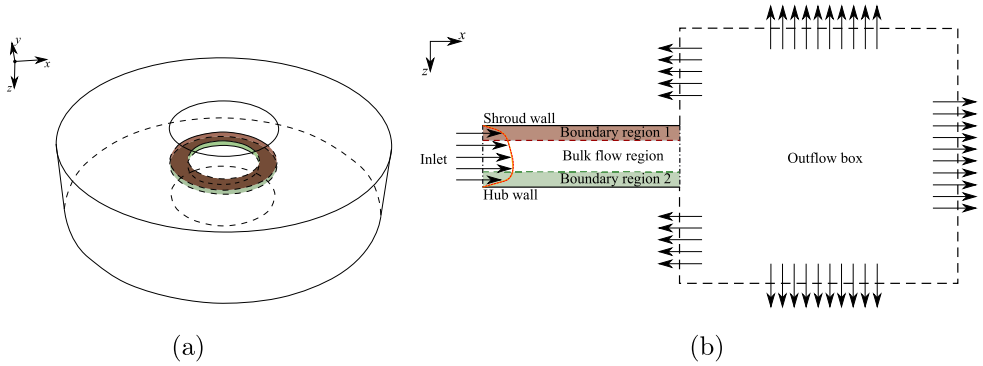

Fig. 5. Schematic of (a) the entire computational domain for the model flow (diffuser shroud and hub walls are marked in red and green respectively) and (b) the meridian section of the simplified numerical model. Note that the outflow box in (b) is not drawn in scale.

$$\text{Bulk flow region,} \qquad z \in [z_{\min} + \delta_1, z_{\max} - \delta_2]: \quad U_* \approx U_*^{\text{bulk}}(z), \tag{3c}$$

where the thickness of the boundary layer regions δ_i is specified for different cases, h denotes the width of the diffuser, a_{*0} and b_{*0} are fitting coefficients, $U_*^{\text{bulk}}(z) = \sum_{i=1}^{n} U_*^{\text{bulk,i}}(z)$ consists of the sum of a linear, a quadratic, a fourth power, and/or a trigonometric function as detailed below.

4.2. Fitting protocol

The fitting has been carried out for five diffuser radius ratios Γ and five rotational speeds ω_{imp} with our three different leakage configurations. For each case, the functional dependence of the coefficients of (3) is derived following a multi-stage algorithm. All coefficients required for the approximation of $U_*(z)$ are determined by minimizing the squared distances between the data and the fit functions within their respective regions. Since the fit functions are nonlinear, a Newton method is employed to solve the non-linear equations governing the least-squares minimization operation. This procedure requires providing an initial guess sufficiently close to the solution and defining a termination criterion for the iteration. The iteration is considered converged when the residual of the fit coefficients is less than 10^{-8} in the absolute norm.

As an example, the fitting steps of the diffuser inlet radial velocity $U_r(z)$ (positive-leakage case) are explained below. Each fitting step consists of multiple stages, and the algorithms are explained in the form of flow charts in Figs. 6 to 11.

Step I: fits the two boundary layer regions with the power law function (eqs. (3a) and (3b)), the final form reads:

$$U_r^{\text{bl1}}(z) = \underbrace{a_{r0}\left(\frac{h}{2} + z\right)^{a_{r1}}}_{\text{boundary region 1}} \left\{ \frac{\tanh\left[a_{r2}\left(c_{\text{rbl1}} - \frac{h}{2} - z\right)\right] + 1}{2} \right\}, \tag{4}$$

$$U_r^{\text{bl2}}(z) = \underbrace{b_{r0}\left(\frac{h}{2} - z\right)^{b_{r1}}}_{\text{boundary region 2}} \left\{ \frac{\tanh\left[b_{r2}\left(c_{\text{rbl2}} - \frac{h}{2} - z\right)\right] + 1}{2} \right\}, \tag{5}$$

where $c_{\text{rbl}i}$ are coefficients specified to control the thickness of the two boundary layers δ_i. As explained in the flow chart in Fig. 6, the algorithm consists of four stages:

Stage 1. The six coefficients $\dagger_{ri}$ (where $\dagger \in \{a, b\}$, $i \in \{0, 1, 2\}$) in the first fit functions are determined by fitting the numerical data $U_r^{\text{num}}(z)$ for each triple $(\Gamma, \omega_{\text{imp}}, \hat{Q})$ with $\Gamma \in \{1.25, 1.50, 1.75, 2.00, 2.50\}$, $\omega_{\text{imp}} \in \{10, 40, 75, 125, 180\}$ rad/s and $\hat{Q} \in \{0.25, 0.50, 0.75, 1.00, 1.25\}$.

Stage 2. Two of the six coefficients $\dagger_{r2}$ obtained in Stage 1 are updated by a secondary fit such that they depend on the flow rate $\hat{Q}$ (see Fig. 12(c)). This yields the corresponding coefficients $A^j_{\dagger_{r2}}$ $(j = 0, 1, 2)$ for $\dagger_{r2}$. The remaining four coefficients, obtained in Stage 1 are corrected by again fitting the numerical velocity function $U_r^{\text{num}}(z)$ in each respective region and for each combination of $\Gamma \in \{1.25, 1.50, 1.75, 2.00, 2.50\}$, and $\omega_{\text{imp}} \in \{10, 40, 75, 125, 180\}$ rad/s and $\hat{Q} \in \{0.25, 0.50, 0.75, 1.00, 1.25\}$ using the same function of Stage 1, but replacing the coefficients $\dagger_{r2}$ with the fitted values $\tilde{\dagger}_{r2}$.

Stage 3. The third iteration of two of the remaining four coefficients $\dagger_{r0}$ in each fit is obtained by fitting the second iteration for the coefficients $\dagger_{r0}$ in $\hat{Q}$ (see Fig. 12(b)). This yields the corresponding coefficients $A^j_{\dagger_{r0}}$ $(j = 0, 1, 2)$ for $\dagger_{r0}$. The remaining coefficients $\dagger_{r1}$ are then determined a third time by fitting to the numerical velocity function $U_r^{\text{num}}(z)$ for each combination of $\Gamma \in \{1.25, 1.50, 1.75, 2.00, 2.50\}$ and $\omega_{\text{imp}} \in \{10, 40, 75, 125, 180\}$ rad/s and $\hat{Q} \in \{0.25, 0.50, 0.75, 1.00, 1.25\}$ using the same function of Stage 1, but replacing $\dagger_{ri}$ with $\tilde{\dagger}_{ri}$ for $i = 0, 2$.

Stage 4. Finally, the coefficients $\dagger_{r1}$ are updated by fitting in flow rate $\hat{Q}$ (see Fig. 12(c)). This yields the coefficients $A^j_{\dagger_{r1}}$ $(j = 0, 1, 2, 3, 4)$ for $\dagger_{r1}$.

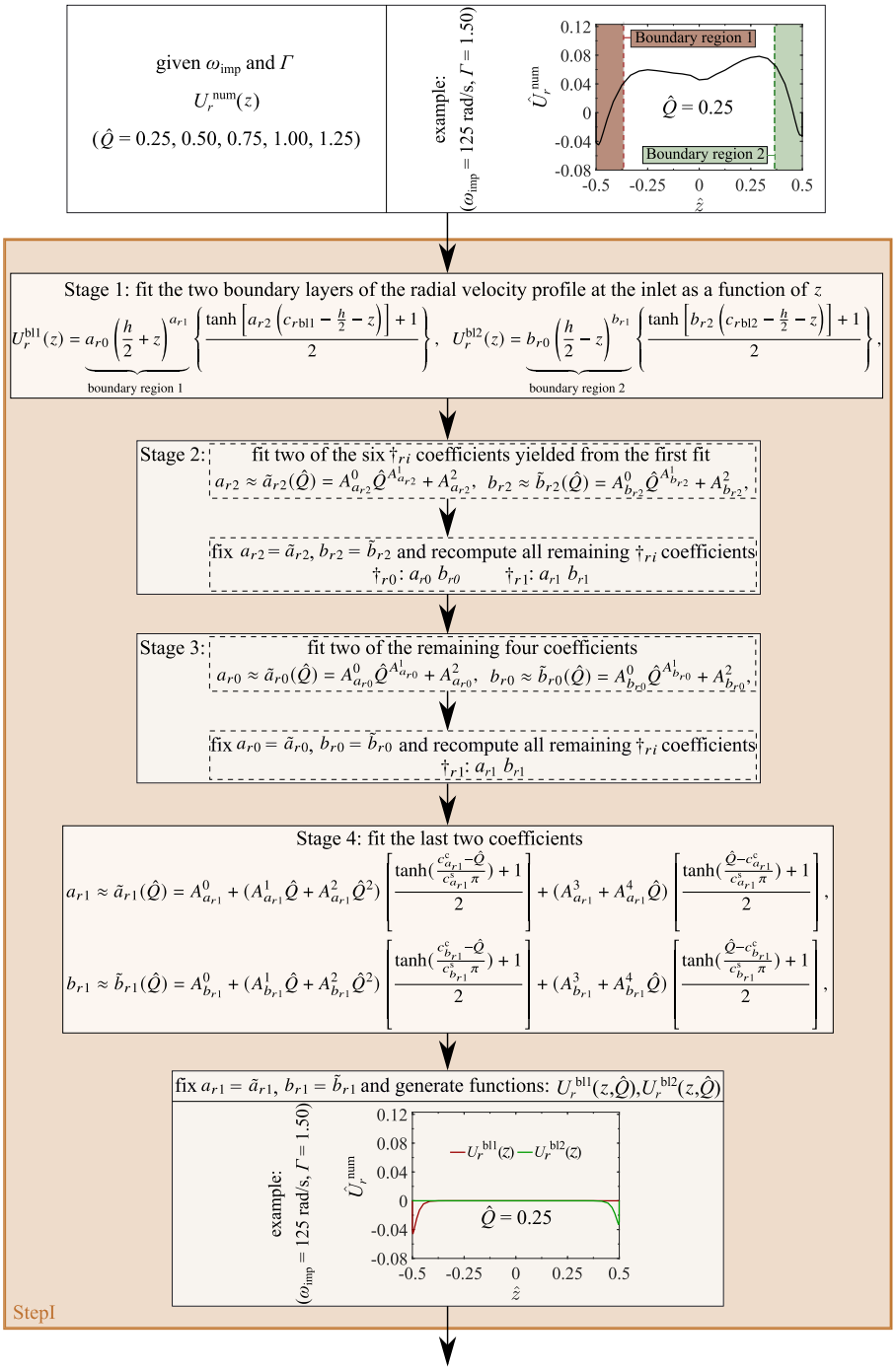

Fig. 6. Flowchart of the first fitting step for the radial velocity function. In output of this step we determine U_r^{bl1} and U_r^{bl2} as explicit functions.

By this procedure, a first set of coefficients †$_{ri}$ (where † ∈ {a, b}, $i \in \{0, 1, 2\}$) is obtained in Stage 1. The dependence on $\hat{Q}$ is then subsequently introduced in Stages 2, 3, and 4 for †$_{r2}$, †$_{r0}$, and †$_{r1}$, respectively. With all the coefficients $A^j_{\dagger ri}$ yielded from secondary fitting, the functions $U_r^{bl1}(z, \hat{Q})$ and $U_r^{bl2}(z, \hat{Q})$ can be generated.

Step II: fits the bulk flow part remaining from Step I

$$U_r^{dif1}(z) = U_r^{num}(z) - U_r^{bl1}(z) - U_r^{bl2}(z), \tag{6}$$

using a fourth power function combined with a trigonometric function

$$U_r^{bulk1}(z) = \underbrace{c_{r0}\left[z^4 - \left(\frac{h}{2}\right)^4\right]}_{\text{full range}} + \underbrace{c_{r1}\cos\left(\frac{2\pi}{h}z + \frac{\pi}{2}\right)}_{\text{bulk flow region}} \left\{\frac{\tanh\left\{c_{r2}\left[\frac{h}{2} - 20\left(\frac{c_{rbl1}+c_{rbl2}}{2}\right)^2 - z^2\right] + 1\right\} + 1}{2}\right\}, \tag{7}$$

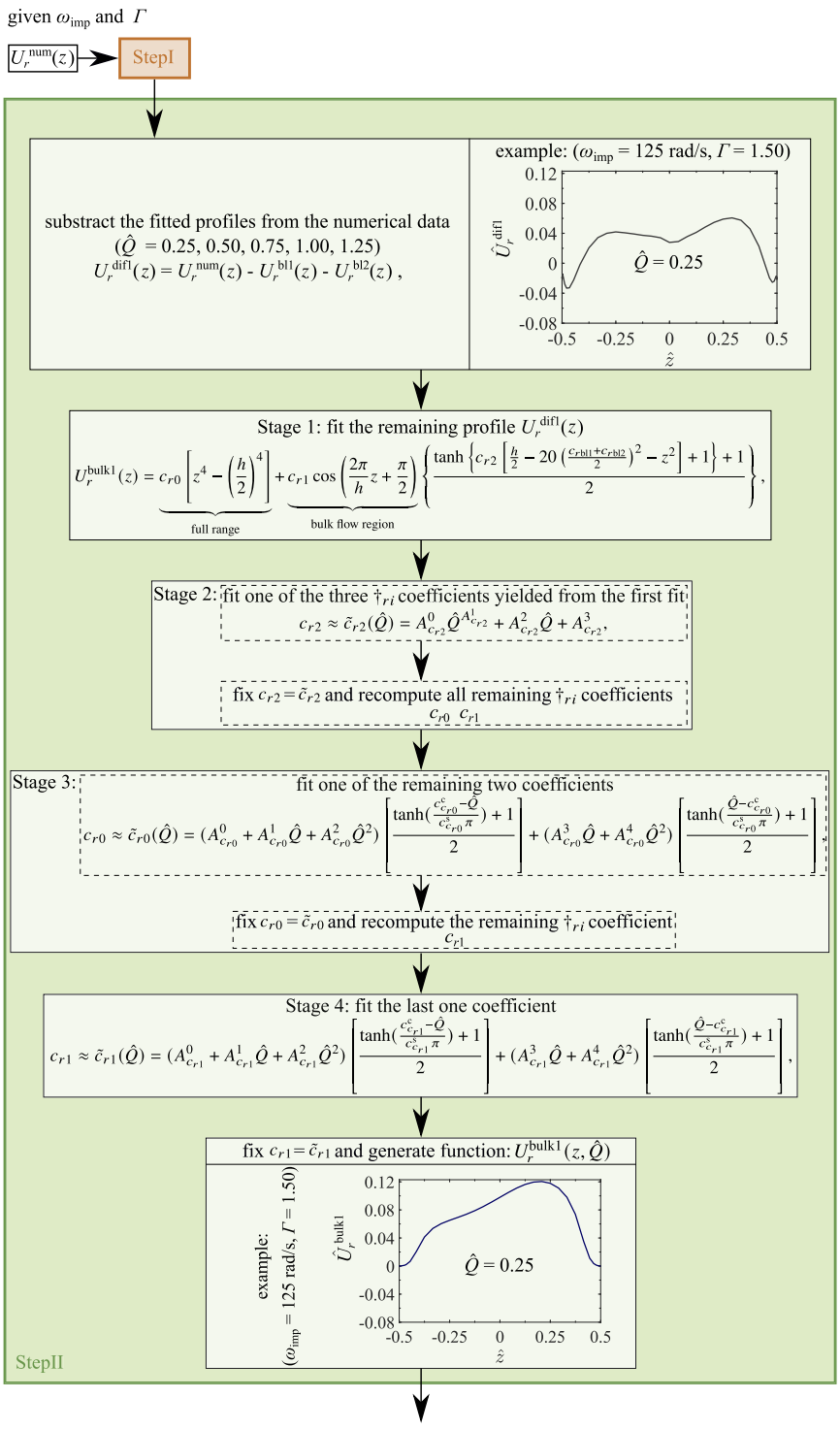

Fig. 7. Flowchart of the second fitting step for the radial velocity function. In output of this step we determine U_r^{bulk1} as an explicit function.

the fitting procedure of this step follows formally the same stages as in Step I (see Fig. 7).

Step III: fits the bulk flow part remaining from Step I and Step II

$$U_r^{dif2}(z) = U_r^{num}(z) - U_r^{bl1}(z) - U_r^{bl2}(z) - U_r^{bulk1}(z), \tag{8}$$

using a quadratic function combined with a trigonometric function

$$U_r^{bulk2}(z) = \underbrace{d_{r0}\left[z^2 - (\frac{h}{2})^2\right]}_{\text{full range}} + \underbrace{d_{r1}\cos\left(\frac{2\pi}{h}z + \frac{\pi}{2}\right)}_{\text{bulk flow region}}\left\{\frac{\tanh\left\{d_{r2}\left[\frac{h}{2} - 50\left(\frac{c_{rbl1}+c_{rbl2}}{2}\right)^2 - z^2\right] + 1\right\} + 1}{2}\right\}, \tag{9}$$

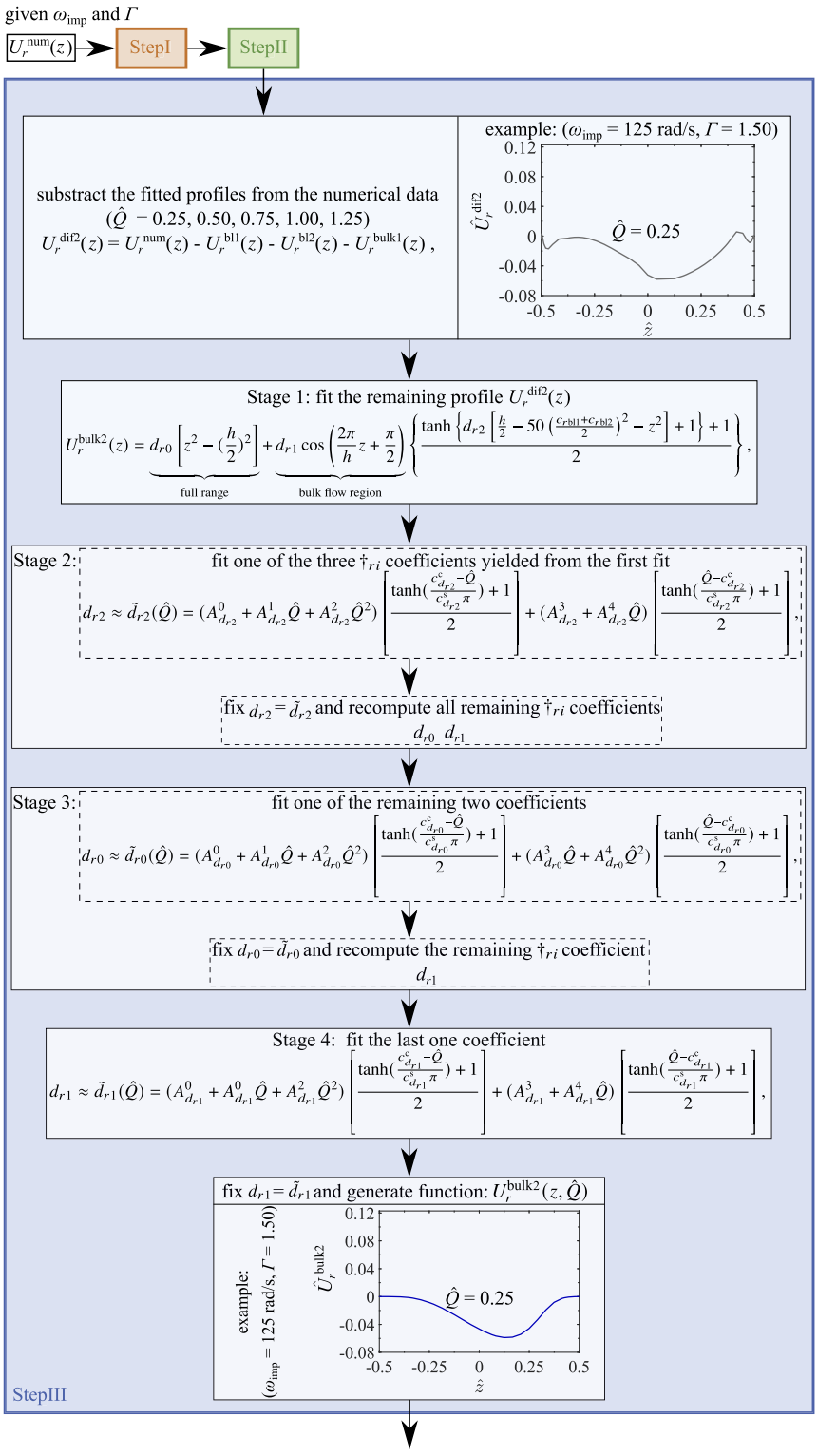

Fig. 8. Flowchart of the third fitting step for the radial velocity function. In output of this step we determine U_r^{bulk2} as an explicit function.

the fitting procedure of this step follows formally the same stages as in Step I and Step II (see Fig. 8).

Step IV: corrects for the high-order approximation at the boundaries by fitting the profile remaining from the previous three steps

$$U_r^{dif3}(z) = U_r^{num}(z) - U_r^{bl1}(z) - U_r^{bl2}(z) - U_r^{bulk1}(z) - U_r^{bulk2}(z), \tag{10}$$

using Gaussian functions

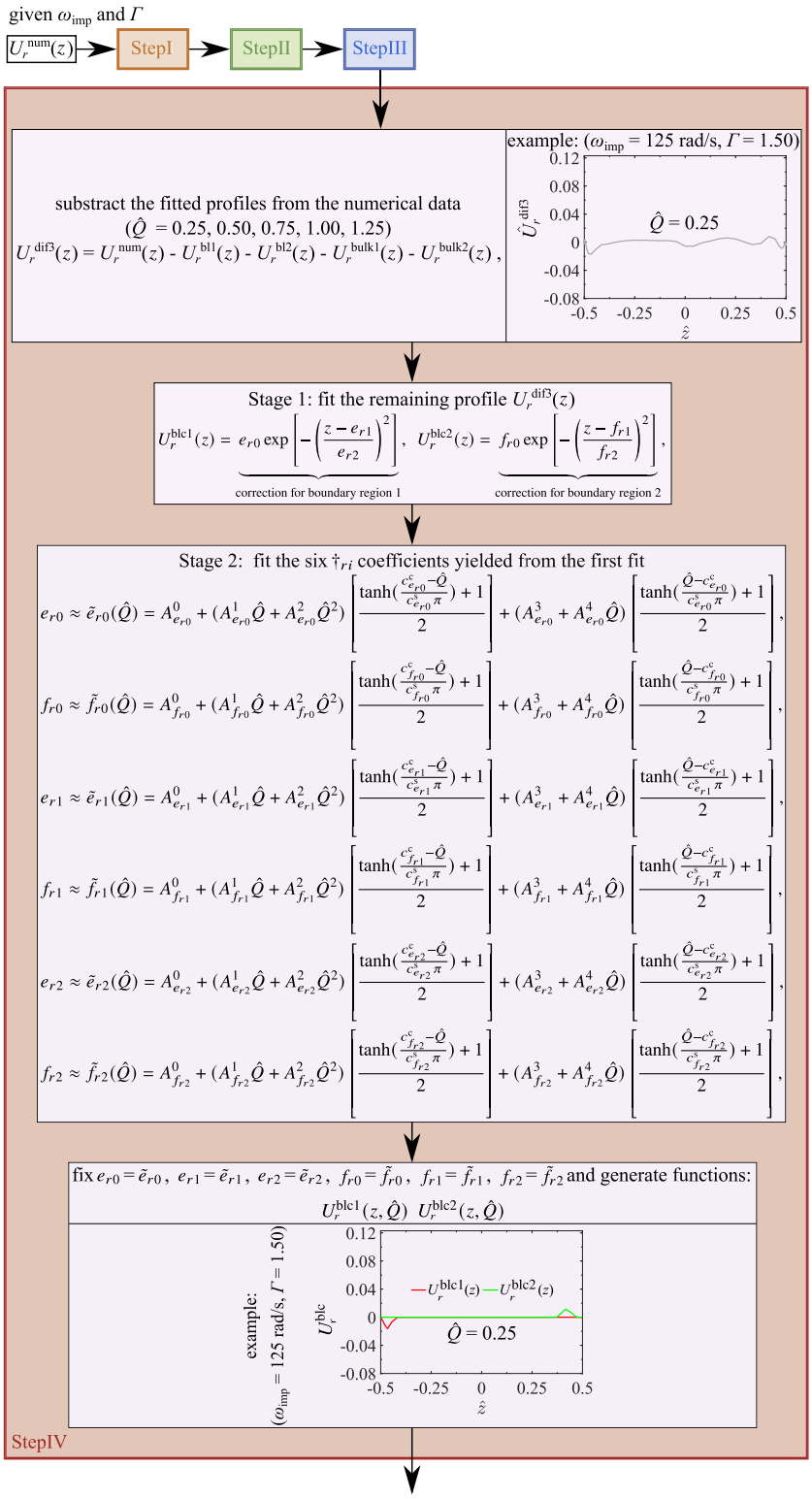

Fig. 9. Flowchart of the fourth fitting step for the radial velocity function. In output of this step we determine U_r^{blc1} and U_r^{blc2} as explicit functions.

$$U_r^{blc1}(z) = \underbrace{e_{r0}\exp\left[-\left(\frac{z-e_{r1}}{e_{r2}}\right)^2\right]}_{\text{correction for boundary region 1}}, \tag{11}$$

$$U_r^{blc2}(z) = \underbrace{f_{r0}\exp\left[-\left(\frac{z-f_{r1}}{f_{r2}}\right)^2\right]}_{\text{correction for boundary region 2}}, \tag{12}$$

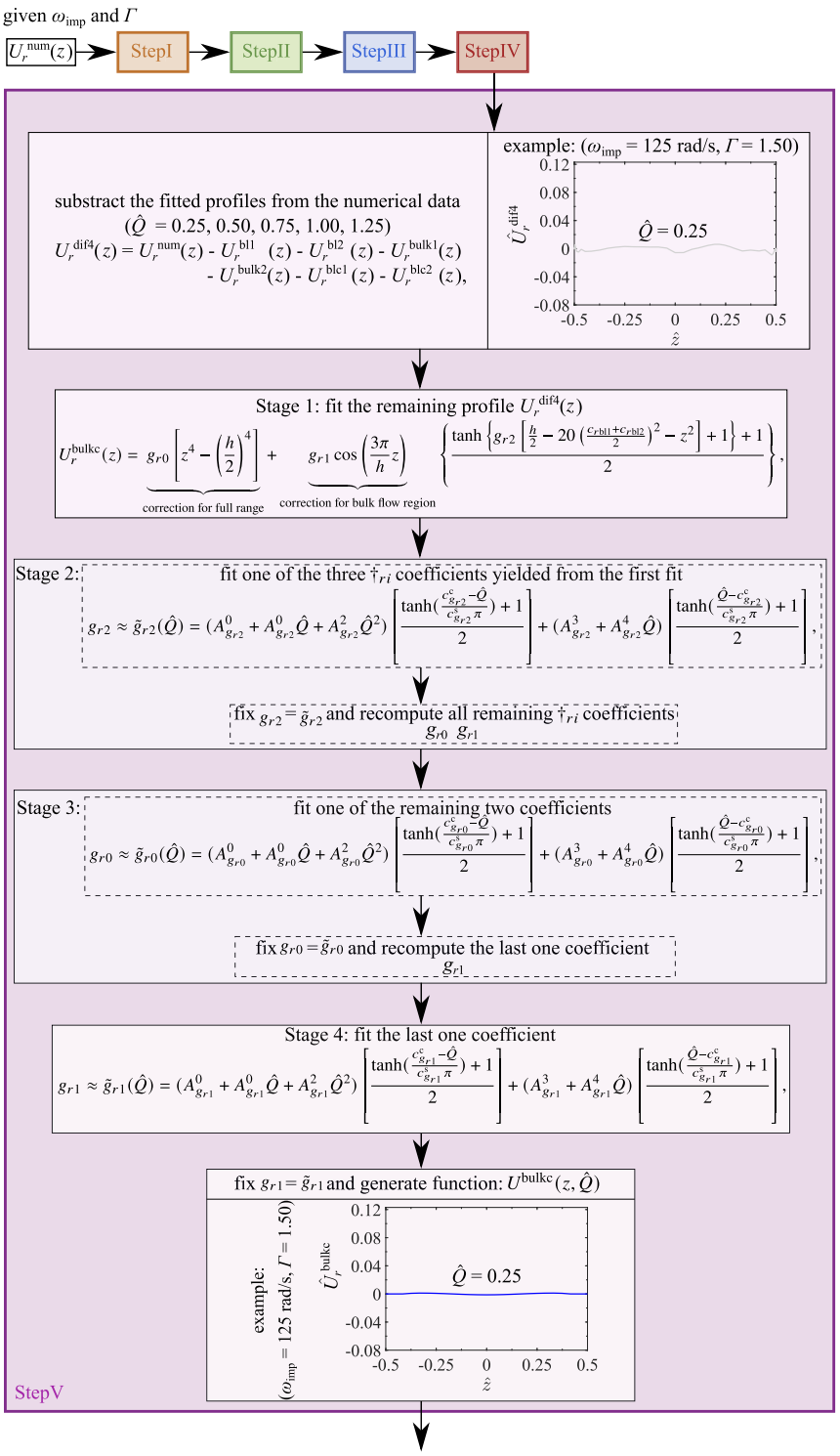

Fig. 10. Flowchart of the fifth fitting step for the radial velocity function. In output of this step we determine U_r^{bulkc} as an explicit function.

the fitting algorithm of this step is different from the others because all the $\dagger_{ri}$ coefficients are fitted in $\hat{Q}$ at the same time without employing four stages. As shown in Fig. 9, it consists of only two stages:

Stage 1. The six coefficients $\dagger_{ri}$ (where $\dagger \in \{e, f\}$, $i \in \{0, 1, 2\}$) in the first fit functions are determined by fitting the profile remaining from the previous three steps U_r^{dif3} for each triple ($\Gamma, \omega_{imp}, \hat{Q}$) with $\Gamma \in \{1.25, 1.50, 1.75, 2.00, 2.50\}$, $\omega_{imp} \in \{10, 40, 75, 125, 180\}$ rad/s and $\hat{Q} \in \{0.25, 0.50, 0.75, 1.00, 1.25\}$.

Stage 2. The six coefficients $\dagger_{ri}$ obtained in Stage 1 are updated by a secondary fit such that they depend on the flow rate $\hat{Q}$ (see Fig. 12). With all the coefficients $A^j_{\dagger_{ri}}$ yielded from secondary fitting, the functions $U_r^{blc1}(z, \hat{Q})$ and $U_r^{blc2}(z, \hat{Q})$ can be generated.

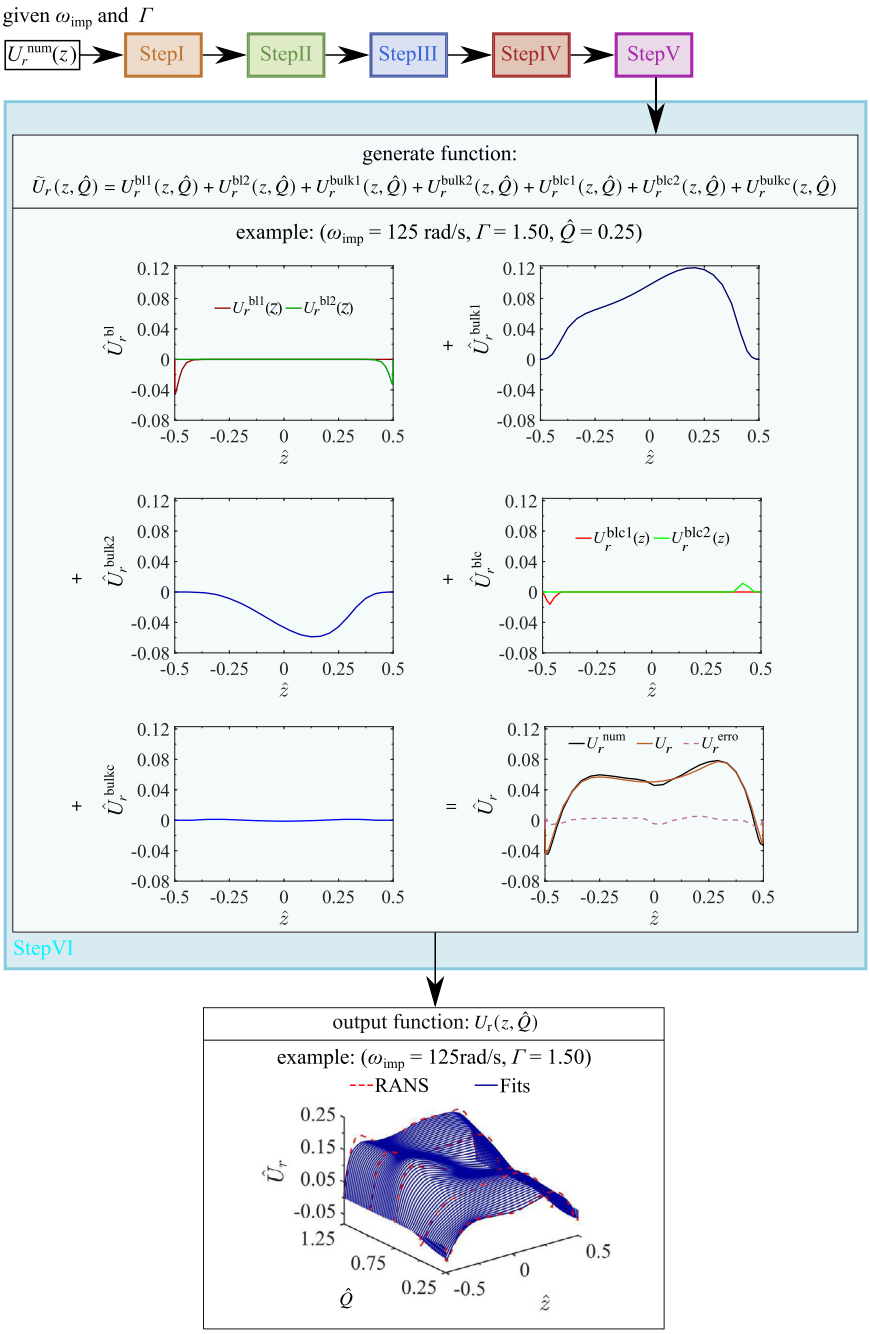

Fig. 11. Flowchart of the sixth fitting stage for the radial velocity function. In output of this step we determine $U_r(z,\hat{Q})$ as an explicit function.

Step V: corrects for the remaining bulk flow deviations by fitting the profile remaining from the previous four steps

$$U_r^{dif4}(z) = U_r^{num}(z) - U_r^{bl1}(z) - U_r^{bl2}(z) - U_r^{bulk1}(z) - U_r^{bulk2}(z) - U_r^{blc1}(z) - U_r^{blc2}(z), \tag{13}$$

using a fourth power function combined with a trigonometric function

$$U_r^{bulkc}(z) = \underbrace{g_{r0}\left[z^4 - \left(\frac{h}{2}\right)^4\right]}_{\text{correction for full range}} + \underbrace{g_{r1}\cos\left(\frac{3\pi}{h}z\right)}_{\text{correction for bulk flow region}} \left\{\frac{\tanh\left\{g_{r2}\left[\frac{h}{2} - 20\left(\frac{c_{rbl1}+c_{rbl2}}{2}\right)^2 - z^2\right] + 1\right\} + 1}{2}\right\}, \tag{14}$$

the fitting procedure of this step follows formally the same stages as in Step I, Step II, and Step III (see Fig. 10).

Step VI: sums all the fitted functions

$$\tilde{U}_r(z,\hat{Q}) = U_r^{bl1}(z,\hat{Q}) + U_r^{bl1}(z,\hat{Q}) + U_r^{bulk1}(z,\hat{Q}) + U_r^{bulk2}(z,\hat{Q}) + U_r^{blc1}(z,\hat{Q}) + U_r^{blc2}(z,\hat{Q}) + U_r^{bulkc}(z,\hat{Q}), \tag{15}$$

and then outputs the final function $\tilde{U}_r(z,\hat{Q})$ as explained in Fig. 11.

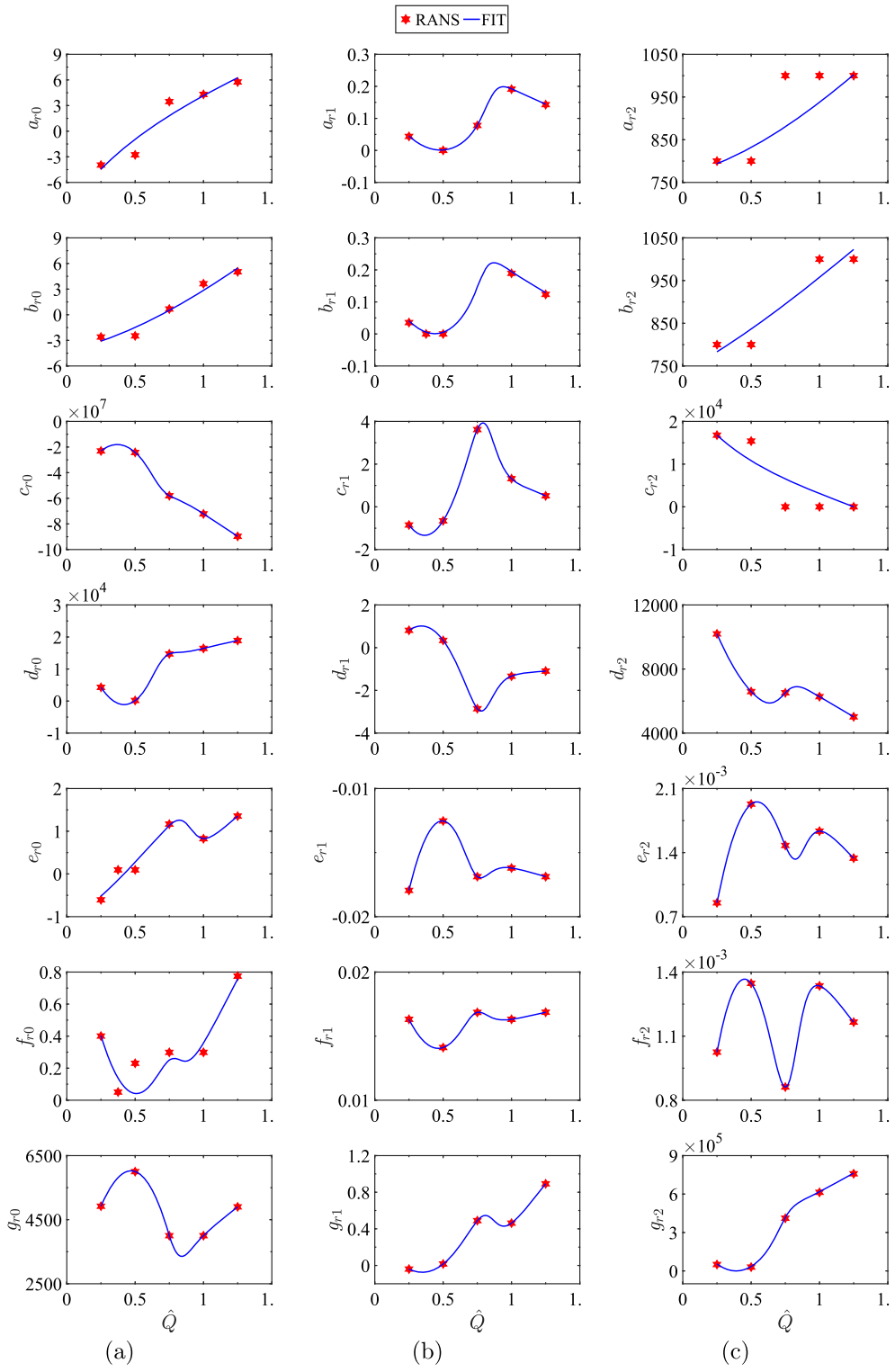

Fig. 12. Secondary fitting for the coefficients $\dagger_{ri}$ of U_r with the rotational speed $\omega_{\text{imp}} = 125$ rad/s and diffuser radius ratio $\Gamma = 1.50$ of the positive-leakage case.

Note the order of fitting the three coefficients $\dagger_{r0}$, $\dagger_{r1}$, and $\dagger_{r2}$ in each step is not fixed and depends on the specific case. The secondary fitting functions we adopted are based on the variation trend of the fitting coefficient $\dagger_{ri}$ with the flow rate $\hat{Q}$, the fitting results of the coefficients $\dagger_{ri}$ of U_r with the rotational speed $\omega_{\text{imp}} = 125$ rad/s and diffuser radius ratio $\Gamma = 1.50$ of the positive-leakage case is given in Fig. 12(a) as an example.

The same fitting procedure is applied for the tangential velocity $U_\theta(z)$ of the positive-leakage case. The fitting procedure is further adapted for the axial velocity $U_z(z)$ owing to the major topological differences of the profile to fit:

Step I: fits the bulk flow firstly using a quadratic function combined with a trigonometric function

$$U_z^{\text{bulk1}}(z) = \underbrace{a_{z0}\left[z^2 - (\frac{h}{2})^2\right] + a_{z1}\cos\left(\frac{2\pi}{h}z + \frac{\pi}{2}\right)}_{\text{full range}}. \tag{16}$$

Step II: fits the bulk flow part remaining from Step I

$$U_z^{\text{dif1}}(z) = U_z^{\text{num}}(z) - U_z^{\text{bulk1}}(z), \tag{17}$$

using a quadratic function combined with another trigonometric function

$$U_z^{\text{bulk2}}(z) = \underbrace{b_{z0}\left[z^2 - (\frac{h}{2})^2\right] + b_{z1}\cos\left(\frac{4\pi}{h}z + \frac{\pi}{2}\right)}_{\text{full range}}. \tag{18}$$

Step III: fits the two boundary layer regions of the profile remaining from the previous two steps

$$U_z^{\text{dif2}}(z) = U_z^{\text{num}}(z) - U_z^{\text{bulk1}}(z) - U_z^{\text{bulk2}}(z), \tag{19}$$

using the power-law function

$$\begin{aligned} U_z^{\text{bl1}}(z) &= \underbrace{c_{z0}\left(\frac{h}{2} + z\right)^{c_{z1}}}_{\text{boundary region 1}}\left\{\frac{\tanh\left[c_{z2}\left(c_{z\text{bl1}} - \frac{h}{2} - z\right)\right] + 1}{2}\right\}, \\ U_z^{\text{bl2}}(z) &= \underbrace{d_{z0}\left(\frac{h}{2} - z\right)^{d_{z1}}}_{\text{boundary region 2}}\left\{\frac{\tanh\left[d_{z2}\left(c_{z\text{bl2}} - \frac{h}{2} - z\right)\right] + 1}{2}\right\}. \end{aligned} \tag{20}$$

Step IV: corrects for the remaining bulk flow deviations by fitting the profile remaining from the previous three steps

$$U_z^{\text{dif3}}(z) = U_z^{\text{num}}(z) - U_z^{\text{bulk1}}(z) - U_z^{\text{bulk2}}(z) - U_z^{\text{bl1}}(z) - U_z^{\text{bl2}}(z), \tag{21}$$

using a quadratic function combined with a trigonometric function

$$U_z^{\text{bulkc}}(z) = \underbrace{e_{z0}\left[z^2 - (\frac{h}{2})^2\right] + e_{z1}\cos\left(\frac{4\pi}{h}z + \frac{\pi}{2}\right)}_{\text{full range}}. \tag{22}$$

Step V: sums all the fitted functions

$$\tilde{U}_z(z, \hat{Q}) = U_z^{\text{bulk1}}(z, \hat{Q}) + U_z^{\text{bulk2}}(z, \hat{Q}) + U_z^{\text{bl1}}(z, \hat{Q}) + U_z^{\text{bl2}}(z, \hat{Q}) + U_z^{\text{bulkc}}(z, \hat{Q}), \tag{23}$$

and then outputs the final function $\tilde{U}_z(z, \hat{Q})$.

Owing to the lower leakage flow, for the zero- and negative-leakage case, the fitting is easier because the step to correct the boundary parts (see Fig. 9) for the radial U_r and tangential velocity U_θ are not needed anymore. The fitting method is flexible with adjustable orders of fitting steps adapt to different cases. Meanwhile, different combinations of different fitting functions are available. All the secondary fitting functions adopted for the coefficients $\dagger_{*i}$ (see Fig. 12) are reported below

$$\dagger_{*i}(\hat{Q}) = A^0_{\dagger_{*i}}, \tag{24a}$$

$$\dagger_{*i}(\hat{Q}) = A^0_{\dagger_{*i}}\hat{Q}^{A^1_{\dagger_{*i}}} + A^2_{\dagger_{*i}}, \tag{24b}$$

$$\dagger_{*i}(\hat{Q}) = A^0_{\dagger_{*i}}\hat{Q}^{A^1_{\dagger_{*i}}} + A^2_{\dagger_{*i}}\hat{Q} + A^3_{\dagger_{*i}}, \tag{24c}$$

$$\dagger_{*i}(\hat{Q}) = A^0_{\dagger_{*i}} + A^1_{\dagger_{*i}}\hat{Q}\left[\frac{\tanh(\frac{c^c_{\dagger_{*i}} - \hat{Q}}{c^s_{\dagger_{*i}}\pi}) + 1}{2}\right] + (A^2_{\dagger_{*i}} + A^3_{\dagger_{*i}}\hat{Q} + A^4_{\dagger_{*i}}\hat{Q}^2)\left[\frac{\tanh(\frac{\hat{Q} - c^c_{\dagger_{*i}}}{c^s_{\dagger_{*i}}\pi}) + 1}{2}\right], \tag{24d}$$

$$\dagger_{*i}(\hat{Q}) = (A^0_{\dagger_{*i}} + A^1_{\dagger_{*i}}\hat{Q})\left[\frac{\tanh(\frac{c^c_{\dagger_{*i}} - \hat{Q}}{c^s_{\dagger_{*i}}\pi}) + 1}{2}\right] + (A^2_{\dagger_{*i}} + A^3_{\dagger_{*i}}\hat{Q} + A^4_{\dagger_{*i}}\hat{Q}^2)\left[\frac{\tanh(\frac{\hat{Q} - c^c_{\dagger_{*i}}}{c^s_{\dagger_{*i}}\pi}) + 1}{2}\right], \tag{24e}$$

Table 2
Functions chosen for secondary fitting of the fitting coefficients $\dagger_{*i}$.

Func	$\dagger_{ri}$	$\dagger_{\theta i}$	$\dagger_{zi}$
positive-leakage case			
(24a)	/	a_2, b_2, d_2	/
(24b)	a_0, a_2, b_0, b_2	a_0, b_0	/
(24c)	c_2	c_2	/
(24d)	/	/	$c_0, c_1, c_2, d_0, d_1, d_2, e_0, e_1$
(24e)	/	/	a_0, a_1, b_0, b_1
(24f)	$a_1, b_1, e_0, e_1, e_2, f_0, f_1, f_2$	$a_1, b_1, e_0, e_1, e_2, f_0, f_1, f_2$	/
(24g)	d_1, d_2, g_0, g_1, g_2	d_1, g_0, g_1, g_2	/
(24h)	c_0, c_1, d_0	c_0, c_1, d_0	/
negative-leakage case			
(24c)	a_1, b_1, c_0	a_1, b_1, c_0	/
(24d)	/	/	$d_0, d_1, d_2, e_0, e_1, e_2$
(24e)	/	/	$a_0, a_1, b_0, b_1, c_0, c_1$
(24f)	a_0, a_2, b_0, b_2	a_0, a_2, b_0, b_2	/
(24g)	$c_1, c_2, d_0, d_1, e_0, e_1$	$c_1, c_2, d_0, d_1, e_0, e_1$	/
zero-leakage case			
(24c)	a_1, b_1, c_0	a_1, b_1, c_0	d_1, e_1
(24d)	/	/	d_0, d_2, e_0, e_2
(24e)	/	/	$a_0, a_1, b_0, b_1, c_0, c_1$
(24f)	$a_0, b_0, a_2, b_2, e_0, e_1$	$a_0, b_0, a_2, b_2, e_0, e_1$	/
(24g)	c_1, c_2, d_0, d_1, d_2	c_1, c_2, d_0, d_1, d_2	/

$$\dagger_{*i}(\hat{Q}) = A^0_{\dagger_{*i}} + (A^1_{\dagger_{*i}}\hat{Q} + A^2_{\dagger_{*i}}\hat{Q}^2)\left[\frac{\tanh(\frac{c^c_{\dagger_{*i}} - \hat{Q}}{c^s_{\dagger_{*i}}\pi}) + 1}{2}\right] + (A^3_{\dagger_{*i}} + A^4_{\dagger_{*i}}\hat{Q})\left[\frac{\tanh(\frac{\hat{Q} - c^c_{\dagger_{*i}}}{c^s_{\dagger_{*i}}\pi}) + 1}{2}\right], \tag{24f}$$

$$\dagger_{*i}(\hat{Q}) = (A^0_{\dagger_{*i}} + A^0_{\dagger_{*i}}\hat{Q} + A^2_{\dagger_{*i}}\hat{Q}^2)\left[\frac{\tanh(\frac{c^c_{\dagger_{*i}} - \hat{Q}}{c^s_{\dagger_{*i}}\pi}) + 1}{2}\right] + (A^3_{\dagger_{*i}} + A^4_{\dagger_{*i}}\hat{Q})\left[\frac{\tanh(\frac{\hat{Q} - c^c_{\dagger_{*i}}}{c^s_{\dagger_{*i}}\pi}) + 1}{2}\right], \tag{24g}$$

$$\dagger_{*i}(\hat{Q}) = (A^0_{\dagger_{*i}} + A^1_{\dagger_{*i}}\hat{Q} + A^2_{\dagger_{*i}}\hat{Q}^2)\left[\frac{\tanh(\frac{c^c_{\dagger_{*i}} - \hat{Q}}{c^s_{\dagger_{*i}}\pi}) + 1}{2}\right] + (A^3_{\dagger_{*i}}\hat{Q} + A^4_{\dagger_{*i}}\hat{Q}^2)\left[\frac{\tanh(\frac{\hat{Q} - c^c_{\dagger_{*i}}}{c^s_{\dagger_{*i}}\pi}) + 1}{2}\right], \tag{24h}$$

and the corresponding functions chosen for different cases are given in the Table 2. As a result of our fitting method, the three components of the velocity profile at the diffuser inlet are approximated as explicit functions of the flow rate $\hat{Q}$.

5. Results

5.1. Accuracy assessment

A comparison between the diffuser inlet velocity profiles determined numerically from the RANS simulation (solid line) and the profiles resulting from the above fitting procedure (dash line) is shown in Fig. 13 for three different leakage configurations with the rotational speed ω_{imp} = 125 rad/s and the diffuser radius ratio Γ = 1.50 at the flow rate Q/Q_{d} = 0.25, 0.50, 0.75, 1.00, and 1.25. For all cases, the simulated and fitted velocity profiles are in excellent agreement over the whole range of z. In addition, the error E of the fits is analyzed with respect to the original numerical data to fit. The normalized error of the radial velocity $\hat{E}_{U_r}$, tangential velocity $\hat{E}_{U_\theta}$ and axial velocity $\hat{E}_{U_z}$ is defined as

$$\hat{E}_{U_r}(z) = \frac{E_{U_r}(z)}{Q/S} = \frac{U_r^{\text{num}}(z) - U_r(z)}{Q/S}, \tag{25}$$

$$\hat{E}_{U_\theta}(z) = \frac{E_{U_\theta}(z)}{\omega_{\text{imp}} R_3} = \frac{U_\theta^{\text{num}}(z) - U_\theta(z)}{\omega_{\text{imp}} R_3}, \tag{26}$$

$$\hat{E}_{U_z}(z) = \frac{E_{U_z}(z)}{U_z^{\text{ref}}(z)} = \frac{U_z^{\text{num}}(z) - U_z(z)}{U_z^{\text{ref}}(z)}, \tag{27}$$

where the U_z^{Ref} is defined differently for different geometries as it depends on the leakage flow rate Q_{leak}. For the cases with leakage, we assume that the axial velocity is symmetric at the diffuser inlet in z direction

$$U_z^{\text{ref}} = \frac{Q_{\text{leak}}}{\pi({R_3}^2 - {R_2}^2)} \simeq \int_0^{\max(z)} \frac{U_z dz}{H_3/2}. \tag{28}$$

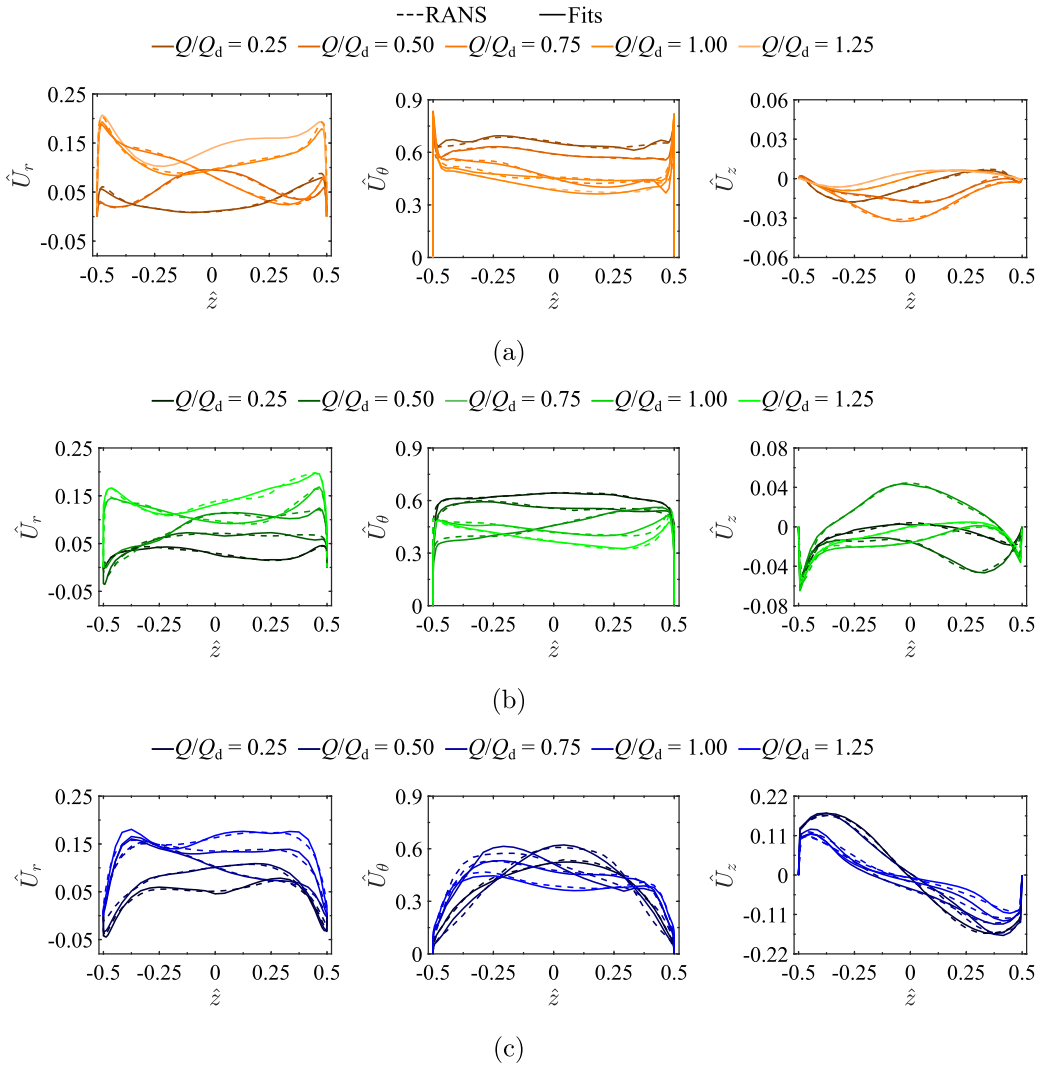

Fig. 13. Comparison of the diffuser inlet radial, tangential, and axial velocity profiles with the rotational speed $\omega_{imp} = 125$ rad/s and the diffuser radius ratio $\Gamma = 1.50$ obtained from the RANS simulation and the fitting of the three computational configurations: (a) zero-, (b) negative-, and (c) positive-leakage case.

For the zero-leakage case, the azimuthally-averaged two-dimensional continuity equation in cylindrical coordinates can be written as

$$\nabla_{rz} \cdot \vec{\bar{U}} = \frac{1}{r}\frac{\partial (r\bar{U}_r)}{\partial r} + \frac{\partial \bar{U}_z}{\partial z} = 0, \tag{29}$$

the parameters can be scaled as

$$r \sim R, \quad z \sim R\delta, \quad U_r \sim Q/S, \quad U_z \sim U_z^{\text{ref}}, \tag{30}$$

then the U_z^{ref} can be derived by balancing the order of magnitude of the two terms

$$\frac{Q}{SR} \sim \frac{U_z^{\text{ref}}}{R\delta} \Rightarrow U_z^{\text{ref}} = \frac{Q\,\delta}{S}. \tag{31}$$

The L2 norm of the scaled errors of the fitting is depicted in Fig. 14, which shows that the error norm is almost always below 15% for $\hat{U}_r$ and $\hat{U}_\theta$ with ω_{imp} = 125 rad/s and Γ = 1.50. The same statement holds true for all our other fits which constitute a clear assessment of accuracy for our fits. Keeping the L2-norm below 15% for $\hat{U}_r$ and $\hat{U}_\theta$ leads to a good quantitative agreement of the pressure and velocity fields when comparing the diffuser model supplemented by our scale-matching-fitted inlet against the full-pump simulations (see following sections for more details). This same condition is not respected when employing classic algebraic polynomial and Gaussian fits, whose performance at reproducing the full-pump results is poor (see Sec. 5.5 for a comparative study). The error on U_z is larger due to the sensitivity of U_z to the local leakage flow. Also in this case, the obtained accuracy is significantly higher than for traditional fitting techniques.

5.2. Inlet profile analysis

The diffuser performance correlates with the impeller outflow angle, non-uniformity, and unsteadiness of the inlet flow. The effect of flow rate Q and the impeller-diffuser leakage on diffuser inlet boundary conditions are discussed in this section. The fitted inlet velocity

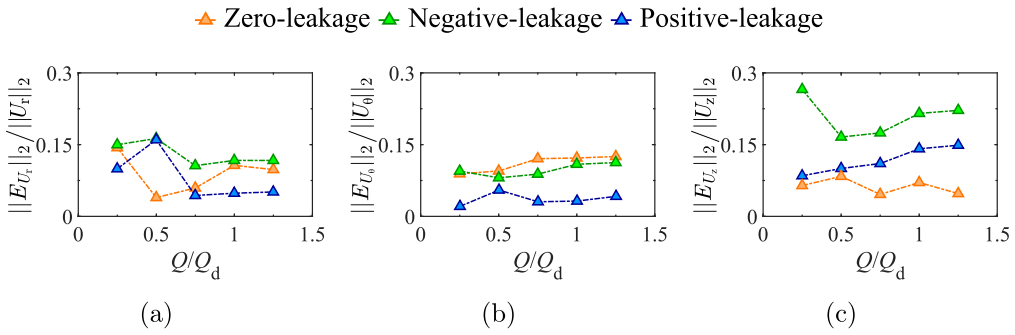

Fig. 14. Comparison of the fitting errors of (a) radial velocity, (b) tangential velocity, and (c) axial velocity for three different computational configurations with the rotational speed $\omega_{imp} = 125$ rad/s and the diffuser radius ratio $\Gamma = 1.50$.

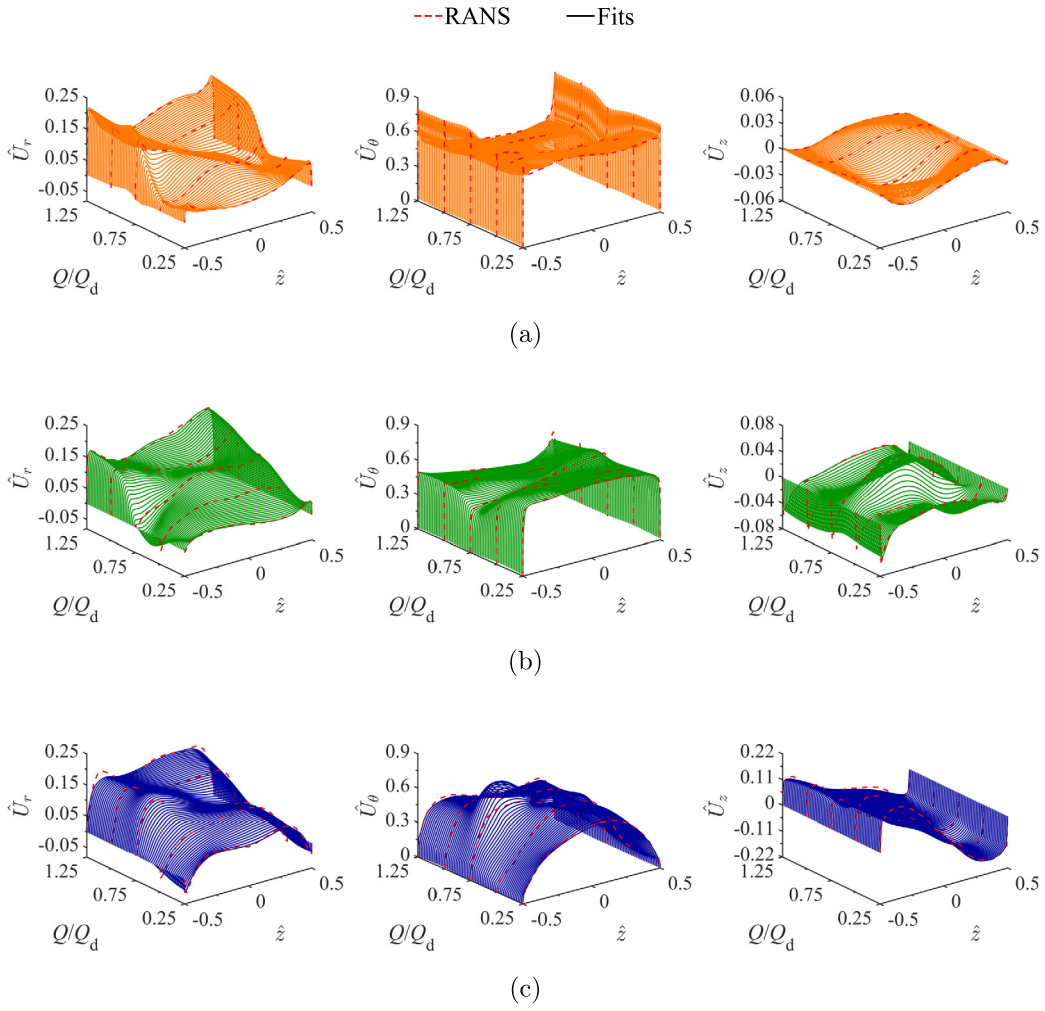

Fig. 15. Comparison of the fitted results of the radial, tangential, and axial velocity profiles with the rotational speed $\omega_{imp} = 125$ rad/s and the diffuser radius ratio $\Gamma = 1.50$ of the three different configurations: (a) zero-, (b) negative-, and (c) positive-leakage case.

profiles of three different leakage configurations with the rotational speed ω_{imp} = 125 rad/s and the diffuser radius ratio Γ = 1.50 are plotted in Fig. 15. The velocity profiles vary smoothly with the change of the flow rate Q.

For the zero-leakage case (see Fig. 15(a)), the radial velocity $\hat{U}_r$ decreased smoothly with the decrease of flow rate Q, and the boundary layer decayed rapidly after the flow rate Q/Q_d decreased below 0.75. The tangential velocity $\hat{U}_\theta$ and axial velocity $\hat{U}_z$ have some small fluctuations, and the amplitude of $\hat{U}_z$ is very low. Besides, we can observe that all the velocity profiles are almost symmetrically distributed in the z-direction over the whole range of flow rate Q except for $\hat{U}_z$ that must compensate for the continuity of mass.

For the negative-leakage case, the velocity profiles do not qualitatively change much compared with the zero-leakage case in $\hat{U}_r$ and $\hat{U}_\theta$. At the large flow rates, the radial velocity is more symmetrically distributed in z direction, but we can still find that the radial velocity near the shroud side is lower than the hub side, and the boundary layer decays much faster than the zero-leakage case. In fact, for this configuration, the pressure difference between the impeller outlet and the impeller inlet section leads to a leakage flow going out at the impeller-diffuser radial gap on the shroud wall, feeding back to the impeller inlet plane. This is the reason for the observed

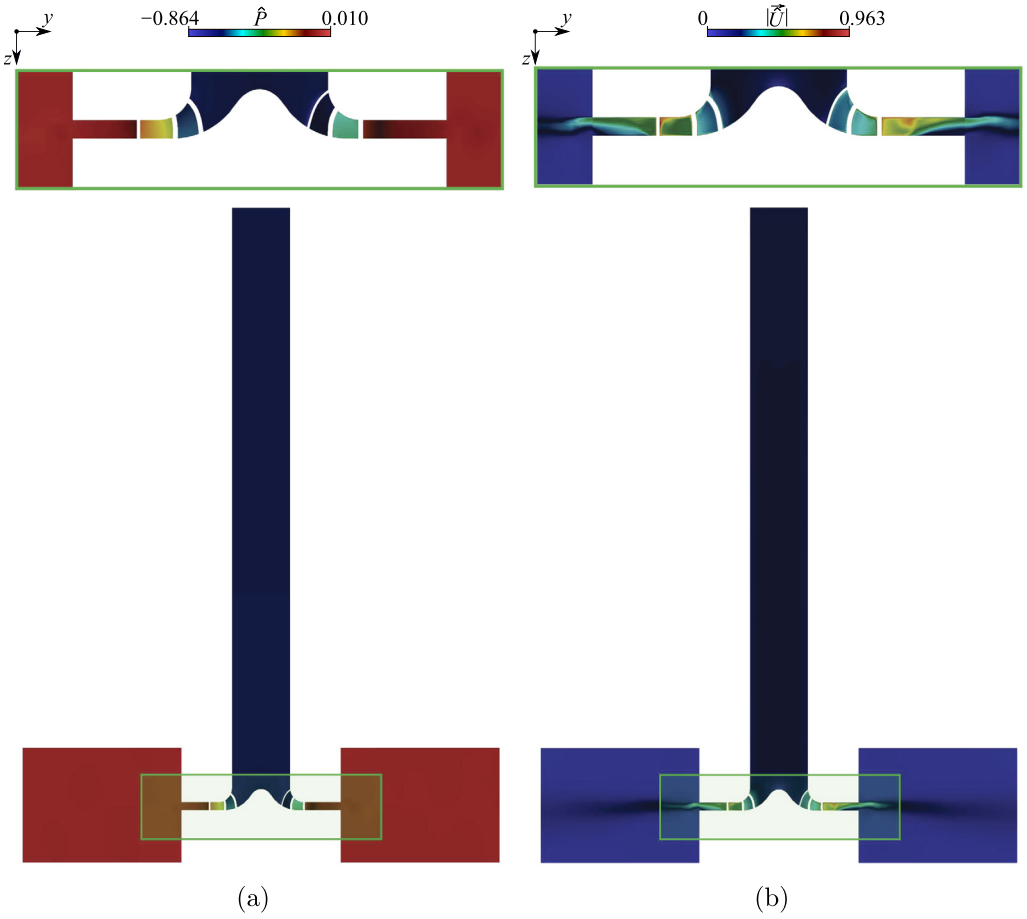

Fig. 16. Instantaneous color maps of the (a) static pressure and the (b) velocity magnitude at the mid-plane of the zero-leakage case of the centrifugal machine with the rotational speed $\omega_{\text{imp}} = 125$ rad/s and the diffuser radius ratio $\Gamma = 1.50$.

asymmetric. At small flow rates, the pressure difference between the impeller inlet and the outlet is larger, hence the velocity profiles are more asymmetrical. Moreover, the axial velocity $\hat{U}_z$ becomes more symmetric.

For the positive-leakage case, the leakage flow goes inside the vaneless diffuser, resulting in a larger boundary layer in $\hat{U}_r$ and $\hat{U}_\theta$. And the increased axial velocity magnitude $|\hat{U}_z|$ on both sides of the diffuser leads to an asymmetric $\hat{U}_z$. The large amplitude of $|\hat{U}_z|$ strongly perturbs the jet wake from the impeller.

Concerning the inlet profiles of the three different cases, we found that the leakage flow has a significant influence on the diffuser inlet boundary condition and leads to different instabilities characteristics which have been analyzed in Fan et al. [14].

5.3. Flow field analysis

For a better understanding of the flow field in the machine and the vaneless diffuser, the color maps of the zero-leakage case at the design condition $Q/Q_{\text{d}} = 1.00$ of the URANS results are shown first. The instantaneous static pressure p and velocity magnitude U_{mag} over the meridian section $x = 0$ are depicted in Fig. 16. The incompressible flow enters the centrifugal machine through the inlet pipe, very thin boundary layers develop in the inlet pipe (not clear at the scale of the color map) and a weak pressure gradient drives the flow down to the impeller. Once the flow reached the impeller, a strong tangential velocity component $\omega_{\text{imp}} r$ adds up to the flow velocity owing to the rotation of the impeller that channels the incoming flow through its blades. The rotating impeller imparts additional kinetic energy into the air stream by increasing the velocity of the air. The kinetic energy is then converted to increase the potential energy/static pressure by decelerating the flow through a vaneless diffuser. Meanwhile, it can be observed that the turbulent flow in the vaneless diffuser is asymmetric and highly skewed owing to the impingement on the hub and the boundary layer development on the diffuser walls.

To confirm that the simplified numerical model using the fitted diffuser inlet velocity profiles can reproduce the flow field inside the vaneless diffuser, the comparison of the azimuthally averaged color maps of the normalized instantaneous static pressure $\hat{p}$, radial $\hat{U}_r$, tangential $\hat{U}_\theta$, and axial velocity $\hat{U}_z$ at the design condition $Q/Q_{\text{d}} = 1.00$ of three different leakage configurations obtained from the RANS simulation of the whole machine model (up) and the simplified model (bottom) is shown in Fig. 17.

Note that for the simplified simulation, we employ the same numerical parameters of the experimentally validated RANS and URANS (see Fan et al. [15,14]). This being said, the simplified simulation with a circumferential-direction averaged velocity or with mimicked jet wakes is not aimed to exactly reproduce the inflow produced by the rotating impeller, but we rather want to reproduce its average flow and understand how this affects, all alone, the rotating instabilities. In fact, the major difference between the two unstable mechanisms observed in the vaneless diffuser is that the mechanism proposed by Tsujimoto et al. [5] only depends on the azimuthally-averaged flow, and the one proposed by Ljevar [8] relies on an azimuthally-modulated inflow. We aim to accurately reproduce the mean flow and then

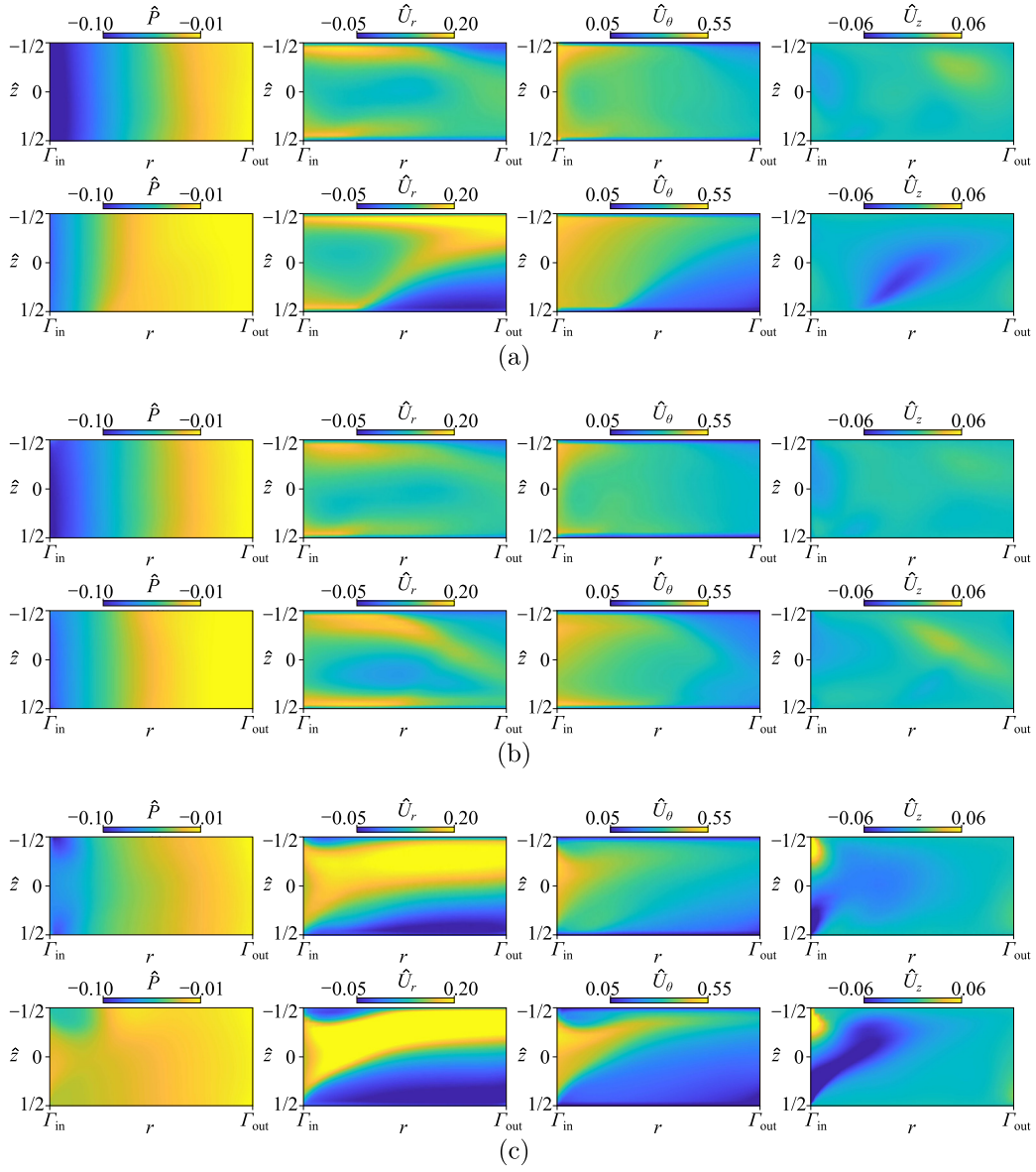

Fig. 17. Comparison of the azimuthally averaged colormaps of the static pressure, radial, tangential and axial velocity (from left to right) of RANS simulation of the entire machine (top), and RANS simulation for the diffuser only using our fit for the mean velocity profile as the inlet boundary condition (bottom) for the design flow rate $Q/Q_d = 1.00$ with the rotational speed ω_{imp} = 125 rad/s and radius ratio Γ = 1.50 for three different leakage configurations: (a) zero-, (b) negative-, and (c) positive-leakage case.

test azimuthal modulations in order to infer which instability mechanism holds in place upon the selected flow parameters. Hence, we do not aim to reproduce exactly the same flow field, but we rather want to build a model that will allow us to investigate in depth the nature of the vaneless diffuser instability keeping a certain consistency with real pump flows. Our results show that the flow field obtained from the simplified model is qualitatively matching and quantitatively close to the results obtained in the diffuser by simulating the whole machine but at 30% of the computational cost.

As the fitting protocol is relatively more accurate for $\hat{U}_r$ and $\hat{U}_\theta$ (see Fig. 14), the quantitative agreement between the colormaps for $\hat{U}_z$ is worse than for the other two velocity components. This also leads to a decrease of accuracy in terms of the pressure field, which, however, does not play an essential role if one aims to use the model for investigating the stability of the flow in the diffuser.

A significant difference between the model flow and the azimuthally-averaged diffuser velocity field of the RANS for the whole machine is however occurring for the zero-leakage case. In the following section, we will carry out a detailed investigation to explain why simulating the model flow leads to a remarkable boundary layer separation at the hub, which separation is not observed when simulating the whole machine.

5.4. Deviation of the mean flow field

As mentioned in the previous section, a significant deviation of the azimuthally-averaged flow field can be observed from the two simulations for the zero-leakage case. As shown in Fig. 17(a), a strong boundary layer separation occurs on the hub wall for the RANS results of the simplified model obtained using the mean flow profile at the inlet. As a consequence, such a separation leads to an ex-

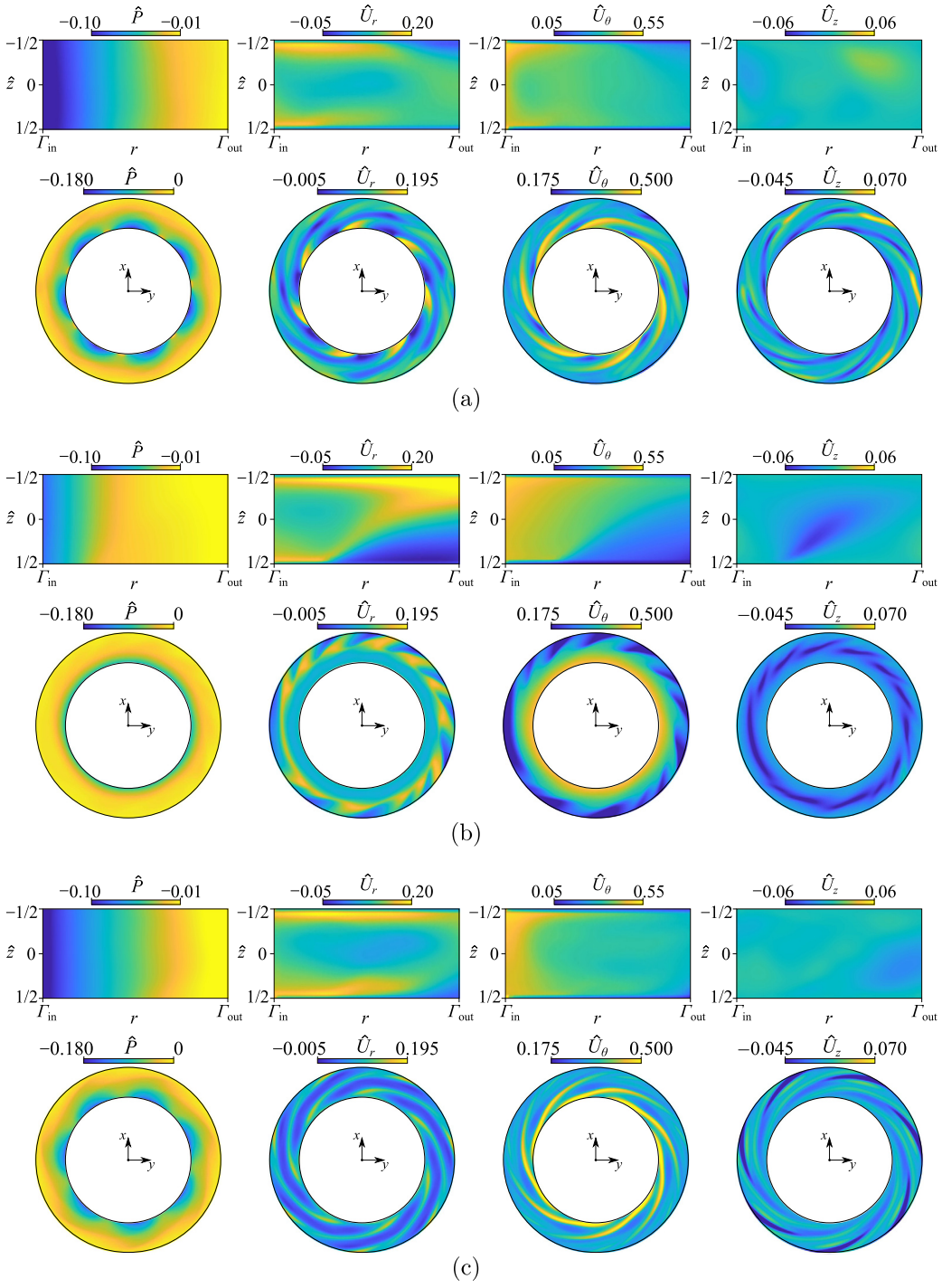

Fig. 18. Color maps of the instantaneous static pressure, radial velocity, tangential velocity, and axial velocity at the design condition $Q/Q_d = 1.00$ obtained by the RANS simulation for (a) the entire machine, (b) the simplified model with mean inlet flow, and (c) the simplified model with a approximately mimicked jet wake at the inlet. The upper figures display the azimuth-averaged value on the meridian section of the diffuser, while the lower figures show the instantaneous value at the mid-height of the diffuser.

tended mean backflow that can be observed near the diffuser outlet. A similar boundary layer separation is not found, however, in the azimuthally-averaged RANS results of the full machine.

To understand the origin of such a discrepancy, we first focus on the mid-height section of the vaneless diffuser. For the RANS of the whole machine, we can clearly identify the impeller jet wake at the inlet of the diffuser (see Fig. 18(a)). This same structure is not supposed to be present whenever simulating the model by enforcing an azimuthally-homogeneous inlet boundary condition. However, the bottom panels of Fig. 18(b) depict an azimuthally-periodic pattern that is typical of boundary layer instabilities. This could well explain why we found a boundary layer separation at the hub of the vaneless diffuser in our simplified diffuser model. We further stress that the instability pattern visible in Fig. 18(b) is confined to the separated region at the hub, which further points towards the diffuser instability as source of the observed discrepancy.

Building on these observations, we speculate that the discrepancies between the two flows are emerging because of the impact of the impeller jet wake that could stabilize the boundary layer. Hence, to test our conjecture, we carried out a new RANS simulation superposing a 7-periodic Fourier mode on the mean inlet profiles of the simplified model in order to approximately mimic the jet wake structure perturbation. The resulting inlet profile for the 7-periodic simplified model is

$$\hat{U}_r(\theta, z) = \tilde{U}_r(z) \cdot [1 + A\ \cos(m\theta)], \tag{32a}$$

$$\hat{U}_\theta(\theta, z) = \tilde{U}_\theta(z) \cdot [1 + A\ \sin(m\theta)], \tag{32b}$$

$$\hat{U}_z(\theta, z) = \tilde{U}_z(z) \cdot [1 + A\ \cos(m\theta)], \tag{32c}$$

where A denotes the amplitude of the perturbation, $m = 7$ denotes the wave number. We set the amplitude $A = 0.35$ which is matched to the amplitude of the tangential velocity of the jet wake for the impeller in full-machine simulations. The phase shift between radial and axial velocities ($\sim \cos(m\theta)$) compared to the tangential velocity ($\sim \sin(m\theta)$) is motivated by the single-Fourier mode continuity equation in cylindrical coordinates.

Fig. 18(c) shows the RANS results for the 7-periodic simplified model. The corresponding flow profile confirms our conjecture: The boundary layer instability that produces the separation at the hub (see Fig. 18(b)) is stabilized by the mimicked impeller jet wake (see Fig. 18(c)), where no major flow separations are observed. As a result, the simplified model with the 7-periodic inlet boundary condition is qualitatively and quantitatively very close to the RANS for the whole machine, which was the target of our model. This points toward the importance of reproducing the impeller jet wake, especially when no leakage flow is responsible for stabilizing the boundary layer in the vaneless diffuser. We further stress that, even if the jet wake produced by RANS results is not supposed to be an accurate approximation of a truly rotating impeller jet wake, its mean effect on the azimuthally-averaged flow is crucial. This points towards the importance of at least mimicking the jet wake (see (32)) whenever simplified inlet models, like ours, are used to reproduce the average inflow.

5.5. Comparison of fitting methods

The classic fitting methods used to approximate inflow profiles by algebraic polynomials or Gaussian functions are compared with our multi-stage fitting approach. To demonstrate the robustness of our scale-matching-like fitting technique, the velocity profiles of the zero-leakage case at the design flow rate are fitted with traditional one-stage fitting methods employing algebraic polynomials

$$\hat{U}_*(z) \approx \sum_{i=0}^{n} a_{*i}^{P} z^i, \tag{33}$$

and Gaussian functions

$$\hat{U}_*(z) \approx \sum_{i=1}^{n} a_{*i}^{G} \exp\left[-\left(\frac{z - b_{*i}^{G}}{c_{*i}^{G}} \right)^2 \right], \tag{34}$$

and then compared with our multi-stage fitting results, where a_i, b_i, and c_i denote the fitting coefficients, P and G are used for the polynomial and Gaussian fits, respectively, n denotes the degree of the polynomial functions or the number of Gaussian bells, and $*$ is either r, θ or z. The fitting results by algebraic polynomials functions for the radial velocity (see top panel of Fig. 19(a)) show that these fitting functions are too sensitive to the presence of boundary layers. Low-order fits do not capture the boundary layer, and higher-order fits introduce fictitious oscillations. The L2 norm of the error (see bottom panel of Fig. 19(a)) for our scale-matching fit is much lower than for the polynomial fits. Concerning the fitting results of the Gaussian functions (see top panel of Fig. 19(b)), the fit also introduces fictitious velocity profile oscillations. The corresponding L2 norm of the error (see bottom panel of Fig. 19(b)) shows that our scale-matching fit is more accurate.

Although implementing classic single-stage fitting functions is much easier and faster than using our method, this cheaper cost comes at the price of a significant reduction of accuracy and a number of numerical artifacts (namely a boundary condition discontinuity and a wavy profile). Our scale-matching fit does not suffer the nonphysical oscillatory artifacts introduced by polynomial and Gaussian functions. We do not see how such traditional single-stage fitting algorithms could reliably be used to supplement the sole diffuser flow in order to study the stability of the flow, which is affected by shear flow oscillations [18]. In fact, employing our scale-matching-like approach avoids the occurrence of such an artificial waviness in the fitted profile, hence increasing the reliability of our method over classic fitting protocols.

Our scale-matching is compared to classic fitting approaches in terms of their performance in reproducing the diffuser flow field velocity and pressure. The choice of the classic fits to compare with is motivated by three reasons: (i) algebraic polynomials of degree lower than 4 are excluded because they are not consistent with no-slip boundary conditions at the diffuser wall, (ii) 8th-degree polynomials maximize the robustness of the fit among the n that admit the minimum root-mean-square distance from the reference profile (see L2-norm in Fig. 19), and (iii) Gaussian fits for $n \geq 4$ are qualitatively capable of reproducing the boundary layer features of the inlet profile. Fig. 20 shows the azimuthally-averaged pressure and velocity components in the meridional plane for (a) the full pump simulations, (b) our scale-matching fit, (c) an 8-th degree polynomial fit, and (d) a Gaussian fit with 4 (top) and 8 (bottom) Gaussian bells. The scale-matching method proposed in this study correctly reproduces the pressure gradient, which is underestimated by polynomial and Gaussian fits. Moreover, whenever traditional methods are used, strong mean flow separation is observed on the hub wall (see the blue region in $\hat{U}_r$, $\hat{U}_\theta$, and $\hat{U}_z$) and the velocity at the shroud wall is over-predicted (see the yellow region in $\hat{U}_r$ and $\hat{U}_\theta$). The artifact of the mean flow separation is tamed down when our scale-matching approach is employed. Moreover, at the inlet of the diffuser, the waviness observed for the polynomial and Gaussian inlet-profile fits leads to the entrainment of a finger of azimuthal velocity in the bulk (see the wavy yellow region in Fig. 20(c,d)). This unphysical artifact is not present when using our scale-matching approach (see Fig. 20(b)), consistent with the corresponding full-pump simulations Fig. 20(a). Based on the above results, we can conclude that our scale-like matching fitting method performs significantly better than the classic fitting techniques we tested.

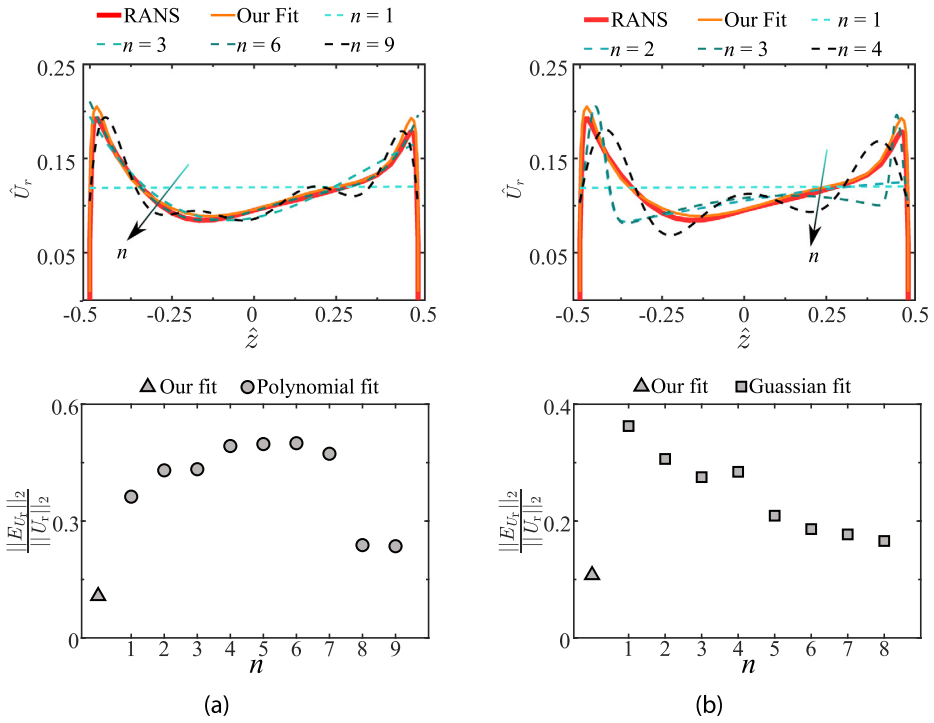

Fig. 19. Comparison between the radial velocity profiles U_r of the zero-leakage case at the design flow rate Q_d fitted by our multi-stage fitting method and (a) algebraic polynomials and (b) Gaussian functions.

5.6. Deviation of the diffuser performance

In order to evaluate the accuracy of the simplified model in predicting the diffuser performance, we define $\psi = \overline{p}_{\text{in}} - \overline{p}_{\text{out}}$, where $\overline{p}_{\text{in}}$ denotes the average pressure at the diffuser inlet and $\overline{p}_{\text{out}}$ the corresponding average pressure at the diffuser outlet. The relative error δ_{r} of the diffuser performance obtained by two different inflow conditions (average inflow with and without jet wake mimicked modulation) is depicted in Fig. 21. The relative error δ_{r} is calculated by

$$\delta_{\text{r}} = \left| \frac{\psi_{(\bullet)\text{ inflow,RANS}} - \psi_{\text{full machine, RANS}}}{\psi_{\text{full machine, RANS}}} \right|, \tag{35}$$

where $(\bullet)$ denotes either mean flow or mimicked jet wake inflow boundary condition.

The result shows that the relative error of diffuser performance obtained by the simplified model with the mean inflow condition is always larger than the result with the mimicked jet wake inflow condition. This further confirmed our previous conclusion that it is important to reproduce the impeller jet wake whenever simplified inlet models are used to reproduce the average inflow, otherwise numerical artifacts such as the mean flow separation at the hub could be induced by the inflow model (cf. Fig. 18(b,c)).

Concerning the results of the simplified case with the jet wake inflow condition, we find that the relative error of the zero-leakage case is very small. For the negative-leakage case, as we mentioned before, there is no leakage flow going inside the vaneless diffuser. The effect of leakage on the inlet velocity profiles is therefore of minor relevance. Hence, the relative error for this case remains small. For the positive-leakage case, the relative error of the jet wake inflow model increased but still remains below 20%, which is consistent with the accuracy of the mean flow profiles (see Fig. 14). The results show that our simplified model has limitations in reproducing the inflow condition when the jet wake entrains some fluid from an inlet radial gap before entering the diffuser. However, at a much lower computational cost and meshing complexity than the full-machine simulations, 20% of the performance deviation is considered acceptable.

5.7. Proof of principle

Finally, we want to prove that by just taking into account our fit to model the azimuthally averaged inlet profiles, we can successfully reproduce the low flow rate instability in the diffuser. To reproduce the rotating stall phenomenon at the small flow rate $Q/Q_{\text{d}} = 0.25$, an additional URANS simulation for the simplified model has been carried out for the zero-leakage case. A rotating inlet boundary condition is enforced in order to include the first harmonic produced by the impeller blades

$$\hat{U}_r(\theta, z, t) = \tilde{U}_r(z) \cdot \{1 + A \cdot \cos[(\theta - \omega_{\text{imp}} t) \cdot m]\}, \tag{36a}$$

$$\hat{U}_\theta(\theta, z, t) = \tilde{U}_\theta(z) \cdot \{1 + A \cdot \sin[(\theta - \omega_{\text{imp}} t) \cdot m]\}, \tag{36b}$$

$$\hat{U}_z(\theta, z, t) = \tilde{U}_z(z) \cdot \{1 + A \cdot \cos[(\theta - \omega_{\text{imp}} t) \cdot m]\}. \tag{36c}$$

The simulation results obtained from the simplified model that considers the sole diffuser are compared hereinafter with the corresponding vaneless diffuser when the entire machine is simulated.

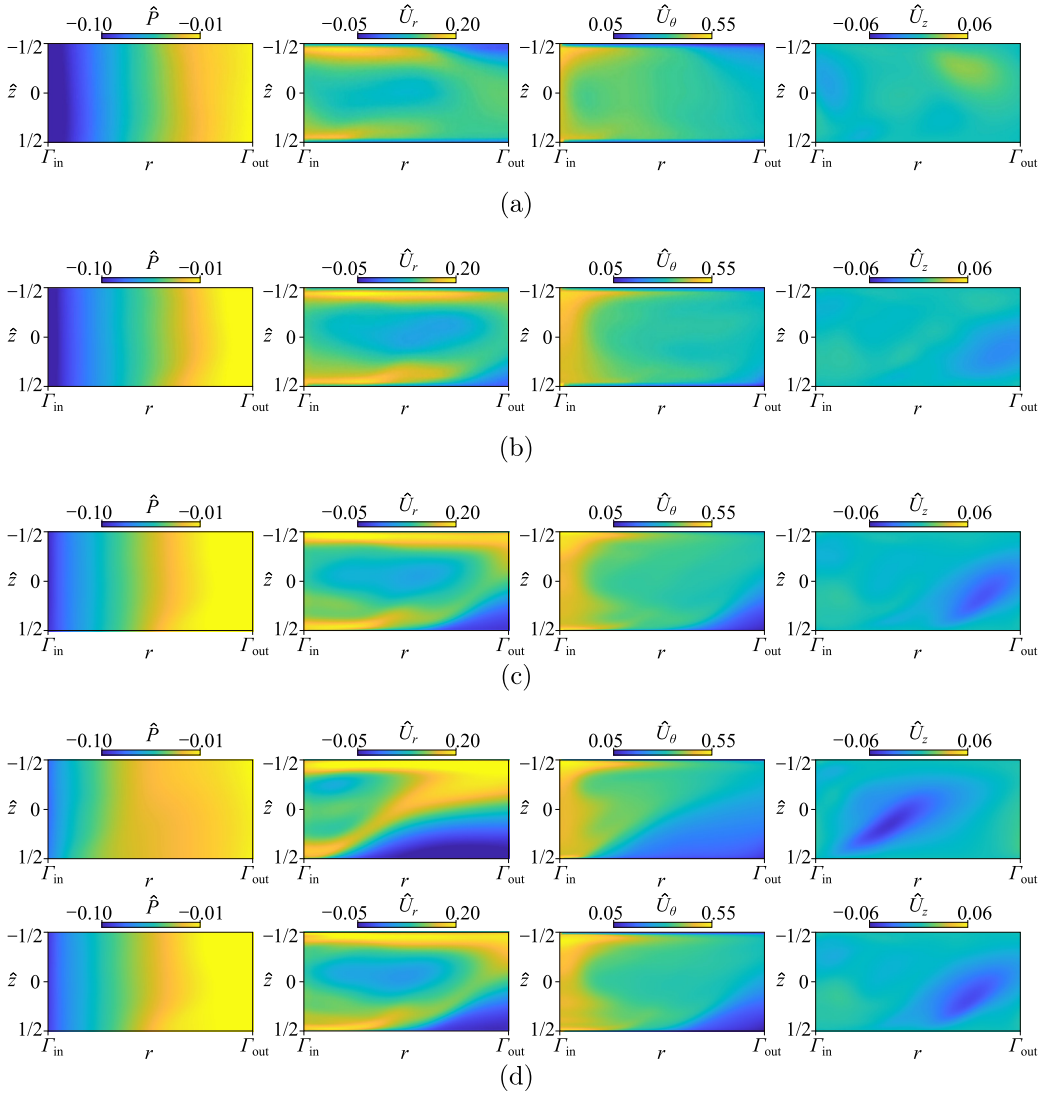

Fig. 20. Comparison of the azimuthally-averaged colormaps of the static pressure, radial, tangential, and axial velocity (from left to right) of RANS simulation for the design flow rate Q_d of (a) the entire machine and of the diffuser only using inlet mean velocity profiles fitted with different approaches: (b) our scale-like matching fit, (c) $n = 8$ polynomial fit, and (d) $n = 4$ (top) and $n = 8$ (bottom) Gaussian fits.

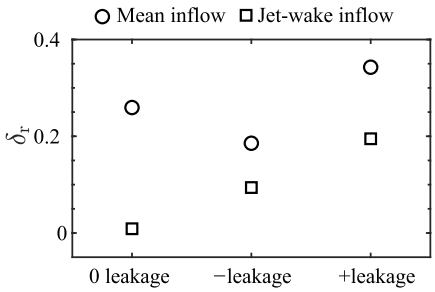

Fig. 21. Relative error δ_r of the diffuser performance predicted by the simplified model with two different inflow boundary conditions.

A Fourier decomposition analysis of the cross-power spectrum is conducted using the URANS simulation results from two numerical probes situated at the mid-radial distance of the diffuser shroud wall, with an angular phase shift of 60°, and verified against the experimental results. This analysis of the cross-power spectra of two pressure probes located at the same radius but at different angular positions enables the detection of rotating phenomena [20,21] and determines their characteristics, including the number of cells and propagation velocity.

The cross-power spectrum of the experiment at fully-developed stall condition Q/Q_d = 0.26 is shown on top of Fig. 22(a). As anticipated, the blade-passing-to-impeller-frequency ratio $f_{blade}/f_{imp} = 7$ is prominently visible in the cross-power spectrum, where f_{blade} and f_{imp} denotes the blade passing and impeller frequency, respectively. Moreover, a frequency associated with the low-flow-rate rotating stall $f_{stall,0.26Q_d}/f_{imp} = 0.840$ is detected. The FFT identifies therefore the propagation velocity of the stall cells $\omega_{stall,0.26Q_d} = 0.28\omega_{imp}$. Besides,

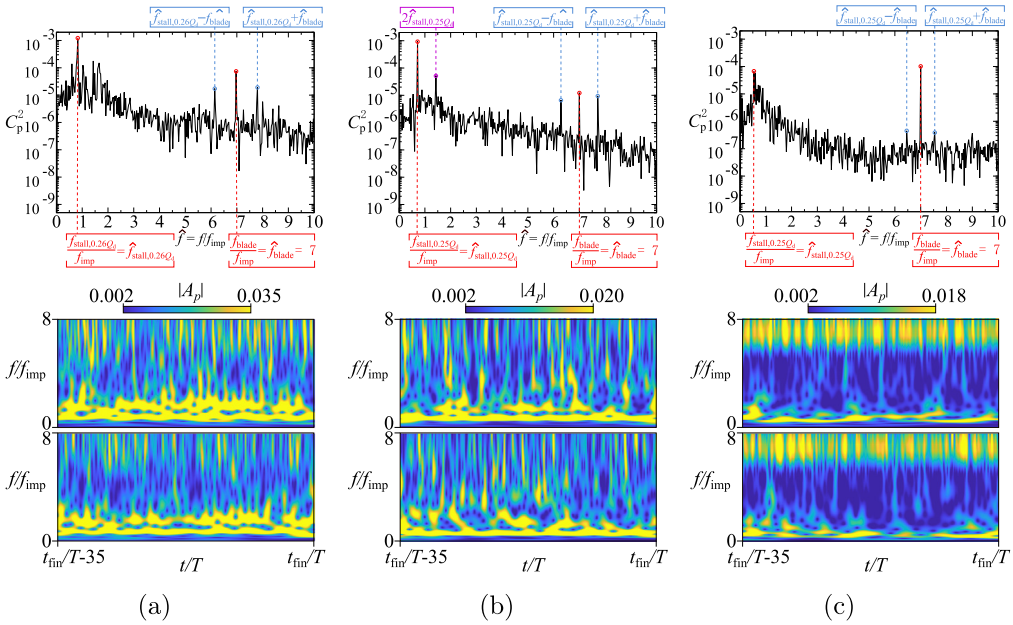

Fig. 22. Fourier and wavelet analysis of (a) the experiment and URANS simulation results of the zero-leakage case for (b) the whole machine and (c) the sole diffuser model at stalled condition.

the non-linear interaction between such two frequencies is also observed in the FFT at $f_{\text{stall},0.26Q_d} - f_{\text{imp}}$ and $f_{\text{stall},0.26Q_d} + f_{\text{imp}}$. As shown at the bottom of Fig. 22(a), the wavelet analysis confirms the presence of the rotating stall frequency, which is clearly identifiable. The complex energy transfer is visible for the frequencies near $f_{\text{stall},0.26Q_d}$. For the numerical results of the zero-leakage case at fully-developed stall condition Q/Q_d = 0.25 obtained from the entire machine, the blade-passing-to-impeller-frequency ratio $f_{\text{blade}}/f_{\text{imp}} = 7$, low-flow-rate rotating stall frequency $f_{\text{stall},0.25Q_d}/f_{\text{imp}} = 0.714$, and the non-linear interaction between such two frequencies $f_{\text{stall},0.25Q_d} - f_{\text{imp}}$ and $f_{\text{stall},0.25Q_d} + f_{\text{imp}}$ also can be clearly identified from the cross-power spectrum (see the top panel of Fig. 22(b)). The wavelet result shows good consistency with the FFT result. And the propagation velocity of the stall cells is identified as $\omega_{\text{stall},0.25Q_d} = 0.238\omega_{\text{imp}}$, which is quantitatively very close to the experimental result.

Fig. 22(c) shows the cross-power spectrum and wavelet analysis results obtained from the simplified model. The rotating stall frequency $\tilde{f}_{\text{stall},0.25Q_d}/f_{\text{imp}} = 0.543$, blade passing frequency $f_{\text{blade}}/f_{\text{imp}} = 7$, and the non-linear interaction between these two frequencies can be identified very clearly in FFT results (see the top of Fig. 22(c)). The FFT identifies therefore the propagation velocity of the stall cells $\tilde{\omega}_{\text{stall},0.25Q_d} = 0.181\omega_{\text{imp}}$, which underpredicts $\omega_{\text{stall},0.25Q_d}/\omega_{\text{imp}}$ of the whole machine. Both, the rotating stall frequency and the blade passing frequency, can be easily identified by the wavelet analysis as shown at the bottom of Fig. 22(c), and the complex non-linear transport of energy at $f \approx f_{\text{stall},0.25Q_d}$ is also qualitatively reproduced by the model. However, as we simplify the impeller jet wake to its first Fourier mode, the mid-range frequency interactions are weaker for the model flow (cf. Fig. 22(b,c)). Compared with the entire machine results, the amplitude of the rotating stall frequency is lower, and the blade passing frequency is higher. This is expected to occur also because of the single-Fourier-mode driving imposed at the inlet, which is less prone to induce non-linear interactions. Nevertheless, our simplified model captures all relevant features of the low-flow-rate instability, reducing the URANS simulation cost of 70%.

This is further confirmed by Fig. 23, which presents the comparison with the color maps of the PIV phase-averaged measurements of Dazin et al. [19] (Fig. 23(a), see Appendix B for more details) and numerical simulation for the entire machine Fig. 23(b) and for the simplified model Fig. 23(c) with 120-time steps of the last revolution at the mid-height of the diffuser in a reference frame rotating with the stall cell propagation velocity $\omega_{\text{stall},0.25Q_d}$ ($\tilde{\omega}_{\text{stall},0.25Q_d}$ for the model). Regarding the results, three stall cells can be observed in the two URANS simulations with a good qualitative agreement in comparison to the corresponding experiment. This means that the rotating stall phenomenon can be reproduced by the simplified simulation approach. From a quantitative point of view, the URANS simulation results of the entire machine are closer to the PIV result. The simulation results here are for the zero leakage case, whereas there is an impeller-to-diffuser gap in the PIV experiment. This leads to quantitative deviations in the tangential velocity distribution. For the URANS simulation of the sole diffuser, the quantitative deviation of the flow field is expectedly larger since only a single Fourier mode is simulated at the inlet in the circumferential direction. We further stress that our aim is to demonstrate that taking our reduced-order simulation approach can reproduce the typical rotational stall instability in a vaneless diffuser, rather than reproducing exactly the same flow field. In fact, our future studies will aim to simulate slightly supercritical conditions for which the instability will admit a much lower amplitude than the one depicted in Fig. 23. By employing our reduced-order modeling approach, the effect of blade numbers and characteristic features of the impeller jet wake can be investigated not too far from critical conditions.

6. Discussion and conclusions

This paper documents a simplified approach for the instabilities identification based on a new centrifugal 3D impeller outflow model. The three-dimensional model pays attention to the multiscale inlet boundary conditions at the impeller outlet plane including non-uniform flow close to reality, which is typically ignored in model simplification for vaneless diffusers. A detailed step-by-step method for fitting the diffuser inlet profiles in a centrifugal machine is documented.

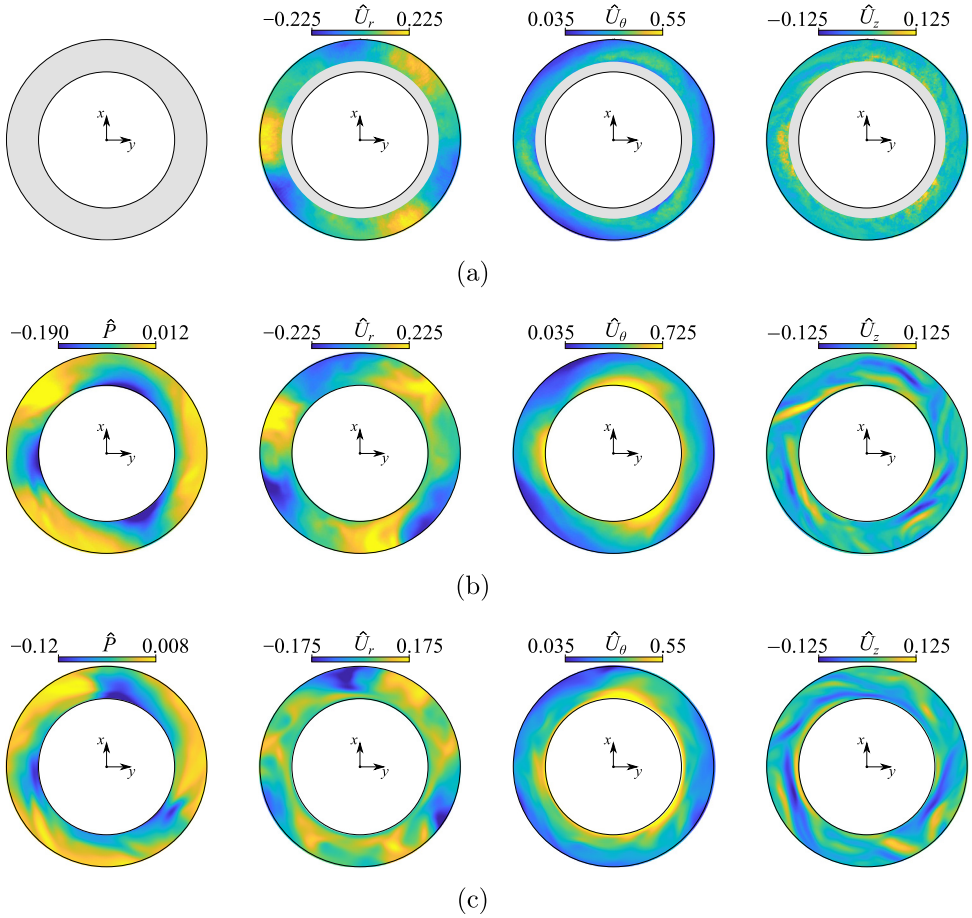

Fig. 23. Color maps of (a) the PIV phase-average measurements of Dazin et al. [19] and phase-average of the URANS simulation results for the zero leakage case for (b) the entire machine and (c) the simplified model at the stalled conditions. Due to laser reflection on the impeller blades, PIV cannot access the grey region near the diffuser inlet. Therefore, the measurements taken near the edge of this region should be regarded as having a significant margin of error.

The fitting results are close to the numerical simulation results, with the L2 norm of the errors being in an acceptable range. The flow field in the vaneless diffuser can be reproduced well by numerical simulation for the simplified model with the fitted inlet velocity profiles.

By superposing a periodic wave (with the wave number and amplitude corresponding to the jet wake from the impeller) to the mean inlet velocity profiles, URANS simulation in the simplified model can also reproduce the main features of the rotating stall instability in the diffuser at 30% of the total cost. The rotating instability phenomenon that occurs in the vaneless diffuser is affected by the leakage configuration via the inlet profile. However, how the boundary layer interacts with the instability mechanism is still not clear, which needs to be further studied.

At a much lower computational cost than the full-machine URANS simulations, the advantage of using our model is therefore that it can be employed to carry out cost-affordable parametric studies in which, not only we can vary the machine parameters such as flow rate Q, rational velocity ω_{imp}, diffuser radius ratio Γ, and different leakage configurations, but we can also investigate the effect of the number of blades and characteristic features of the impeller jet wake.

There are a few literature studies focused on this subject. Therefore, this work can provide some guidance for similar problems, that require a reduction of the computational cost. It is expected that the fitted inlet flow profile in the diffuser with the simplified numerical model can be useful to understand the different instability patterns and could also be used as a boundary condition for fundamental studies like linear stability analysis in the sole diffuser.

Declaration of competing interest

The authors declare the following financial interests/personal relationships which may be considered as potential competing interests:

Meng FAN reports financial support was provided by China Scholarship Council. Francesco ROMANO reports equipment, drugs, or supplies was provided by Grand Équipement National De Calcul Intensif.

Data availability

Data will be made available on request.

Acknowledgements

We kindly acknowledge the GENCI (grand équipement national de calcul intensif) for the numerical resources granted to conduct this study under project A0102A01741. Furthermore, we appreciate the support of the China Scholarship Council for the doctoral students of M. Fan (CSC student number 201908320328).

Appendix A. Evaluation of local Mach number

For the centrifugal machine we studied, the impeller tip velocity, which determines the maximum velocity in the centrifugal machine, is about 32 m/s, corresponding to a Mach number of about 0.1 which is safely lower than 0.3. To better justify the choice of incompressible Navier-Stokes equations, we now further employ simulations that include the whole pump to evaluate the Mach number throughout our simulation. Fig. A.24 depicts five color maps of the local Mach number at different instants on a longitudinal section (zoom in on the region of the impeller). They demonstrate the Mach number throughout the simulations is less than 0.3.

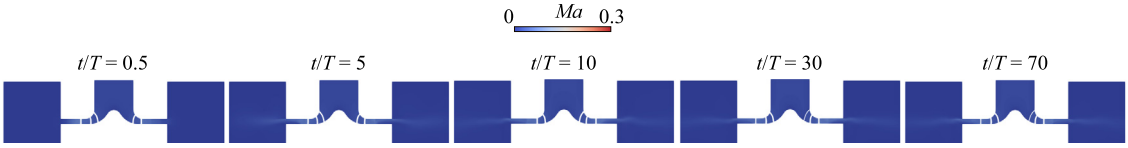

Fig. A.24. Color maps of the Mach number at the meridional section of the entire machine at the design condition Q_d at different simulation times.

Appendix B. Experimental apparatus

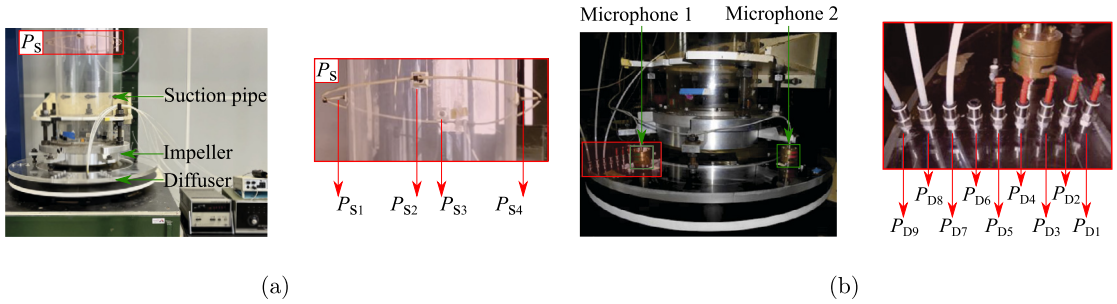

Fig. B.25. Experimental set-ups of the radial flow machine with (a) a zoom-in view of the four static pressure probes equipped on the suction pipe (red rectangle) and (b) two microphones and a zoom-in view of nine static pressure taps installed on the vaneless diffuser (red rectangle).

The experimental set-up including a radial impeller coupled with a vaneless diffuser is depicted in Fig. B.25 as already presented in previous works [14,15,19]. This arrangement allows positive leakage flow into the vaneless diffuser inlet due to the radial gap between the outlet rotating impeller section and the fixed inlet diffuser section. The inflow condition is given by a tank, equipped with a honeycomb flow straightener placed on the top of the suction pipe. The flow rate Q can be adjusted by a set of changeable diaphragms (with different radii) installed at the tank inlet.

The static pressure variation between the suction pipe (P_s) and impeller outlet is measured to determine the entire machine's performance. The suction pipe is equipped with four steady pressure probes as depicted in Fig. B.25(a), and the static pressure in the suction pipe is calculated as the average of four positions ($P_{s1} - P_{s4}$). In addition, nine steady pressure taps are radially and equally spaced on the diffuser wall (see Fig. B.25(b)). Therefore, the diffuser performance in terms of pressure recovery from the inlet to the diffuser outlet can be characterized. It is estimated that there is a margin of uncertainty of ± 2 Pa in these measurements. To detect the instabilities occurring in the vaneless diffuser, two Brüel & Kjaer (Nærum, Denmark) condenser micro-phones (Type 4135) were employed to measure the unsteady pressure fluctuation. The probes are positioned at the same radial distance of $r = 320$ mm on the diffuser wall, but with a relative angular displacement of $\Delta\theta = 60°$. The measurement uncertainty of these probes is less than 1%. Data was collected using LMS Test Xpress (SIEMENS, Munich, Germany) for a total duration of 600 s, with a sampling frequency of 4096 Hz.

The experiments were conducted in air, covering a wide range of flow rate ratios relative to the design condition, with Q/Q_d ranging from 0.26 to 1.53. Here, Q and Q_d represent the actual and design flow rates, respectively, and were measured at the inlet pipe with a constant rotating speed of $N = 1200$ rpm (i.e. $\omega_{imp} = 125$ rad/s).

The measurements of Dazin et al. [19] reported in Fig. 23 result from a 2D/3C high-repetition-rate PIV. Particles of incense smoke, which are smaller than 1 μm, were employed for seeding. Spectral analysis, both linear and non-linear, was employed to examine and categorize the unsteady phenomena within the signals. Subsequently, a specialized phase-averaging method was devised to effectively track and visualize the evolution of instabilities. A dedicated PIV averaging protocol was applied to the PIV flow fields such to capture and visualize the topology of the spectrally identified phenomena. The PIV results have been interpolated to a new mesh and then phase averaged during the acquisition process. As the interrogation window is fixed and the flow is rotating in the laboratory reference frame,

the experimental output consists of an ensemble of measurements that leads to the phase-averaged velocity components reproduced in dimensionless form in Fig. 23.

More detailed descriptions of the experimental measurements, data acquisition, and adopted pump operating points can be found in previous papers [15,19,22–25] that operate the same apparatus.

Appendix C. Grid independence analysis

Table C.3
Grid independence verification. The relative error, δ, is calculated with respect to the finest grid (denoted by Case 4), and is given by the equation: $\delta = |\text{PSICase 4} - \text{PSICase }^*|/|\text{PSI}_{\text{Case 4}}|$. Here, PSI represents the mass-weighted average static pressure difference between the inlet of the pipe and the outlet of the diffuser, and the asterisk denotes either Grid 1, Grid 2, or Grid 3.

Grid #	Cells number					PSI	δ
	inlet pipe	impeller	diffuser	outflow box	total		
1	113155	267008	145728	91800	617691	0.3843	1.75%
2	238853	493920	210600	175446	1118819	0.3864	2.30%
3	406462	1051176	590976	267786	2316400	0.3742	0.93%
4	1218825	2456160	1379448	352350	5406783	0.3777	–

To ensure grid independence, four different grid resolutions were tested in our study. Table C.3 compares the mass-weighted average static pressure difference between the inlet of the pipe and the outlet of the diffuser (PSI) predicted by each grid at the design condition. As the grid resolution increases from 618k cells (Grid 1) to approximately 1.1M cells (Grid 2), the relative error in predicting the machine performance also increases. However, the error decreases for 2.3M cells (Grid 3) and reaches a minimum of 0.93%. Therefore, a total mesh of 2.3M finite volumes was selected for the numerical simulations. Besides, to ensure the robustness of the flow to the mesh resolution in the boundary layer, we tested three different mesh stretchings, namely: (i) 13 wall layers with expansion ratios of 1.4, (ii) 11 wall layers with expansion ratios of 1.5, and (iii) 10 wall layers with expansion ratios of 1.6. The simulation results depicted in Fig. C.26 show that the flow in our setup is not very sensitive to the mesh stretching near the wall. Hence, all the conclusions of this study can safely be considered robust upon a change in the wall mesh refinement. Fig. C.26 further justifies our choice of using an expansion ratio of 1.5 for all the results presented in this paper.

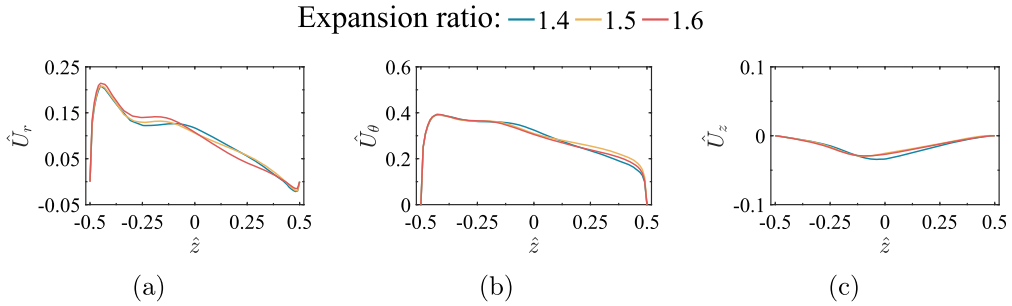

Fig. C.26. Comparison of the (a) radial, (b) tangential, and (c) axial velocity profiles in the middle of the diffuser at $r = (R_3 + R_4)/2$. The profiles are obtained for RANS simulations at the design flow rate Q_d with three different meshes that employ (blue) 13 layers with expansion ratios of 1.4, (orange) 11 layers with expansion ratios of 1.5, and (red) 10 layers with expansion ratios of 1.6.

Appendix D. Turbulence model independence analysis

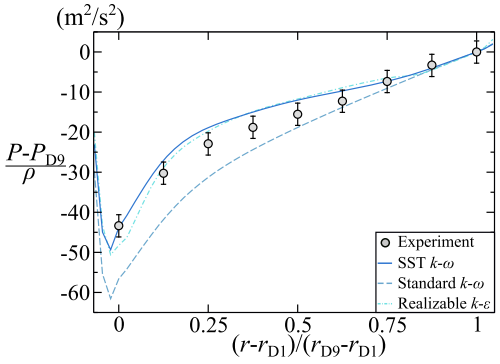

Fig. D.27. Diffuser pressure recovery of the positive-leakage case at the design condition Q_d predicted by RANS simulation of the entire pump employing different turbulence models.

Several turbulence models commonly used for the numerical simulation of turbomachinery are compared. The standard $k-\epsilon$ turbulence model is excluded due to a high y^+ requirement, hence it is not compatible with the boundary layers we aim at fitting. The turbulence model independence analysis is carried out for standard $k-\omega$, $k-\omega$ SST, and realizable $k-\epsilon$ turbulence models. The diffuser pressure recovery curves of the positive-leakage case at the design condition Q_d obtained by RANS simulations employing these three turbulence models are verified against the experimental result as shown in Fig. D.27. The results show the standard $k-\omega$ model does not correctly predict the pressure recovery in the diffuser. On the other hand, our $k-\omega$ SST and the realizable $k-\epsilon$ model provide very similar results. Therefore we choose the $k-\omega$ SST model which is considered a more suitable choice for the centrifugal pump over the realizable $k-\epsilon$ model as it takes into account the transport of the principal turbulent shear stress. The $k-\omega$ SST model has also been demonstrated as reliable, robust, and efficient for predicting global performance and capturing essential flow characteristics in centrifugal machine simulations through various examples in literature [26–30] and validated by experiments.

References

[1] W. Jansen, Rotating stall in a radial vaneless diffuser, J. Fluids Eng. 86 (4) (1964) 750–758.
[2] D. Japikse, Centrifugal Compressor Design and Performance, Wilder, Concepts ETI, VT, 1996.
[3] Y. Senoo, Y. Kinoshita, Influence of inlet flow conditions and geometries of centrifugal vaneless diffusers on critical flow angle for reverse flow, J. Fluids Eng. Trans. ASME (1977) 98–102.
[4] P. Frigne, R. Van den Braembussche, A theoretical model for rotating stall in the vaneless diffuser of a centrifugal compressor, J. Eng. Gas Turbines Power 107 (2) (1985) 507–513, https://doi.org/10.1115/1.3239760.
[5] Y. Tsujimoto, Y. Yoshida, Y. Mori, Study of vaneless diffuser rotating stall based on two-dimensional inviscid flow analysis, J. Fluids Eng. 118 (1) (1996) 123–127, https://doi.org/10.1115/1.2817489.
[6] A.N. Abdelhamid, Effects of vaneless diffuser geometry on flow instability in centrifugal compression systems, in: Turbo Expo: Power for Land Sea, and Air, vol. 101, 1981, 79610, V001T03A008.
[7] F.K. Moore, Weak rotating flow disturbances in a centrifugal compressor with a vaneless diffuser, J. Turbomach. 111 (4) (1989) 442–449.
[8] S. Ljevar, H.C.D. Lange, A.A.V. Steenhoven, Two-dimensional rotating stall analysis in a wide vaneless diffuser, Int. J. Rotating Mach. 2006 (2006) 056420.
[9] C. Gao, C. Gu, T. Wang, B. Yang, Analysis of geometries' effects on rotating stall in vaneless diffuser with wavelet neural networks, Int. J. Rotating Mach. 2007 (2007) 076476.
[10] H.-S. Dou, S. Mizuki, Analysis of the flow in vaneless diffusers with large width-to-radius ratios, J. Turbomach. 120 (1) (1998) 193–201.
[11] C. Hu, C. Yang, X. Shi, R. Zou, L. Liu, H. Chen, Investigation of rotating stall in radial vaneless diffusers with asymmetric inflow, Aerosp. Sci. Technol. 96 (2020) 105546.
[12] P. Emvin, L. Davidson, A numerical comparison of three inlet approximations of the diffuser in case E1 Annex 20, vol. 1, in: Proc. Roomvent'96, 1996, pp. 219–226.
[13] B. Deng, J. Wang, J. Tang, J. Gao, Improvement of the momentum method as the diffuser boundary condition in CFD simulation of indoor airflow: discretization viewpoint, Build. Environ. 141 (2018) 55–60.
[14] M. Fan, A. Dazin, G. Bois, F. Romanò, Effect of inlet leakage flow on the instability in a radial vaneless diffuser, Phys. Fluids 35 (1) (2023) 014105, https://doi.org/10.1063/5.0133948.
[15] M. Fan, A. Dazin, F. Romanò, G. Bois, Effect of leakage on the performance of the vaneless diffuser of a centrifugal pump model, in: Conference on Modelling Fluid Flow (CMFF'22), Budapest, Hungary, 2022, pp. 51–58.
[16] F.R. Menter, Ten years of industrial experience with the SST turbulence model, Turbul. Heat Mass Transf. 4 (2003) 625–632.
[17] A. Palumbo, F. Capuano, L. Luca, Performances of two open-source solvers in the numerical simulation of synthetic jets, in: Proceedings of the 7th European Conference on Computational Fluid Dynamics (ECCM-ECFD 2018), Glasgow, UK, 2018, pp. 11–15.
[18] F. Romanò, Stability of generalized Kolmogorov flow in a channel, Phys. Fluids 33 (2) (2021) 024106.
[19] A. Dazin, High-speed stereoscopic PIV study of rotating instabilities in a radial vaneless diffuser, Exp. Fluids 51 (2011) 83–93.
[20] S. Suzuki, U. Yoshio, H. H., Noise characteristics in partial discharge of centrifugal fans: 1st report, low-frequency noise due to the rotating stall, Bull. JSME 21 (154) (1978) 689–696.
[21] G. Caignaert, B. Desmet, D. Stevenaert, Experimental investigations on the flow in the impeller of a centrifugal fan, in: Turbo Expo: Power for Land, Sea, and Air, American Society of Mechanical Engineers, 1982, 79566, V001T01A013.
[22] A. Dazin, O. Coutier-Delgosha, P. Dupont, S. Coudert, G. Caignaert, G. Bois, Rotating instability in the vaneless diffuser of a radial flow pump, J. Therm. Sci. 17 (4) (2008), https://doi.org/10.1007/s11630-008-0368-3.
[23] G. Pavesi, A. Dazin, G. Cavazzini, G. Caignaert, G. Bois, G. Ardizzon, Experimental and numerical investigation of unforced unsteadiness in a vaneless radial diffuser, in: 9th European Conference on Turbomachinery: Fluid Dynamics and Thermodynamics, ETC 2011 - Conference Proceedings, vol. 1, 2011.
[24] Y.G. Heng, A. Dazin, M.N. Ouarzazi, Q.R. Si, Experimental study and theoretical analysis of the rotating stall in a vaneless diffuser of radial flow pump, in: IOP Conference Series: Earth and Environmental Science, vol. 49, 2016, 032006.
[25] Y. Heng, A. Dazin, M. Ouarzazi, Linear stability analysis of rotating stall in a wide vaneless diffuser, in: 12th European Conference on Turbomachinery Fluid Dynamics and Thermodynamics, ETC 2017, 2017.
[26] L. Gibson, L. Galloway, S. Spence, Assessment of turbulence model predictions for a centrifugal compressor simulation, J. Glob. Power Propuls. Soc. 1 (2017) 142–156.
[27] I. Chalghoum, H. Kanfoudi, S. Elaoud, M. Akrout, R. Zgolli, Numerical modeling of the flow inside a centrifugal pump: influence of impeller–volute interaction on velocity and pressure fields, Arab. J. Sci. Eng. 41 (11) (2016) 4463–4476.
[28] O. Borm, H.P. Kau, Unsteady aerodynamics of a centrifugal compressor stage: validation of two different CFD solvers, in: Turbo Expo: Power for Land, Sea, and Air, 2012, 44748, 2753–2764.
[29] J.H. Kim, J.H. Choi, K.Y. Kim, Design optimization of a centrifugal compressor impeller using radial basis neural network method, in: Turbo Expo: Power for Land, Sea, and Air, 2009, 48883, 443–451.
[30] M. Asuaje, F. Bakir, S. Kouidri, F. Kenyery, R. Rey, Numerical modelization of the flow in centrifugal pump: volute influence in velocity and pressure fields, Int. J. Rotating Mach. 3 (2005) 244–255.

Appended papers

C.4 Paper D

"Instabilities in a turbulent swirling source flow between parallel rings",
M. Fan, A. Dazin, G. Bois, F. Romanò,
Phys. Fluids, 35(10) (2023), 101701.

Physics of Fluids

LETTER | OCTOBER 02 2023

Instabilities in a turbulent swirling source flow between parallel rings

M. Fan ; A. Dazin ; G. Bois ; F. Romanò

Physics of Fluids 35, 101701 (2023)
https://doi.org/10.1063/5.0166446

AIP Publishing

Physics of Fluids LETTER pubs.aip.org/aip/pof

Instabilities in a turbulent swirling source flow between parallel rings

Cite as: Phys. Fluids **35**, 101701 (2023); doi: 10.1063/5.0166446
Submitted: 5 July 2023 · Accepted: 7 September 2023 ·
Published Online: 2 October 2023

M. Fan,[a] A. Dazin, G. Bois, and F. Romanò

AFFILIATIONS

Univ. Lille, CNRS, ONERA, Arts et Métiers Institute of Technology, Centrale Lille, UMR 9014-LMFL-Laboratoire de Mécanique des Fluides de Lille - Kampé de Fériet, F-59000 Lille, France

[a]Author to whom correspondence should be addressed: meng.fan@ensam.eu

ABSTRACT

Instabilities in a source flow between parallel rings with spatially modulated inflow conditions rotating at angular rate Ω are investigated in this Letter. Numerical simulations are conducted for five flow rates. Two inlet conditions are considered: an idealized one, in which the inlet flow is sealed, and a more realistic one, in which a leakage flow is entrained to enter the diffuser. The resulting fast Fourier transforms, wavelet analyses, and phase averages unravel the primary rotating instability that propagates in the parallel rings and leads to severe blockage for the mean flow. Moreover, secondary instabilities are triggered. Their identification is eased by the idealized inflow. We further discuss the imprinting of such instabilities in determining the route to chaos observed in the diffuser with more realistic inlet conditions. Special attention is here paid to identifying how the secondary instability mechanism is affected by the inflow.

Radial flows between parallel disks and rings are paradigmatic configurations to investigate radial expansion[1,2] and diffusion,[3,4] depending on the flow being either sinking or sourcing from the axis. Radial diffusers,[5,6] radial flow nozzles,[7] double disk valves,[8] and thrust bearings[9] are some of the practical applications of parallel radial flows. Natural flows that involve radial expansion/diffusion include the outlet of geothermal energy reservoirs[10] and soil chemical processes.[11]

Moreover, such a canonical setup has served to study relaminarization in radial sources confined by parallel plates.[12,13] As the inertial forces scale like $\sim r^{-2}$ Re,[14] where Re is the Reynolds number, an order of magnitude analysis suggests that the flow in a radial diffuser will always enter a creeping regime if the diffuser is large enough, regardless of the flow rate.[15] The reverse transition has since then been an active topic of investigation. Several authors studied the instabilities in source flows between parallel disks, reporting the occurrence of inflection points[16,17] and the self-sustained separation and reattachment of shear layers.[18]

In this Letter, we focus on the turbulent source air flow between parallel rings of finite spans, with a major focus on the instabilities that originate considering a swirling jet wake inflow periodically modulated in space and rotating at angular rate Ω (Fig. 1). To produce the inflow condition, we employ a seven-periodic device rotating at a constant rate Ω (see the supplementary material for details). Two configurations are numerically investigated: (i) the idealized case in which the jet wake is directly injected into the diffuser and (ii) the more realistic case in which the jet wake entrains some fluid from an inlet radial gap of length L_1 before entering the parallel rings. The motivation behind such a thorough consideration given to the inlet boundary conditions relies on numerical and experimental evidence, which demonstrates how crucial the leakage between rotating and steady walls can be when dealing with swirling source flow between parallel rings.[6]

Our previous study[6] demonstrates that two different kinds of two-dimensional primary instabilities occur for the core flow between the parallel rings subject to a rotating spatially modulated inflow. On the one hand, at low flow rates, a core-flow instability has been reported by several researchers.[19–21] Theoretical studies[6,22,23] concluded that this rotating instability does not get significantly influenced by the spatial modulation of the inflow, but it rather relies on the mean skewness of the flow at the diffuser inlet. On the other hand, at large flow rates, another instability can potentially occur. This latter one is associated with the jet-wake features of the inflow, being sensitive to the intensity of the jet-wake, the mode of the periodic modulation in the azimuthal direction, and the inlet flow angle. Such an instability was first reported and discussed by Ljevar *et al.*[24]

In our previous study,[6] we compared the flow field of three different inflows at the reference flow rate $\tilde{Q}$. We found that no jet-wake instability occurs at $\tilde{Q}$ whenever we allow leakage to be entrained from the outside. Indeed, large-flow-rates instabilities can be suppressed

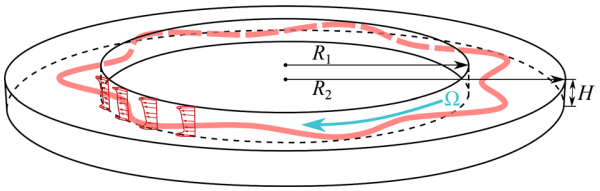

FIG. 1. Schematic of the source flow between parallel rings of finite spans.

owing to the weakening of the jet-wake intensity produced by the leakage. In this Letter, we extend the previous investigation by further focusing on the instability at large flow rates here reported for the first time also for realistic conditions beyond $\tilde{Q}$. We will point out the major differences between idealized and realistic cases for the instabilities occurring in a finite-span parallel ring diffuser.

Figure 1 depicts a sketch of our diffuser. The 7-periodic spatially modulated inlet is set at $r = R_1$ and rotates with a constant angular velocity Ω such that $\mathrm{Re}_\Omega = \Omega R_1^2/\nu = 5.52 \times 10^5$ for all cases we consider hereinafter, where ν is the kinematic viscosity of the fluid (air in our case) and Re_Ω is a first Reynolds number scaled on the nominal tangential velocity at inlet. A second Reynolds number is defined based on a volumetric flow rate Q entering the parallel annular plates, i.e., $\mathrm{Re}_Q = Q/2\pi H\nu$. We employ a reference value $\tilde{\mathrm{Re}}_Q = \tilde{Q}/2\pi H\nu = 6.46 \times 10^4$ and vary the parameter $\alpha_Q = \mathrm{Re}_Q/\tilde{\mathrm{Re}}_Q = Q/\tilde{Q} \in [0.75, 1.25]$ to investigate the turbulent flow instabilities in the parallel plates with radial aspect ratio $\Gamma = R_2/R_1 = 1.5$ and a cross-sectional aspect ratio $\Lambda = (R_2 - R_1)/H = 3.325$ kept constant throughout. These parameters are selected to match with values used in the literature for carrying out numerical simulations (Fan *et al.*[6]) and experiments (Dazin *et al.*[20]) in our same configuration. In particular, $\tilde{\mathrm{Re}}_Q$ is selected because it corresponds to design conditions for the impeller used to produce the spatially modulated flow at the inlet of the parallel plate ring; hence, it promotes smooth inflow conditions. Corresponding URANS simulations are performed in this study and for more details about their implementation, validation and verification, we refer the reader to the supplementary material, as well as to our previous studies.[6,25,26]

The flow field in the annular parallel rings with idealized inlet conditions has already been analyzed by Fan *et al.*[6,25] The azimuthal arithmetic-averaged color maps at the meridian section of the diffuser and the instantaneous color maps at the mid-height of the diffuser for the velocity magnitude (Fig. 2) are depicted for $\alpha_Q \in \{0.75, 1, 1.25\}$ in Figs. 2(a)–2(c), respectively. The azimuthally averaged instantaneous color map [Fig. 2(c, top)] demonstrates that the bulk flow in the radial diffuser passage is dominated by inviscid effects at the largest Reynolds number, i.e., $\alpha_Q = 1.25$. Under the influence of the spatially modulated swirling inflow, the incoming jet wake induces a partial blockage of the system. Flow separation can be observed near the outlet of the hub wall. At the mid-height of the diffuser, the velocity is regularly distributed [Fig. 2(c, bottom)], and the main flow streamlines are nearly logarithmic spiral curves. The jet-wake pattern can be clearly observed in the velocity magnitude distribution with seven high-velocity jets due to the 7-periodic inflow modulation. As α_Q decreases to the reference conditions $\alpha_Q = 1$, the flow separation area becomes surface-filling over the hub, occupying almost half of the diffuser passage in the z-direction [Fig. 2(b, top)]. A 7-periodic instability is clearly observed at the mid-height of the diffuser [Fig. 2(b, bottom)]. The massive flow separation area observed at the meridian section of the diffuser is due to a core-flow rotating instability of the same type described by Ljevar *et al.*[24] and the flow separation area appears to be further reinforced by the instability as explained by Fan *et al.*[6] As Re_Q further decreases, i.e., for $\alpha_Q = 0.75$, the intensity of the inflow velocity weakens [Fig. 2(a, top)] and no rotating instability is observed [Fig. 2(a, bottom)]. This is consistent with the interpretation of the rotating instability being responsible of the azimuthally averaged flow separation and with the mechanism discussed by Ljevar *et al.*[24]

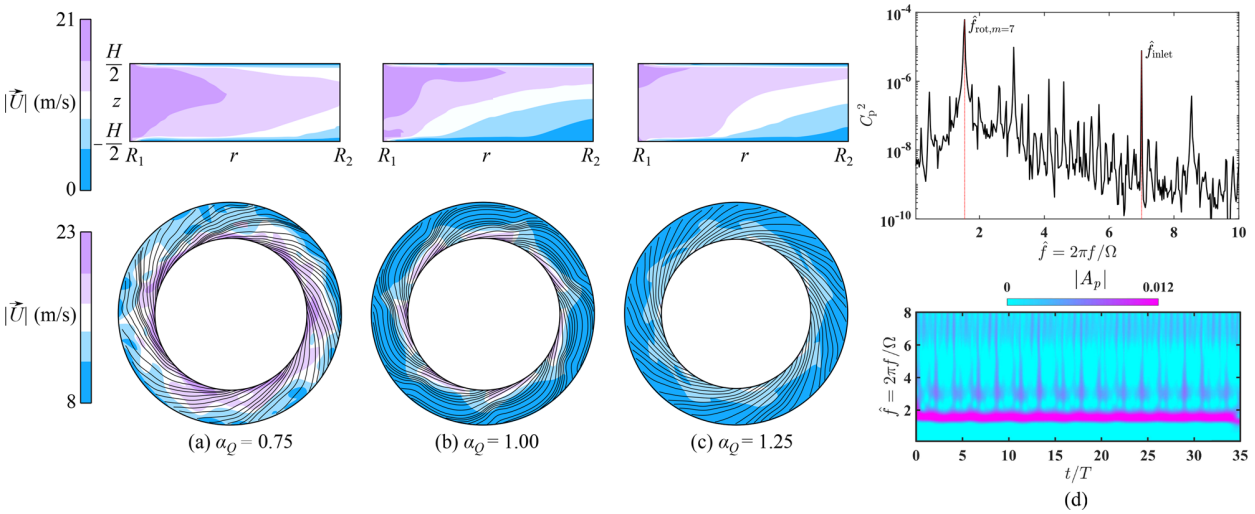

FIG. 2. Velocity magnitude of the idealized case at (a) $\alpha_Q = 0.75$, (b) $\alpha_Q = 1$, and (c) $\alpha_Q = 1.25$. Top panels: Azimuthal arithmetic-average fields at the meridian section. Bottom panels: Instantaneous fields at the mid-height of the diffuser and streamlines (black). (d) Fourier and wavelet analyses for $\alpha_Q = 1$.

To further study the core-flow instability, a quantitative analysis was carried out using a fast Fourier transform (FFT) of the cross-power spectrum from two numerical probes with an angular phase shift of 60° and located at the mid-radial distance of the top annular plate [Fig. 2(d, top)]. We also carried out a wavelet analysis of the idealized inflow configuration at $\alpha_Q = 1$ [Fig. 2(d, bottom)]. The 7-periodic inlet frequency $2\pi f_{\text{inlet}}/\Omega = 7$ can be clearly observed in the FFT. In addition, a low frequency $2\pi f_{\text{rot},m=7}/\Omega = 1.543$ has already proven to be due to a 7-periodic pattern emerging from a primary instability (see Fan *et al.*[6]) rotating with an angular velocity $\omega_{\text{rot},m=7}/\Omega = 0.22$. A summary of the instability scenario for the idealized inflow conditions is depicted in Fig. 3. Figure 3(a) depicts the jet wake (in terms of static pressure field at mid-height) produced by the 7-periodic inlet and obtained by phase-averaging in a reference frame rotating with Ω. By subtracting it from the instantaneous pressure field and phase-averaging in a reference frame rotating with $\omega_{\text{rot},m=7}$, we identify the 7-periodic instability [Fig. 3(b)]. In a reference frame rotating with Ω, such an instability travels in the counterclockwise direction [arrow $\omega_{\text{rot},m=7} - \Omega$ in Fig. 3(b)]. The wavelet analysis confirms the FFT results and further points out a pulsating signal. This boils down to be a secondary instability, itself 7-periodic and characterized by a frequency that is twice the one of the primary instability $f_{\text{rot},m=7}$. In a reference frame rotating with the primary instability ($\omega_{\text{rot},m=7}$), the secondary instability advects the perturbation pattern radially [Fig. 3(c)]. The other frequencies observed in the FFT and the wavelet analysis are due to more intricate non-linear interactions and are not discussed in this Letter.

To investigate the effect of the leakage between rotating and steady walls on the flow field, we first consider realistic conditions with 1% radial gap ratio, i.e., $L_1/R_0 = 0.01$ (see the supplementary material for a detailed sketch). At the largest Re_Q, for $\alpha_Q = 1.25$, under the effect of the leakage flow, the flow separation area observed at the meridian section is much larger than for the idealized case (Fig. 7 of the supplementary material). The azimuthally averaged flow field for the realistic case at $\alpha_Q = 1.25$ demonstrates features similar to the ones observed for the unstable idealized case ($L_1/R_0 = 0$) at $\alpha_Q = 1$. An $m = 7$ pattern is observed at the mid-height of the realistic diffuser for $L_1/R_0 = 1\%$. As α_Q decreases, i.e., for $\alpha_Q = 1$ and 0.75, the boundary layer thickness increased due to the leakage flow effect. The inflow velocity becomes more symmetrically distributed, and no coherent $m = 7$ pattern is observed (Fig. 7 of the supplementary material). Hence, we remark that no massive flow separation is found for the realistic inflow conditions whenever the $m = 7$ pattern is not observed. This is consistent with the observation of the idealized case, even if occurring at different α_Q. In fact, the instability mechanism identified by Ljevar *et al.*[24] in two-dimensional flows and confirmed by Fan *et al.*[6] in three-dimensional conditions relies on the intensity of the inlet modulation. The leakage flow of the realistic conditions weakens the jet-wake intensity at the diffuser inlet. As a result, the flow entrained at the radial gap between rotating and steady walls tends to

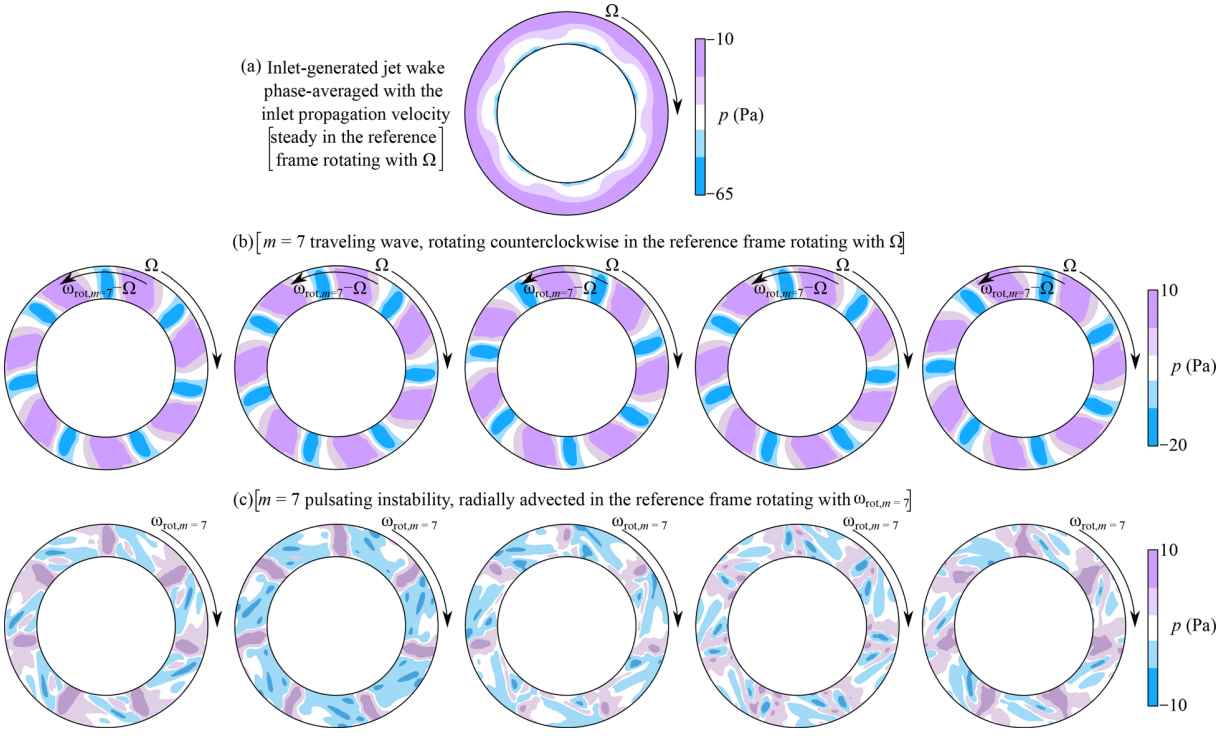

FIG. 3. (a) Phase-averaged static pressure distribution in a reference frame rotating with the inlet propagation velocity. (b) Traveling wave depicted in the reference frame rotating with Ω and computed by subtracting the phase-averaged wake (a) to the instantaneous static pressure and phase-averaging with $\omega = \Omega + \omega_{\text{rot},m=7}$. (c) Pulsating instability traveling in the reference frame rotating with $\Omega + \omega_{\text{rot},m=7}$ and computed with respect to the difference between the phase-averaged wake (a), the traveling wave (b), and the instantaneous static pressure. All figures refer to ideal boundary conditions at the mid-height of the annular ring for $\alpha_Q = 1$.

shift the modulated-core instability toward higher Re_Q. Such observations point toward a potentially unstable scenario also for the realistic inflow conditions, with an unstable boundary shifted to higher α_Q.

In order to confirm such a hypothesis, we carry out the FFT and wavelet analyses. We can still clearly observe the 7-periodic inlet condition $2\pi f_{\text{inlet}}/\Omega = 7$ in the FFT (see Fig. 4). However, no prominent instability frequencies were found in the FFT although the two-dimensional jet-wake instability patterns were clearly observed in the snapshot of the instantaneous flow field. This is understood by means of wavelet analysis (see the supplementary material), where one can observe several low-frequency patterns intermingling during the whole simulation period. Hence, one cannot expect to find a distinct peak in the Fourier transform (other than the inlet modulation frequency) because, if a rotating instability exists, it is expected to be a non-modal wave rather than a harmonic as in the idealized case. This makes the identification of potential rotating instabilities much more complicated for realistic inflow.

Therefore, we performed a cross correlation analysis of the two probe signals and captured several distinct propagation velocities. By phase-averaging the flow field for $\alpha_Q = 1.25$ and $L_1/R_0 = 0.01$ with the captured propagation velocities, the frequency $2\pi f_{\text{rot},m=1-}/\Omega = 0.514$ is proven to correspond to a 1-periodic pattern, rotating with an angular velocity $\omega_{\text{rot},m=1-}/\Omega = 0.514$. Moreover, the frequency $2\pi f_{\text{rot},m=1+,7}/\Omega = 1.486$ observed in the FFT is proven to correspond to another 1-periodic pattern rotating at $\omega_{\text{rot},m=1+}/\Omega = 1.486$. Employing the same technique, we found a third rotating pattern, this time mode-7-dominated, which rotates with an angular velocity $\omega_{\text{rot},m=7}/\Omega = 0.21$. We stress that this last angular velocity is very similar to the one found for the 7-periodic harmonic produced by the rotating instability in the idealized case. We can, therefore, conclude

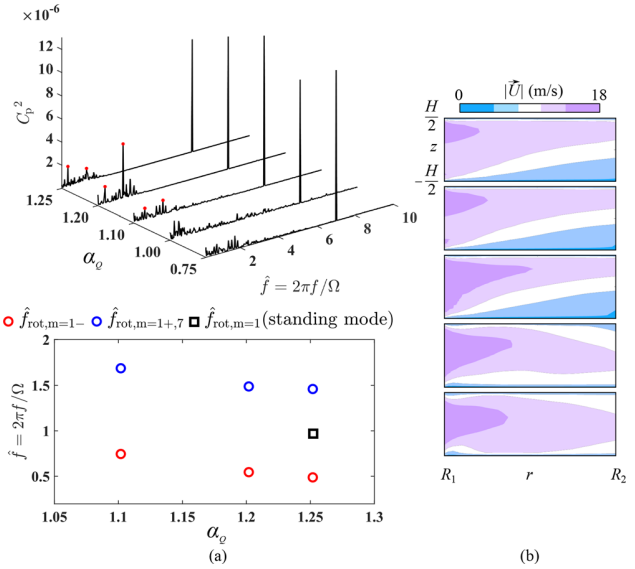

FIG. 4. (a) Fourier analysis and stability diagram. (b) Azimuthal arithmetic-average velocity fields of the more realistic case with the largest leakage size at different flow rates. From top to bottom are $\alpha_Q = 1.25$, $\alpha_Q = 1.20$, $\alpha_Q = 1.10$, $\alpha_Q = 1.00$, and $\alpha_Q = 0.75$.

that the two-dimensional jet-wake instability is still persistent in the realistic case, and the entrained leakage flow from the radial gap interacts with such instability leading to the 1-periodic traveling patterns discussed above. A summary of the instability scenario for the realistic inflow conditions is depicted in Fig. 5. Figure 5(a) shows the jet-wake pattern produced by the 7-periodic inlet and obtained by phase-averaging in a reference frame rotating with Ω. By subtracting it from the instantaneous pressure field and phase-averaging in a reference frame rotating with $\omega_{\text{rot},m=1-}$, we identify the 1-periodic traveling wave. By further subtracting the phase-averaged jet-wake pattern and the 1-periodic instability pattern from the instantaneous pressure field and phase-averaging again in a reference frame rotating with $\omega_{\text{rot},m=1+}$, we identify the other (weaker) 1-periodic traveling wave. The two 1-periodic waves propagate in the opposite circumferential direction and rotate with the same rate in a reference frame rotating with Ω. The superposition of two 1-periodic waves results, therefore, in a 1-periodic traveling wave and a 1-periodic standing wave in a reference frame rotating with Ω. This clarifies the main features introduced by the intricate leakage flow inside the parallel rings.

After removing the phase averaged two 1-periodic instabilities and the jet-wake patterns from the instantaneous pressure field and phase-averaging again in a reference frame rotating with $\omega_{\text{rot},m=7}$, the $m = 7$ traveling pattern resulting from the jet-wake instability emerges in the form of a wave that does not carry the symmetries of a Fourier mode. The qualitative and quantitative similarities with the instability we found in the idealized case are self-evident [cf. Figs. 5(b) and 3(b)]. The secondary instability observed for the idealized case [Fig. 3(c)] is not found for the realistic inflow case. On the contrary, for the realistic flow, an intermittent non-linear interaction between the mode $m = 7$ and the modes $m = 1$ leads to the chaotic dynamics observed in the wavelet analysis (see the supplementary material). In order to determine the critical conditions for the instabilities occurring for $L_1/R_0 = 0.01$, we carried out a parametric study in terms of α_Q and post-processing the results by Fourier analysis (see top panel of Fig. 4). We found out the jet-wake instability must occur for the critical flow rate $\alpha_{Qc} \in [1, 1.1]$. Moreover, the $m = 1$ traveling wave is present also for $\alpha_Q = 1.1$ and 1.2; however, the standing wave in the reference frame rotating with Ω occurs only for $\alpha_Q = 1.25$ because $(\hat{f}_{m=7} + \hat{f}_{m=1^-})/2 = 1$. Hence, the standing wave in the reference frame rotating with the inlet frequency is a by-product of the two traveling waves. A graphical summary of such a scenario is now depicted in the bottom panel of Fig. 4(a).

In order to understand the origin of the $m = 1$ traveling wave, we performed additional simulations selecting two new radial gaps between the impeller and the diffuser, i.e., $L_1/R_0 = 0.33\%$ and 0.66% for $\alpha_Q = 1$ and 1.25. Figures 6(a) and 6(b) present the results for $\alpha_Q = 1$. In this case, the $m = 7$ jet-wake instability is present up until $L_1/R_0 = 0.66\%$, as also confirmed by the corresponding mean flow separation reported in Fig. 6(b). Hence, the critical radial gap must be $(L_1/R_0)_{c,\alpha_Q=1} \in [0.66, 1]\%$ [see the bottom panel of Fig. 6(a)]. No trace of the $m = 1$ traveling wave is observed for any of the simulations at $\alpha_Q = 1$, as also confirmed by the Fourier spectra depicted in the top panel of Fig. 6(a). This leads to the conclusion that the jet-wake instability is a primary instability mechanism that does not necessarily imply the $m = 1$ traveling wave as a consequence of its interaction with the leakage flow. If the jet-wake instability is too strong [see amplitudes in the Fourier spectra of Fig. 6(a)], the leakage flow is too

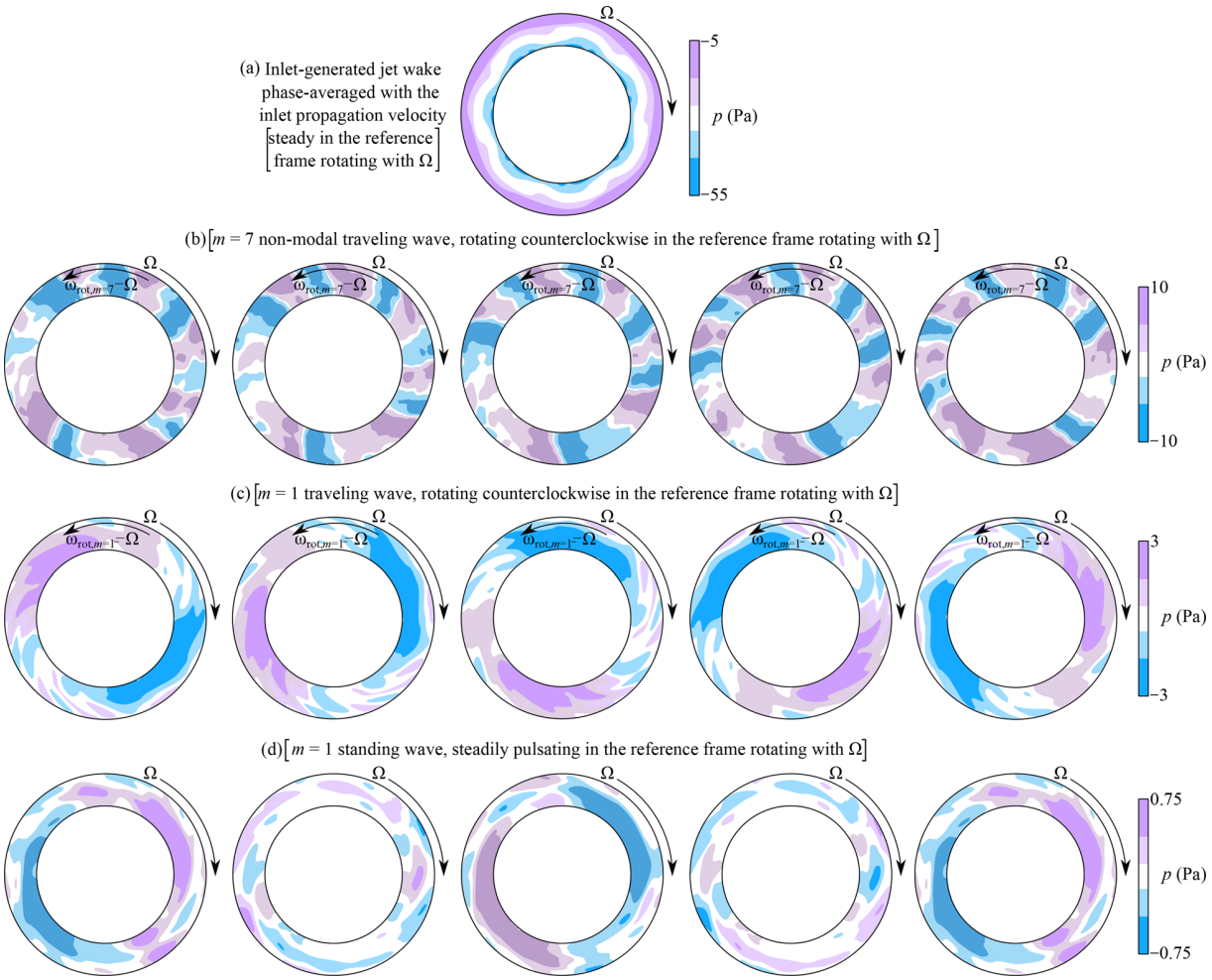

FIG. 5. (a) Phase-averaged static pressure distribution in a reference frame rotating with the inlet propagation velocity. (b) Traveling non-modal wave of mode $m = 7$ depicted in the reference frame rotating with Ω and computed by subtracting the phase-averaged wake (a) and the traveling wave (c) to the instantaneous static pressure and phase-averaging with $\omega = \omega_{\mathrm{rot},m=7}$. (c) Traveling wave of mode $m = 1$ depicted in the reference frame rotating with Ω and computed by subtracting the phase-averaged wake (a) from the instantaneous static pressure and phase-averaging with $\omega = \omega_{\mathrm{rot},m=1}$. (d) Standing wave steady in the reference frame rotating with Ω and computed with respect to the difference between the phase-averaged wake (a), the traveling wave (c), and the instantaneous static pressure and phase-averaging with $\omega = \Omega$. All figures refer to realistic boundary conditions at the mid-height of the annular ring for $\alpha_Q = 1.25$.

weak in comparison to the primary instability and the $m = 1$ traveling wave does not get triggered. Still, the importance of the leakage flow is further confirmed by our simulations, as we find that the jet-wake instability passes from $m = 7$ for $L_1/R_0 = 0$ and $\alpha_Q = 1$, to $m = 8$ for $L_1/R_0 = 0.33\%$ and to $m = 6$ for $L_1/R_0 = 0.66\%$ [see the stability diagram in Fig. 6(a)]. As already mentioned, the flow is stable for $L_1/R_0 = 1\%$ at $\alpha_Q = 1$.

Ramping up the flow rate to $\alpha_Q = 1.25$, the idealized case ($L_1/R_0 = 0$) turns out to be stable and a bandwidth of frequencies is observed in its Fourier spectrum [see Fig. 6(c)]. This is related to the chaotic dynamics due to the interaction of the inflow and the mean-flow separation occurring on the bottom plate [see Fig. 6(d) and wavelet analysis in the supplementary material]. Upon an increase in the radial gap, the jet-wake instability occurs for $L_1/R_0 = 0.33\%$; hence, the critical gap size for the primary instability is $(L_1/R_0)_{c,1^\circ,\alpha_Q=1.25} \in [0, 0.33]\%$ for $\alpha_Q = 1.25$ [see the stability diagram in Fig. 6(c)]. Even if the jet-wake instability is weaker than at $\alpha_Q = 1$, the radial gap $L_1/R_0 = 0.33\%$ is too small and the interaction between the corresponding leakage flow and the primary instability does not give rise to the $m = 1$ traveling wave. On the other hand, for comparable amplitudes of the jet-wake instability [see Fourier spectra in Fig. 6(c)], the radial gap $L_1/R_0 = 0.66\%$ entrains a stronger flow capable of triggering the secondary traveling-wave instability (see the $m = 1$ frequency in the corresponding Fourier spectrum), which becomes even clearer for $L_1/R_0 = 1\%$ as the primary instability further reduced its amplitude. Therefore, the critical radial gap for the secondary instability must be $(L_1/R_0)_{c,2^\circ,\alpha_Q=1.25} \in [0.33, 0.66]\%$ for $\alpha_Q = 1.25$. Note that for $L_1/R_0 = 0.66\%$, the $m = 1$ traveling wave rotates clockwise in a

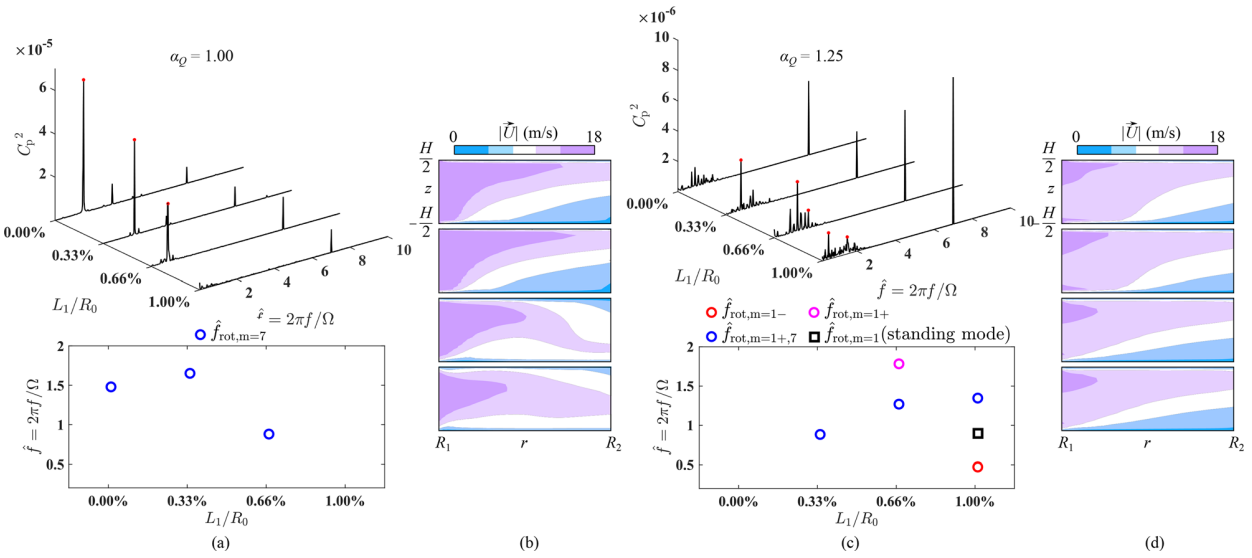

FIG. 6. (a) Fourier analysis and stability diagram, (b) azimuthal arithmetic-average velocity fields at the meridian section of the diffuser at $\alpha_Q = 1.00$, (c) Fourier analysis and stability diagram, and (d) azimuthal arithmetic-average velocity fields at $\alpha_Q = 1.25$ of the more realistic with different leakage size. (b) and (d) From top to bottom are $L_1/R_0 = 0.00\%$, $L_1/R_0 = 0.33\%$, $L_1/R_0 = 0.66\%$, and $L_1/R_0 = 1.00\%$.

reference frame rotating with the inlet Ω. Once again, the leakage flow influences the dominant mode of the primary instability, as the jet-wake instability passes from $m = 6$ for $L_1/R_0 = 0.33\%$ to $m = 9$ for $L_1/R_0 = 0.66\%$ to $m = 7$ for $L_1/R_0 = 1\%$ at $\alpha_Q = 1.25$ [see the stability diagram in Fig. 6(c)].

As the critical mode changes upon a change in the radial gap, we investigated the flow control of the primary instability by instantaneous reduction of the radial gap. To mimic it in our simulations, the fully developed flow for $L_1/R_0 = 1\%$ is assumed as initial condition, and we suddenly enforce the no-slip condition for 1/3 ($L_1/R_0 = 0.66\%$) or 2/3 ($L_1/R_0 = 0.33\%$) of the radial gap. Tracking the maximum of the $m = 7$ mode amplitude inherited as initial condition from the $L_1/R_0 = 1\%$ flow, it turns out that the instantaneous reduction in the radial gap leads to a hyperbolic decay of the large-gap instability pattern whose amplitude scales like $\sim(t/T)^{-0.95}$ [see Fig. 7(a)]. Such a rapid decay of the large-gap flow allows to unravel the growth of the most dangerous mode consistent with the $m = 6$ and $m = 9$ jet-wake instability for $L_1/R_0 = 0.33\%$ and $L_1/R_0 = 0.66\%$, respectively. By carrying out a wavelet analysis and keeping solely the frequencies $2\pi f/\Omega \in [0, 4]$, which encompasses up to twice the range for the expected instability, we extract the maximum amplitude. The corresponding values are plotted in Fig. 7. They signal that the growth of the jet-wake instability is a phenomenon that triggers non-linear interactions throughout the perturbation growth. Moreover, the non-modal character of the instability is confirmed by the non-orthogonality of the perturbation energy amplification.

In summary, the turbulent source flow between parallel rings of finite spans considering a swirling jet-wake inflow periodically modulated in space rotating at angular rate Ω has numerically been investigated for two different configurations. A two-dimensional jet-wake instability occurring at $\alpha_Q = 1$ has been identified for idealized inflow conditions, consistently with our previous study.[6] This rotating instability has a major impact on the mean flow and is responsible for a large mean flow separation near the bottom wall. Wavelet analysis revealed the presence of secondary pulsating instability in a reference frame rotating with the primary instability. The secondary instability is found to migrate from the inlet wake shear layer to the diffuser outlet. It needs to be mentioned that an open question that deserves to be investigated concerns the type of intermittency scenario in such a parallel plate system. Owing to the flow complexity and multi-space/time scales interactions, we avoided investigating the intermittency in depth by using our URANS calculations. We rather recommended the use of

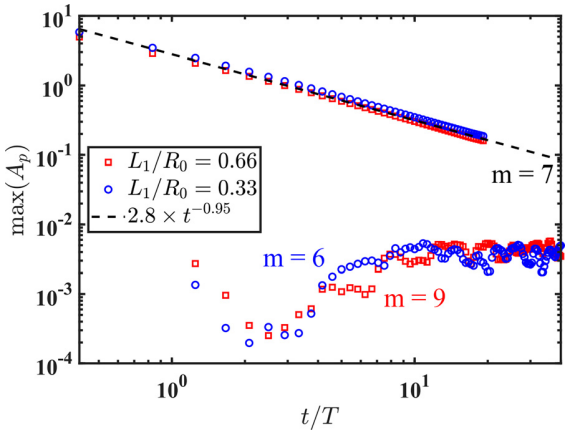

FIG. 7. Decay upon a sudden reduction in the gap size of the flow instability amplitude ($m = 7$) inherited as an initial condition generated for $L_1/R_0 = 1\%$ and $\alpha_Q = 1.25$. The lower amplitudes depict the growth of the primary instability amplitude for $L_1/R_0 = 0.33\%$ ($m = 6$) and 0.66% ($m = 9$).

LES simulations for assessing the intermittency scenario occurring in swirling flow between parallel plates.

The effect of a more realistic inflow condition has also been investigated assuming that a leakage flow could enter the parallel ring diffuser. A remarkable impact on the leakage flow has been reported, leading to a distortion of the rotating instability pattern, and an intricate interaction between the leakage and the primary instability. This non-linear interaction can produce a chaotic transfer of kinetic energy that intermittently transfers from the instability pattern to the 1-periodic traveling waves produced by the leakage. The $m = 1$ traveling wave is subordinated to the jet-wake instability and its interaction with the leakage flow. Moreover, if the jet-wake instability occurs and its amplitude is not too strong in comparison to the leakage flow, a secondary instability gets triggered in form of an $m = 1$ traveling-wave owing to the interaction of the jet-wake instability and the leakage flow. For $L_1/R_0 = 0.01$ and $\alpha_Q = 1.25$, two 1-periodic waves are induced by the leakage flow and propagate with the same velocity magnitude but in opposite directions in the reference frame rotating with Ω. Hence, we identified a distinct signature of the leakage flow that leads to an $m = 1$ traveling wave and potentially an $m = 1$ standing wave in the reference frame rotating with Ω. To the best of the authors' knowledge, this feature has been reported here for the first time and has direct implications for overly-simplified systems that do not include realistic inflow conditions in annular source flows. Moreover, the boundaries of the primary and secondary instabilities have been bracketed in terms of α_Q and L_1/R_0, and the non-linear non-modal growth of the primary instability has been demonstrated for $\alpha_Q = 1.25$ and $L_1/R_0 = 0.33\%$ and 0.66%.

See the supplementary material for details of the problem configuration, numerical method, turbulence model, and the flow field.

We kindly acknowledge the GENCI (Grand Equipement National de Calcul Intensif) for the numerical resources granted to conduct this study under project No. A0102A01741. Furthermore, we appreciate the support of the China Scholarship Council for the doctoral students of M. Fan (CSC Student No. 201908320328).

AUTHOR DECLARATIONS

Conflict of Interest

The authors have no conflicts to disclose.

Author Contributions

Meng Fan: Data curation (lead); Investigation (equal); Methodology (equal); Software (lead); Visualization (lead); Writing – original draft (equal); Writing – review & editing (equal). **Antoine Dazin:** Conceptualization (equal); Data curation (equal); Investigation (equal); Supervision (equal); Writing – review & editing (equal). **Gérard Bois:** Conceptualization (equal); Investigation (equal); Supervision (equal); Writing – review & editing (equal). **Francesco Romanò:** Conceptualization (equal); Data curation (equal); Investigation (equal); Methodology (equal); Software (supporting); Supervision (equal); Writing – original draft (equal); Writing – review & editing (equal).

DATA AVAILABILITY

The data that support the findings of this study are available from the corresponding author upon reasonable request.

REFERENCES

[1]S. Mochizuki and W.-J. Yang, "Self-sustained radial oscillating flows between parallel disks," J. Fluid Mech. **154**, 377–397 (1985).
[2]H. D. Murphy, M. Coxon, and D. M. McEligot, "Symmetric sink flow between parallel plates," J. Fluid Eng. **100**(4), 477–484 (1978).
[3]M. Tabatabai and A. Pollard, "Turbulence in radial flow between parallel disks at medium and low reynolds numbers," J. Fluid Mech. **185**, 483–502 (1987).
[4]J. Raal, "Radial source flow between parallel disks," J. Fluid Mech. **85**, 401–416 (1978).
[5]C. Hu, C. Yang, X. Shi, R. Zou, L. Liu, and H. Chen, "Investigation of rotating stall in radial vaneless diffusers with asymmetric inflow," Aerosp. Sci. Technol. **96**, 105546 (2020).
[6]M. Fan, A. Dazin, G. Bois, and F. Romanò, "Effect of inlet leakage flow on the instability in a radial vaneless diffuser," Phys. Fluids **35**(1), 014105 (2023).
[7]T. Hagiwara, "Studies on the characteristics of radial-flow nozzles: (1st report, theoretical analysis of outward flow," Bull. JSME **5**, 656–663 (1962).
[8]Y. Qin, J. Chen, X. Zhao, D. Liao, R. Mu, S. Wang, H. Wu, and H. Guo, "Transcatheter closure of perimembranous ventricular septal defect using a modified double-disk occluder," Am. J. Cardiol. **101**, 1781–1786 (2008).
[9]J. Hunt and I. Torbe, "Characteristics of a hydrostatic thrust bearing," Int. J. Mech. Sci. **4**, 503–516 (1962).
[10]M. Smith, "Geothermal energy. A bibliography with abstracts. Period covered: 1964–April 1975," Technical Report (National Technical Information Service, Springfield, VA, USA, 1975).
[11]H. A. Stone and H. Brenner, "Dispersion in flows with streamwise variations of mean velocity: Radial flow," Ind. Eng. Chem. Res. **38**, 851–854 (1999).
[12]J. C. Chen, "Simultaneous radiative and convective heat transfer in an absorbing, emitting, and scattering medium in slug flow between parallel plates," AIChE J. **10**, 253–259 (1964).
[13]F. Kreith, "Transfert de chaleur et de masse dans un ecoulement radial entre deux disques paralleles fixes, ou tournant a la meme vitesse," Int. J. Heat Mass Transfer **9**, 265–282 (1966).
[14]S. Savage, "Laminar radial flow between parallel plates," J. Appl. Mech. **31**(4), 594–596 (1964).
[15]S. Wilson, "A note on laminar radial flow between parallel plates," Appl. Sci. Res. **25**, 349–354 (1972).
[16]E. Bakket, J. Kreider, and F. Kreith, "Turbulent source flow between parallel stationary and co-rotating disks," J. Fluid Mech. **58**, 209–231 (1973).
[17]J. Guo, H. Shan, Z. Xie, C. Li, H. Xu, and J. Zhang, "Exact solution to Navier-Stokes equation for developed radial flow between parallel disks," J. Eng. Mech. **143**, 04017026 (2017).
[18]S. Mochizuki, S. Yamada, and H. Osaka, "Management of a plane turbulent wall jet by the large-eddy break-up device," JSME Int. J. Ser. B**49**, 921–927 (2006).
[19]A. Dazin, O. Coutier-Delgosha, P. Dupont, S. Coudert, G. Caignaert, and G. Bois, "Rotating instability in the vaneless diffuser of a radial flow pump," J. Therm. Sci. **17**, 368 (2008).
[20]A. Dazin, "High-speed stereoscopic PIV study of rotating instabilities in a radial vaneless diffuser," Exp. Fluids **51**, 83–93 (2011).
[21]G. Pavesi, A. Dazin, G. Cavazzini, G. Caignaert, G. Bois, and G. Ardizzon, "Experimental and numerical investigation of unforced unsteadiness in a vaneless radial diffuser," in *9th European Conference on Turbomachinery: Fluid Dynamics and Thermodynamics, ETC 2011 - Conference Proceedings* (EUROTURBO, 2011), Vol. 1.
[22]Y. Tsujimoto, Y. Yoshida, and Y. Mori, "Study of vaneless diffuser rotating stall based on two-dimensional inviscid flow analysis," J. Fluids Eng. **118**, 123–127 (1996).

[23]Y. Heng, A. Dazin, and M. Ouarzazi, "Linear stability analysis of rotating stall in a wide vaneless diffuser," in *12th European Conference on Turbomachinery Fluid Dynamics and Thermodynamics, ETC 2017* (EUROTURBO, 2017).
[24]S. Ljevar, H. C. D. Lange, and A. A. V. Steenhoven, "Two-dimensional rotating stall analysis in a wide vaneless diffuser," Int. J. Rotating Mach. **2006**, 056420.
[25]M. Fan, A. Dazin, F. Romano, and G. Bois, "Effect of leakage on the performance of the vaneless diffuser of a centrifugal pump model," in *Conference on Modelling Fluid Flow (CMFF'22)*, Budapest, Hungary (2022), pp. 51–58.
[26]M. Fan, A. Dazin, G. Bois, and F. Romanò, "Instabilities identification based on a new centrifugal 3D impeller outflow model," Aerosp. Sci. Technol. **140**, 108466 (2023).

Supplementary Document

Instabilities in a turbulent swirling source flow between parallel rings

M. Fan,[1] A. Dazin,[1] G. Bois,[1] and F. Romanò[1]
Univ. Lille, CNRS, ONERA, Arts et Métiers Institute of Technology, Centrale Lille, UMR 9014-LMFL-Laboratoire de Mécanique des Fluides de Lille - Kampé de Fériet, F-59000, Lille, France

(*Electronic mail: meng.fan@ensam.eu)

(Dated: 10 August 2023)

I. PROBLEM CONFIGURATION

The computational domain of the problem configuration is depicted in fig. 1. It consists of a suction pipe (orange), a seven-periodic rotating device (gray), a radial vaneless diffuser, also referred to as "parallel rings" in the manuscript (dark green), and an outflow box (light green) attached to the outlet of the parallel rings. The inlet velocity boundary conditions are specified at the top of the circular suction pipe, and the static pressure outlet boundary conditions are applied at the boundaries of the outflow box. The geometry characteristics of the numerical model match the experimental setup, and the simulation results of the entire machine are validated against the experimental results[1,2].

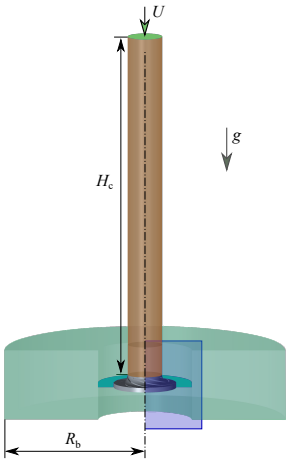

FIG. 1. Schematic of the entire computational domain for the problem configuration.

To inspect the effect of leakage between rotating and steady walls on the swirling source flow between parallel rings, two conceptually different configurations are studied as depicted in fig. 2: (i) the idealized case in which the jet wake is directly injected into the diffuser (see fig. 2(a)), and (ii) the more realistic case in which the jet wake entrains some fluid from an inlet radial gap of length L_1 (see fig. 2(b)) before entering the parallel rings.

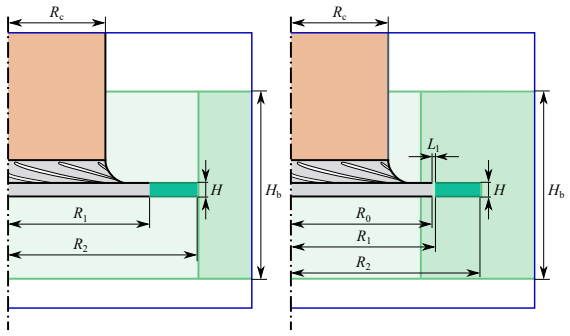

FIG. 2. Zoom-in view of the two conceptually different configurations: (a) the ideal case and (b) the more realistic case.

II. NUMERICAL METHOD

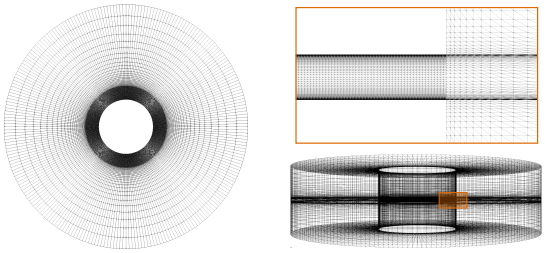

FIG. 3. Top (a) and side (b) view of a typical mesh employed for carrying out the three-dimensional URANS numerical simulations in OpenFOAM. The inset in (b) shows a closeup (orange) of the refined grid in the radial diffuser.

The commercial software ANSYS ICEM-CFD is employed for meshing. The multi-block structure employed by ICEM CFD allows for more flexibility and accuracy in the mesh generation process, carried out using hexahedral cells. They are known to provide better accuracy at lower computational cost than tetrahedral cells for comparable meshes. Our computational grid for the source flow between parallel rings is depicted in Fig. 3. An outflow box of height $15 \times H$ and radius

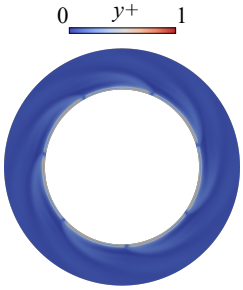

FIG. 4. Example of the typical y^+ distribution on the top wall of the radial diffuser.

$3 \times R_2$ is attached to the diffuser domain in order to avoid setting outlet conditions directly at the diffuser outflow. The grid in the parallel rings domain is finer, while the grid in the outflow box is coarser, as the main focus of our study is the flow in the radial diffuser. The mesh of the parallel rings is refined close to the walls by using a stretching factor of 1.5 in axial direction, which leads to values for y^+ lower than 1 all over the parallel walls (see Fig. 3(c)). All the numerical results presented in the letter are obtained in OpenFOAM v1912 using a total mesh number of 859k finite volumes for the diffuser and the outflow box. This resolution has been chosen after conducting a grid-independence verification that compared four resolutions with a total of 238k, 386k, 859k, and 1.7M cells for diffuser and outflow box. For more details, we refer to Fan et al.[1,2].

III. TURBULENCE MODELLING

An appropriate choice of the turbulence model is key, hence four modeling options available in OpenFOAM are here compared; namely: (i) the standard $k-\varepsilon$, (ii) the $k-\omega$, (iii) the $k-\omega$ SST and (iv) the realizable $k-\varepsilon$ models.

Considering that the boundary layers at the parallel plates are especially important for our study, the standard $k-\varepsilon$ model is excluded since it requires $y^+ > 30$. This would lead to embed the whole boundary layer on the parallel plates within one computational cell, which would lead to over-diffused boundary layers.

The turbulence model analysis is therefore restricted to the standard $k-\omega$, the $k-\omega$ SST, and the realizable $k-\varepsilon$ models. We expect that our URANS reproduce the experimental mean pressure rise due to the radial diffusion. Figure 5 shows the experimental measurements of[2] along the top wall of the diffuser (gray bullets and error bars), compared to the corresponding azimuthally-averaged static pressure p evaluated at the top ring. Based on the results shown in fig. 5, the $k-\omega$ SST and the realizable $k-\varepsilon$ models produce similar results, both very close to the experimental measurements. On the contrary, the $k-\omega$ model overpredicts the mean pressure drop at inlet and the radial pressure gradient throughout. As the adverse pressure gradient is a major feature of our source flow, the standard $k-\omega$ model is not appropriate for the URANS

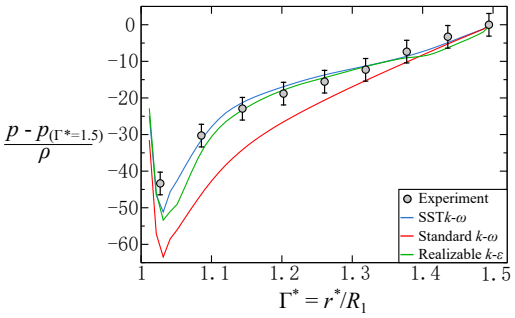

FIG. 5. Azimuthally-averaged pressure rise measured at the top ring along the radial coordinate $\Gamma^* = r^* - R_1$, where r^* is a dimensional quantity. The experimental measurements of[2] are depicted by the gray bullets and the corresponding error bars. The numerical results are shown in red ($k-\omega$), blue ($k-\omega$ SST), and green (realizable $k-\varepsilon$). The simulations refer to $\alpha_Q = 1$ for the realistic inflow conditions.

of our study.

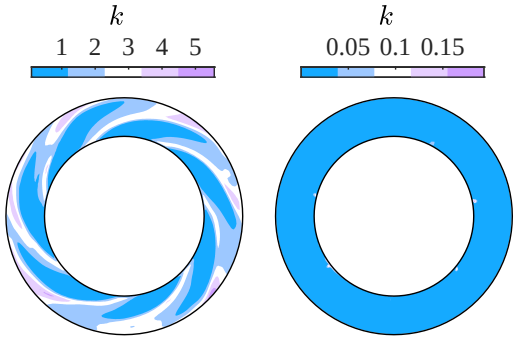

FIG. 6. Turbulent kinetic energy at mid-height produced by the $k-\omega$ SST (a), and the realizable $k-\varepsilon$ (b) models at $\alpha_Q = 1$ for the realistic case.

One also expects that the URANS results should be capable of reproducing the signature features of the seven-periodic inlet flow in terms of turbulent kinetic energy k, at least for the core flow. Comparing the two remaining turbulence models, i.e. the $k-\omega$ SST and realizable $k-\varepsilon$, fig. 6 shows that the latter one incorrectly predicts very low levels of k, even at the inlet of the diffuser, where the inflow condition is supposed to produce the highest turbulent kinetic energy. On the contrary, the $k-\omega$ SST model produces a coherent result, consistent with the expected 7-periodic jet-wake injected at inlet. This leads to conclude that the $k-\omega$ SST model is the most appropriate model to simulate our swirling radial source between finite-span parallel rings. All the results presented in the letter are therefore obtained with the $k-\omega$ SST model.

REFERENCES

[1]M. Fan, A. Dazin, F. Romano, and G. Bois, "Effect of leakage on the performance of the vaneless diffuser of a centrifugal pump model," Conference on Modelling Fluid Flow (CMFF'22), Budapest, Hungary , 51–58 (2022).
[2]M. Fan, A. Dazin, G. Bois, and F. Romanò, "Effect of inlet leakage flow on the instability in a radial vaneless diffuser," Physics of Fluids **35(1)**, 014105 (2023).

Appended papers

C.5 Paper E

"Effect of radius ratio on the instabilities in a vaneless diffuser",

M. Fan, A. Dazin, G. Bois, F. Romanò,

Eur. J. Mech. B/Fluids, 104 (2024), 1–7.

European Journal of Mechanics / B Fluids 104 (2024) 1–7

Contents lists available at ScienceDirect

European Journal of Mechanics / B Fluids

journal homepage: www.elsevier.com/locate/ejmflu

Effect of radius ratio on the instabilities in a vaneless diffuser

Meng Fan *, Antoine Dazin, Gérard Bois, Francesco Romanò

Univ. Lille, CNRS, ONERA, Arts et Métiers Institute of Technology, Centrale Lille, UMR 9014-LMFL-Laboratoire de Mécanique des Fluides de Lille - Kampé de Fériet, Av. Paul Langevin, Villeneuve-d'Ascq, Lille, F-59000, Hauts de France, France

ARTICLE INFO

Keywords:
Vaneless diffuser
Instability
Radius ratio

ABSTRACT

The prominent features of the primary instabilities of a turbulent source flow between finite-span parallel rings with spatially modulated inflow conditions rotating at angular rate Ω are investigated. Two different two-dimensional instabilities that occur at large ($\alpha_Q \gtrsim 1.00$) and low ($\alpha_Q \lesssim 0.65$) flow rates have been traced back to two different physical mechanisms related to jet-wake and mean-core flow, respectively. The effect of the radial aspect ratios Γ on the instability characteristics of the flow between parallel rings is also considered in this paper. Numerical URANS simulations are conducted for three different radial aspect ratios, i.e. $\Gamma = 1.25$, 1.5, and 2, the corresponding cross-sectional aspect ratios $\Lambda = 2(\Gamma - 1) \times 3.325$, and two conceptually different inflow conditions. Their impact on the rotating instabilities in terms of instability mode number and instability frequency is the main focus of this study and is analyzed by fast Fourier transform (FFT) and wavelet analysis. Realistic inflow conditions with a leakage flow are found to overtake the instability for small radius ratios and affect the primary instabilities for large radius ratios.

1. Introduction

The study of radial incompressible flow between parallel circular disks is relevant in several physical systems, including hydrostatic air bearings [1], radial diffusers [2,3], double disk valves [4], and radial flow nozzles [5]. In these flows, two limiting cases can be identified. The first one, approaching a creeping flow, occurs when the gap between the disks and the flow rate is very small, resulting in a local Reynolds number that is less than unity throughout [6]. On the other hand, the second extreme case is an incompressible, strong inertial flow where the disk spacing and flow rate are large, resulting in a Reynolds number that is much greater than unity at inflow [7]. The local Reynolds number falls somewhere between the two extremes mentioned earlier in most practical scenarios. However, for strongly inertial flows, an order-of-magnitude analysis predicts that the flow in a long-enough radial diffuser will transition to a creeping regime irrespective of the flow rate [8].

Various authors have conducted research on instabilities in source flow between parallel disks, with some reporting the presence of inflection points [9,10] and self-sustained separation and reattachment of shear layers [11]. In our study, we are concerned with the flow instability in a radial vaneless diffuser. Such rotating instabilities have been theoretically investigated using two different approaches: (i) 3D wall boundary layer stability analysis for narrow vaneless diffuser [12], and (ii) 2D approaches that employ the inviscid core flow to investigate the stability of wide vaneless diffusers [13]. Experimental and numerical studies have also been conducted by several researchers [14–16], and they suggest that there is no clear single-parameter geometry ratio for advocating that wide vaneless diffuser and their narrow counterparts must lead to different instability mechanisms. Although these studies enhanced our understanding of unsteady phenomena, they did not provide a comprehensive characterization of the several instabilities that could occur in turbulent vaneless diffusers with a periodically spatially-modulated jet wake inflow rotating at an angular rate Ω. Our study aims therefore to extend the previous investigations by carrying out a comprehensive numerical characterization. Our previous results shed light on two different mechanisms leading to different instabilities occurring at high and low flows respectively [3]. The impeller-to-diffuser leakage effect on such instabilities has also been evaluated [17]. However, how the boundary layer interacts with such instabilities remains unclear for radial aspect ratios other than $\Gamma = R_2/R_1 = 1.5$. The main focus of this study is to examine how the instability characteristics of the flow between parallel rings are influenced by the radial aspect ratio Γ, with $\Gamma \in \{1.25,\ 1.5,\ 2\}$, keeping constant the inlet radius-to-height ratio $R_1/H = 6.65$, i.e. for a cross-sectional aspect ratio $\Lambda = 2(\Gamma - 1) \times 3.325$ (see Fig. 1). For all the cases considered in this study, an experimentally realizable (see Fan et al. [3]) 7-periodic spatially-modulated inlet is located at $r = R_1$ and rotates at a constant angular velocity Ω, resulting in a Reynolds number of $\mathrm{Re}_\Omega = \Omega R_1^2/\nu = 5.52 \times 10^5$, where ν is the kinematic viscosity of the fluid. This Reynolds

* Corresponding author.
E-mail address: meng.fan@ensam.eu (M. Fan).

https://doi.org/10.1016/j.euromechflu.2023.11.003
Received 28 July 2023; Received in revised form 20 September 2023; Accepted 4 November 2023
Available online 7 November 2023

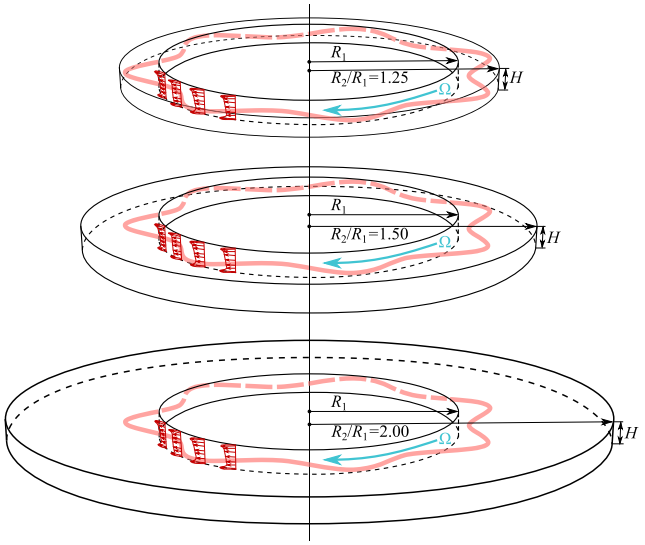

Fig. 1. Schematic of the source flow between parallel rings of finite spans. The three configurations show $\Gamma = 1.25$ (top), $\Gamma = 1.5$ (middle), and $\Gamma = 2$ (bottom).

number Re_Ω is based on the nominal tangential velocity at the radial diffuser inlet and serves as the first Reynolds number that characterizes the flow. Besides, a second Reynolds number $\mathrm{Re}_Q = Q/2\pi H\nu$ is defined based on the volumetric flow rate Q entering the parallel annular plates with a reference value $\tilde{\mathrm{Re}}_Q = \tilde{Q}/2\pi H\nu = 6.46 \times 10^4$. A corresponding control parameter $\alpha_Q = \mathrm{Re}_Q/\tilde{\mathrm{Re}}_Q = Q/\tilde{Q}$ is used hereinafter to vary the flow rate Reynolds number.

In our previous study [17], we kept $\alpha_Q \geq 0.75$ and focused on the jet-wake instability discovered by Lejvar et al. [18]. We showed that the fluid entrainment at the radial diffuser inlet can be significant for secondary instabilities. In this study, we follow the same research line and investigate the same two conceptually-different inflows of Fan et al. [17]:

(i) an idealized scenario where the jet wake is injected directly into the diffuser,
(ii) a more realistic scenario where the jet wake entrains some fluid from an inlet radial gap before entering the parallel rings.

2. Methodology

2.1. Problem formulation

A centrifugal impeller is employed to produce the inflow boundary condition for our problem. The geometrical features of the entire numerical model of our problem configuration are matched with the experimental setup (see Fig. 2), which includes a suction pipe (orange), a rotating impeller (gray), a radial vaneless diffuser, also known as the *parallel disks* (dark green), and an outflow box (light green) connected to the outlet of the vaneless diffuser.

We performed a parametric analysis of a centrifugal pump by means of URANS (unsteady Reynolds-averaged Navier–Stokes) simulations, as they provide an effective methodology capable of reasonable accuracy for complex turbomachinery configurations at limited computational costs [19]. Each case required about 70 impeller revolutions to make sure that the flow in the radial diffuser is fully developed. This implies a wall-clock time of $\approx$ 150 h using 320 processors, i.e. $\approx 50k$ CPU-hours per simulation with $2.3M$ finite volumes. Instead, if one wants to perform our same study by means of LES (large eddy simulations), the literature suggests that similar pumps with comparable Reynolds numbers would require $\approx 460M$ finite volumes (see [20]), which is about 200 times our grid resolution. Hence, we can estimate that each case would require 10^7 CPU hours if simulated by LES, which is impractical for the $\approx$ 50 simulations of this study. Using URANS instead of LES limits the relevance of our simulations, as small-scale turbulence structures are not well captured by Reynolds-averaged approaches. We however stress that URANS simulations have been proven capable of capturing the key large-scale flow features in centrifugal pumps like ours, as also confirmed by the several examples reported in the literature and validated by experiments [14,21–23]. The scope of our study is to identify large-scale flow instabilities, and we refer to our previous studies to provide further experimental validation of our URANS approach [3,17,24,25].

The mass, momentum, and energy conservation equations are solved in the form of URANS equations as following

$$\frac{\partial \vec{U}}{\partial t} + (\vec{U}\cdot\nabla)\vec{U} + \nabla P = \nabla\cdot(2\nu\vec{\vec{S}} - \vec{\vec{\tau}}), \quad \nabla\cdot\vec{U} = 0, \tag{1}$$

where $\vec{U} = \vec{U}(\vec{x};\ t) = (U_1, U_2, U_3)$ denotes the mean part of the velocity vector, p denotes the mean part of the static pressure, ν is the constant kinematic viscosity, $\vec{x}$ is the position vector, t denotes the time, $\vec{\vec{S}} = \frac{1}{2}(\nabla\vec{U} + \nabla^T\vec{U})$ is the mean rate of the strain tensor, and $\vec{\vec{\tau}}$ is the Reynolds stress tensor.

2.2. Computational setup

Hexahedral meshes which are more accurate and resource-efficient than tetrahedral meshes are utilized for this study. A mesh with 2.3 million finite volumes was selected for URANS simulations after a mesh-independent analysis. To ensure the accuracy of the boundary layer calculation, the mesh is refined near the walls with an expansion ratio of 1.5 resulting in y^+ values close to 1 on the walls of the main computational domain. The incompressible Navier–Stokes equations are computed by the SST $k-\omega$ turbulence model based on a turbulence model independence analysis (for more details, we refer to Fan et al. [3,24,25]).

The large time-step transient solver `pimpleFoam` in OpenFOAM is employed for solving the transient incompressible flows, and the specific numerical schemes are reported in Fan et al. [3]. The inlet velocity is specified using a Dirichlet-type boundary condition named `flowRateInletVelocity`, and the static pressure $p = 0$ Pa is applied at the outflow contours. The `noSlip` boundary condition is applied to fixed walls, while the `rotatingWallVelocity` option is utilized for rotating walls. The inlet values for the turbulent kinetic energy k_{in} and the specific dissipation rate ω_{in} are estimated with the following equations:

$$k_{\mathrm{in}} = \frac{3}{2}(I|u_{\mathrm{ref}}|)^2, \qquad \omega_{\mathrm{in}} = \frac{k_{\mathrm{in}}^{0.5}}{C_\mu^{0.25} l}, \tag{2}$$

where u_{ref} is a reference velocity given by the radial velocity at the suction pipe inlet, I is the turbulence intensity defined by $I = 0.16(\mathrm{Re}_Q)^{-\frac{1}{8}}$, C_μ is a constant equal to 0.09, and l is a reference length scale given by the inlet pipe diameter in our simulations. The impeller rotational speed is set as 125 rad/s and the time step Δt is set to correspond to 0.5° of the impeller revolution. URANS simulations were run for 70 revolutions of the impeller. For more details on the numerical settings, refer to Fan et al. [3].

The simulation results have been previously validated against corresponding experiments in the same pump, including performance curves, pressure recovery profiles, FFT spectra, and PIV phase-averaged flow fields [3,17,24,25]. The very good agreement between numerical and experimental results further highlights the capability of the URANS technique and the $k-\omega$ SST model to correctly predict the large-scale flow feature in our centrifugal pump.

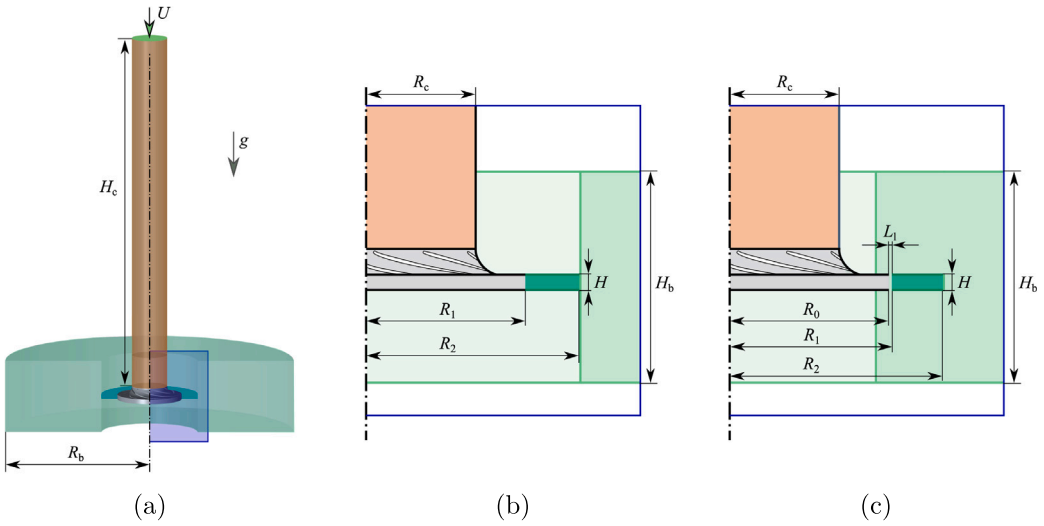

Fig. 2. Schematic of (a) the entire computational domain for the problem configuration and the zoom-in view of the two conceptually different configurations: (b) the ideal case and (c) the more realistic case. (For interpretation of the references to color in this figure legend, the reader is referred to the web version of this article.)

3. Results

3.1. Identification of the instability

The equilibrium state (or basic state) in our diffuser with a 7-periodic spatially-modulated inflow is intended to be the mean flow, steady in the reference frame rotating with Ω. By employing steady simulations (RANS, see Fig. 3(a)) for idealized conditions with $\Gamma = 1.5$, such an equilibrium state can be retrieved for $\alpha_Q = 1$ (left) and $\alpha_Q = 1.25$ (right). A well-identified instability rotating at a rate different than Ω is however supposed to strongly perturb the flow for $\alpha_Q = 1$ and disappear for $\alpha_Q = 1.25$ [24]. This is captured by using URANS simulations (see Fig. 3(b)), which are capable of simulating unstable phenomena that break the time-symmetry of the mean-flow basic state in the reference frame rotating with Ω. It is the occurrence of the instability observed for $\Gamma = 1.50$ and $\alpha_Q = 1$ that turns the periodic large-scale basic state with period $\hat{T} = 2\pi f_{\text{inlet}}/\Omega = 7$ into a (quasi-)periodic large-scale flow with period $2\pi f_{\text{inlet}}/\Omega + 2\pi f_{\text{inlet}}/\omega_{\text{inst}}$, where ω_{inst} is the normalized frequency of the instability.

We anticipate that the identification of the instability flow patterns will be based on systematic phase averages of the URANS simulations. In general, for turbulent flows in which the large scales are not clearly separated in frequencies, non-linear interactions can dominate the energy spectra. In our case, however, the Fourier spectra are quasi-modal for the stable cases and quasi-bimodal for the unstable cases except when significant chaotic patterns are observed. This implies that, for the stable state, the large scales are dominated by their phase-averaged component resulting from the 7-periodic spatially-modulated inlet flow rotating at rate Ω. For unstable configurations, to such a mean-flow basic state a second dominant frequency is added to the spectrum, which frequency is incommensurate with respect to $2\pi f_{\text{inlet}}/\Omega$ and results from the large-scale instability pattern depicted by phase averaging. We refer to the appendix for further details.

3.2. Instabilities near design flow rate

To study the effect of the radial aspect ratio Γ on the 2D jet-wake instability occurring at large flow rate Reynolds numbers ($\alpha_Q \gtrsim 1$), the instantaneous color maps at the mid-height of the diffuser for the idealized inflow (case (i)) at the reference condition $\alpha_Q = 1$ with radial aspect ratio $\Gamma = 1.25$ and $\Gamma = 2$ are firstly plotted as shown in Fig. 4(a). The results show that seven high-speed jets corresponding to the seven-periodic inflow modulation are observed for both radial aspect ratios Γ. Besides, a 7-periodic 2D jet-wake instability pattern can be found for $\Gamma = 1.25$ (see the top panel of Fig. 4(a)) which is consistent with what is reported for $\Gamma = 1.5$ (see Fan et al. [17]). For $\Gamma = 2$, as the outflow is further away, the non-linear effects due to the interactions of radial diffuser boundary layers took over and a complex chaotic regime (see the bottom panel of Fig. 4(a)) overtook the quasi-periodic instability pattern observed with the other two smaller radial aspect ratios.

To better understand the instability characteristics and the underlying mechanisms leading to the chaotic regime, a comprehensive analysis utilizing FFT and wavelet transform is conducted for the idealized inflow configuration at $\alpha_Q = 1$ (see Fig. 4(b)). Two numerical probes located at $r = 1.25R_1$ on the top wall with an angular phase shift of 60° are employed. For more details on the numerical method, data acquisition, and processing methods, we refer to Fan et al. [3,25]. For $\Gamma = 1.25$, the 7-periodic inlet condition $2\pi f_{\text{inlet}}/\Omega = 7$ can be easily detected from the FFT result. The corresponding peak is overcome by a low frequency $2\pi f_{\text{rot},m=7}/\Omega = 1.314$, which is confirmed to be a 2D jet-wake instability frequency with a 7-periodic pattern propagating in the circumferential direction with an angular velocity of $\omega_{\text{rot},m=7}/\Omega = 0.188$. The wavelet analysis shows good consistency with the FFT results. The jet-wake pattern produced by the 7-periodic inlet is phase-averaged in a reference frame rotating with Ω (basic state) and subtracted from the instantaneous pressure field; a second phase-average in a reference frame rotating with $\omega_{\text{rot},m=7}$ is employed to identify the 7-periodic instability pattern that traces back the low frequencies observed in the FFT and wavelet analysis to a jet-wake instability consistent with the prediction of Ljevar et al. [18] (see corresponding video at https://github.com/fromano88/CentrifugalPump.git). Such an instability travels in the counterclockwise direction in a reference frame rotating with Ω. Hence, for $\Gamma = 1.25$, the flow is consistent with the instability reported for $\Gamma = 1.5$, which is thoroughly analyzed in our previous studies [3,17]. For $\Gamma = 1.5$, the 7-periodic jet-wake instability has a characteristic frequency $2\pi f_{\text{rot},m=7}/\Omega = 1.543$ and propagates in the circumferential direction with an angular velocity of $\omega_{\text{rot},m=7}/\Omega = 0.220$. Moreover, for $\Gamma = 1.5$ we also found a secondary instability pulsating at a frequency of about 3 times $f_{\text{rot},m=7}$. Such secondary instability occurred because of the nonlinear interactions between the primary instability and the shear layer of the inlet jet wave [3,17]. For $\Gamma = 1.25$, the secondary instability is not observed because the radial diffuser is too short to allow for intense nonlinear interactions.

For $\Gamma = 2$, only the 7-periodic inlet frequency $2\pi f_{\text{inlet}}/\Omega = 7$ can be clearly detected from the FFT result (see the bottom panel

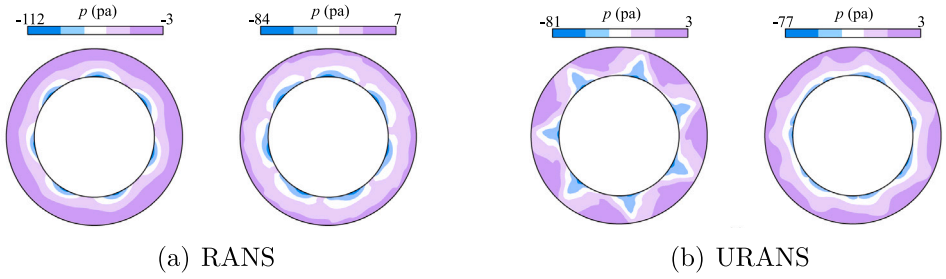

Fig. 3. Instantaneous static pressure distribution at the mid-height of the diffusers obtained by (a) RANS and (b) URANS simulations. All figures refer to the idealized inflow (case (i)) for $\alpha_Q = 1$ (left) and $\alpha_Q = 1.25$ (right).

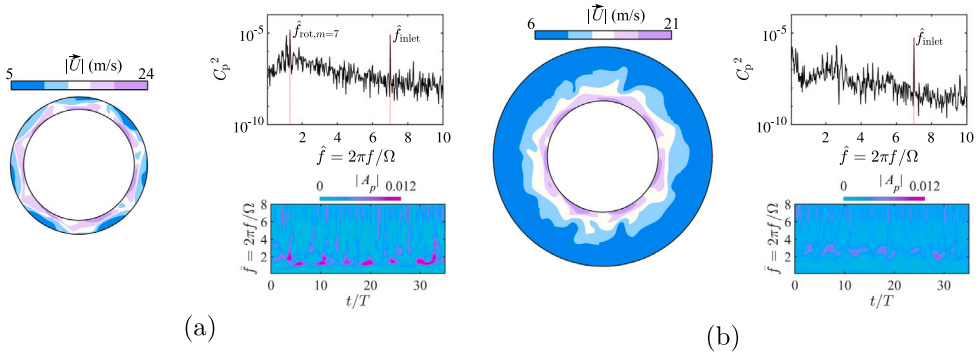

Fig. 4. Color maps of instantaneous velocity magnitude distribution at the mid-height of the diffusers (left) and Fourier and wavelet analysis results (right) for (a) $\Gamma = 1.25$ and (b) $\Gamma = 2$. All figures refer to the idealized inflow (case (i)) for $\alpha_Q = 1.00$. (For interpretation of the references to color in this figure legend, the reader is referred to the web version of this article.)

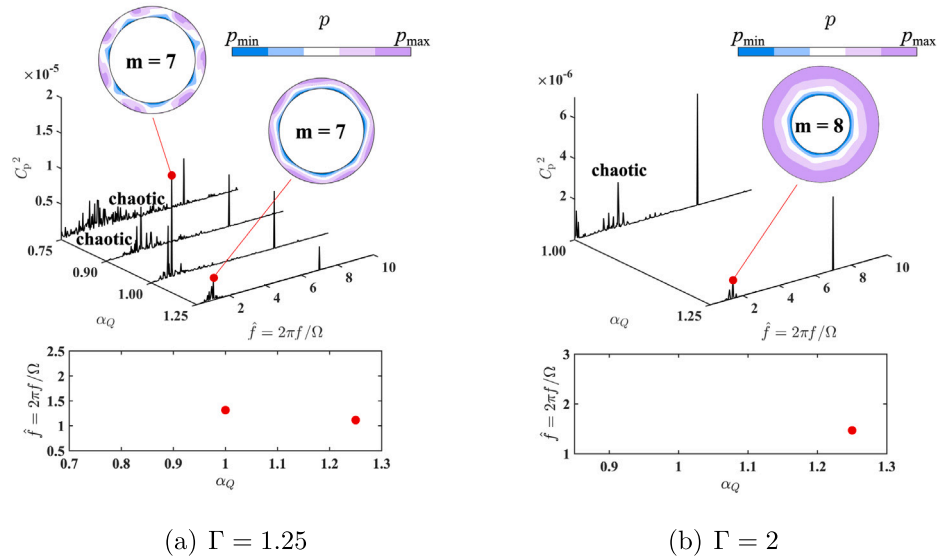

Fig. 5. Fourier analysis and stability diagram near design flow rate for (a) $\Gamma = 1.25$ and (b) $\Gamma = 2$ with idealized inflow. The identified instabilities are pictured phase averaging the URANS in a reference frame rotating with the instability propagation velocity.

of Fig. 4(b)). However, a non-linear interaction is responsible for the complex chaotic dynamics observed in the FFT by a relatively wide population of bandwidths between 2 and 3 times the inflow frequency f_{inlet}. This is consistent with the wavelet analysis, where it is observed a wide spectrum of low-intensity interactions. In frequency, they are quantitatively located correspondingly to the intermittent chaotic nonlinear interactions observed for $\Gamma = 1.25$. Ramping up the flow rate, i.e. for $\alpha_Q = 1.25$, an 8-periodic jet-wake instability is found for $\Gamma = 2$ (see Fig. 5(b)). A characterization of the stability boundaries for $\Gamma = 1.25$ and 2 is reported in Fig. 5, demonstrating by FFTs that the jet-wake instability occurs for α_Q beyond a critical value for the large-flow rate instability, i.e. $\alpha_c^{\mathrm{jet-wake}} \in [0.9,\ 1]$ for $\Gamma = 1.25$. Fig. 5 also demonstrate that the critical α_Q for the jet-wake instability shifts to $\alpha_c^{\mathrm{jet-wake}} \in [1,\ 1.25]$ for $\Gamma = 2$. This leads to the conclusion that the radius ratio Γ of the radial rings significantly impacts the flow dynamics even from the qualitative point of view, as it suppresses the primary instability even for idealized inflow conditions.

We now investigate the more realistic inflow conditions (case (ii)). When a more realistic inflow with positive leakage is considered, the jet-wake instability is supposed to occur at higher flow rates (see Fan

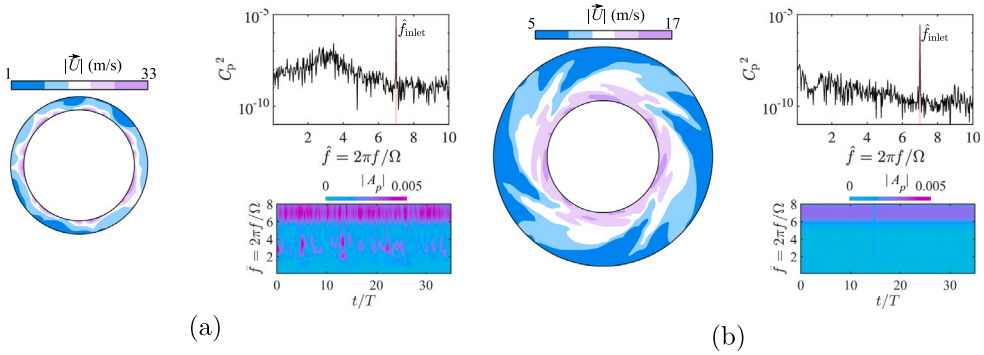

Fig. 6. Color maps of instantaneous velocity magnitude distribution at the mid-height of the diffusers (left) and Fourier and wavelet analysis results (right) for (a) $\Gamma = 1.25$ and (b) $\Gamma = 2$. All figures refer to the more realistic inflow (case (ii)) for $\alpha_Q = 1.25$. (For interpretation of the references to color in this figure legend, the reader is referred to the web version of this article.)

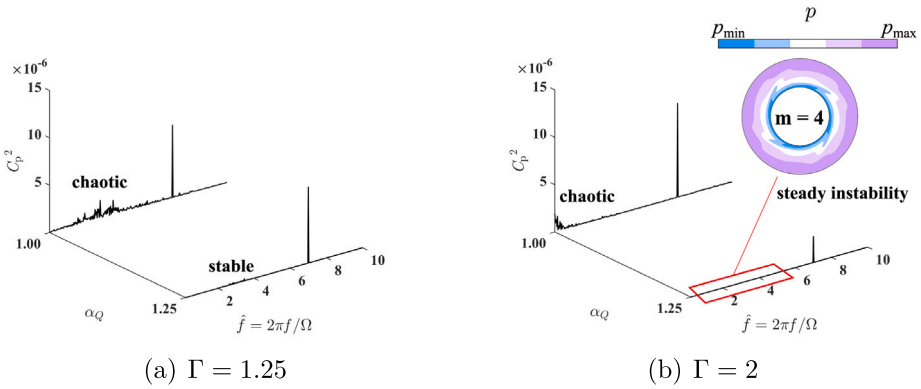

Fig. 7. Fourier analysis and stability diagram near design flow rate for (a) $\Gamma = 1.25$ and (b) $\Gamma = 2$ with realistic inflow. The identified instability for $\Gamma = 2$ is pictured phase averaging the URANS in a steady reference frame.

et al. [17]). We focus therefore on the instantaneous flow field for $\alpha_Q = 1.25$ (see Fig. 6(a)), and we observe that the instability pattern for $\Gamma = 1.25$ is not identifiable at the contrary than for the idealized case.

This is confirmed by the FFT and wavelet results, where only the 7-periodic inlet condition $2\pi f_{\text{inlet}}/\Omega = 7$ can be clearly detected for $\Gamma = 1.25$ (see the top panel of Fig. 6(b)). By subtracting the phase-averaged flow from the instantaneous pressure field in a reference frame rotating with Ω, the remaining flow field is chaotic for $\Gamma = 1.25$. This demonstrates that an entrained leakage flow for a short diffuser can suppress even the primary instability (see Fig. 7(a) for $\alpha_Q = 1$ and 1.25). This is qualitatively different than what was observed for $\Gamma = 1.5$, where a leakage only transforms the secondary instability (see Fan et al. [17]).

For $\Gamma = 2$, the FFT and wavelet analyses still cannot find any frequency other than the 7-periodic inlet $2\pi f_{\text{inlet}}/\Omega = 7$. However, an unexpected 4-periodic instability pattern can be observed in the snapshots (see Fig. 6(b) and Fig. 7(b)). By phase-averaging the flow field in a fixed reference frame after subtracting the phase-averaged flow from the instantaneous pressure field in a reference frame rotating with Ω, the instability is proven to be a 4-periodic spiraling mode (see corresponding video at https://github.com/fromano88/CentrifugalPump.git), that concentrates its energy production at the region of interaction between the boundary layers of two parallel plates (not shown). This is readily understood considering that the entrained leakage thickens the boundary layers and promotes their interaction. The resulting Kelvin–Helmholtz instability could not be observed for the idealized inflow because the boundary layers were too thin. This instability phenomenon in the source flow between two parallel rings is reported here for the first time for a 7-periodic rotating inflow.

3.3. Instabilities at low flow rate

The effect of the radial aspect ratio Γ on the low-flow-rate instability is analyzed in this section. For the idealized case at $\alpha_Q = 0.25$, 5 cells with a frequency $2\pi f_{\text{rot},m=5}/\Omega = 1.714$ rotating with an angular velocity $\omega_{\text{rot},m=5}/\Omega = 0.34$ are detected for $\Gamma = 1.25$; 3 cells with a frequency $2\pi f_{\text{rot},m=3}/\Omega = 0.714$ rotating with an angular velocity $\omega_{\text{rot},m=3}/\Omega = 0.238$ are detected for $\Gamma = 1.5$; 2 cells with a frequency $2\pi f_{\text{rot},m=2}/\Omega = 0.343$ rotating with an angular velocity $\omega_{\text{rot},m=2}/\Omega = 0.172$ are detected for $\Gamma = 2$. All such instabilities are understood as mean-core flow instabilities and well captured by the model of Tsujimoto et al. [13], as also demonstrated by Fan et al. [3]. By means of FFTs, we reconstructed the stability diagram of the three radius ratios (see Fig. 8) and identified the critical α_Q below which the mean-core-flow instability occurs. For $\Gamma = 1.25$ $\alpha_c^{\text{core-flow}} \in [0.4,\ 0.5]$, while for $\Gamma = 1.5$ $\alpha_c^{\text{core-flow}} \in [0.5,\ 0.75]$, and for $\Gamma = 2$ $\alpha_c^{\text{core-flow}} \in [0.75,\ 1]$ under idealized inflow conditions (see Fig. 8(a)).

For the more realistic inflow, the flow field of $\Gamma = 1.25$ is once again controlled by the entrained leakage that tames down the instability and gives rise to strong chaotic dynamics for all the investigated flow rates (see the top panel in Fig. 8(b)). For $\Gamma = 1.5$, 3 cells with a frequency $2\pi f_{\text{rot},m=3}/\Omega = 0.486$ rotating with an angular velocity $\omega_{\text{rot},m=3}/\Omega = 0.162$ are detected for $\alpha_Q = 0.25$. Hence, for such an intermediate Γ, no qualitative difference is observed at the lowest α_Q when leakage is entrained. However, a strong quantitative difference is reported in Fig. 8 when comparing the amplitudes of the FFTs. This points out that the leakage flow strongly reduces the amplitude of the core-flow instability. Also for realistic inflow conditions, the critical α_Q is bracketed in $\alpha_c^{\text{core-flow}} \in [0.25,\ 0.5]$ for $\Gamma = 1.5$. For $\Gamma = 2$, 3 cells with a frequency $2\pi f_{\text{rot},m=3}/\Omega = 0.343$ rotating with an angular

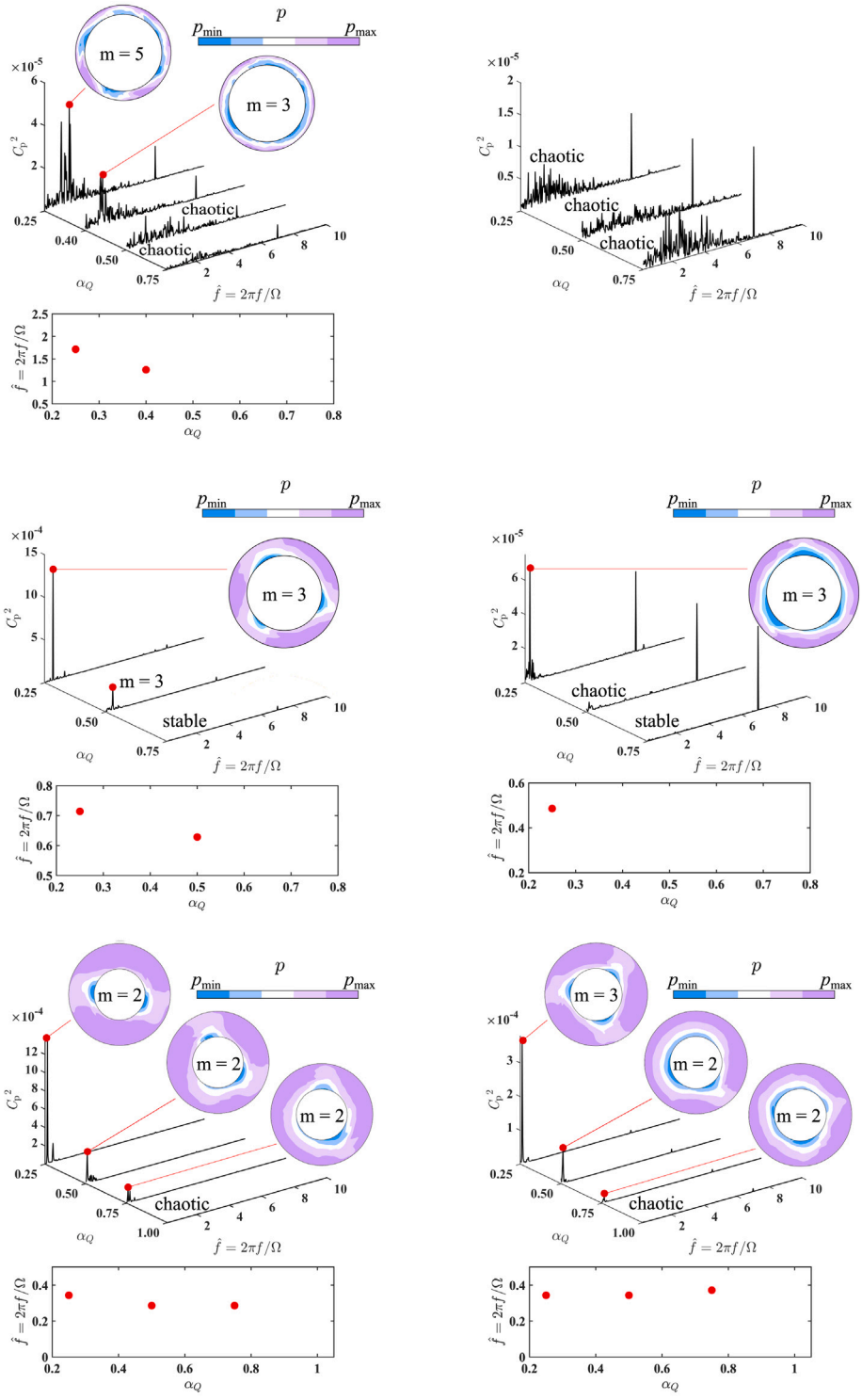

(a) idealized inflow (b) realistic inflow

Fig. 8. Fourier analysis and stability diagram at low flow rates for $\Gamma = 1.25$ (top), $\Gamma = 1.5$ (middle), and $\Gamma = 2$ (bottom) with (a) idealized and (b) realistic inflow. The identified instabilities are pictured phase averaging the URANS in a reference frame rotating with the instability propagation velocity.

velocity $\omega_{\mathrm{rot},m=3}/\Omega = 0.114$ are found when the more realistic inflow is considered for $\alpha_Q = 0.25$. This qualitative difference (2 cells for the idealized inflow and 3 cells for the more realistic inflow) can be explained by considering the linear stability analysis of the mean core flow model proposed by Tsujimoto et al. [13]. As explained in our previous paper [3], the modes $m = 2$ and 3 are both supercritical at $\alpha_Q = 0.25$. Once again, the realistic inflow condition has a significant quantitative impact on the instability amplitude, as seen by comparing

the FFTs for $\Gamma = 2$ under idealized (see Fig. 8(a)) and realistic (see Fig. 8(b)) inflows. The critical conditions are still bracketed in $\alpha_c^{\text{core-flow}} \in [0.75,\ 1]$ for $\Gamma = 2$ under realistic inflow conditions.

4. Conclusions

The radial flow between parallel rings with a jet-wake inflow periodically modulated in space and rotating at angular rate Ω was studied. We considered several different inflow conditions mainly focusing on the effect of the radial aspect ratio Γ on the instability characteristics, varying the radial aspect ratio in the range $\Gamma \in \{1.25, 1.5, 2\}$ and adjusting the constant cross-sectional aspect ratio as $\Lambda = 2(\Gamma-1)\times 3.325$.

A jet-wake instability that usually occurs at a large flow rate ($\alpha_Q \gtrsim 1$) triggers a secondary instability that has first been reported by Fan et al. [3] for $\Gamma = 1.5$. For idealized inflow conditions, the primary 7-periodic instability pattern is here reported for $\Gamma = 1.25$. However, the secondary pulsating instability detected for $\Gamma = 1.5$ does not occur for $\Gamma = 1.25$. As the radial aspect ratio Γ increases to $\Gamma = 2$, nonlinear effects take over and a complex chaotic regime hinders the quasi-periodic pattern observed with the other two smaller radial aspect ratios and shifts it to a higher α_c. For the more realistic inflow, the flow field for $\Gamma = 1.25$ is always chaotic under the effect of leakage flow. As Γ increased to $\Gamma = 1.5$, we previously found 7-periodic jet-wake instability patterns as observed for idealized inflow (case (i)). Additionally, two 1-periodic instability patterns propagate with the same propagation velocity but in opposite directions in a reference frame rotating with Ω, owing to the leakage flow (see Fan et al. [17]). For $\Gamma = 2$, a 4-periodic steady Kelvin–Helmholtz instability is reported here for the first time.

Concerning the well-known low-flow-rate ($\alpha_Q \lesssim 0.65$) mean core-flow instability, its characteristics are significantly affected by the radius aspect ratio Γ, especially in terms of the wave number, that passes from 4 to 3 and then to 2 for $\Gamma = 1.25$, 1.5, and 2, respectively, for $\alpha_Q = 0.25$. Besides, the instability mode number and propagation velocity are also found to be very sensitive to the inlet leakage flow for $\Gamma = 2$. For short diffusers, the instability is entirely suppressed by the leakage. Finally, a detailed quantification of the critical conditions is also provided in this paper for both the instability mechanisms.

Declaration of competing interest

Meng FAN reports financial support was provided by China Scholarship Council. Francesco ROMANO reports numerical resources provided by Grand Équipement Natonal e Calcul Intensif.

Data availability

Data will be made available on request.

Acknowledgments

We kindly acknowledge the GENCI (Grand Equipement National de Calcul Intensif) for the numerical resources granted to conduct this study under project A0102A01741. Furthermore, we appreciate the support of the China Scholarship Council for the doctoral students of M. Fan (CSC student number 201908320328).

Appendix. Phase-average model

To further prove that phase-averaging produces a leading-order model reduction of the URANS dynamics, we produced three videos (available at https://github.com/fromano88/CentrifugalPump.git) to compare the URANS results with the mean-flow basic state superposed to the instability mode in a steady reference frame. We demonstrate that the phase-average model (denoted by 'PAM' in the videos) obtained by summing up the large-scale basic state (phase-average of the URANS with Ω and denoted by 'BS' in the videos) and the large-scale instability mode (phase-average of the URANS with ω_{inst} after subtracting the basic state, 'Pert' in the video) is capable of capturing the key features of the large-scale dynamics in the diffuser obtained by non-phase-averaged URANS simulations (denoted by 'URANS' in the videos). This is demonstrated in three representative cases:

- Low-flow rate rotating instability for $\Gamma = 2$ and $\alpha_Q = 0.25$ under idealized inlet conditions (Movie 1).
- High-flow rate rotating instability for $\Gamma = 1.25$ and $\alpha_Q = 1$ under idealized inlet conditions (Movie 2).
- High-flow rate steady instability for $\Gamma = 2$ and $\alpha_Q = 1.25$ under realistic inlet conditions (Movie 3).

References

[1] J. Hunt, I. Torbe, Characteristics of a hydrostatic thrust bearing, Int. J. Mech. Sci. 4 (6) (1962) 503–516.
[2] C. Hu, C. Yang, X. Shi, R. Zou, L. Liu, H. Chen, Investigation of rotating stall in radial vaneless diffusers with asymmetric inflow, Aerosp. Sci. Technol. 96 (2020) 105546.
[3] M. Fan, A. Dazin, G. Bois, F. Romanò, Effect of inlet leakage flow on the instability in a radial vaneless diffuser, Phys. Fluids 35 (1) (2023) 014105.
[4] Y. Qin, J. Chen, X. Zhao, D. Liao, R. Mu, S. Wang, H. Wu, H. Guo, Transcatheter closure of perimembranous ventricular septal defect using a modified double-disk occluder, Am. J. Cardiol. 101 (12) (2008) 1781–1786.
[5] T. Hagiwara, Studies on the characteristics of radial-flow nozzles: (1 st report, theoretical analysis of outward flow), Bull. JSME 5 (20) (1962) 656–663.
[6] L. Licht, D. Fuller, A preliminary investigation of an air-lubricated hydrostatic thrust bearing, Am. Soc. Mech. Engrs (1954) 54–Lub–18.
[7] H.W. Woolard, A Study of the Flow in a Narrowly-Spaced Radial Diffuser (Ph.D. thesis), State University of New York, Buffalo, 1954.
[8] S. Wilson, A note on laminar radial flow between parallel plates, Appl. Sci. Res. 25 (1972) 349–354.
[9] E. Bakket, J. Kreider, F. Kreith, Turbulent source flow between parallel stationary and co-rotating disks, J. Fluid Mech. 58 (2) (1973) 209–231.
[10] J.-L. Peube, Sur L'Ecoulement radial permanent d-un fluide viszuex incompressible entre deux plans paralleles fixes, J. Mec. 2 (4) (1963) 377–395.
[11] S. Mochizuki, S. Yamada, H. Osaka, Management of a plane turbulent wall jet by the large-eddy break-up device, JSME Int. J. Ser. B Fluids Therm. Eng. 49 (4) (2006) 921–927.
[12] W. Jansen, Rotating stall in a radial vaneless diffuser, J. Fluid Eng. (1964).
[13] Y. Tsujimoto, Y. Yoshida, Y. Mori, Study of vaneless diffuser rotating stall based on two-dimensional inviscid flow analysis, J. Fluids Eng. 118 (1996) 123–127.
[14] G. Pavesi, A. Dazin, G. Cavazzini, G. Caignaert, G. Bois, G. Ardizzon, Experimental and numerical investigation of unforced unsteadiness in a vaneless radial diffuser, in: European Turbomachinery Conference, EUROTURBO, 2011.
[15] A. Dazin, O. Coutier-Delgosha, P. Dupont, S. Coudert, G. Caignaert, G. Bois, Rotating instability in the vaneless diffuser of a radial flow pump, J. Therm. Sci. 17 (2008) 368–374.
[16] A. Dazin, G. Cavazzini, G. Pavesi, P. Dupont, S. Coudert, G. Ardizzon, G. Caignaert, G. Bois, High-speed stereoscopic PIV study of rotating instabilities in a radial vaneless diffuser, Exp. Fluids 51 (2011) 83–93.
[17] M. Fan, A. Dazin, G. Bois, F. Romanò, Instabilities in a turbulent swirling source flow between parallel rings, Phys. Fluids (2023) (accepted).
[18] S. Ljevar, H.C.D. Lange, A.A.V. Steenhoven, Two-dimensional rotating stall analysis in a wide vaneless diffuser, Int. J. Rotating Mach. 2006 (2006) 056420.
[19] S. Shah, S. Jain, R. Patel, V. Lakhera, CFD for centrifugal pumps: a review of the state-of-the-art, Procedia Eng. 51 (2013) 715–720.
[20] A. Posa, A. Lippolis, A LES investigation of off-design performance of a centrifugal pump with variable-geometry diffuser, Int. J. Heat Fluid Flow 70 (2018) 299–314.
[21] B. Kim, M.H. Siddique, S. Bellary, S.-W. Choi, D.-E. Lee, et al., Investigation of a centrifugal pump for energy loss due to clearance thickness while pumping different viscosity oils, Results Eng. 18 (2023) 101038.
[22] L. Gibson, L. Galloway, S. Spence, et al., Assessment of turbulence model predictions for a centrifugal compressor simulation, J. Glob. Power Propul. Soc. 1 (2017) 142–156.
[23] J.F. Oro, R.B. Perotti, M.G. Vega, J. Gonzalez, Effect of the radial gap size on the deterministic flow in a centrifugal pump due to impeller-tongue interactions, Energy 278 (2023) 127820.
[24] M. Fan, A. Dazin, G. Bois, F. Romanò, Instabilities identification based on a new centrifugal 3D impeller outflow model, Aerosp. Sci. Technol. (2023) 108466.
[25] M. Fan, A. Dazin, F. Romano, G. Bois, Effect of leakage on the performance of the vaneless diffuser of a centrifugal pump model, in: Conference on Modelling Fluid Flow (CMFF'22), Budapest, Hungary, 2022, pp. 51–58.

Appendix D

Extended French summary

Fondement de la recherche. Les turbomachines sont largement utilisées dans divers secteurs tels que l'approvisionnement en eau [3], l'aviation [4], le transport maritime [5], et la climatisation [6]. Cependant, la capacité opérationnelle des turbomachines est limitée par des écoulements internes instables. Un exemple marquant de ces instabilités est le décrochage tournant d'un compresseur ou d'une pompe. Le décrochage tournant a des conséquences indésirables telles que le bruit [7], les vibrations [8], les dommages mécaniques [9], et une performance réduite [10], et doit être évité. Afin d'élargir le champ d'application, il est essentiel d'améliorer la compréhension de la dynamique des écoulements liés au mécanisme du décrochage tournant en tant que première étape pour le contrôle.

Le champ d'écoulement au sein des machines centrifuges est plutôt complexe en raison d'une large gamme d'échelles temporelles et spatiales, ainsi que de l'apparition d'instabilités de l'écoulement [13]. Pendant les conditions de fonctionnement normales, l'écoulement d'air à travers le compresseur est essentiellement stable et périodique dans le système de coordonnées tournant. Cependant, la plage de fonctionnement des compresseurs centrifuges est significativement limitée par l'apparition de deux instabilités à faibles débits massiques : le décrochage tournant et le pompage [14]. Le pompage du compresseur centrifuge se produit en raison d'un décrochage de l'étage, qui peut être décrit soit comme un décrochage collectif de plusieurs éléments du compresseur, soit comme un décrochage intense d'un seul composant. De telles instabilités conduisent généralement à d'importantes vibrations et à des niveaux sonores élevés. Une exploitation prolongée dans de telles conditions défavorables peut entraîner une défaillance mécanique. Bien que l'instabilité dans les turbomachines ait fait l'objet d'études approfondies dans la littérature, peu d'efforts ont été consacrés au décrochage tournant

dans les compresseurs centrifuges par rapport au décrochage dans les compresseurs axiaux. De plus, l'induction du décrochage tournant dans les compresseurs centrifuges est généralement plus complexe en raison des différents types de décrochage tournant. En fonction de l'endroit où le décrochage se produit, le décrochage tournant dans les compresseurs centrifuges peut être grossièrement classifié comme décrochage tournant de la roue et du diffuseur, pouvant être ensuite subdivisé en décrochage tournant du diffuseur aubés et du diffuseur lisse. L'occurrence du décrochage tournant dans les roues et les diffuseurs aubés présente des similitudes avec le décrochage tournant dans les compresseurs axiaux, car il est causé par un angle d'attaque positif excessif. Cependant, dans le cas des diffuseurs lisses, où les aubes sont absentes, le mécanisme derrière le décrochage tournant ne peut être expliqué uniquement par le concept de l'angle d'attaque. Comprendre la dynamique des écoulements et les mécanismes sous-jacents du décrochage tournant est crucial pour la conception et le fonctionnement de machines centrifuges efficaces et fiables.

Les diffuseurs des machines centrifuges sont spécifiquement conçus pour convertir l'énergie cinétique à grande vitesse du fluide quittant la roue en une augmentation de la pression statique, en élargissant progressivement la zone d'écoulement et en ralentissant la vitesse du fluide. Les diffuseurs lisses sont largement utilisés dans les compresseurs de process, les compresseurs frigorifiques et les turbocompresseurs automobiles en raison de leur large plage de fonctionnement et de leur faible coût. En règle générale, le diffuseur lisse nécessite un grand rapport de rayon en raison de son faible rapport de diffusion [16]. Le diffuseur lisse présente une récupération de pression inférieure de 20% et une efficacité d'étage inférieure de 10% par rapport à un diffuseur aubé classique [17]. Cependant, l'absence d'aubes dans un diffuseur réduit réduit les perturbations de l'écoulement causées par l'interaction entre l'écoulement du fluide et les aubes et permet une décélération sans risque de désadaptation avec une conception simple qui est plus résistante à la corrosion et à l'encrassement qu'un diffuseur aubé. Pour ces raisons, ils sont souvent préférés aux diffuseurs aubés qui permettent une récupération à haute pression mais dont la plage de fonctionnement est limitée. En même temps, l'absence d'aubes directrices réduit la capacité des diffuseurs lisses à contrôler l'angle d'écoulement α (défini comme l'angle entre la trajectoire de l'écoulement et la direction tangentielle) et favorise une distribution uniforme de l'écoulement. Par conséquent, les diffuseurs lisse sont plus sensibles aux instabilités de l'écoulement et au décrochage tournant que les diffuseurs à aube. Le décrochage tournant du diffuseur est le type de décrochage le plus courant dans les compresseurs centrifuges. Bien que le décrochage

tournant ait été étudié sous de nombreux aspects, certains des mécanismes de l'instabilité et leurs effets sur le comportement du diffuseur sont encore inconnus. Il n'y a pas d'accord uniforme sur les mécanismes conduisant au décrochage rotatif. Pour les raisons susmentionnées, cette étude se concentre uniquement sur le décrochage rotatif des diffuseur lisses, dans le but de faire la lumière sur la physique sous-jacente de l'instabilité.

Bien que le décrochage tournant du diffuseur lisse ait été largement étudié sous de nombreux aspects tels que ceux énumérés ci-dessus (mécanismes, caractéristiques, influences, contrôle, etc.), la distinction entre un diffuseur épais et un diffuseur étroit entraînant des mécanismes d'instabilité différents n'est toujours pas claire. De plus, de nombreuses études ont montré que plusieurs modes instables peuvent coexister dans un diffuseur lisse dans une plage de fonctionnement donnée. Les analyses de stabilité linéaire bidimensionnelles précédentes ne peuvent pas prendre en compte les interactions entre ces modes et sont limitées aux conditions critiques. De plus, l'effet de l'écoulement asymétrique et les caractéristiques du sillage du jet sur l'instabilité ne sont pas entièrement étudiés. En fonction des raisons évoquées ci-dessus, les objectifs et les approches de ce travail sont énumérés comme suit:

(1) Réaliser de nouvelles expériences pour tester les performances de l'ensemble de la machine et deu diffuseur seul, qui serviront de base à la vérification des travaux de simulation numérique ultérieurs.

(2) Réaliser des simulations numériques pour l'ensemble de la machine centrifuge dans OpenFOAM afin d'étudier l'effet du débit de fuite et des rapports de rayon du diffuseur sur les performances de la machine et les caractéristiques d'instabilité dans le diffuseur.

(3) Développer un modèle tridimensionnel d'ordre réduit basé sur une approche d'ajustement de correspondance d'échelle qui prend en compte l'effet de couche limite pour une étude paramétrique abordable afin de tester les effets des écoulements d'entrée asymétriques sur l'instabilité dans le diffuseur.

(4) Comparer les résultats de l'analyse de stabilité linéaire bidimensionnelle avec les solutions non linéaires de la simulation numérique bidimensionnelle et les simulations tridimensionnelles pour notre modèle d'ordre réduit afin d'analyser les modes instables associés aux différents mécanismes d'instabilité qui coexistent dans un diffuseur lisse.

Appareil expérimental. Le dispositif expérimental composé d'une roue radiale et d'un diffuseur, sans volute est illustré à la Fig. 2.1(a). Ce cas d'essai expérimental, qui comprend une roue et un diffuseur mais pas de volute, a été spécialement conçu pour fournir un accès optique expérimental à l'analyse des écoulements instationnaires et présente une condition limite de pression de sortie constante bien définie, comme décrit précédemment par Fan et al.[47], Wuibaut et al. [48] et Dazin et al.[10]. Un réservoir d'entrée équipé de diaphragmes remplaçables (avec différents diamètres d'entrée) est placé en haut du tuyau d'aspiration pour contrôler le débit Q. Parallèlement, un nid d'abeille est installé au bas du réservoir pour stabiliser l'écoulement d'air avant qu'il ne pénètre dans le tuyau d'aspiration.

Par rapport aux conceptions conventionnelles des machines radiale, cet arrangement diffère par l'absence de carter reliant l'entrée du diffuseur et la sortie du tuyau d'entrée, c'est-à-dire que la roue n'a pas de carter. La pression statique de sortie étant maintenue aux conditions atmosphériques, le jeu radial entre l'entrée fixe du diffuseur et la sortie rotative de la roue de ce banc d'essai admet un débit de fuite positif. Par conséquent, toutes les pressions statiques locales à l'intérieur de la pompe restent inférieures à la pression atmosphérique.

Pour évaluer l'impact du décrochage tournant, les performances de l'ensemble de la machine et du diffuseur seul sont mesurées. La pression statique dans le tuyau d'aspiration est calculée en faisant la moyenne des données obtenues par quatre sondes de pression placées uniformément sur une circonférence ($P_{s1} - P_{s4}$), comme l'illustre la Fig. 2.1(a). Par conséquent, les performances de l'ensemble de la machine sont caractérisées par la variation de la pression statique entre le tuyau d'aspiration (P_s) et la sortie du diffuseur. En outre, neuf prises de pression statique sont équipées de chasse d'eau le long d'une ligne radiale (espacée régulièrement de $r = 264\,\text{mm}$ à $r = 384\,\text{mm}$) sur la paroi de l'enveloppe du diffuseur. Les performances du diffuseur sont donc caractérisées par la récupération de la pression entre l'entrée et la sortie du diffuseur. L'incertitude des mesures de pression statique ci-dessus est est estimée à $\pm 2\,\text{Pa}$.

La fluctuation transitoire de la pression est mesurée par deux microphones à condensateur (Brüel & Kjaer, Type 4135)) montés affleurant à la même position radiale ($r = 320\,\text{mm}$) avec un décalage angulaire de $\Delta\theta = 60\,^\circ$ sur la paroi de l'enveloppe du diffuseur. Le LMS Test Xpress (SIEMENS, Munich, Allemagne) est utilisé pour acquérir des données sur une durée totale de 600 s, avec une fréquence d'échantillonnage de 4096 Hz. L'incertitude de la mesure ci-dessus est estimée à moins

de 1%. De plus amples détails sur le dispositif expérimental peuvent être trouvés dans des études antérieures [39, 10] qui ont utilisé le même appareil. Les mesures de pression instable seront utilisées pour effectuer la FFT et l'analyse par ondelettes.

Les expériences ont été réalisées dans l'air avec une vitesse de rotation constante $N = 1200$,rpm (c'est-à-dire $\omega_{\text{imp}} = 125$,rad/s). Le débit passe d'un état stable à un état instable $Q/Q_{\text{d}} \in [0,26,\ 1,53]$, où Q représente les débits réels mesurés au niveau de la conduite d'aspiration et Q_{d} représente le débit de conception.

Géométries. Pour étudier l'écoulement dans un diffuseur lisse, on considère une pompe centrifuge tridimensionnelle. La géométrie du modèle numérique correspond à la config uration expérimentale (voir détails dans Sec.2.1), qui correspond à un modèle d'air agrandi appelé pompe de la Société Hydrotechnique de France (SHF). La Fig. 2.2 représente la configuration tridimensionnelle composée d'un tuyau d'aspiration (jaune), d'une roue centrifuge (grise), d'un diffuseur radial sans vannes (vert foncé) et d'une boîte d'écoulement (vert clair) attachée au domaine du diffuseur pour éviter que les conditions limites d'écoulement ne soient fixées trop près de la machine. Les conditions limites de vitesse d'entrée sont données au sommet du tuyau d'aspiration circulaire d'une longueur de $H_c = 10R_1$, où R_1 représente le rayon d'entrée de l'extrémité de la roue R_1. Les conditions limites de sortie de la pression statique sont fixées aux limites de la boîte de sortie avec une hauteur de $H_b = 15b_3$ et un rayon de $R_b = 3R_4$. Afin d'inspecter l'effet des fuites sur le champ d'écoulement du diffuseur radial sans vannes, trois configurations de fuites différentes sont étudiées. En fonction de la direction de l'écoulement de fuite entrant dans la machine, on parle de cas de fuite nulle, négative et positive (voir les détails à la Sec. 2.2.1.1).

Pour effectuer une analyse paramétrique de l'écoulement dans le diffuseur sans palette à un coût de calcul abordable, une simulation d'ordre réduit est proposée. Ce modèle ne comprend ni la conduite d'aspiration ni la roue centrifuge, c'est-à-dire que seuls les domaines du diffuseur lisses et le domaine externe en aval du diffuseur sont simulés (voir Fig. 2.3). La condition limite d'écoulement est donnée par l'ajustement du profil de vitesse d'entrée du diffuseur moyenné azimutalement, obtenu à partir de la simulation complète de la machine, et par la superposition d'un mode de Fourier (voir les détails à la Sec.2.3.3).

Pour étudier l'instabilité de l'écoulement central dans le diffuseur lisse, l'écoulement bidimensionnel à mi-hauteur du diffuseur avec un rapport d'aspect radial fini $\Gamma = R_4/R_3$ (comme représenté sur la

Fig. 2.4) est modélisé. En se basant sur l'hypothèse que l'écoulement est bidimensionnel, la largeur du diffuseur n'est pas prise en compte ici, c'est-à-dire que l'effet des couches limites de la paroi est négligé. L'analyse de stabilité linéaire et les simulations URANS sont effectuées sur ce modèle avec un écoulement homogène en θ auquel on supperpose un écoulement qui imite le jet/sillage (voir les détails dans la Sec.2.3.3).

Configurations numériques. Comme démontré dans l'annexe A, le modèle $k-\omega$ SST est l'approche la plus appropriée pour simuler l'écoulement dans le diffuseur. En outre, l'efficacité, la robustesse et l'efficience du modèle $k-\omega$ SST ont été mises en évidence dans plusieurs simulations de machines centrifuges dans la littérature, comme le démontrent de nombreux exemples [49, 50, 51, 52, 53].

Les maillages hexaédriques sont choisis dans cette étude en raison de leur grande précision, efficacité, stabilité et facilité de post-traitement. Pour les simulations bidimensionnelles, la fonctionnalité `blockmesh` dans OpenFOAM est utilisée pour le maillage. Le maillage est construit à travers un ensemble de blocs hexaédriques dans `blockmesh` en plaçant les sommets, en créant des blocs et en définissant les faces avec la bonne orientation [55].

Pour chaque bloc et dans chaque direction, le nombre de cellules et le rapport d'expansion (le rapport des longueurs des premières et dernières cellules) peuvent être personnalisés. Le maillage bidimensionnel dans `blockmesh` peut être réalisé en spécifiant une cellule dans la direction axiale (voir Fig. 2.5). Pour la simulation de l'ensemble de la machine, la génération du maillage devient une tâche plus complexe en raison de la géométrie complexe des surfaces des aubes et des passages d'écoulement de la roue centrifuge. Le logiciel commercial ICEM CFD est utilisé pour générer un tel maillage complexe. Le maillage généré par ICEM CFD est exporté au format `msh` puis converti en OpenFOAM par la fonctionnalité `fluent3DmeshToFoam`. Comme mentionné précédemment, une longue partie du tuyau d'aspiration et une boîte de sortie sont simplement incluses pour éviter que les conditions aux limites d'entrée/sortie soient placées trop près de la machine; le maillage dans ces deux régions est plus grossier. D'autre part, le maillage dans la partie courte du tuyau d'aspiration, de la roue centrifuge et des régions du diffuseur est plus fin comme illustré dans la Fig. 2.6. Un exemple de maillage représenté dans la Fig. 2.6 correspond au cas idéal (pas de fuite entre la roue et le diffuseur). Pour garantir que le maillage capture avec précision la physique des écoulements, le maillage est raffiné en utilisant un rapport d'expansion de 1.5 dans la direction normale aux parois pour maintenir les valeurs

de y^+ proches de 1 près des parois du court tuyau d'aspiration, de la roue centrifuge et du diffuseur sans aube. Nous soulignons en outre que la valeur maximale de y^+ est inférieure à 1 dans les zones d'intérêt (sur toute la paroi du diffuseur et sur la plupart des aubes de la roue). Pour les simulations tridimensionnelles réduites, le maillage est également généré en utilisant la fonctionnalité `blockmesh`, puisque la région complexe de la roue est exclue. Les paramètres (nombre de cellules et le rapport d'expansion) se réfèrent au même réglage dans ICEM CFD. Afin de déterminer si la solution dépend du maillage, des calculs de test sont effectués pour l'ensemble de la machine avec quatre résolutions de grille différentes. Le Tab. 2.2 présente une comparaison de la différence de pression statique moyenne pondérée par la masse prédite (PSI) entre l'entrée du tuyau d'aspiration et la sortie du diffuseur de la machine centrifuge au débit de conception Q_{d}, en utilisant différentes résolutions de grille. Alors que la taille de la grille passait de 618k cellules (Grille 1) à ≈1.1M cellules (Grille 2), l'erreur relative dans la performance prédite de la pompe augmentait mais diminuait ensuite à 0,93% pour 2,3M cellules (Grille 3). Par conséquent, une taille de maillage de 2,3M de volumes finis a été choisie pour les simulations numériques de l'ensemble de la machine dans notre étude. Pour les simulations bidimensionnelles et tridimensionnelles à ordre réduit, la taille du maillage est adaptée par rapport à la configuration avec la machine complète.

OpenFOAM, un logiciel open-source écrit en C++, a été utilisé dans cette étude. Les simulations numériques sous OpenFOAM emploient des schémas de discrétisation en volumes finis pour résoudre les équations de Navier-Stokes incompressibles sur un maillage informatique. Les solveurs `simpleFoam` et `pimpleFoam` d'OpenFoam v19212 ont été utilisés respectivement pour les simulations RANS et URANS. OpenFOAM utilise des solveurs linéaires pour un système d'équations et ceux-ci se divisent en 4 types : Gradient conjugué préconditionné (bi-) (PCG/PBiCG), solveur lisse, multi-grille géométrique-algébrique généralisée (GAMG) et solveur diagonal pour les systèmes explicites (diagonal) [56]. L'équation de correction de pression est résolue en utilisant l'algorithme GAMG. Les équations de vitesse et de turbulence sont résolues à l'aide du smoothSolver. Le lisseur Gauss-seidel est utilisé pour le lissage multi-grille. Les facteurs de sous-relaxation sont utilisés afin d'améliorer la stabilité du calcul et les niveaux de résidu sont contrôlés en réglant les tolérances de solution. Pour coupler la pression et la vitesse, l'algorithme SIMPLE (Méthode Semi-Implicite pour les Équations Liées à la Pression) est appliqué pour les calculs en régime permanent, tandis que l'algorithme PIMPLE (PISO/SIMPLE) est appliqué pour les calculs transitoires. Ce dernier est un algorithme hybride qui combine des carac-

téristiques des algorithmes SIMPLE et PISO (Pressure-Implicit with Splitting of Operators), alternant entre une approche ségrégée (similaire à SIMPLE) et une approche couplée (similaire à PISO) pour améliorer la convergence et la stabilité. Les termes de discrétisation temporelle sont discrétisés en utilisant un schéma de différenciation `backward` du second ordre dans OpenFOAM pour les simulations URANS. Les termes de gradient sont discrétisés en utilisant le schéma du premier ordre `Gauss linear`. Les termes de convection des équations de mouvement sont discrétisés en utilisant le schéma précis du second ordre `Gauss linear upwind`. Les termes laplaciens sont discrétisés en utilisant le schéma conservateur du second ordre `Gauss linear corrected` et pour les termes d'interpolation, les schémas d'interpolation `linear` sont employés pour calculer les valeurs aux faces ou interfaces de cellules à l'intérieur d'un maillage informatique.

Conditions limites. Pour la simulation bidimensionnelle, une condition aux limites utilisée pour spécifier une valeur fixe à une frontière d'un domaine de calcul, dénommée `codedFixedValue` dans OpenFOAM, est adoptée pour l'entrée. Cette condition aux limites est mise en œuvre à l'aide d'un code défini par l'utilisateur, ce qui permet une plus grande flexibilité et personnalisation par rapport aux autres conditions aux limites intégrées. La vitesse tangentielle moyenne est spécifiée comme $\overline{U}_\theta = \omega_{\mathrm{imp}} R_2$, et la vitesse radiale est spécifiée comme $\overline{U}_r = Q/2\pi R_2 b_2$ correspondant à une valeur prédéfinie du débit d'entrée Q. De plus, une perturbation de la structure du sillage du jet est approximativement imitée en superposant un mode de Fourier périodique m_{F} dans la direction circonférentielle, qui n'est pas inclus dans l'analyse de stabilité linéaire (voir Fig. 2.7 pour un exemple):

$$U_r(\theta) = \overline{U}_r \cdot \{1 + A_{\mathrm{inlet}} \cos[m_{\mathrm{F}}(\theta - \omega_{\mathrm{imp}} t)]\}, \tag{D.1a}$$

$$U_\theta(\theta) = \overline{U}_\theta \cdot \{1 + A_{\mathrm{inlet}} \sin[m_{\mathrm{F}}(\theta - \omega_{\mathrm{imp}} t)]\}, \tag{D.1b}$$

où A dénote l'amplitude du mode de Fourier et m est son nombre d'onde. Pour la sortie, une condition aux limites utilisée pour spécifier une valeur constante d'un domaine de calcul, nommée `fixedValue` dans OpenFOAM, est utilisée avec la pression statique $p = 0\,\mathrm{Pa}$. Pour la simulation tridimensionnelle de la machine entière, une condition aux limites qui peut être utilisée pour imposer un débit volumétrique fixe à une frontière d'entrée d'un domaine de calcul, nommée `flowRateInletVelocity` dans OpenFOAM, est adoptée pour l'entrée. Pour la sortie, une condition aux limites permettant un écoulement bidirectionnel à travers la frontière (une combinaison des conditions aux limites d'entrée et de sortie), nommée `inletOutlet`, est employée avec la pression statique réglée à 0 Pa dans la boîte de sortie. Cette condition aux limites est couramment utilisée lorsque l'écoulement à travers la frontière

n'est pas complètement développé et que la direction de l'écoulement peut changer. La routine `noSlip` dans OpenFOAM est utilisée pour les parois fixes, tandis que la routine `rotatingWallVelocity` est employée pour les parois tournantes afin de spécifier la vitesse de rotation constante de l'impulseur. Les interfaces entre différentes régions du domaine de calcul sont couplées par la routine `cyclicAMI`. En assurant la conservation de la masse et de la quantité de mouvement, la routine `cyclicAMI` garantit que le fluide s'écoule de manière fluide entre deux régions connectées par une interface tournante ou oscillante. Les routines OpenFOAM utilisées pour toutes les conditions aux limites dans la simulation tridimensionnelle de la machine entière sont listées en détail dans le Tab. 2.4. L'énergie cinétique turbulente k et le taux de dissipation spécifique turbulent ω à l'entrée sont calculés par:

$$k_{\text{in}} = \frac{3}{2}(I|u_{\text{ref}}|)^2, \tag{D.2}$$

$$\omega_{\text{in}} = \frac{k_{\text{in}}^{0.5}}{C_{\mu}^{0.25} l}, \tag{D.3}$$

où u_{ref} désigne la vitesse de référence déterminée à partir de la vitesse radiale à l'entrée du tuyau d'aspiration, I désigne l'intensité de la turbulence définie comme suit:

$$I = 0.16(Re)^{-\frac{1}{8}}, \tag{D.4}$$

C_{μ} est une constante empirique spécifiée dans le modèle de turbulence, égale à 0,09, et l est la longueur de turbulence déterminée à l'aide du diamètre du tuyau d'aspiration dans nos simulations. Pour la condition limite du modèle de turbulence le long des parois, nous fixons

$$k_{\text{wall}} = 0, \tag{D.5}$$

$$\omega_{\text{wall}} = \frac{60\nu}{0.075} y_1^2, \tag{D.6}$$

où y_1 représente la distance entre le centre de la première cellule et le mur le plus proche [55]. Nous soulignons que les propriétés caractéristiques de la turbulence ne sont pas mesurées dans les expériences, elles ne peuvent donc pas être reproduites exactement dans les simulations. Cependant, la robustesse de notre solution numérique est validée par comparaison avec les mesures expérimentales (voir les sections suivantes pour une discussion détaillée). Cela nous permet de conclure que l'écoulement n'est pas trop sensible aux caractéristiques de turbulence à l'entrée, étant donné qu'un bon accord entre les calculs numériques et les expériences est obtenu même si les grandeurs turbulentes ne sont pas parfaitement fixées à l'entrée du domaine. Pour la simulation tridimensionnelle

d'ordre réduit, seuls le diffuseur et la boîte contenant le domaine aval sont simulés, comme décrit précédemment. Les conditions aux limites de la sortie et des parois du diffuseur restent cohérentes avec l'ensemble des paramètres de simulation de la machine. Pour la condition limite d'écoulement en entrée de diffuseur, les profils de vitesse moyenne azimutale des trois composantes de vitesse ($\overline{U}_r(z)$, $\overline{U}_\theta(z)$, et $\overline{U}_z(z)$) à la sortie de la roue, dérivés des simulations numériques, sont ajustés à des fonctions analytiques explicites puis insérées avec un mode de Fourier m-périodique dans OpenFOAM par la routine `codedFixedValue`:

$$U_r(\theta, z) = \overline{U}_r(z) \cdot \{1 + A_{\text{inlet}} \cos[m_{\text{F}}(\theta - \omega_{\text{imp}} t)]\}, \tag{D.7a}$$

$$U_\theta(\theta, z) = \overline{U}_\theta(z) \cdot \{1 + A_{\text{inlet}} \sin[m_{\text{F}}(\theta - \omega_{\text{imp}} t)]\}, \tag{D.7b}$$

$$U_z(\theta, z) = \overline{U}_z(z) \cdot \{1 + A_{\text{inlet}} \cos[m_{\text{F}}(\theta - \omega_{\text{imp}} t)]\}, \tag{D.7c}$$

le déphasage entre les vitesses radiales et axiales ($\sim \cos(m_{\text{F}}\theta)$) par rapport à la vitesse tangentielle ($\sim \sin(m_{\text{F}}\theta)$) est motivé par l'équation de continuité à un seul mode de Fourier en coordonnées cylindriques. Pour équilibrer la précision numérique et le coût global du calcul, un pas de temps $\Delta t = \Delta\theta/(2\pi\omega_{\text{imp}}) \times 2\pi/180°$ correspondant à $\Delta\theta = 0,5°$ de la révolution de la roue, a été choisi. Le pas de temps Δt conduit à un déplacement angulaire du maillage inférieur à la moitié d'une cellule de la grille à l'interface rotor-stator et se traduit par un nombre de Courant moyen pour l'ensemble du domaine de $\overline{C} = 0,0075$ pour toutes nos simulations au débit nominal. Plusieurs études bibliographiques [57] soutiennent l'utilisation de $\Delta\theta \leq 1°$, ce qui est cohérent avec notre choix. En mettant l'accent sur les instabilités entièrement développées dans le diffuseur, la phase de démarrage de la machine est exclue en initialisant les simulations URANS avec les résultats de simulation RANS correspondants (simulés pour 10000 pas de temps). Pour s'assurer que tous les résultats présentés sont dans des conditions de développement complet, un long temps de simulation physique $t_{\text{fin}} = 70T$ (où T représente une période de révolution de la roue) est fixé pour toutes les simulations URANS afin de résoudre la gamme des basses fréquences, étant donné que la vitesse de rotation de la roue est supérieure à la vitesse de propagation des instabilités qui nous intéressent dans cette étude.

Approche adaptée. Une approche de simulation simplifiée est proposée pour permettre une étude paramétrique de l'écoulement dans le diffuseur à un coût de calcul abordable. Afin de modéliser l'écoulement d'entrée du diffuseur, un protocole d'ajustement paramétrique sera utilisé, basé sur trois

hypothèses sous-jacentes:

- Le protocole d'ajustement suppose que les conditions d'écoulement à l'entrée du diffuseur peuvent être extraites des résultats de simulation RANS moyennés uniquement dans la direction tangentielle pour plusieurs débits.

- On suppose implicitement qu'il n'y a pas d'interactions mutuelles entre une roue et le diffuseur en ce qui concerne les instabilités de rotation. Cette hypothèse est également motivée par l'étude des instabilités d'écoulement [2], dont le mécanisme est lié au comportement de l'écoulement uniquement à l'intérieur du diffuseur lui-même.

- Les trois composantes de la vitesse à la sortie de la roue seront ajustées avec des fonctions analytiques explicites.

Pour reproduire les conditions limites d'entrée, le profil de vitesse d'entrée du diffuseur est ajusté en fonction du débit $hatQ = Q/Q_d$, en utilisant les résultats de la simulation RANS comme base de données d'ajustement. Nous commençons par ajuster les profils d'écoulement moyennés azimutalement à l'entrée du diffuseur. Pour ajuster le profil de vitesse d'entrée dépendant de z $\vec{U}(z)$, la plage complète $z \in [-b_3/2, b_3/2]$ est subdivisée en deux régions de couche limite et une région d'écoulement en vrac (voir Fig.2.3(b)). L'ajustement a été construit selon une logique de correspondance d'échelle, en commençant par les effets d'ordre principal avec les gradients les plus élevés (les couches limites ont la plus grande sensibilité), puis les effets d'ordre principal avec des gradients plus faibles (région de l'écoulement) et enfin les effets d'ordre supérieur (oscillations). En d'autres termes, nous faisons correspondre une échelle par étape d'ajustement, puis nous faisons correspondre toutes les échelles dans la dernière étape. Nous insistons sur le fait que notre approche nous permet d'inclure la couche limite, qui est la clé pour préserver la physique du modèle. Les deux régions limites sont ajustées avec une fonction de loi de puissance, et leur épaisseur δ_i est déterminée numériquement en trouvant la longueur qui permet d'ajuster au mieux la couche limite. La composante de vitesse $U_*(z)$, où $*$ désigne la direction r, θ, et z, est approximée par des dépendances fonctionnelles dédiées à l'intérieur

de chaque région conformément à

$$\text{Région frontalière 1,} \qquad z \in [z_{\min}, z_{\min}+\delta_1]: \quad U_* \approx a_{*0}\left(\frac{b_3}{2}+z\right)^{a_{*1}}, \tag{D.8a}$$

$$\text{Région frontalière 2,} \qquad z \in [z_{\max}-\delta_2, z_{\max}]: \quad U_* \approx b_{*0}\left(\frac{b_3}{2}-z\right)^{b_{*1}}, \tag{D.8b}$$

$$\text{Région d'écoulement en vrac,} \qquad z \in [z_{\min}+\delta_1, z_{\max}-\delta_2]: \quad U_* \approx U_*^{\text{bulk}}(z), \tag{D.8c}$$

où l'épaisseur des régions de la couche limite δ_i est spécifiée pour différents cas, h représente la largeur du diffuseur, a_{*0} et b_{*0} sont des coefficients d'ajustement, $U_*^{\text{bulk}}(z) = \sum_{i=1}^{n} U_*^{\text{bulk,i}}(z)$ consiste en la somme d'une fonction linéaire, quadratique, puissance 4 et/ou trigonométrique, comme indiqué ci-dessous. Pour plus de détails, nous nous référons à notre publication précédente [58].

En nous appuyant sur l'ajustement développé dans cette étude, nous serons en mesure de contrôler davantage le flux d'entrée du diffuseur et de le perturber de manière ad hoc pour étudier l'effet des modulations de première harmonique sur le flux d'entrée moyen obtenu par l'ajustement.

Résultats et conclusions. Le champ d'écoulement dans une pompe centrifuge a été étudié de manière approfondie en combinant la modélisation théorique, les simulations URANS et les expériences (voir les détails dans la Sec. 3.1).

Une analyse théorique approfondie a été réalisée pour faire la lumière sur les mécanismes au cœur de cette instabilité. En utilisant le modèle bidimensionnel non visqeux de Tsujimoto et al. [1], nous avons démontré que le début du décrochage tournant est prédit par l'analyse de stabilité linéaire, en supposant que l'écoulement est homogène en θ. Cependant, l'approche linéaire 2D est incapable de déterminer le mode dominant, et l'interaction non linéaire entre les différents modes n'est pas non plus résolue. En outre, en effectuant une analyse du bilan énergétique sur la perturbation critique, nous avons démontré pour la première fois que l'instabilité à faible débit est produite par la contribution des mécanismes de 'left-up' et de décélération de l'écoulement ; de plus, nous avons écarté l'hypothèse d'un mécanisme de type centrifuge comme origine du décrochage tournant.

Pour comprendre l'effet de la modulation de l'écoulement entrant dans θ sur l'instabilité et l'interaction non-linéaire entre les différents modes d'instabilité, une simulation 2D d'ordre réduit qui considère un mode de Fourier imposé à l'écoulement entrant est réalisée. Les résultats montrent une bonne cohérence avec l'approche linéaire 2D. Les instabilités sont toutes cohérentes avec l'instabilité linéaire de l'écoulement moyen en 2D. En même temps, le mode de Fourier de l'écoulement entrant utilisé pour

modéliser le sillage de la roue peut déclencher d'autres modes instables. Cependant, il n'est pas clair si ces instabilités résultent toujours des mêmes mécanismes, des études numériques plus approfondies doivent être menées pour le comprendre.

En outre, pour étudier l'effet de la couche limite sur les instabilités, un modèle 3D d'ordre réduit est également simulé. Pour obtenir des conditions limites d'entrée du diffuseur plus réalistes, une méthode de modélisation est développée en ajustant la vitesse d'entrée du diffuseur dérivée des simulations numériques de l'ensemble de la machine. Les méthodes d'ajustement classiques utilisées pour approximer les profils d'écoulement par des polynômes algébriques ou des fonctions gaussiennes introduisent des artefacts numériques qui peuvent affecter de manière significative l'écoulement et donc sa stabilité. L'approche d'ajustement par correspondance d'échelle en plusieurs étapes développée dans cette étude est conçue comme une approximation robuste d'ordre successif des conditions d'écoulement, ce qui nous permet de prédire avec précision l'instabilité de l'écoulement se produisant dans le diffuseur de la pompe. Deux mécanismes d'instabilité différents sont dérivés de cette étape, l'un est l'instabilité du débit moyen à faible débit qui peut être correctement prédite par l'analyse de stabilité linéaire en 2D, et l'autre est associé à l'écoulement de sillage de jet. Pour cette dernière, le mécanisme d'instabilité a été retracé jusqu'à l'instabilité bidimensionnelle de sillage de jet rapportée par Ljevar et al. en vérifiant que nous obtenons un début paramétrique de l'instabilité ainsi qu'un nombre d'onde cohérent avec leurs prédictions. C'est la première fois qu'une telle instabilité rotative inattendue est rapportée dans un diffuseur 3D sans van à un grand débit $Q > Q_{\mathrm{D}}$.

Enfin, la simulation 3D de l'ensemble de la pompe est réalisée. L'effet de fuite produit par un jeu radial entre la roue et le diffuseur lisse est d'abord étudié. Trois géométries ont donc été considérées : (i) un cas de fuite nulle (cas idéal couramment simulé dans la littérature), un cas de fuite positive (correspondant à notre installation expérimentale), et (iii) un cas de fuite négative (le plus souvent utilisé dans les applications industrielles). Les simulations numériques ont d'abord été validées en les comparant aux expériences correspondantes. Les performances de la pompe et du diffuseur prédites par URANS sont en très bon accord avec les mesures expérimentales, avec une erreur maximale d'environ 5% observée pour les cas de fuite nulle et positive. De plus, l'apparition et les caractéristiques du décrochage tournant à faible débit observées dans les expériences ont été reproduites par nos simulations URANS. L'outil numérique validé a donc été utilisé pour étudier plus en profondeur les instabilités tournantes se produisant dans le diffuseur pour les trois configurations susmentionnées, en

prenant le cas idéal (c'est-à-dire le cas de fuite nulle) comme référence.

Les résultats de la simulation 3D de l'ensemble de la pompe montrent que l'instabilité à grand débit que nous avons identifiée dans la simulation 3D d'ordre réduit existe toujours dans le modèle réel de la pompe. Cette instabilité tournante a un impact majeur sur le débit moyen et est responsable d'une grande zone de séparation sur la paroi du diffuseur, côté moyeu. Par conséquent, les performances du diffuseur se dégradent considérablement. En outre, au moyen d'une analyse par ondelettes, nous avons identifié une instabilité secondaire pulsant et migrant de la couche de cisaillement du sillage de la roue vers la sortie du diffuseur. A la connaissance des auteurs, cette instabilité secondaire a été rapportée dans notre étude pour la première fois dans un diffuseur . Le même décrochage rotatif a été trouvé pour le cas de fuite négative au débit de conception ; cependant, la perturbation due à l'entraînement du débit de fuite était suffisamment forte pour perturber presque totalement l'instabilité secondaire, même s'il en reste une signature claire dans l'analyse des ondelettes. EN revanche, lorsqu'on considère un cas de fuite positive, la modification de l'angle de sillage du jet amène l'écoulement dans le régime stable, et aucun décrochage tournant n'est observé. Ceci est en accord avec la prédiction du modèle bidimensionnel de Ljevar et al. et est confirmé par nos expériences. Cela nous amène à la conclusion que même de petits écarts radiaux entre la roue et le diffuseur, comme l'écart de 1% que nous considérons, peuvent affecter l'écoulement de manière significative, comme l'ont également souligné d'autres études sur les configurations de turbomachines, et qu'ils doivent être inclus dans la conception de la pompe lors de l'optimisation numérique de son dessin.

En outre, nous avons constaté l'instabilité de l'écoulement moyen pour $\mathrm{Q} < 0{,}65Q_\mathrm{d}$. Ce décrochage tournant à faible débit a déjà été signalé dans la littérature par plusieurs auteurs (voir, par exemple, Dazin et al. [39, 10]), et un bon accord est trouvé également en termes de début d'instabilité (Barrand et al. rapporte un début à $\mathrm{Q} = 0{,}6Q_\mathrm{d}$). Le décrochage rotatif a été caractérisé numériquement pour nos trois configurations de fuite, et un bon accord qualitatif et quantitatif a été démontré en comparaison avec les mesures PIV rapportées dans la littérature et avec l'analyse FFT et par ondelettes réalisée dans nos expériences. En outre, en mettant arbitrairement à l'échelle la perturbation critique et en la superposant à l'état de base du modèle de Tsujimoto, il a été démontré un accord remarquablement bon avec nos résultats URANS moyennés par phase pour les conditions supercritiques. Cela confirme la conclusion selon laquelle le décrochage tournant émerge d'une instabilité de l'écoulement central et qu'il n'est pas influencé de manière significative par la présence de couches limites turbulentes

sur l'enveloppe et sur le moyeu du diffuseur. Nous soulignons que, même si les deux décrochages tournant sont des instabilités de l'écoulement central, ils sont essentiellement différents parce que le décrochage à faible débit ne nécessite pas d'écoulement de jet/sillage, mais dépend plutôt de l'asymétrie de l'écoulement à l'entrée du diffuseur.

Pour étudier l'effet du rapport d'aspect radial Γ sur les caractéristiques de l'instabilité, le rapport d'aspect radial varie dans la plage $\Gamma \in \{1.25, 1.5, 2\}$ et en ajustant le rapport d'aspect constant de la section transversale comme $\Lambda = 2(\Gamma - 1) \times 3,325$. Pour $\Gamma = 1.50$, nous avons d'abord signalé que l'instabilité du sillage se produit à un débit important ($Q/Q_{\mathrm{d}} \gtrsim 1$), ce qui déclenche une instabilité secondaire. Dans le cas d'une fuite nulle (conditions d'écoulement idéales), le modèle d'instabilité primaire avec un mode 7 est présent pour $\Gamma = 1.25$. Cependant, l'instabilité pulsatoire secondaire détectée pour $\Gamma = 1.5$ ne se produit pas pour $\Gamma = 1.25$. Lorsque le rapport d'aspect radial Γ augmente jusqu'à $\Gamma = 2$, les effets non linéaires prennent le dessus et un régime chaotique complexe entrave le modèle quasi-périodique observé avec les deux autres rapports d'aspect radial plus petits. Pour l'écoulement à fuite positive, le champ d'écoulement pour $\Gamma = 1.25$ est toujours chaotique sous l'effet de l'écoulement à fuite. Lorsque Γ augmente jusqu'à $\Gamma = 1.5$, nous avons trouvé les modèles d'instabilité jet-sillage à périodicité 7 observés pour le cas de fuite nulle. En outre, deux modèles d'instabilité 1-périodique se propagent avec la même vitesse de propagation mais dans des directions opposées dans un cadre de référence tournant avec Ω, en raison de l'écoulement de fuite (voir Fan *et al.* [60]). Pour $\Gamma = 2$, une instabilité de Kelvin-Helmholtz stable et quadri-périodique est signalée pour la première fois. En ce qui concerne l'instabilité bien connue à faible débit ($Q/Q_{\mathrm{d}} \lesssim 0.65$), ses caractéristiques sont significativement affectées par le rapport d'aspect du rayon Γ, en particulier en termes de nombre d'ondes, qui passe de 4 à 3 puis à 2 pour $\Gamma = 1.25$, 1.5, et 2, respectivement. En outre, le nombre de modes d'instabilité et la vitesse de propagation se révèlent également très sensibles au débit de fuite à l'entrée pour $\Gamma = 2$. Les diffuseurs courts ($\Gamma = 1.25$) sont plus stables que les autres diffuseurs, ce qui correspond bien aux résultats de l'analyse de stabilité linéaire. De plus, l'écoulement de fuite entraîne une augmentation de l'angle de l'écoulement d'entrée. Par conséquent, l'instabilité est entièrement supprimée.

Pour étayer ces conclusions, nous résumons une partie de nos résultats dans la Fig. 4.1 qui représente les limites de stabilité dans l'espace paramétrique, en mettant en évidence la nature des instabilités identifiées par les différentes approches.

Travaux futurs. Diverses pistes pour approfondir le travail de recherche développé dans ce manuscrit sont détaillées ci-dessous. Tout d'abord, il sera intéressant d'effectuer des simulations numériques pour les modèles 2D et 3D d'ordre réduit avec de nouvelles conditions limites d'entrée, par exemple les sillages d'entrée non modaux utilisés par Levjar et al. [26]. Cela peut aider à mieux comprendre comment les conditions limites d'entrée peuvent affecter l'instabilité et à clarifier si l'instabilité est principalement due à des effets 3D ou à un mécanisme 2D. Ensuite, une inspection plus poussée de l'instabilité de Kelvin-Helmholtz observée dans les résultats de la simulation 3D avec $\Gamma = 2.00$ pourrait confirmer le mécanisme d'instabilité supposé. Ensuite, nous pouvons caractériser les composantes du bilan énergétique conduisant à un transfert d'énergie de l'état de base bidimensionnel à la perturbation du sillage du jet. Enfin, plusieurs améliorations du banc d'essai peuvent être proposées. La première pourrait consister à tester des diffuseurs avec différents rapports de rayon pour confirmer les résultats numériques. La deuxième pourrait consister à modifier les conditions de fuite à l'entrée du diffuseur. Une dernière modification pourrait être l'installation d'une vanne de contrôle du débit d'entrée. Cela nous permettra d'effectuer des mesures expérimentales plus continues et des comparaisons plus qualitatives et quantitatives entre les résultats expérimentaux et numériques.

Arts et Métiers Sciences et Technologies

Meng FAN

Instabilités tournantes dans un diffuseur lisse de machine centrifuge

HESAM UNIVERSITÉ

Résumé: Les instabilités des écoulements dans un diffuseur lisse d'une machine centrifuge sont étudiées théoriquement, numériquement et expérimentalement. Sous l'hypothèse d'un écoulement 2D, (i.e. loin des couches limites) la stabilité de chaque mode de décrochage a été étudiée par analyse linéaire, et les composantes du bilan énergétique conduisant à un transfert d'énergie de l'état de base à la perturbation infinitésimale la plus dangereuse sont caractérisées. En considérant les effets des interactions non linéaires et de l'écoulement inhomogène en θ, des simulations numériques sont effectuées pour un modèle 2D d'ordre réduit avec un mode de Fourier imposé sur l'écoulement pour modéliser l'effet du sillage. En outre, une simulation 3D est également réalisée pour étudier l'effet de la couche limite sur les instabilités. Pour produire les conditions limites d'entrée du diffuseur, une approche d'adaptation d'échelle en plusieurs étapes est développée pour déterminer la vitesse de l'écoulement entrante. Elle est dérivée des simulations RANS de l'ensemble de la machine. Enfin, des simulations URANS et des expériences sur l'ensemble de la pompe ont été réalisées, en se concentrant particulièrement sur l'effet sur les instabilités des fuites entre la roue et le diffuseur et l'effet du rapport d'aspect radial du diffuseur.

Mots clés: Décrochage tournant, Instabilités, Diffuseur lisse, Machine centrifuge, Simulation numérique.

Abstract: The flow instabilities in a vaneless diffuser of a radial flow machine are theoretically, numerically, and experimentally investigated. Under the hypothesis of a 2D core flow mechanism, the stability of each stall mode was studied by linear analysis, and the components of the energy budget leading to a transfer of energy from the basic state to the most dangerous infinitesimal perturbation are characterized. Considering the effects of the non-linear interactions and of an inhomogeneous inflow in θ, numerical simulations are performed for a reduced-order 2D model with a Fourier mode imposed on the inflow to mimic the jet wake pattern. Moreover, a reduced-order 3D simulation is also carried out to study the boundary layer effect on the instabilities. To produce the inflow boundary conditions, a multi-stage scale-matching fitting approach is developed to fit the diffuser inflow velocity. It is derived from RANS simulations of the entire machine. Finally, URANS simulations and experiments are conducted on the entire pump, especially focusing on the effect of impeller-to-diffuser leakage and the effect of the radial aspect ratio on the instabilities.

Keywords: Rotating stall, Instabilities, Vaneless diffuser, Centrifugal machine, Numerical simulation.